National Technical University of Athens

School of Chemical Engineering

Doctoral Thesis

Design of micro- and nano-structured surfaces with tunable wettability

by

Nikolaos T. Chamakos

Supervisor:

Assist. Prof. Athanasios G. Papathanasiou

March 22, 2017

Εθνικο Μετσοβιο Πολυτεχνειο

Σχολη Χημικων Μηχανικων

Διδακτορικη Διατριβη

Σχεδιασμός μικρο- και νανο-δομημένων επιφανειών με ελεγχόμενη διαβρεκτικότητα

του

Νικολάου Θ. Χαμάκου

Επιβλέπων:

Επίκ. Καθ. Αθανάσιος Γ. Παπαθανασίου

22 Μαρτίου 2017

Examination committee

- **Athanasios G. Papathanasiou**, Assistant Professor, National Technical University of Athens (NTUA)
- **Andreas G. Boudouvis**, Professor, NTUA
- **Evangelos Gogolides**, Director of Research, Institute of Nanoscience and Nanotechnology, NCSR "Demokritos"
- **Doros N. Theodorou**, Professor, NTUA
- **Periklis Papadopoulos**, Assistant Professor, University of Ioannina
- **Antonis Karantonis**, Assistant Professor, NTUA
- **Nikolaos M. Tsoukias**, Associate Professor, NTUA

To my family, Thodoris Chamakos, Anastasia, Giota for their ceaseless support and to Antonia Theofani for all her love and encouragement throughout these years.

Also, to those who struggle, with Sisyphean patience, for "unreachable" tasks.

Abstract

The original contribution of this Thesis in scientific knowledge is the development of a novel, continuum-level, sharp-interface modeling approach, which has been proven particularly efficient for simulating wetting phenomena on complex (geometrically or chemically textured) solid surfaces. The above task is particularly useful for the rational design and optimization of solid surfaces with tailor-made and tunable wetting behavior. Such micro- and nano-structured surfaces have been observed in a variety of plants and living organisms, endowed with fascinating wetting properties. Some examples are the lotus leaf (*Nelumbo nucifera*), known for its self-cleaning ability, the desert beetle (*Stenocara gracilipes*) which uses its body surface as fog collector, and the wings of the *Morpho aega* butterfly that are covered with asymmetric micro-structures exhibiting anisotropic flow friction. The latter is essential for maintaining flying stability at the butterfly's humid habitat. The design of such artificially micro- and nano-patterned surfaces, inspired by the natural ones, has a great technological impact and could be exploited, among others, for reducing drag in ship hulls, transporting liquids in miniaturized lab-on-a-chip devices and collecting fresh water from fog in arid areas. Despite their significance, the above-mentioned applications are, however, limited due to severe restrictions in the micro-fabrication methods as well as the inadequate capability to precisely model the liquids behavior on complex, micro-textured surfaces (considering that a geometrically patterned substrate can accommodate a large cardinality of meta-stable wetting states). The method presented in this Thesis contributes to the tackling of the latter limitation, enabling the efficient modeling of both statics and dynamics of wetting on any kind of heterogeneous surface.

The conventional modeling approaches of wetting phenomena have been proven insufficient for the design of such functional surfaces since: either they fail to adequately describe the complicated behavior of a droplet on a rough substrate, or demand vast computational resources for real-life applications with millimeter-sized droplets. On one hand, the main drawback of the continuum-level approaches is the tedious implementation of explicit boundary conditions to an *a priory* unknown number of the droplet's three-phase contact lines (where the three different phases, liquid-ambient-solid, meet). On the other hand, the fine scale approaches (lattice-Boltzmann, molecular dynamics), usually implemented for the same task, do not suffer from the above restriction, however, demand prohibitively high computational power. In order to overcome these limitations, in this Thesis we propose a new continuum-level approach where a unified formulation (avoiding the boundary conditions at the three-phase contact lines)

for the liquid-ambient and liquid-solid interfaces of the droplet is adopted. In addition, the material wettability, in our approach, is determined by micro-scale liquid-solid interactions. This way, we bypass the implementation of any explicit boundary condition at each three-phase contact line, thus enabling the efficient simulation of entire millimeter-sized droplets on structured substrates. The proposed formulation can be used to perform both static (by reformulating the Young-Laplace equation, which states the force balance along a droplet surface) and dynamic wetting computations (by modifying the Navier-Stokes equations in the hydrodynamic model).

The efficiency of the proposed method is initially demonstrated by computing multiple meta-stable equilibrium wetting states of droplets resting on geometrically patterned solid surfaces. We also present the evaluation of the energy barriers, separating the meta-stable wetting states, the height of which is of utmost importance for designing robust water-repellent surfaces, inspired by the lotus leaf. We also successfully compare our results against the a conceptually different mesoscopic lattice-Boltzmann model. Then, we utilize the proposed formulation to simulate the electrowetting phenomenon (where the shape of the droplet is modified by applying an electric field) on structured solid dielectric surfaces. Additionally, based on the above electrowetting simulations, we experimentally demonstrate the real-time tuning of the wettability of structured surfaces. The proposed formulation is also utilized to perform dynamic simulations of droplets impacting and spreading on geometrically complex substrates -an essentially tedious task for conventional hydrodynamic models. It is notable here that our predictions totally agree with corresponding experimental measurements. We then examine the droplet motion on asymmetrically structured substrates, inspired by the *Morpho aega* butterfly wings, under the influence of forced vibrations. The latter methodology can be used to transfer droplets in miniaturized devices. By studying these problems, we demonstrate that our modeling approach can be utilized as an exceptional tool for designing functional structured surfaces that can be potentially used in technological applications.

Περίληψη

Η συνεισφορά της παρούσας διδακτορικής διατριβής στην υπάρχουσα επιστημονική γνώση είναι η ανάπτυξη μίας νέας μεθοδολογίας, συνεχούς μέσου, για τη μοντελοποίηση φαινομένων διαβροχής σε σύνθετες (τραχιές ή χημικά ετερογενείς) στερεές επιφάνειες, βασιζόμενη στη θεώρηση της διεπιφάνειας μηδενικού πάχους (sharp-interface). Αυτή η προσέγγιση είναι εξαιρετικά σημαντική για τον σχεδιασμό και τη βελτιστοποίηση της τραχύτητας στερεών επιφανειών με επιθυμητή και πλήρως ελεγχόμενη διαβρεκτικότητα. Αντίστοιχες μικρο- και νανο-δομημένες επιφάνειες συναντώνται σε πολλά φυσικά συστήματα, προσδίδοντας τους αξιοζήλευτες διαβρεκτικές ιδιότητες. Τέτοια παραδείγματα είναι το φύλλο του λωτού (*Nelumbo nucifera*) που έχει τη δυνατότητα αυτοκαθαρισμού με το νερό της βροχής, το σκαθάρι της ερήμου (*Stenocara gracilipes*) που συλλέγει πόσιμο νερό αξιοποιώντας την πρωινή ομίχλη και το φτερό της πεταλούδας *Morpho aega,* το οποίο καλύπτεται με κεκλιμένες, ασύμμετρες, μικρο-δομές που ευνοούν την αποβολή της υγρασίας και συνεπώς ενισχύουν την πτητική της ικανότητα. Ο σχεδιασμός τεχνητών μικρο- και νανο-δομημένων επιφανειών, με πρότυπο τις φυσικές μορφολογίες, είναι πολύ σημαντικός σε επίπεδο τεχνολογικών εφαρμογών όπως, μεταξύ άλλων, για τη μείωση της αντίστασης τριβής του νερού στο κύτος πλοίων, για τη διαχείριση υγρών σε μικρο-συσκευές αναλύσεων (lab-on-a-chip) και για τη συλλογή πόσιμου νερού από τα σταγονίδια της ομίχλης σε περιοχές με λειψυδρία. Η υλοποίηση των παραπάνω εφαρμογών, ωστόσο, δεν έχει ακόμα πλήρως επιτευχθεί λόγω περιορισμών στις μεθόδους κατασκευής τεχνητών μικρο- και νανο-δομημένων επιφανειών, καθώς και λόγω των ανεπαρκών δυνατοτήτων για ακριβή μοντελοποίηση της συμπεριφοράς υγρών σε τέτοιες σύνθετες επιφάνειες (δεδομένου ότι μια τραχιά επιφάνεια μπορεί να φιλοξενήσει ένα μεγάλο πλήθος μετασταθών καταστάσεων διαβροχής). Η μέθοδος που προτείνεται σε αυτή τη διατριβή συμβάλλει ουσιαστικά στην αντιμετώπιση του τελευταίου περιορισμού, επιτρέποντας τη μοντελοποίηση τόσο της στατικής όσο και της δυναμικής διαβρεκτικότητας σε κάθε είδους ετερογενή επιφάνεια.

Οι συμβατικές μεθοδολογίες μοντελοποίησης των φαινομένων διαβροχής αποδεικνύονται ως ανεπαρκή εργαλεία για τον σχεδιασμό της μικρο-δομής των παραπάνω επιφανειών καθώς: είτε αποτυγχάνουν να περιγράψουν επαρκώς την περίπλοκη συμπεριφορά μιας σταγόνας σε ένα τραχύ υπόστρωμα, ή έχουν απαγορευτικά μεγάλο υπολογιστικό κόστος για σταγόνες συνηθισμένου μεγέθους (ακτίνας μερικών χιλιοστών). Αφενός μεν, τα μοντέλα συνεχούς μέσου περιορίζονται λόγω της ανάγκης εφαρμογής συνοριακών συνθηκών σε πολλαπλές (άγνωστες σε αριθμό)

γραμμές επαφής των τριών φάσεων (υγρού-στερεού-αέρα) της σταγόνας. Αφετέρου δε, τα μοντέλα μέσο- (lattice-Boltzmann) ή νάνο- (molecular dynamics) κλίμακας, που χρησιμοποιούνται συνήθως για τέτοιου είδους προβλήματα, ξεπερνούν τον παραπάνω περιορισμό, εντούτοις έχουν απαγορευτικά μεγάλες υπολογιστικές απαιτήσεις. Για να αντιμετωπιστούν τα παραπάνω προβλήματα, σε αυτή τη διδακτορική διατριβή προτείνεται μια νέα μεθοδολογία συνεχούς μέσου, στην οποία υιοθετείται μια ενιαία αντιμετώπιση (αποφεύγοντας τις συνοριακές συνθήκες στις γραμμές επαφής) για τις διεπιφάνειες υγρού-αέρα και υγρού-στερεού της σταγόνας. Επίσης, η διαβρεκτικότητα του στερεού, στην προτεινόμενη προσέγγιση, καθορίζεται πλέον από διαμοριακές αλληλεπιδράσεις μεταξύ στερεής και υγρής φάσης. Με την παραπάνω θεώρηση, καθίσταται μη αναγκαία η εφαρμογή οποιασδήποτε συνοριακής συνθήκης στις γραμμές επαφής των τριών φάσεων, επιτρέποντας έτσι την προσομοίωση ολόκληρων σταγόνων (ακτίνας μερικών χιλιοστών) σε στερεές επιφάνειες με τραχύτητα. Η παραπάνω προσέγγιση μπορεί να εφαρμοστεί τόσο για υπολογισμούς ισορροπίας σταγόνων (επαναδιατυπώντας την εξίσωση Young-Laplace, η οποία διέπει την μηχανική ισορροπία της επιφάνειας της σταγόνας) όσο και για δυναμικές προσομοιώσεις (τροποποιώντας τις εξισώσεις ροής (Navier-Stokes) στο υδροδυναμικό μοντέλο).

Η προτεινόμενη μεθοδολογία προσομοίωσης χρησιμοποιήθηκε αρχικά για την εύρεση πολλαπλών μετασταθών καταστάσεων ισορροπίας σταγόνων σε στερεές επιφάνειες με τραχύτητα. Επιπλέον, παρουσιάστηκε ο υπολογισμός των ενεργειακών φραγμάτων που διαχωρίζουν τις παραπάνω καταστάσεις ισορροπίας. Το ύψος των ενεργειακών φραγμάτων είναι εξαιρετικά σημαντικό για τον σχεδιασμό αυτοκαθαριζόμενων επιφανειών, με πρότυπο το φύλλο του λωτού. Παρατηρήθηκε επίσης, ότι τα αποτελέσματα της προτεινόμενης μεθόδου συμφωνούν με αντίστοιχα αποτελέσματα από υπολογισμούς μέσο-κλίμακας (lattice-Boltzmann), παρ' όλες τις θεμελιώδεις διαφορές στις δύο προσεγγίσεις. Στη συνέχεια χρησιμοποιήσαμε την προτεινόμενη μεθοδολογία για να μελετήσουμε συστήματα ηλεκτροδιαβροχής (electrowetting) (όπου το σχήμα της επιφάνειας της σταγόνας μεταβάλλεται με την εφαρμογή ηλεκτρικού πεδίου) σε περιπτώσεις όπου σταγόνες διαβρέχουν τραχιές διηλεκτρικές επιφάνειες. Επιπρόσθετα, βασιζόμενοι στις παραπάνω προσομοιώσεις συστημάτων ηλεκτροδιαβροχής, επαληθεύσαμε πειραματικά τον δυναμικό έλεγχο των διαβρεκτικών ιδιοτήτων μικρο-δομημένων επιφανειών. Η προτεινόμενη προσέγγιση εφαρμόστηκε επίσης με επιτυχία για τη μελέτη της δυναμικής συμπεριφοράς σταγόνων που προσκρούουν σε τραχιές επιφάνειες. Συγκεκριμένα, παρατηρήθηκε ότι οι υπολογιστικές μας προβλέψεις συμφωνούν, με μεγάλη ακρίβεια, με αντίστοιχες πειραματικές μετρήσεις. Στη συνέχεια μελετήθηκε η μετακίνηση σταγόνων, υπό την επίδραση εξαναγκασμένων ταλαντώσεων, σε επιφάνειες με ασύμμετρη τραχύτητα, έχοντας ως πρότυπο τη μορφολογία του φτερού της πεταλούδας *Morpho aega.* Η συγκεκριμένη τεχνική μπορεί να εφαρμοστεί για τη μεταφορά υγρών σε μικρο-συσκευές. Με τη μελέτη των παραπάνω προβλημάτων, αποδεικνύεται ότι η προτεινόμενη μεθοδολογία

είναι ένα πολύτιμο εργαλείο για τον σχεδιασμό της μικρο-δομής επιφανειών με πλήρως ελεγχόμενη διαβρεκτικότητα, απαραίτητες σε τεχνολογικές εφαρμογές.

Contents

Preface

Multidisciplinary teams of scientists and engineers are currently working on wetting and capillary phenomena research; indicatively we mention physicists, mathematicians, biologists, chemical, metallurgical and mechanical engineers. Why a chemical engineer, however, is interested in wetting phenomena? A chemical engineer cares about technological applications that involve exchange of momentum, mass, energy as well as material properties. Wetting phenomena is a relatively new frontier that definitely comprise all of the above. The research on wetting phenomena aims to initially understand the underlying physics and then to fabricate smart, functional, micro-textured surfaces with desirable wetting properties. Such examples were firstly observed in nature, e.g. the fascinating self-cleaning properties of the lotus leaf. At this juncture, we are a screwdriver's turn away from mimicking or even surpassing nature's magnificent creations, however, this last turn is proving to be rather tedious. What impedes us are the emerging limitations in the micro-fabrication methods as well as the currently inadequate capability to efficiently predict the behavior of liquids on such micro-textured surfaces. The latter is a highly tedious task, considering the several meta-stable equilibrium droplet shapes that can be accommodated on a certain structured substrate as well as the possible dynamic transitions between these states. Overall, the modeling of such wetting phenomena is of utmost importance since it would enable us to design and optimize surfaces, featuring tailor-made wetting behavior, without fabricating tons of trial cases. Here, in this Thesis, we present a novel modeling approach which, unlike the current conventional methodologies, is proved to be particularly efficient for such applications. Specifically, the current Thesis is organized in four parts as follows:

- Part I: *Theory and modeling of wetting phenomena* (Chapters 1, 2, 3). In Chapter 1 we demonstrate several examples of natural surfaces with fascinating wetting properties. We also present some currently available technological applications, inspired by these natural examples, as well as interesting future challenges. In Chapter 2 we present the basic theoretical concepts of wetting and capillary phenomena. We also demonstrate the conventional models for describing the equilibrium shape of droplets, particularly focusing on heterogeneous (geometrically structured) solid surfaces. Then, we introduce a novel modeling approach, by explaining its advantages when dealing with complex surface topographies. In Chapter 3 we focus on the dynamic behavior of droplets. In particular, after demonstrating the conventional formulations for predicting the droplet dynamics on structured substrates, we present our advantageous modeling suggestion.

- Part II: *Static computations* (Chapters 4, 5). Chapter 4 includes computational predictions of the proposed model for the equilibrium of sessile droplets on flat as well as geometrically structured solid surfaces. In particular, we initially successfully validate our method against a conceptually different, mesoscopic modeling approach. Then, we demonstrate the computation of co-existing, meta-stable droplet shapes on structured substrates, that have also been observed experimentally. In Chapter 5 we augment our model with electric stresses, derived from the electrostatics equations, in order to predict the droplet equilibrium behavior under the effect of electric field (electrowetting phenomenon) on a textured solid dielectric surface. This actuation technique is commonly used to actively control the wetting properties of surfaces in technological applications.

- Part III: *Dynamic computations* (Chapters 6, 7). In Chapter 6 we utilize the proposed formulation in order to perform dynamic simulations of axisymmetric droplets spreading on solid substrates covered with arbitrary asperities. We initially successfully compare our results against experimental measurements. Then, we examine the early spreading dynamics ($t \sim 10$ ms) on a variety of textured surfaces, concluding that a universal law is obeyed for all cases, as was also observed in recent experiments. In Chapter 7 we examine the dynamics of droplets on substrates with asymmetric textures (inspired by surfaces found in nature), under the effect of a periodic force induced by oscillating the bottom plate. Such a technique can be exploited in order to transfer droplets more efficiently in contemporary applications.

- Part IV: *Conclusions and future perspectives* (Chapters 8, 9). Chapter 8 includes concluding annotations, concerning the advantages of the proposed method for modeling static and dynamic wetting phenomena. Finally, early experimental validations of our model's innovative predictions and suggestions regarding the future research are presented in Chapter 9.

- Part V: *Appendices.* Appendix A contains supplementary material for Part I, Appendix B for Part II, Appendix C for Part III and Appendix D for Part IV, respectively.

We also note that for the shake of readability, each of the five Parts of the current Thesis contains a separate References Chapter.

Publications

The results in this Thesis have been presented in the following publications and conferences:

In peer-reviewed journals

- G. Karapetsas, N. T. Chamakos and A. G. Papathanasiou, "Thermocapillary droplet migration on structured surfaces", *to be submitted*, (2017).
- M. E. Kavousanakis, N. T. Chamakos, K. Ellinas, A. Tserepi and A. G. Papathanasiou, "How to make reversible electrowetting on superhydrophobic surfaces", *to be submitted*, (2017).
- N. T. Chamakos, G. Karapetsas and A. G. Papathanasiou, "How asymmetric surfaces induce directional droplet motion", *Colloids and Surfaces A: Physicochemical and Engineering Aspects*, 511 (2016), pp. 180-189.
- G. Karapetsas, N. T. Chamakos and A. G. Papathanasiou, "Efficient modelling of droplet dynamics on complex surfaces", *Journal of Physics: Condensed Matter*, 28.8 (2016), p. 085101.
- N. T. Chamakos, M. E. Kavousanakis, A. G. Boudouvis and A. G. Papathanasiou, "Droplet spreading on rough surfaces: Tackling the contact line boundary condition", *Physics of Fluids*, 28.2 (2016), p. 022105.
- M. E. Kavousanakis, N. T. Chamakos and A. G. Papathanasiou, "Connection of Intrinsic Wettability and Surface Topography with the Apparent Wetting Behavior and Adhesion Properties", *The Journal of Physical Chemistry C*, 119.27 (2015), pp. 15056-15066.
- N. T. Chamakos, M. E. Kavousanakis and A. G. Papathanasiou, "Neither Lippmann nor Young: Enabling Electrowetting Modeling on Structured Dielectric Surfaces", *Langmuir*, 30.16 (2014), pp. 4662-4670.
- N. T. Chamakos, M. E. Kavousanakis and A. G. Papathanasiou, "Enabling efficient energy barrier computations of wetting transitions on geometrically patterned surfaces", *Soft Matter*, 9.40 (2013), pp. 9624-9632.

International conferences

- V. Charitatos, N. T. Chamakos, A. G. Papathanasiou, "Droplet mobility on rough substrates: Effect of the ambient phase", *11^{th} HSTAM International Congress on Mechanics*, Athens, Greece, 27 - 30 May, 2016.
- N. T. Chamakos, G. Karapetsas, A. G. Papathanasiou, "Modeling of droplet mobility on bio-inspired asymmetrically structured substrates", *Smart and Green Interfaces Conference*, Athens, Greece, 4 - 6 May, 2016.
- G. Karapetsas, N. T. Chamakos, A. G. Papathanasiou, "Effect of substrate topography on the thermocapillary migration of droplets under microgravity", *22^{nd} ELGRA*

Symposium and General Assembly, Corfu, Greece, 29 September - 1 October, 2015.

- N. T. Chamakos, G. Karapetsas, M. E. Kavousanakis and A. G. Papathanasiou, "Efficient modeling of droplet spreading on rough surfaces", *8th GRACM International Congress on Computational Mechanics*, Volos, Greece, 12 - 15 July, 2015.
- A. G. Papathanasiou, M. E. Kavousanakis, N. T. Chamakos, "Reversible electrowetting on rough surfaces", *6th International Workshop on Bubble and Drop Interfaces*, Potsdam-Golm, Germany, 6 - 10 July, 2015.
- G. Karapetsas, N. T. Chamakos, M. E. Kavousanakis and A. G. Papathanasiou, "Modeling of dynamic contact lines", *Smart and Green Interfaces Conference, Joint with COST MP1106 Annual MC meeting*, Belgrade, Serbia, 30 March - 1 April, 2015.
- N. T. Chamakos, A. J. Petsi, M. E. Kavousanakis and A. G. Papathanasiou, "Effect of solid surface topography on the dynamics of droplet spreading assisted by electrowetting" (poster), *9th International Meeting on Electrowetting and Related Micro/Electrofluidic Science and Technology*, Cincinnati, Ohio, USA, 23 - 25 June, 2014.
- N. T. Chamakos, M. E. Kavousanakis and A. G. Papathanasiou, "Modeling contact angle hysteresis on flat and geometrically patterned solid surfaces" (poster), *555th WE-Heraeus-Seminar*, Bad Honnef, Germany, 16 - 19 March, 2014.
- M. E. Kavousanakis, N. T. Chamakos and A. G. Papathanasiou, "Surface topography design through efficient computation of wetting transitions energy barriers" (poster), *555th WE-Heraeus-Seminar*, Bad Honnef, Germany, 16 - 19 March, 2014.
- D. P. Papageorgiou, N. T. Chamakos, A. Syrigou and A. G. Papathanasiou, "Effect of the surrounding medium on the contact angle saturation: leakage current measurements and simulations" (poster), *8th International Meeting on Electrowetting*, Athens, Greece, 21 - 23 June, 2012.
- N. T. Chamakos, A. G. Boudouvis and A. G. Papathanasiou, "Simulation of electrowetting beyond the Lippmann equation" (poster), *7th Chemical Engineering Conference for Collaborative Research in Eastern Mediterranean Countries*, Corfu, Greece, 27 April - 1 May, 2012.

Greek conferences

- N. T. Chamakos, G. Karapetsas, M. E. Kavousanakis and A. G. Papathanasiou, "Droplet passive movement on asymmetric patterned surfaces", *10th Panhellenic Scientific Chemical Engineering Congress*, Patras, 4 - 6 June, 2015.
- G. Karapetsas, N. T. Chamakos and A. G. Papathanasiou, "Modelling droplet interaction with flat or structured solid surfaces", *10th Panhellenic Scientific Chemical*

Engineering Congress, Patras, 4 - 6 June, 2015.

- N. T. Chamakos, M. E. Kavousanakis and A. G. Papathanasiou, "Equilibrium of droplets on micro/nano-structured surfaces: Reformulating the Young-Laplace equation", *9th Panhellenic Scientific Chemical Engineering Congress*, Athens, 23 - 25 May, 2013.

Acknowledgements

The completion of this Thesis would not be possible without the contribution of the following professors, colleagues and friends:

I would like to express my deepest appreciation to my supervisor, Assist. Prof. Thanasis Papathanasiou, for his support and guidance all these years. He supplied me with valuable knowledge regarding the computational analysis as well as experimental research. One of the most important lessons I learned is to address scientific problems with an engineering perspective.

Special thanks to Prof. Andreas Boudouvis, member of the examination committee, for giving me the impetus to start working in this topic. This Thesis could not be completed without his guidance on theoretical, computational and philosophical issues.

I would like to thank Prof. Doros Theodorou and Dr Evangelos Gogolides, also members of the examination committee of my doctoral candidacy, for their knowledge and advice offered me.

I am indebted to Dr Mihalis Kavousanakis for tutoring me in the finite element computations, programming and scientific thinking, as well as for the patience he showed when training me.

I would like to thank Dr George Karapetsas for his guidance regarding computational analysis and dynamic modeling.

I wish to thank Dr George Kokkoris, from the Institute of Nanoscience and Nanotechnology, NCSR "Demokritos", for our constructive discussions, especially in the beginning of my PhD studies.

I would like to thank Dr George Pashos for his valuable support and guidance in computations as well as in side-work projects.

I wish to thank Dr Antony Spyropoulos for tutoring me in Linux systems and Fortran programming.

Many thanks go to Dr Giannis Aviziotis for his encouragement all these years. In addition, I wish to thank the graduate student Vassilis Charitatos, Dr Dimitris Papageorgiou and Dr Anastasia Petsi for the excellent cooperation.

I wish also to thank Dr Kosmas Ellinas, from the Institute of Nanoscience and Nanotechnology, NCSR "Demokritos", for fabricating the substrates used in electrowetting experiments in Section 9.1.

I kindly acknowledge funding from the European Research Council Starting Grant of my supervisor, Assist. Prof. A. G. Papathanasiou, under the Europeans Community's Seventh Framework Programme (FP7/2007-2013)/ERC grant agreement no. [240710].

Lastly, many thanks to all those who contributed, in any way, for the completion of this Thesis and I did not mention explicitly.

N. T. Chamakos

March 22, 2017

Nomenclature

Following is a list of symbols used frequently in this Thesis. Some symbols that appear only in one chapter are not included. Note that, in general, vectors are denoted with bold font.

Roman letters

A	substrate oscillation amplitude
A_{LA}	liquid-ambient interfacial area
A_{LS}	liquid-solid interfacial area
A_{SA}	solid-ambient interfacial area
A_{droplet}	droplet's cross-sectional area
C	local mean curvature
C_1, C_2	parameters controlling the disjoining pressure range
Ca	capillary number
d	distance between the solid protrusions (usually) or dielectric thickness in Chapter 5
D_0	characteristic droplet diameter
E	surface energy (usually) or electric field strength in Chapter 5
E_{diss}	dissipated energy
F	retention force that resists droplet motion
f	oscillation frequency
f_{res}	resonance frequency
g	gravitational constant
$\boldsymbol{g}$	gravitational acceleration
h	height of the solid protrusions

H_a	Hamaker constant
K	reference pressure
K_s	power law prefactor
L_s	slip length
M_droplet	droplet's mass
$\boldsymbol{n}$	unit normal of the liquid-ambient interface
$\boldsymbol{n}_\mathrm{s}$	unit normal of the solid surface
N_e	electric bond number
N_g	gravitational bond number
p	liquid pressure
p^LS	disjoining pressure
p_el	electrostatic pressure
$\boldsymbol{R}$	Galerkin residuals vector
R_0	characteristic droplet radius
R_cl	contact radius of the droplet and the solid surface, in equilibrium
R_s	dynamic contact radius
Re	Reynolds number
r_f	roughness factor
s	arc-length of the effectively one-dimensional droplet surface (usually) or scale factor of the solid structure in Chapter 7
$\boldsymbol{s}$	total stress tensor
S_LS	spreading coefficient
t	time
t_c	inertio-capillary time
$\boldsymbol{t}$	unit tangent of the liquid-ambient interface
T_f	oscillation period
T_res	oscillation period corresponding to the resonance
$\boldsymbol{u}$	fluid velocity field
u_x	horizontal component of the velocity field (u_r, in an axially symmetric case)
u_z	vertical component of the velocity field
u_mean	mean droplet velocity
u	electric potential
u_{cl}	contact line velocity
u_0	characteristic velocity
$\boldsymbol{U}$	solution vector
V	applied voltage
V_droplet	droplet's volume
w	width of the solid protrusions
w^LS	wetting parameter
W	work
We	Weber number
x_cm	droplet's center of mass (the horizontal position)

Greek letters

α	spreading exponent (usually) or tilt angle of the solid surface in Chapter 7
β_{eff}	effective slip coefficient
β_{LS}	slip parameter
γ_{LA}	liquid-ambient interfacial tension
γ_{LS}	liquid-solid interfacial tension
$\gamma_{\mathrm{LS}}^{\mathrm{eff}}$	effective (incorporating electrostatic forces) liquid-solid interfacial tension
γ_{SA}	solid-ambient interfacial tension
δ	Euclidean distance between the liquid and the solid phases
Δp	pressure jump across the droplet surface
$\Delta\rho$	density difference between the liquid and ambient
ϵ	disjoining pressure parameter
ϵ_0	vacuum permittivity
ϵ_r	dielectric constant (ϵ_s for the ambient phase and ϵ_d for the solid dielectric)
η	electrowetting number
θ_{Y}	Young's contact angle
θ_{a}	apparent (mascroscopic) contact angle
θ_{d}	dynamic contact angle
θ_{adv}	advancing contact angle
θ_{rec}	receding contact angle
λ_κ	capillary length
λ_F	relative strength of the electric stress over the disjoining pressure
μ	dynamic viscosity
ρ	fluid density
σ	disjoining pressure parameter
$\boldsymbol{\tau}$	viscous stress tensor
τ_{nn}	normal stress
τ_{nt}	shear stress
ϕ	viscous dissipation function
ϕ^{k}	basis functions of the Finite Element Method
ϕ_{s}	fraction of solid in contact with the liquid
ω	effective interface potential (usually) or angular frequency in Chapter 7
ω^*	modified (incorporating electrostatic forces) effective interface potential
ω_0	resonance angular frequency

Special symbols

$\cdot$	dot product operator
:	double-dot product operator
$\times$	vector product operator (usually) or multiplication sign of scalars

∇	gradient operator
∇_s	surface gradient operator
$\nabla \cdot$	divergence operator
∇^2	Laplacian operator
$\widehat{\ }$	dimensionless quantity

PART I

Theory and modeling of wetting phenomena

CHAPTER 1

Introduction

In this Chapter we highlight several examples of functional micro- and nano-textured surfaces found in nature, which are expected to benefit various technological applications. The most famous example is the lotus leaf, which has the ability to self-clean. Among others, the potential uses of such bioinspired materials include drag reduction during moving in water, liquid transport in lab-on-a-chip devices and collecting water from fog in arid areas. We present the contribution of computational modeling in the potential applications, as well as the limitations of the current approaches. Finally, we discuss the impact of the current Thesis in both fields of applied and theoretical research in wetting and capillary phenomena.

1.1 From natural surfaces to applications

Micro- and nano-textured surfaces, which appear in a variety of living organisms and plants, feature fascinating or even enviable properties such as self-cleaning, directional liquid transport, anti-icing and drag reduction. One of the most famous examples of structured morphology is the leaf of *Nelumbo nucifera* (or simply lotus) (see Fig. 1.1a) which is known, even from the Asian traditions, for its self-cleaning ability. The water-repellency of the lotus was firstly explained by Barthlott and Neinhuis [1] (described as "lotus effect") by imaging the leaves with scanning electron microscopy (SEM). In particular, they reported that epicuticular wax crystalloids, covering the leaf, minimize the adhesion between the substrate and an impinging water droplet (see Fig. 1.1b). As a result, raindrops behave like "liquid-spheres" rolling off the leaf and carrying any dirt particles which is necessary for sufficient photosynthesis of the plant.

Even though the lotus leaf can resist wetting from water droplets, it fails to repel oils or water containing surfactants. Such liquids can penetrate more easily in the lotus micro-structure, thus limiting its self-cleaning ability. In was only recently that an other natural micro-structured surface was found to address this drawback, exhibiting both water and oil-repellency. In particular, Helbig et al. [2] reported that the cuticle of springtails (*Collembola*) is covered with surface features with overhanging (mushroom-shaped) profiles, giving them exceptional self-cleaning properties (see Fig. 1.2a, b). This

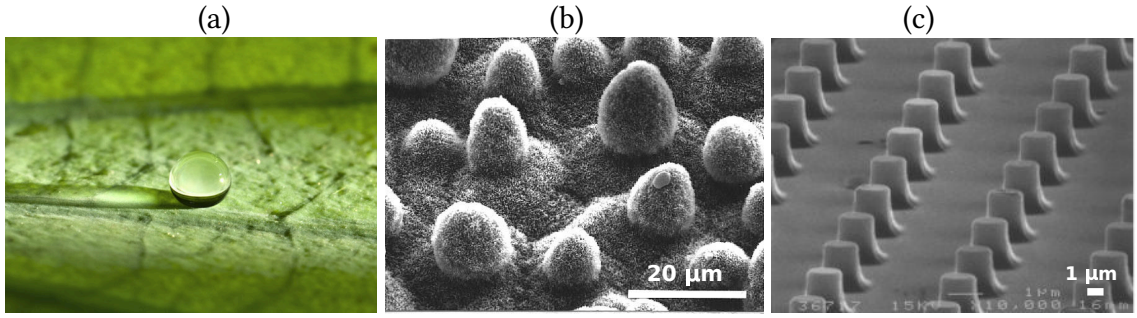

Figure 1.1: (a) Water droplet forming an almost perfect sphere on the leaf of *Nelumbo nucifera* (or simply lotus) (from Munich botanical garden). (b) SEM image of a lotus leaf structure of wax crystals (reprinted from [1]). (c) SEM image of lotus leaf inspired, artificial micro-posts, obtained from a photolithography process (reprinted from [4]).

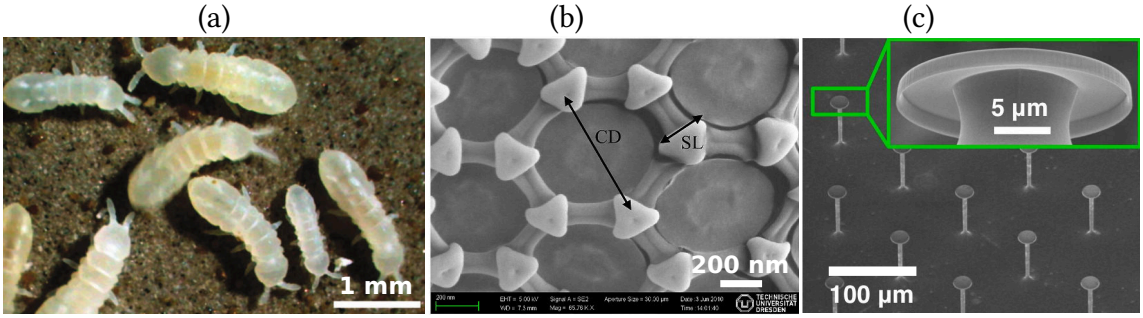

Figure 1.2: (a) Colony of *Orthonychiurus stachianus* springtails (reprinted from [3]). (b) Skin morphology of *Sinella tenebricosa* springtail, featuring mushroom-shaped asperities, obtained from SEM (reprinted from [2]). (c) SEM images of a superrepellent double re-entrant structure inspired by the surface topography of the springtail (reprinted from [5]).

ability emerged from an evolutionary adaptation to continue the cutaneous respiration even in flooded soil habitats [3].

Inspired by the above examples of self-cleaning materials, several approaches for artificially structured surfaces have been proposed in order to facilitate the daily life. Artificially structured surfaces are usually fabricated by a photolithography process on a photoresist material (see Fig. 1.1c) [4]. Up to now, the state-of-the-art in fabricating water and oil-repellent surfaces is double re-entrant, mushroom-shaped, structures [5] (see Fig. 1.2c), inspired by the cuticle of springtails (*Collembola*) [3]. We indicatively mention that some of the already exploited applications of such surfaces are: self-cleaning paints (Ultra Ever Dry®), roof tiles (Erlus Lotus®), fabrics (NanoSphere®) and glass windows (SunClean®). The above broad spectrum of current applications, triggered a strong interest in studying a wider range of biological materials, concluding that nature abounds with multifunctional surfaces [6] varying from insects which can walk on water (water strider) [7] to surfaces with antibacterial properties (gecko skin) [8]. We are just in the beginning of exploiting more and more fascinating physical mechanisms in order to face intractable engineering challenges. In the next Section, we discuss some of the most promising and challenging applications.

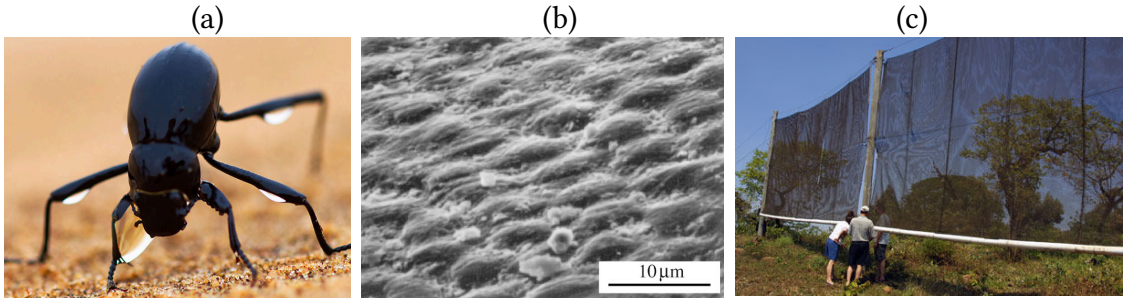

Figure 1.3: (a) Namib desert beetle collecting water from the fog. Droplets accumulate on the micro-bumps of the surface until they are large enough to coalesce and roll into the beetle's mouth (photo by Martin Harvey/Alamy). (b) SEM image of the textured surface of the Namib desert beetle, covered with "bump-like" micro-structures (reprinted from [9]). (c) Fog harvesting nets, set in South Africa (courtesy of University of South Africa)

1.2 Challenges of tomorrow

1.2.1 Fog harvesting

Freshwater shortage is one of the major problems for the people of developing countries and is expected to worsen in the coming decades. In order to quantify the problem we mention that, according to World Health Organization, 663 million people lack access to clean water. The surviving of some organisms in extremely arid condition, like the beetle *Stenocara gracilipes* found in the Namib Desert, has recently drew to scientific attention, indicating that nature has already found a solution. The desert beetle uses its body surface as water collector when facing the fog-laden wind and thus manages to survive in one of the driest habitats on Earth (see Fig. 1.3a) [9, 10]. In particular, water droplets accumulate on non-waxy bumps on the beetle's back until they are large enough to coalesce and roll, through wax-coated paths, into the beetle's mouth (see Fig. 1.3b).

The above mechanism can be exploited for developing synthetic, industrial scale, surfaces to collect freshwater in arid areas. Such an application is, however, still hypothetical, and the only current large scale device is polymer mesh installations in coastal areas where the fog periods are frequent, without the implementation of the complex beetle micro-structure (see Fig. 1.3c). These simple pilot systems can not yet be commercially exploited, until the harvesting efficiency is considerably improved. To implement this, it is imperative that we must not only mimic but also combine and improve the observed biological systems in order to adapt them in larger scales. In this direction, Park et al. [11] fabricated a complex solid topography, which is based on principles derived from Namib desert beetles [9], cacti [12], and the pitcher plant *Nepenthes* [13], and can be used to collect water with an improved efficiency. Such a combination of distinct natural mechanisms is more efficient than using the structures based only from the Namib desert beetle topography. There are several other studies arguing for the ideal fog harvesting surface [14, 15, 16], however, a general conclusion is that the design of

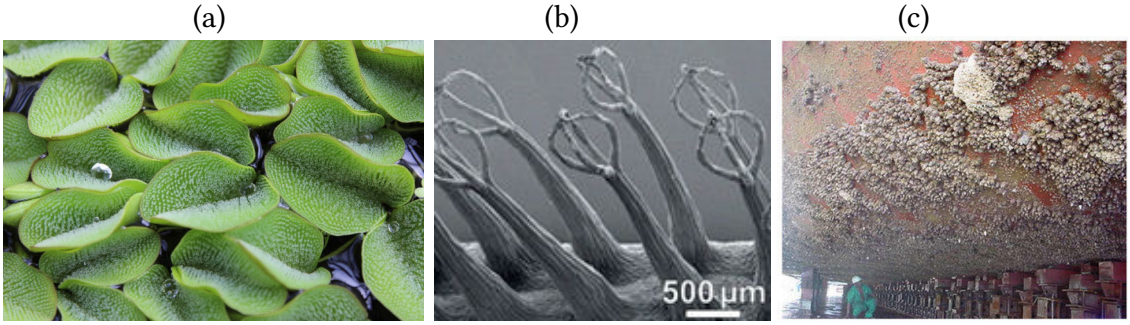

Figure 1.4: (a) The *Salvinia molesta* fern which can stabilize an air layer, required for respiration, when submerged under water (CC BY-SA 3.0). (b) SEM image of a frozen *Salvinia molesta* leaf exhibiting eggbeater-shaped hairs coated with nanoscopic wax crystals (reprinted from [17]). (c) Ship hull fouling by barnacles (reprinted from [18]).

the micro-structure is an important factor for the system's efficiency.

1.2.2 Drag reduction

The reduction of drag force for marine vessels has always been an important concern for the shipping industry. In addition, the fuel burn of a ship can increase up to 50% when fouled (by barnacles, oysters, mussels, algae or bacteria) versus a clean hull (see Fig. 1.4c) [19]. There are several studies where lotus leaf inspired surfaces have been found to reduce drag in fluid channels [20]. In particular, a layer of air is trapped between the water and the surface which acts as a lubricating film reducing the drag force which, however, can be retained only for a short period of time [21]. Recently, an other natural surface, the floating fern of the genus *Salvinia*, has been observed to maintain air layers, when submerged, for several days or even months (see Fig. 1.4a) [17]. The leaves of *Salvinia molesta* are covered with hairs, of total height about 2 mm, which form terminal ends of four (eggbeater-shaped) which stabilize the water-air interface (see Fig. 1.4b).

The above morphology can be exploited for reducing the drag on ship hulls and thus the fuel consumption. Moreover, the air layer will potentially have an antifouling effect and could thereby reduce the need of toxic antifouling agents, currently used in marine industry [22]. For such an application, however, the eggbeater-shaped structure must withstand stressed due to hydrostatic pressure and turbulent flow conditions. Recently, Mayser and Barthlott [23] have examined the sustainability of the air layer trapped in the *Salvinia* micro-structure, under a maximum pressure of 2.5 bar, which corresponds to the flow conditions at the bottom of a ship hull. Although the work of Mayser and Barthlott [23] indicate that some *Salvinia* species were capable of maintaining an air layer under this pressure, it is questionable whether such artificial surfaces can be made with the current fabrication methods, especially considering that an entire hull has to be covered. It is reasonable that the *Salvinia* micro-structure has to be simplified with, however, retaining the air trapping ability. Again we conclude that the micro-structure design is the key factor for applying this idea in industrial level.

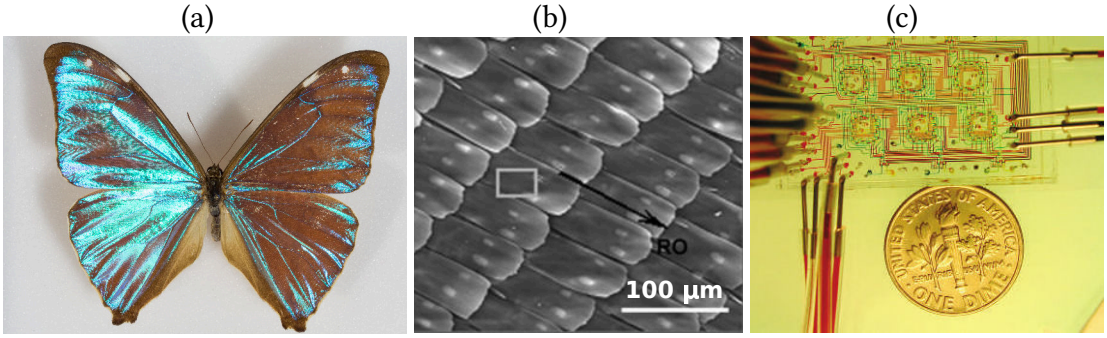

Figure 1.5: (a) An iridescent blue *Morpho aega* butterfly found in South America (CC BY-SA 4.0). (b) Asymmetrical structure of the *Morpho aega* wing, exhibiting anisotropic wetting properties. Water rolls easily along the direction denoted by the black arrow (reprinted from [24]). (c) Microfluidic lab-on-a-chip device, including pneumatic valves, used to study the growth of microbial populations (chemostat) (reprinted from [25]).

1.2.3 Lab-on-a-chip devices

Lab-on-a-chip devices are systems that process or manipulate small amounts of fluids using micro-channels (see Fig. 1.5c) [26, 27]. Such systems were initially created after the end of the cold war to serve as detectors for chemical and biological threats, supported by the US Department of Defense. Current applications of Lab-on-a-chip devices include sensors in laboratories (e.g. water analysis) (Micronit®), diagnostic devices in medicine (Illumina®) and optofluidics (Varioptic®), however, are not yet become widely used. In most of the cases, the liquid manipulation in lab-on-a-chip devices is performed by applying pressure gradients [25], electric fields (electrowetting phenomenon) [28] or by thermal gradients along the substrate (thermocapillary convection) [29]. The conventional applications of lab-on-a-chip devices do not usually require any sophistacated surface texture (e.g. micro-posts), however, as the dimensions of the channels shrink (for enabling more complex processes, e.g. lab-on-a-chip devices that simulate the activities of an entire biological organ for *in vitro* medical studies [30]) the solid structure impact on the device efficiency will be crucial [31]. In such a complex device, it would be useful to minimize the liquid-solid friction so as to use as less energy supply as possible. Once again, we will look at nature's marvelous designs.

Recently, *Morpho aega* butterflies (see Fig. 1.5a), which live in the South American rainforest, arouse the curiosity of researches due to their exceptional flying stability, by keeping their wings light-loaded, despite the high humidity of their environment. The thought that the butterfly wing is covered by lotus leaf type structures did not seem logical since the condensed water droplets would easily roll towards their body, preventing them from flying. The answer was finally given by Zheng et al. [24], by examining the micro-structure of the *Morpho aega* wings. In particular, they reported that the wing surface exhibit asymmetric ratchet-like structures, leading to anisotropic wetting properties. Therefore, a droplet can roll off the surface of the wings along only the outward direction (see Fig. 1.5b). The application of this finding in lab-on-a-chip devices would

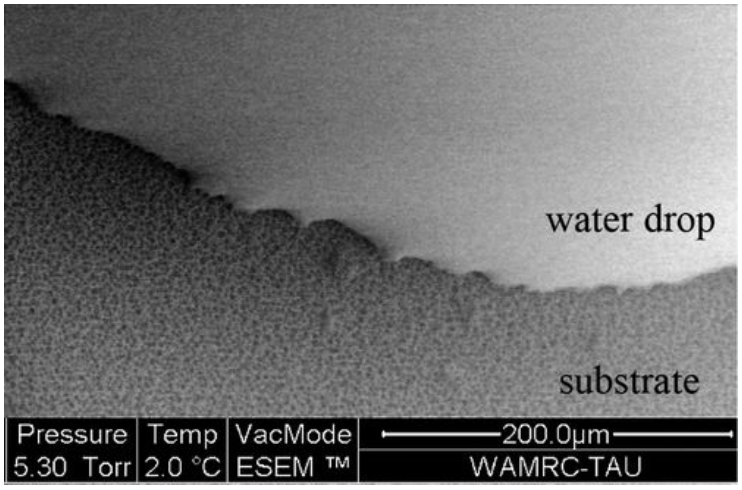

Figure 1.6: Environmental scanning electron microscopy (ESEM) image of a droplet edge on an porous polycarbonate surface (reprinted from [33]).

greatly enhance the efficiency of liquid transport along a prescribed route, however, such a design would require the ability to predict the behavior of droplets on geometrically structured surfaces. This is a rather difficult task, by using the current approaches, as we will present in the following Section.

1.3 Why computational modeling is important

We have previously presented commercially available applications of artificially roughened, water-repellent surfaces. Even those paradigms, however, suffer from vulnerabilities due to the inadequate mechanical robustness of the structures at high external pressure or due to a collapse wetting transition (where the liquid impales the solid protrusions) resulting in the loss of their water-repellency ability. In addition, Cavalli et al. [32] demonstrated that the micro-structure robustness and water-repellency ability have an antagonistic action; the higher the mechanical stability, the less the water-repellent performance of the surface. The above indicates that an *ad hoc* topography optimization is required for a specific application. Overall, in order to efficiently design and optimize functional substrates with tailor-made wetting properties, keeping in mind that the fabrication cost may be prohibitive to experimentally test a plethora of solid topographies, a predictive model of the droplet behavior on complex surfaces and under the effect of different external forces (pressure, electric field effect, thermal gradient) is deemed necessary.

Such a complex system of a droplet moving on a geometrically of chemically structured substrate, requires an accurate computation model, rather than simplified phenomenological approaches. In order to understand the complexity of the studied system, we demonstrate in Fig 1.6 the edge of a droplet in contact with a porous polymer substrate. From the above it is clear that roughness greatly distorts the droplet shape, thus a phe-

nomenological model that accounts only for the macroscopic fluid characteristics is not acceptable for designing and optimizing the previously referred applications.

1.4 The objective of this Thesis

Despite the vast amount of the developed modeling approaches for predicting the droplet equilibrium (including multiple distinct wetting states) and dynamics on a geometrically structured solid surface, according to our knowledge, none of them has a general applicability to all the aforementioned applications. In particular, either they are based on significant simplifications failing to adequately describe the complex behavior of a droplet on a rough substrate, or are too expensive, in terms of computational resources, for real-life applications with millimeter-sized droplets. In this Thesis, we propose a novel modeling approach, particularly efficient to predict the static and dynamic behavior of entire millimeter-sized droplets on any kind of structured (geometrically of chemically) substrate. The mathematical formulation of the proposed model is presented in Chapters 2 and 3. Then, we demonstrate numerical predictions of our model for a variety of static and dynamic problems, in Chapters 4, 5, 6 and 7. The incorporation of additional forces (e.g. electric field, thermocapillary stresses) that affect the droplet behavior, can also be readily performed in our approach, which renders it, to our opinion, an extremely valuable and efficient tool.

The scope of the research presented here is twofold. Firstly, from the applications point of view, the throughout simulations performed by our modeling approach can be exploited for designing, optimizing and then fabricating functional materials (e.g. efficient fog harvesters, low friction surfaces, micro-channels with directional adhesion) inspired by the above natural mechanisms. The evaluation, for example, of a solid structure performance, in terms of its water-repellency, is demonstrated in Chapter 4. Moreover, in Chapter 6 we examine the effect of the solid topography, featuring asymmetric protrusions inspired by the *Morpho aega* wings, on the directional adhesion of droplets. As previously stated, such tasks could not be addressed up to now, with the current modeling methodologies. Secondly, our model can also contribute to the active theoretical research regarding wetting phenomena on complex solid surfaces. In particular, our detailed simulations can shed light to several physical mechanisms and explain experimental findings that cannot be clarified by the current theoretical description. Such an example is presented in Chapter 5, where we interpret recent experiments, by performing simulations of a droplet impacting on an arbitrary roughened solid surface. Our proposed modeling approach will be introduced in the following Chapter, after presenting the basic concepts of wetting and capillary phenomena.

CHAPTER 2

Statics

In this Chapter we present the fundamental concepts of wetting of solids by liquids in equilibrium (also referred as capillary phenomena), particularly focusing on how roughness of a solid surface affects its wetting properties. We refer to the conventional theoretical models for predicting the shape of a droplet on the solid surface, which however, either fail to adequately describe the complex behavior of a droplet on a rough substrate, or prove to be too expensive in terms of computational resources for real-life millimeter-sized droplets. After reporting these limitations we introduce a novel, continuum-level, sharp-interface modeling approach which is particularly efficient for predicting entire droplet equilibrium profiles on any kind of textured (geometrically or chemically) solid surface. According to our approach, the liquid-ambient and the liquid-solid interfaces of the droplet are treated in a unified framework under the influence a disjoining pressure term modeling the molecular interactions.

2.1 Basic aspects of wetting phenomena

2.1.1 Interfacial tension

A liquid surface can be considered as a stretched membrane featuring an interfacial tension that opposes any distortion. A demonstration of the surface tension (interfacial tension of water-air interface) is presented in Fig. 2.1. In particular, surface tension supports a raft of ants linked together. Such a structure allows the ants to sail for months to survive floods [34]. The physical origin of interfacial tension can be understood by considering a liquid at the molecular scale. A molecule in the midst of a liquid interacts with all its neighbors. On the other hand a molecule on the surface loses half of these cohesive interactions and is in an unfavorable energy state. This is the reason why liquids adjust their shape so as to reduce the surface area as much as possible. Interfacial tension may be equally though as (a) force per unit length and (b) free energy per unit area. Next, we will present two examples to explain these viewpoints.

First, we consider a soap film stretched over a wire frame with a rod at the end which

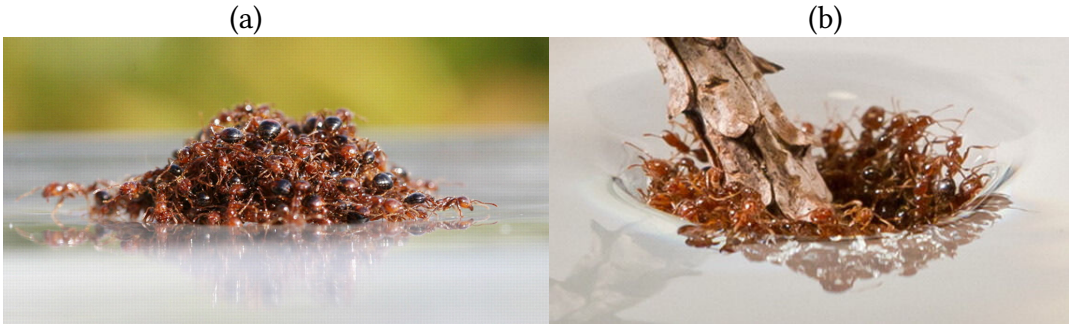

Figure 2.1: Manifestation of surface tension: (a) a waterproof raft of 500 fire ants (*Solenopsis invicta*) floating on water. (b) The water-repellency of the ants prevents them from sinking when submerged (reprinted from [34]).

is movable (see Fig. 2.2a). If the rod is displaced by $\mathrm{d}x$, we can measure that a force is acting on the movable rod in the direction indicated by the red arrow in the figure. The value of that force per unit length is the interfacial tension, which is denoted by γ (the corresponding SI units are N/m), and the work done is:

$$W = \gamma \, \lambda \, \mathrm{d}x, \tag{2.1}$$

where, λ, is the length of the wire frame.

Now, we will think of γ in terms of energy per unit area (the corresponding SI units are $\mathrm{J/m^2}$). In Fig. 2.2b we depict a droplet of oil submerged in water. In the absence of gravitational field the oil droplet is spherical, since this the shape of the minimum surface area for an enclosed volume. If the oil-water interface is displaced by $\mathrm{d}R$ (see Fig. 2.2b), the work done is:

$$W = -p_{\mathrm{oil}} \, \mathrm{d}V_{\mathrm{oil}} - p_{\mathrm{water}} \, \mathrm{d}V_{\mathrm{water}} + \gamma_{\mathrm{ow}} \, \mathrm{d}A, \tag{2.2}$$

where $\mathrm{d}V_{\mathrm{oil}} = 4\,\pi\,R^2\,\mathrm{d}R = -\mathrm{d}V_{\mathrm{water}}$, and $\mathrm{d}A = 8\,\pi\,R\,\mathrm{d}R$ are the increase in volume and surface of the droplet, respectively; p_{oil} and p_{water} are the pressures in the oil and water phases, and γ_{ow} is the oil-water interfacial tension. In equilibrium, Eq. 2.2 equals to zero, which amounts to the fundamental equation, given in 1805 by Young and by Laplace [35]:

$$\Delta P = p_{\mathrm{oil}} - p_{\mathrm{water}} = \frac{2\,\gamma_{\mathrm{ow}}}{R}. \tag{2.3}$$

From the above, we conclude that the smaller the droplet, the greater the pressure inside compared to the outside phase.

2.1.2 Three-phase contact line

When a droplet is placed on a solid surface, forms, in equilibrium, a spherical cap with a contact angle, θ_{Y}, with the solid surface. The line where the three different phases, liquid-solid-ambient, intersect, is called three-phase contact line (TPL) (see Fig. 2.3). According

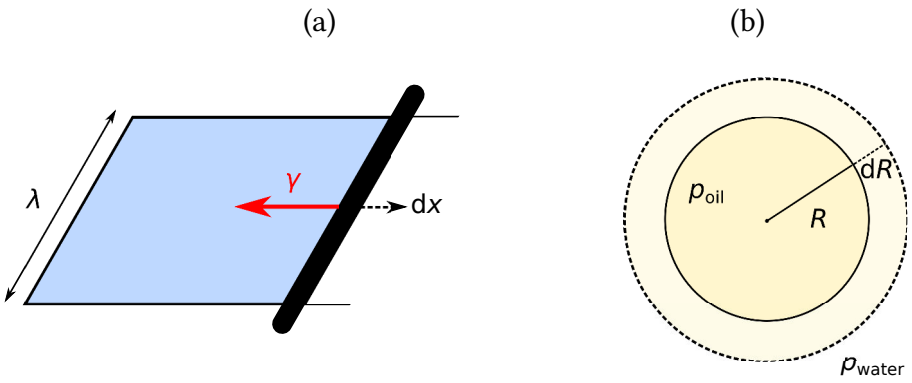

Figure 2.2: (a) Interfacial tension, γ, as a force per unit length normal to a mobile rod. (b) Schematic of an oil droplet immersed in water, used to highlight the second formulation of interfacial tension as energy per unit area.

to the work of Young, the equilibrium contact angle (also known as Young's contact angle) of a droplet on a smooth solid surface depends on the solid-ambient, γ_{SA}, liquid-solid, γ_{LS}, and liquid-ambient, γ_{LA}, interfacial tensions [35, 36, 37]. The surface free energy in this case is defined as:

$$E = \gamma_{LS}\, A_{LS} + \gamma_{SA}\, A_{SA} + \gamma_{LA}\, A_{LA}, \tag{2.4}$$

where A_{LS}, A_{SA}, A_{LA} is the liquid-solid, solid-ambient and liquid-ambient interfacial area, respectively. The work done (the variation of the surface free energy) for a contact line displacement by a distance, dx (Fig. 2.4) is:

$$\begin{aligned} W = \mathrm{d}E = \gamma_{LS}\,\mathrm{d}A_{LS} - \gamma_{SA}\,\mathrm{d}A_{LS} + \gamma_{LA}\cos\theta_Y\,\mathrm{d}A_{LS} \;\Rightarrow \\ \frac{\mathrm{d}E}{\mathrm{d}A_{LS}} = \gamma_{LS} - \gamma_{SA} + \gamma_{LA}\cos\theta_Y, \end{aligned} \tag{2.5}$$

where, $\mathrm{d}A_{LS} = 2\,\pi\, R_{cl}\,\mathrm{d}x$ (with R_{cl} the contact radius of the droplet), is the change in the liquid-solid interfacial area. We note that the bulk energy is unaffected in this case since the liquid pressure does not change. In equilibrium ($\lim\limits_{\mathrm{d}A_{LS}\to 0} \dfrac{\mathrm{d}E}{\mathrm{d}A_{LS}} = 0$), Eq. 2.5 amounts to the Young equation:

$$\gamma_{SA} = \gamma_{LS} + \gamma_{LA}\cos\theta_Y. \tag{2.6}$$

The above equation connects the Young contact angle, θ_Y, with the liquid-solid, solid-ambient and liquid-ambient interfacial tensions. We note that Young's equation is valid only for perfectly smooth solid surfaces; such an assumption, however, does not usually stand in real life since a small amount of roughness may be present even in macroscopically smooth materials. Moreover, it is interesting that although Eq. 2.6 is generally accepted and widely used in the literature, it has never been verified experimentally due to the virtually impossible estimation of the interfacial tension of solids.

By definition, when the Young contact angle lies between 0° and 90°, the solid material is

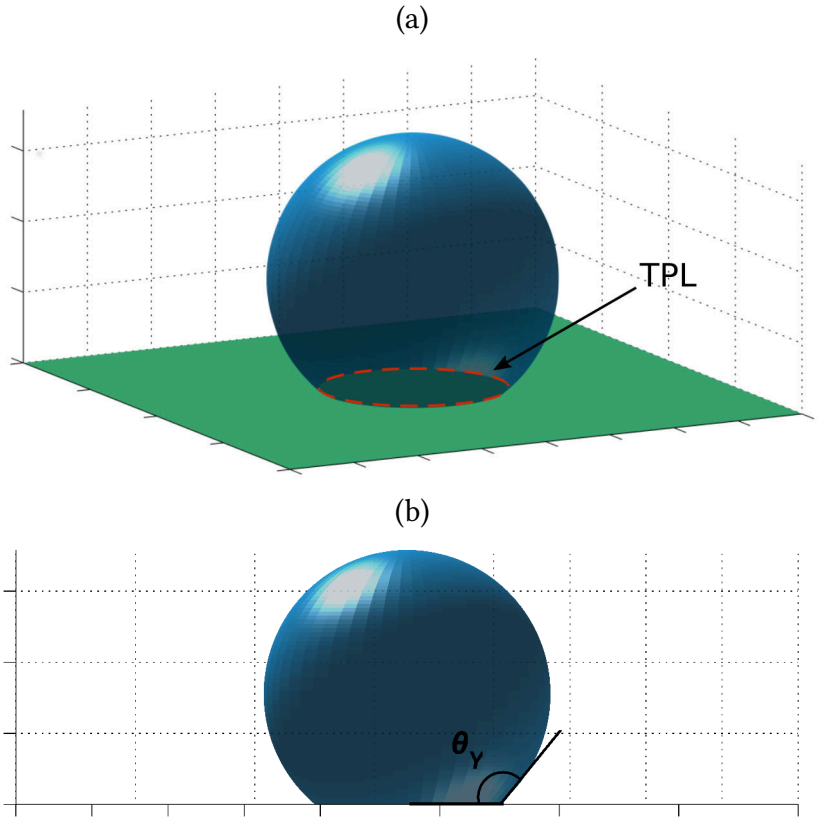

Figure 2.3: Droplet resting on a smooth solid surface. (a) The three-phase contact line (TPL) is depicted with the dashed red line. (b) The Young contact angle, formed at the intersection of the liquid-ambient and the liquid-solid interfaces, is demonstrated.

called hydrophilic, whereas it is called hydrophobic for θ_Y greater than 90^o. We note that Young's contact angle has an upper limit in experimental practice. In particular, common hydrophobic materials (e.g. waxes and fluoropolymers such as Teflon® AF 1600) do not exhibit $\theta_Y > 120^o$. Apparent (macroscopically observed) contact angles higher than 120^o, however, can be observed on geometrically structured surfaces as discussed in Chapter 1. When the apparent contact angle is at least 150^o and the rolling-off angle (the minimum inclination angle at which the droplet rolls-off the substrate) do not exceed 5-10^o, then the solid surface is called superhydrophobic. This term was initially introduced in 1996 by Onda et al. [38].

In the case where a liquid fully wets a solid surface ($\theta_Y = 0$, for e.g. a water droplet on noble metals such as gold or platinum [39]), Eq. 2.6 ceases to hold and the imbalance of the interfacial tensions is now given by a spreading coefficient:

$$S_{LS} = \gamma_{SA} - \gamma_{LS} - \gamma_{LA}. \tag{2.7}$$

In the above case, the adhesion tension, $\gamma_{SA} - \gamma_{LS}$, which is a quantity introduced by Bartell et al. [35], exceeds γ_{LA}.

The fact that wetting and capillary phenomena have been studied even from the early 18th century by great scientists of physics and mathematics (Francis Hawksbee, James

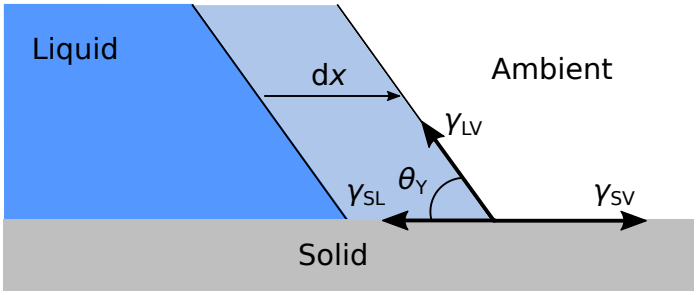

Figure 2.4: Mechanical force balance at the three-phase contact line (or simply contact line), where the different phases (solid, liquid, ambient) meet.

Jurin, Thomas Young, Pierre-Simon Laplace) [40] is attributed to their close relation with classical geometry. In particular, the static shape of a droplet on a smooth substrate can be derived geometrically, in the absence of any gravitational field, as presented in the next Section.

2.1.3 Droplet shape on smooth surfaces

The shape of an axisymmetric droplet on a smooth solid surface can be analytically calculated, providing that the effect of gravity is negligible, for a given liquid volume and Young's contact angle. The negligible gravity effect assumption is valid only when the initial droplet radius is smaller than the capillary length, $\lambda_\kappa = \sqrt{\frac{\gamma_{LA}}{\rho\, g}}$, where ρ is the liquid density and g the gravitational constant, respectively. Considering that a droplet forms a spherical cap at equilibrium, the droplet shape can be obtained by solving the following system of equations:

$$\frac{\mathrm{d}z}{\mathrm{d}x}\,|_{z=0} = \tan\left(\pi - \theta_Y\right), \tag{2.8a}$$

$$V_{\text{droplet}} = \int_0^{z_{\max}} \pi\, x^2\, \mathrm{d}z, \tag{2.8b}$$

$$(z - z_c)^2 + x^2 = R^2, \tag{2.8c}$$

where, V_{droplet}, is the droplet volume, z_c is the center of the circle (with radius R) which adapts to the liquid-ambient interface and $z_{\max} = z_c + R$ (see Fig. 2.5). From Eqs. 2.8a and 2.8c for z=0, yields:

$$\tan\left(\pi - \theta_Y\right) \overset{x=R_{cl}}{=} \frac{-R_{cl}}{\sqrt{R^2 - R_{cl}^2}}, \text{ for } z_c \geqslant 0, \tag{2.9a}$$

$$\tan\left(\pi - \theta_Y\right) \overset{x=R_{cl}}{=} \frac{R_{cl}}{\sqrt{R^2 - R_{cl}^2}}, \text{ for } z_c < 0, \tag{2.9b}$$

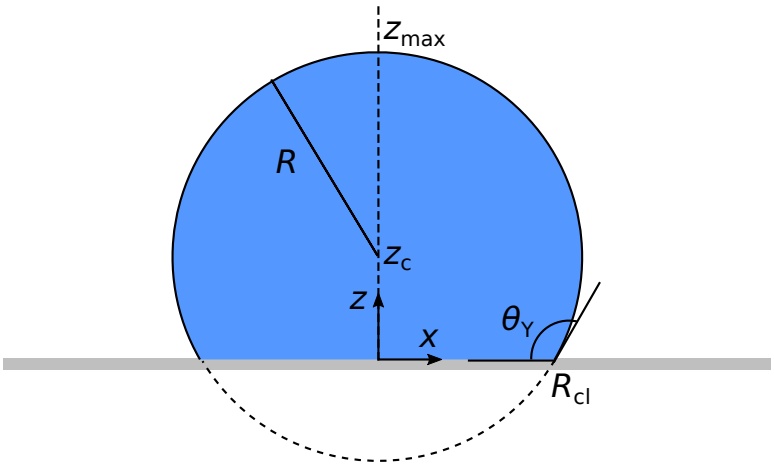

Figure 2.5: Droplet shape obtained by the analytical solution of Eqs. 2.8a, 2.8b and 2.8c.

which in combination with:

$$z_c = -\sqrt{R^2 - R_{cl}^2}, \text{ for } z_c \geqslant 0, \tag{2.10a}$$

$$z_c = \sqrt{R^2 - R_{cl}^2}, \text{ for } z_c < 0, \tag{2.10b}$$

(from Eq. 2.8c) yields:

$$z_c = \frac{R_{cl}}{\tan(\pi - \theta_Y)}. \tag{2.11}$$

Moreover, from Eqs. 2.8b and 2.8c, yields:

$$V_{droplet} = \pi R^2 z_c + \frac{2\pi R^3}{3} - \frac{\pi z_c^3}{3}, \tag{2.12}$$

which in combination with, $R^2 = \sqrt{z_c^2 + R_{cl}^2}$, and Eqs. 2.11 yields:

$$R_{cl} = \left[\frac{V_{droplet}}{2\pi \frac{\left(\frac{1}{\tan^2\theta_Y}+1\right)^{3/2}}{3} - \frac{2\pi}{3\tan^3\theta_Y} - \frac{\pi}{\tan\theta_Y}} \right]^{1/3}. \tag{2.13}$$

Overall, in order to calculate the shape of droplet, for given liquid volume and Young's contact angle, we:

1. compute the contact radius, R_{cl}, from Eq. 2.13,
2. compute the center of the circle, z_c, which adapts to the liquid-ambient interface from Eq. 2.11 and
3. calculate the radius of the circle, R, from $R^2 = \sqrt{z_c^2 + R_{cl}^2}$.

Unfortunately, there is no such analytical solution in the case of a rough solid surface due to the complex shape of the contact line which can form multiple contact regions

with the substrate. The problem originates from the complex contact line shape (forming multiple contact regions with the substrate), when the solid surface is geometrically or chemically textured (see for example an ESEM image of the three-phase contact line on an porous substrate in Fig 1.6). Wetting phenomena on structured surfaces were initially studied in the work of Cassie and Wenzel more than 60 years ago [41], however, only recently has become a highly attractive research field due to the modern applications presented in Chapter 1. In the next Section, we present the theoretical models, starting from elementary approaches to more complex ones, for predicting the static behavior of droplets on solid surfaces, mainly focusing on heterogeneous (geometrically structured) substrates.

2.2 Modeling of equilibrium wetting phenomena

2.2.1 Wenzel and Cassie-Baxter models

The solid wettability can be greatly affected by the surface topography and surface heterogeneities in general (chemical patterns, impurities). In the case of a geometrically structured surface, the apparent (experimentally observed) contact angle, θ_a, differs from what expected from Eq. 2.6. Such a behavior can be theoretically explained by the Wenzel and the Cassie-Baxter equations [41]. In particular, the Wenzel model is based on the assumption that the liquid fully penetrates the solid roughness, by following all the topological variations (see Fig. 2.6a) [42, 41]. The work done in this case (the surface free energy variation, $\mathrm{d}E$) as the contact line advances by a distance, $\mathrm{d}x$, is defined as:

$$\begin{aligned} W = \mathrm{d}E = r_f\,\gamma_{LS}\,\mathrm{d}A_{LS} - r_f\,\gamma_{SA}\,\mathrm{d}A_{LS} + \gamma_{LA}\cos\theta_a\,\mathrm{d}A_{LS} \;\Rightarrow \\ \frac{\mathrm{d}E}{\mathrm{d}A_{LS}} = r_f\,(\gamma_{LS} - \gamma_{SA}) + \gamma_{LA}\cos\theta_a, \end{aligned} \tag{2.14}$$

where the roughness factor, r_f, is the ratio of the actual over the apparent surface area. In equilibrium ($\lim_{\mathrm{d}A_{LS}\to 0}\frac{\mathrm{d}E}{\mathrm{d}A_{LS}} = 0$), the above equation, combined with Eq. 2.6, reads:

$$\cos\theta_a = r_f\cos\theta_Y. \tag{2.15}$$

The Wenzel equation predicts that the apparent contact angle, θ_a, is larger than Young's for hydrophobic materials ($\theta_Y > 90^o$) whereas it is smaller than the Young contact angle in the case of hydrophilic materials ($\theta_Y < 90^o$). The latter case is referred as superhydrophilic. Overall, the Wenzel equation concludes that roughness enhances solid wettability. Despite that such an argument was validated by experiments [43], the Eq. 2.15 may predict unphysical apparent wettabilities in some cases (e.g. $\cos\theta_a > 1$ or $\cos\theta_a < -1$, for a large roughness factor, r_f).

A different approach is adopted in the Cassie-Baxter model [44, 41]. In particular, as

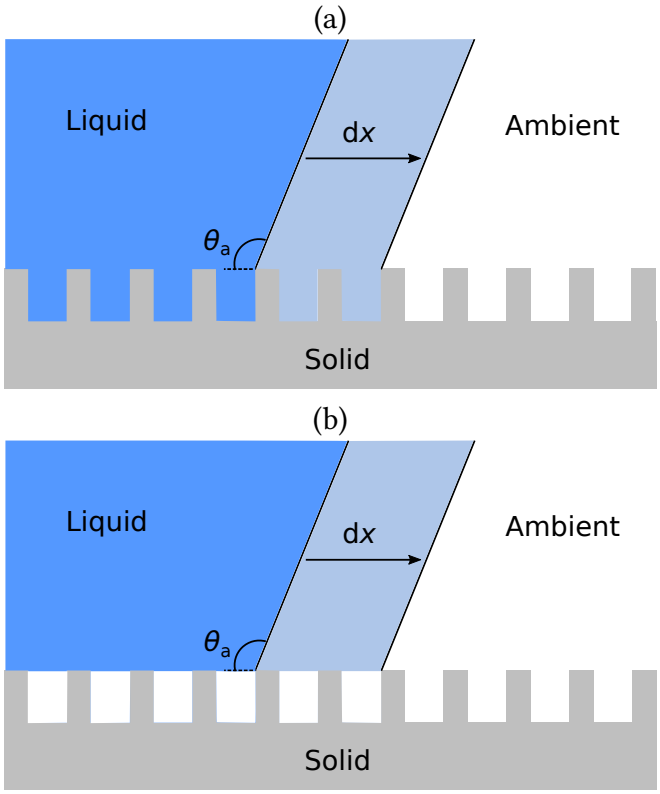

Figure 2.6: Contact line displacement by a distance, dx, in (a) a Cassie-Baxter regime and (b) a Wenzel regime. The apparent contact angle, θ_a, is evaluated above the solid protrusions.

observed in Fig. 2.6b, it is assumed that air remains trapped below the droplet. The variation of the surface free energy as the droplet advances in this case reads:

$$W = \mathrm{d}E = \phi_s \left(\gamma_{LS} - \gamma_{SA}\right) \mathrm{d}A_{LS} + \left(1 - \phi_s\right) \gamma_{LA} \, \mathrm{d}A_{LS} + \gamma_{LA} \, \mathrm{d}A_{LS} \cos\theta_a, \tag{2.16}$$

where ϕ_s is the fraction of solid in contact with the liquid ($\phi_s < 1$). In equilibrium, i.e. for a minimum surface free energy, the above equation, combined with Eq. 2.6, reads:

$$\cos\theta_a = -1 + \phi_s(1 + \cos\theta_Y). \tag{2.17}$$

The Cassie-Baxter equation predicts that the solid wettability is reduced by decreasing the liquid-solid contact area, however, the air entrapment assumption is only valid for large Young's contact angles, thus Eq. 2.17 ceases to hold for hydrophilic materials.

Lafuma and Quéré [45], in an attempt to combine these two theories and to extend our understanding on roughness effect on wetting, assumed that Cassie-Baxter approach (Eq. 2.17) should hold for substrates either very hydrophobic (large θ_Y) or very rough (large roughness factor, r_f), where air entrapment should be favored. Similarly, they expected that the Wenzel approach (Eq. 2.15) should hold for substrates that are hydrophilic ($\theta_Y < 90^o$) and slightly hydrophobic (θ_Y just above 90^o) when air pockets should not be favored. Moreover, they calculated the critical Young's contact angle, $\cos\theta_{C1} = (\phi_s - 1)(r_f - \phi_s)$, which is the threshold between these regimes for a given

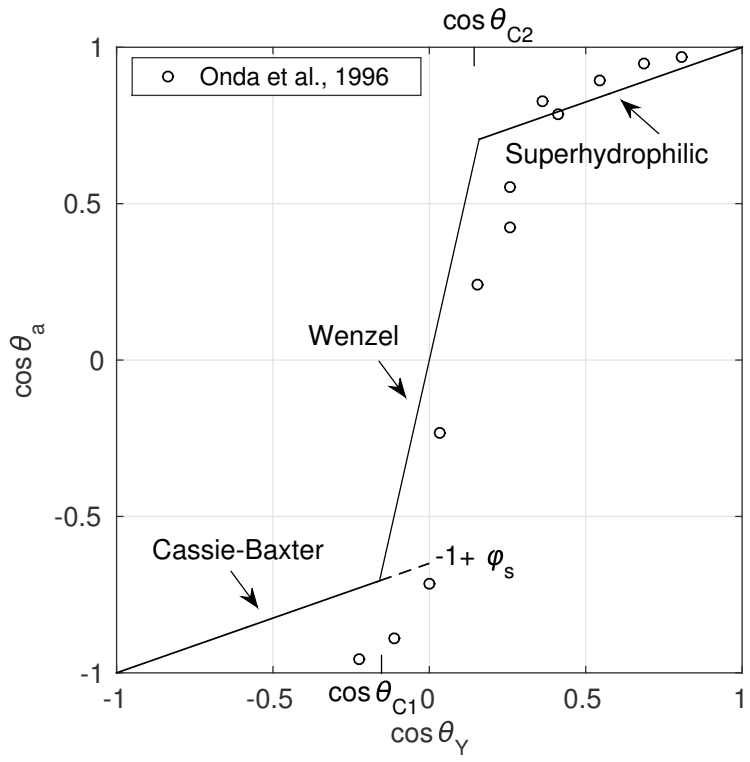

Figure 2.7: The dependence of the apparent wettability, θ_a, on the Young contact angle, as measured by Onda et al. [38]. The solid lines show the behavior expected by the Cassie-Baxter (Eq. 2.17), the Wenzel (Eq. 2.15) and the superhydrophilic (Eq. 2.19) theoretical models, with r_f = 4.43 and ϕ_s = 0.35. The dotted line represents a meta-stable situation where Cassie-Baxter states were observed by Lafuma and Quéré [45].

solid structure, by equating Eq. 2.17 and Eq. 2.15. This combined model is presented in Fig. 2.7. Lafuma and Quéré, also performed experiments to validate their hypothesis. In particular, by compressing a water droplet between superhydrophobic micro-structured surfaces, they have noticed wetting transitions between Cassie-Baxter and Wenzel states for moderate solid hydrophobicity, $\theta_Y < \theta_{C1}$, where the liquid impales the solid protrusions. They reported that the apparent contact angles in both states were comparable, however, the adhesive properties greatly differ; unlike Cassie-Baxter state, the droplet in the Wenzel state was highly pinned to the solid. Moreover, they observed that Cassie-Baxter to Wenzel wetting transitions were irreversible, i.e. the droplet does not return to the Cassie-Baxter state when relaxing the pressure.

An attempt to experimentally validate the Wenzel and Cassie-Baxter theoretical models, for a wide range of Young's contact angles, has been also performed by Onda et al. [38] by modifying the roughness, and thus the wetting properties, of surfaces made of alkylketene dimer (AKD) and using liquids of various interfacial tensions (see Fig. 2.7). In particular, it is observed that the apparent wettability of hydrophobic materials ($\cos\theta_Y < 0$ in Fig. 2.7), can be adequately predicted by the previous theoretical description of Wenzel and Cassie-Baxter equations, however, in the case of hydrophilic materials ($\cos\theta_Y > 0$), the Wenzel regime was not obeyed when the Young contact an-

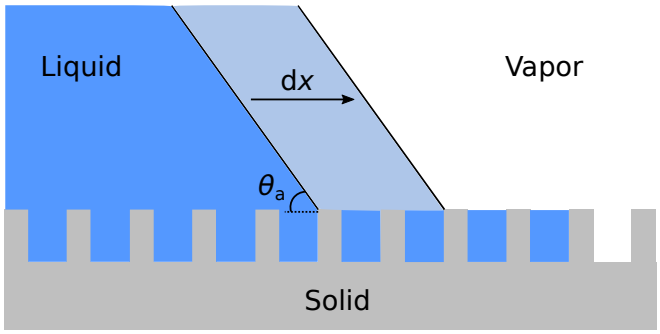

Figure 2.8: Contact line displacement by a distance, dx, in the superhydrophilic regime, where a liquid film propagates within the solid structure.

gle becomes smaller than some critical value (θ_{C2} in Fig. 2.7). Thus a new regime was assumed for this region, known as superhydrophilic, which can be characterized by a liquid film that propagates within the material textures [41] as presented in Fig. 2.8. The work done in this case as the contact line advances by a distance, dx, is defined as:

$$W = \mathrm{d}E = \phi_s \left(\gamma_{LS} - \gamma_{SA}\right) \mathrm{d}A_{LS} - \left(1 - \phi_s\right) \gamma_{LA} \, \mathrm{d}A_{LS} + \gamma_{LA} \, \mathrm{d}A_{LS} \cos\theta_a . \tag{2.18}$$

In equilibrium, the above, combined with Eq. 2.6, reads:

$$\cos\theta_a = 1 + \phi_s \left(\cos\theta_Y - 1\right), \tag{2.19}$$

and the critical critical value of the Young contact angle, separating the Wenzel and the superhydrophilic regime (see Fig 2.7), is calculated as $\cos\theta_{C2} = (1 - \phi_s)(r_f - \phi_s)$, by equating Eq. 2.15 and Eq. 2.19. We observe that the above equation can successfully capture the experimental measurements of Onda et al. [38] for $\cos\theta_Y > \cos\theta_{C2}$ (see Fig. 2.7).

As a summary, Wenzel and Cassie-Baxter equations do succeed in capturing some experimental trends (see [38, 43]), however, they should be used with caution since there are also inconsistent with some publications [46, 47]. Recently, a discussion has been started regarding the range of applicability of these classic modeling approaches. In particular, recent experimental and computational studies on surfaces with heterogeneous islands, criticize Wenzel and Cassie-Baxter equations, arguing that wetting behavior is determined by liquid-solid interactions at the outer three-phase contact line alone, and that the interfacial area within the contact perimeter is irrelevant [48, 49, 40, 50]. Such a statement, however, does not contradict with Wenzel and Cassie-Baxter approach, provided that local values (in the vicinity of the outer three-phase contact line) of the roughness factor and of the liquid-solid area fraction are used in Eqs. 2.15 and 2.17, respectively. A more reasonable argument is made by McHale [51] where he suggested that Wenzel and Cassie-Baxter equations apply only (a) when the surface is similar and isotropic everywhere and (b) when the size ratio of the droplet to the wavelength of roughness or chemical heterogeneity is large enough. Even if the above assumptions are valid,

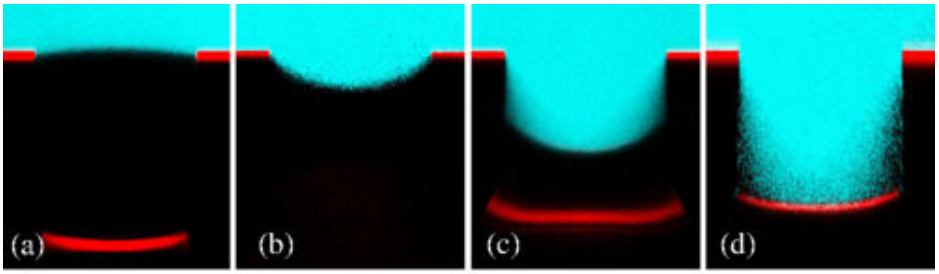

Figure 2.9: Confocal microscopy images of a water miniscus in a unit cell of a pillar-structured surface under different liquid pressures (a) 0 kPa, (b) 14 kPa, (c) 50 kPa and (d) 50 kPa after collapse. Reprinted from [53].

however, it is difficult to imagine that simple approaches like Eq. 2.15 and Eq. 2.17 can adequately describe the complexity of the contact line behavior on a structured surface (see e.g. the magnified view of a contact line on a porous solid surface presented in Fig. 1.6 of Chapter 1).

In addition, recent experimental studies, by using confocal microscopy techniques, reveal that composite meta-stable wetting states can also be formed, where the liquid has partially penetrated the solid roughness (see e.g. the shape of a water meniscus for various applied pressures in Fig. 2.9) [52, 53]. It is obvious that the multiplicity of meta-stable equilibrium states, presented in Fig. 2.9, renders the prediction of the wetting behavior on structured substrates extremely difficult. In particular, Cassie-Baxter states, where air is trapped underneath a droplet footprint (see Fig. 2.9a), can coexist with Wenzel states (in the sense that the particular geometry can accommodate both states) where the liquid has impaled the surface patterning (see Fig. 2.9d). The case is even more complicated when the surface protrusions are partially filled, and the resulting apparent wetting behavior lies between those of the Cassie-Baxter and the Wenzel (Fig. 2.9b). The complete picture of the states' space can be notably complex with an extended range of the possible apparent contact angles, θ_a, as well as of the adhesion properties. Obviously, such a behavior is not predicted by the Wenzel and Cassie-Baxter equations. To our opinion, the complete picture of the apparent wettability dependence can not be revealed by using Wenzel and Cassie-Baxter equations alone since a throughout study would require a detailed computational approach. Several modeling approaches have been proposed in order to compute the different attainable wetting states on rough solid surfaces (e.g. the suspended and collapsed states in Fig. 2.9a and Fig. 2.9d, respectively) as presented in the following Sections. We begin with the solution of the Young-Laplace (YL) equation, which is the simplest and most efficient computational approach for the determination of equilibrium wetting states.

2.2.2 Conventional Young-Laplace equation

The Young-Laplace equation, which is a generalized form of Eq. 2.3 (see Section A.1, of the Appendix A, for a rigorous derivation), states the force balance between interfacial

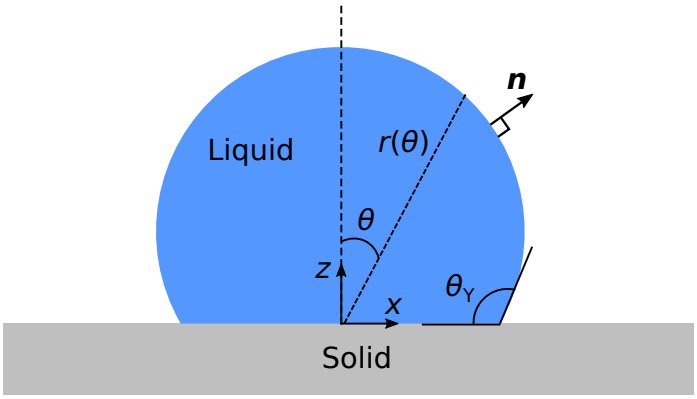

Figure 2.10: Schematic illustration of a droplet wetting a flat solid surface, with contact angle θ_Y. The droplet surface is parameterized with the angular coordinate, ($r = r(\theta)$).

tension, capillary (Laplace) pressure and gravity along a droplet surface [35]:

$$\gamma_{LA}\, C + \Delta\rho\, g\, z = \Delta p \;\Rightarrow\; \gamma_{LA}\frac{\widehat{C}}{R_0} + \Delta\rho\, g\, \widehat{z} R_0 = \Delta p \;\Rightarrow\; \widehat{C} + N_g\, \widehat{z} = K, \tag{2.20}$$

where, C, is the local mean curvature of the droplet free surface ($C = \nabla_s \cdot \boldsymbol{n}$, with ∇_s the surface gradient operator and $\boldsymbol{n}$ the unit normal of the droplet surface) and $\widehat{C}$ its dimensionless form, Δp is the pressure jump across the free surface, R_0 is the characteristic droplet radius and $K = R_0\,\Delta p/\gamma_{LA}$, is a reference pressure, constant along the interface. The effect of gravity is also included in Eq. 2.20 through the hydrostatic pressure term, $N_g\,\widehat{z}$, where, $N_g = \frac{\Delta\rho\, g\, R_0^2}{\gamma_{LA}}$, is the gravitational Bond number, with $\Delta\rho$ the density difference between the liquid and ambient, and g the gravitational constant. More details about derivation of the local mean curvature expressions can be found in the Section A.2 of the Appendix A. The Young-Laplace equation can be solved for both axisymmetric (spherical) and cylindrical droplets, by assuming axial symmetry around the z-axis and translational symmetry along a direction perpendicular to the xz-plane, respectively (see Fig. 2.10). Cylindrical droplets can be formed in an experiment where the liquid is held captive between two parallel plates to the xz-plane, and the plates' material wettability is such that the contact angle is equal to 90°. In both cases, the droplet can be conveniently defined in polar coordinates (r, θ) since the problem is considered two-dimensional (see Fig. 2.10). Note that for a three-dimensional case, the droplet would be defined in spherical coordinates (r, θ, ϕ) when considering axial symmetry and cylindrical coordinates (r, θ, y) when considering translational symmetry, respectively.

2.2.2.a Axial symmetry

We initially present the mathematical formulation for spherical droplets, where axial symmetry is considered around the z-axis (see Fig. 2.10). The characteristic length R_0, in this case, corresponds to the radius of a sphere the volume of which is equal to the

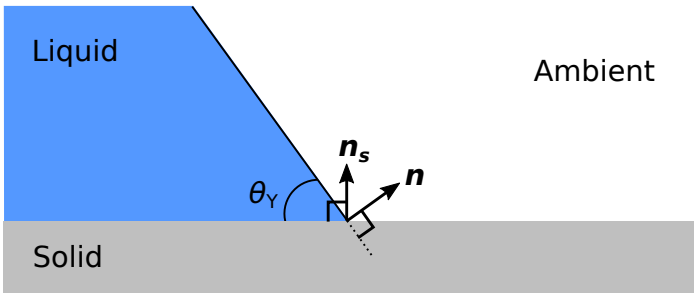

Figure 2.11: Unit normals used in the Young contact angle boundary condition at the three-phase contact line (Eq. 2.23).

droplet volume ($R_0 = \sqrt[3]{\frac{3}{4\pi}V_{\text{droplet}}}$, where V_{droplet} is the droplet volume). By parameterizing the droplet surface with the angular coordinate, θ, (i.e., $r(\theta)$) the problem becomes one-dimensional, where r is the distance from the substrate center $(x, z) = (0,0)$ and θ the angular coordinate (see Fig. 2.10). The local mean curvature of the droplet surface formulated as a function of the angular coordinate, θ, reads (see Section A.2 of the Appendix A for the evaluation of the local mean curvature):

$$C = \frac{1}{r^2 \sin\theta}\left[\frac{2\,r^2\sin^2\theta + r_\theta^2\sin^2\theta}{\sqrt{\sin^2\theta\left(r^2 + r_\theta^2\right)}} - \frac{\mathrm{d}}{\mathrm{d}\theta}\frac{r\,r_\theta\sin^2\theta}{\sqrt{\sin^2\theta\left(r^2 + r_\theta^2\right)}}\right], \tag{2.21}$$

where $r_\theta = \frac{\mathrm{d}r}{\mathrm{d}\theta}$. The Young-Laplace equation (2.20) is then solved subject to the following boundary conditions in dimensionless form:

$$\frac{1}{R_0}\frac{\mathrm{d}r}{\mathrm{d}\theta} = 0 \quad \text{at} \quad \theta = 0, \tag{2.22}$$

$$\frac{1}{R_0^2}\boldsymbol{n}\cdot\boldsymbol{n}_\mathrm{s} - \cos\theta_\mathrm{Y} = 0 \quad \text{at} \quad \theta = \theta_{\max}, \tag{2.23}$$

where $\theta_{\max}$ is the maximum value of the angular coordinate. We keep the terms $\frac{1}{R_0}$ and $\frac{1}{R_0^2}$ in Eqs. 2.22 and 2.23, respectively, in order to be consistent with the dimensionless formulation of the problem. The first, Neumann-type, boundary condition (Eq. 2.22), prescribes the axial symmetry around the z-axis (see Fig. 2.10). The latter boundary condition (Eq. 2.23) prescribes the Young contact angle, θ_Y, at the three-phase contact line, where $\boldsymbol{n}$ and $\boldsymbol{n}_\mathrm{s}$ are the corresponding unit normals of the droplet and solid surface respectively (see Fig. 2.11). We note that in case of a flat and smooth solid surface, the angular coordinate $\theta \in [0, \pi/2]$ with $\theta_{\max} = \pi/2$ and $\boldsymbol{n}_\mathrm{s}$ equals to the unit vector in the z direction. Finally, the solution of the Young-Laplace equation (2.20) is singled out by using a constraint prescribing the droplet volume. In particular, considering that the volume of the droplet equals to that of a sphere with radius R_0, then the volume

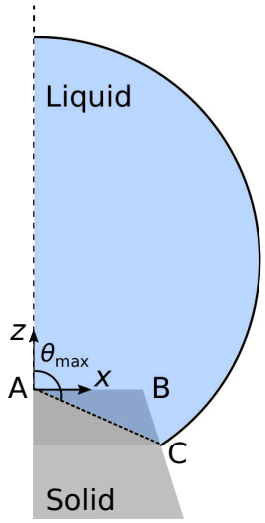

Figure 2.12: Schematic illustration of a droplet resting on a single-corrugated substrate (only the half side of the droplet is presented). In this case, the maximum value of the angular coordinate, $\theta_{\max}$, is unknown.

constraint in dimensionless form reads:

$$\int_0^{\theta_{\max}} \left(\frac{r}{R_0}\right)^3 \sin\theta \, \mathrm{d}\theta = 2, \tag{2.24}$$

where, $\theta_{\max} = \pi/2$, for a smooth substrate case.

In case where the solid surface is structured (see Fig 2.12 where a droplet is hanging on a solid micro-post), the maximum value of the angular coordinate, $\theta_{\max}$, which delimits the boundary of the computational domain, is unknown. This suggests a free boundary problem where the following extra algebraic equation is required:

$$\frac{1}{R_0} r \cos\theta = \widehat{f}_{\text{solid}}(\widehat{x}), \;\; \text{at} \;\; \theta = \theta_{\max}. \tag{2.25}$$

In the above, $\widehat{f}_{\text{solid}}(\widehat{x})$ is a dimensionless function that defines the shape of the solid structure. Essentially, Eq. 2.25 states that the liquid surface touches the solid at $\theta = \theta_{\max}$. In addition, in the case of a structured substrate, the volume constraint has also to be modified:

$$\int_0^{\theta_{\max}} \left(\frac{r}{R_0}\right)^3 \sin\theta \, \mathrm{d}\theta - \widehat{V}_{\text{solid}} = 2, \tag{2.26}$$

where, $\widehat{V}_{\text{solid}}$, is the dimensionless excess volume calculated by rotating the triangular solid domain ABC around the z-axis (see Fig. 2.12).

From the above we conclude that the conventional YL equation suffers from the following limitations:

1. the structure height must be analytically expressed in a function form, $f_{\text{solid}}(x)$, thus no re-entrant structure (mushroom-like structures) or arbitrary roughness

can be used,

2. the Young contact angle boundary condition (Eq. 2.23), the extra algebraic equation (Eq. 2.25), as well as the volume constraint (Eq. 2.26) have to be defined *ad hoc*, for each solid surface topography.

Next, we present the mathematical formulation for the case of cylindrical droplets (translational symmetry).

2.2.2.b Translational symmetry

When translational symmetry along a direction perpendicular to the xz-plane is considered (cylindrical droplets) (see Fig. 2.10), the local mean curvature of the droplet surface reads (see Section A.2 of the Appendix A for details about derivation of the local mean curvature expressions):

$$C = \frac{1}{\sqrt{r^2 + r_\theta^2}} - \frac{1}{r}\frac{\mathrm{d}}{\mathrm{d}\theta}\frac{r_\theta}{\sqrt{r^2 + r_\theta^2}}. \tag{2.27}$$

The Young-Laplace equation (2.20) is then solved by using the same boundary conditions as in the axisymmetric droplet case (Eqs. 2.22 and 2.23). The characteristic length R_0, in this case, corresponds to radius of a circle, the area of which is equal to the cross-sectional area of the droplet, A_{droplet}. In particular, $R_0 = \sqrt{A_{\text{droplet}}/\pi}$. The constraint that singles out the solution of the Young-Laplace equation, now prescribes the droplet cross-sectional area, A_{droplet}:

$$\int_0^{\theta_{\max}} \left(\frac{r}{R_0}\right)^2 \mathrm{d}\theta = \pi, \tag{2.28}$$

where, $\theta_{\max} = \pi/2$, for a flat and smooth substrate case. In addition, in the case of a structured solid surface, the cross-sectional area constraint reads:

$$\int_0^{\theta_{\max}} \left(\frac{r}{R_0}\right)^2 \mathrm{d}\theta - \widehat{A}_{\text{solid}} = \pi, \tag{2.29}$$

where, $\widehat{A}_{\text{solid}}$, is now the dimensionless area of the triangular domain ABC (see Fig. 2.12). Moreover, the extra algebraic equation for defining the maximum value of the angular coordinate, $\theta_{\max}$, (Eq. 2.25) is not modified in the cylindrical droplet case.

Overall, the Young-Laplace (Eq. 2.20), along with the volume constraint for spherical droplets (Eq. 2.24 or Eq. 2.26 for a structured substrate), or the area constraint for cylindrical droplets (Eq. 2.28 or Eq. 2.29 for a structured substrate), and the algebraic equation 2.25 in the case of a structured substrate, are discretized using the finite element method (FEM) [54] accounting for the boundary conditions 2.22 and 2.23. The resulting set of non-linear dimensionless equations is solved iteratively (with Newton-

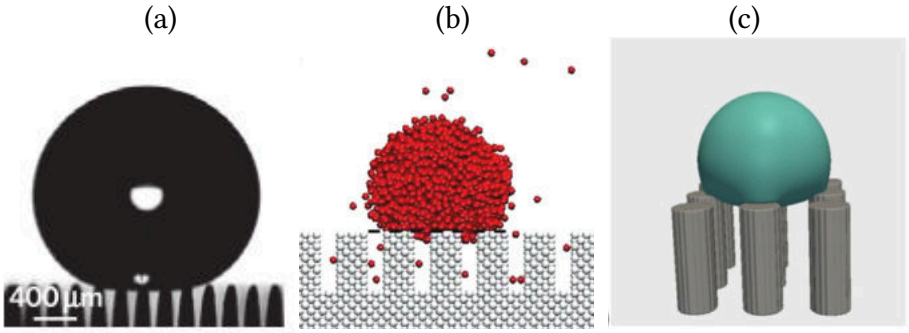

Figure 2.13: (a) Water droplet featuring multiple contact lines on a structured solid surface (reprinted from [62]). Simulations of a similar system, by using molecular dynamics and lattice-Boltzmann models, are demonstrated in (b) and (c), respectively (reprinted from [63] and [64]).

Raphson method) with an in-house code for the distance, $r(\theta)$, the reference pressure, $K = R_0\Delta p/\gamma_{\mathrm{LA}}$, and the maximum value of the angular coordinate, $\theta_{\max}$, only in the case of a structured substrate ($\theta_{\max} = \pi/2$ for a flat and smooth substrate).

The above formulation can be employed to predict the shape of axisymmetric, or cylindrical, droplets on geometrically heterogeneous surfaces, however, we note that the current parameterization, in terms of the angular coordinate, θ, would be sufficient only for solid surfaces with smooth corrugations (or single-corrugated substrates like Fig. 2.12), where $r(\theta)$ is a single value function. In particular, when wetting occurs on solid surfaces of increased topographic complexity, different r values can correspond to the same angular coordinate, thus the angular parameterization would be deficient. In addition, the implementation of the Young contact angle boundary condition (Eq. 2.23) is of limited efficiency on complex heterogeneous solid surfaces, since wetting states with multiple TPLs -the number and position of which is unknown- can be admitted (see e.g. Fig. 2.13a). Computations of such composite solid-liquid-ambient states are feasible in a unit cell of the surface pattern [55], however, they are of acceptable accuracy only when the droplet size is considerably larger than the roughness scale since they disregard the significant pinning effects at the droplet endings.

Alternatively, wetting states with multiple contact lines can be predicted by using fine-scale computational approaches, such as molecular dynamics (MD) [56, 57, 58] and mesoscopic lattice-Boltzmann (LB) models [59, 60, 61] (see Fig. 2.13b, c). However, the required computational cost is considerably higher, especially in cases where real-life millimeter-sized droplets are simulated. Fine-scale computational approaches are briefly described in the following Section.

2.2.3 Fine-scale modeling

In the fine-scale models, the liquid-ambient and liquid-solid interfaces are actually diffuse (have a finite thickness), due to thermal fluctuations and the action of molecular forces. Such an approach does not require any contact angle boundary condition which

is imperative in the sharp-interface continuum-level methods (e.g. Young-Laplace equation). Bellow we present more details regarding the molecular dynamics and the lattice-Boltzmann approaches.

2.2.3.a Molecular dynamics

Molecular dynamics simulation consists of the numerical solution of the classic equations of motion (Newton's equations) [56]. The forces acting on the atoms are derived from a potential energy, U_{ab}, (usually modeled with Lennard-Jones potentials), which is usually truncated at a relatively small cut-off radius:

$$U_{ab} = 4\,\epsilon_{ab}\left[C_{ij}\left(\frac{\sigma_{ab}}{r_{ij}}\right)^{12} - D_{ij}\left(\frac{\sigma_{ab}}{r_{ij}}\right)^{6}\right], \tag{2.30}$$

where, for a given pair of atoms a and b, the coefficients ϵ_{ab} and σ_{ab} are related with the depth of the potential well and the effective molecular diameter; r_{ij} is the distance of separation and the coefficients C_{ij} and D_{ij} regulate the repulsive (C_{ij}) and attractive (D_{ij}) parts of the potential. Furthermore, if electrostatic charges are present, Coulomb potentials are also included. Finally, the solid wettability is regulated by the strength of the liquid-solid interaction (strong forces imply wetting whereas weak forces imply non-wetting), thus Young's contact angle derives implicitly in this case.

The first molecular dynamics simulations of wetting phenomena were presented in the pioneer work of Saville in 1977 [65], where by using simple Lennard-Jones potentials to describe molecular interactions, he concluded that wetting phenomena in the nano-scale deviate from the Young's equation predictions (2.6). Since then, the shape of droplets on smooth as well as on rough substrates has been extensively studied, by performing larger-scale simulations ($\sim 10^6$ atoms) made possible by the growth of computer power [56, 57]. Cassie-Baxter to Wenzel wetting transitions on structured surfaces, however, have low probability of occurring ("rare events") and thus the MD simulation procedure has to be highly accelerated. Such a task is made possible by using forward flux sampling (FFS) techniques [66] as presented in the recent publication of Savoy and Escobedo [58] who have studied wetting transitions on rough solid surfaces. Even in this case, however, the droplet size is far from realistic. Overall, MD is powerful tool and can lead to a better understanding of the physics of wetting, however, current simulations are still restricted to physically small systems (nano-droplets).

2.2.3.b Lattice-Boltzmann

The mesoscopic lattice-Boltzmann method, where a fluid is represented in terms of the probability of finding a particle (fictitious basic unit of the fluid) at a certain position in space and time, has been widely used in simulating flow phenomena [67]. LB offers the

advantage of modeling microscopic liquid-ambient and liquid-solid interactions, with lower computational resources compared to molecular dynamics simulations. In wetting systems, the Boltzmann-BGK equation is solved [60, 61]:

$$\frac{\mathrm{d}f}{\mathrm{d}t} + \boldsymbol{v} \cdot \nabla f = -\frac{f - f^{eq}}{\tau} + \frac{\delta f}{\delta t}, \tag{2.31}$$

where, f, is the probability distribution function, f^{eq}, the equilibrium distribution of particle velocities, τ, the relaxation time of the system and, $\boldsymbol{v}$, the discretized velocity space. The term $\frac{\delta f}{\delta t}$ on the right-hand side of Eq. 2.31 accounts for the action of both external and internal forces. The liquid-solid interactions in this approach are modeled by using a pseudo-potential with a repulsive and an attractive component, in direct analogy with DLVO theory [60, 61]. The Young contact angle, θ_{Y}, is then tuned by the attraction and repulsion parameters of the liquid-solid pseudo-potential.

Similar to the MD simulations, the solution procedure here has to be accelerated, since dynamic simulations converge to stable equilibrium states only after long execution times. Such an acceleration has been performed through a time-stepper based computational framework, described in [60, 61], which wraps around the LB dynamic simulator and enables the computation of steady state solutions, utilizing relatively short and appropriately initialized LB executions. Overall, mesoscopic simulations can successfully describe wetting behavior on complex surfaces (including Cassie-Baxter to Wenzel wetting transitions [60]), however, the required computational cost is considerably higher compared to the continuum-level methods.

Conclusively, fine-scale models can handle cases with multiple contact lines by modeling microscopic liquid-solid interactions, however, the computational power requirements increase dramatically when the ratio of the droplet size over roughness is large (millimeter size droplets). Alternatively, and in order to preserve the computational cost at a reasonable level, the Young-Laplace equation (2.20) can be reformulated so as to encompass molecular details, lumped into a liquid-solid interaction term, and avoid the implementation of the Young contact angle boundary condition, as described in the next Section.

2.2.4 Augmented Young-Laplace equation

Here, in order to overcome the previously referred limitations in continuum-level modeling, we present a new formulation of the Young-Laplace equation. From our point of view, the liquid-ambient and the liquid-solid interface must be treated in a unified context. In particular, it is suggested that the application of the Young-Laplace equation should not end at the three-phase contact line but it should govern the entire droplet surface (both liquid-ambient and liquid-solid interfaces). This approach requires that the liquid and solid phases are always separated by an thin layer (see Fig. 2.14). Young's angle, in this framework, would emerge "naturally" as the result of the combined action

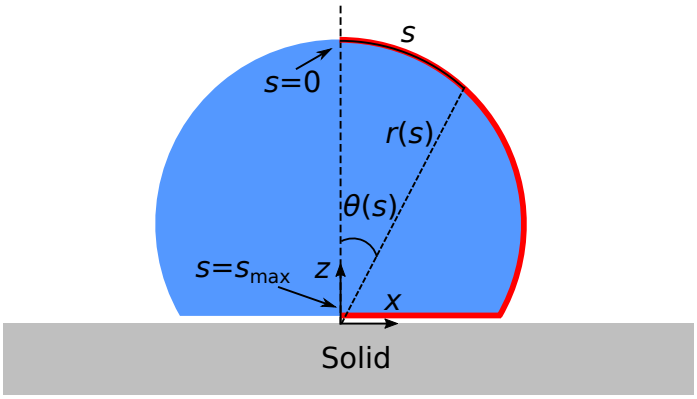

Figure 2.14: Unified conception of the proposed augmented Young-Laplace (Eq. 2.32). The red line depicts the liquid-ambient and the liquid-solid interfaces which are now treated uniformly and parameterized with the arc-length, s.

of the surface tension and liquid-solid interactions.

In particular, we consider that the molecular interactions (van der Waals and electrostatic forces) are incorporated in a disjoining (or Derjaguin) pressure term [68], active in the vicinity of solid surface, which can be included in the Young Laplace equation. Thus, starting from the conventional form (Eq. 2.20), the reformulated (or augmented) Young-Laplace equation, which states the force balance between surface tension, gravity, the disjoining and the Laplace pressure, reads in dimensionless form:

$$\frac{R_0}{\gamma_{\mathrm{LA}}} p^{\mathrm{LS}} + \widehat{C} + N_{\mathrm{g}}\,\widehat{z} = K, \tag{2.32}$$

where, p^{LS}, is the disjoining pressure which consists of a short range, repulsive, and a long range, attractive, term (see Section 2.2.4.b for more details about the disjoining pressure formulation). The above equation now governs the whole droplet surface, enabling the computation of droplet profiles with an unknown cardinality of three-phase contact lines, on geometrically heterogeneous solid surfaces. This consideration, however, requires an appropriate parameterization of the droplet surface, as discussed in the following Section.

2.2.4.a Arc-length parameterization

The previously presented parameterization (in terms of the angular coordinate, θ) would not be sufficient in the case of the augmented Young-Laplace equation, since different r values (from the upper and the low part of the droplet) can correspond to the same angular coordinate (see Fig. 2.14). An alternative approach is to parameterize polar coordinates (r, θ) as a function of the arc-length, s, of the intersection of the droplet surface with a vertical plane (i.e., $r(s)$, $\theta(s)$) (see Fig. 2.14). This parameterization enables the tracking of the droplet surface in a natural way while the problem is maintained one-dimensional. In particular, the local mean curvature of an axisymmetric droplet,

formulated as a function of the arc-length, s, reads:

$$C = \frac{1}{r \sin\theta \sqrt{r^2 \theta_s^2 + r_s^2}} \left[2\, r\, \theta_s \sin\theta - r_s \cos\theta + r \sin\theta \frac{\mathrm{d}}{\mathrm{d}s} \arctan\left(\frac{r\, \theta_s}{r_s} \right) \right]. \tag{2.33}$$

where $\theta_s = \frac{\mathrm{d}\theta}{\mathrm{d}s}$ and $r_s = \frac{\mathrm{d}r}{\mathrm{d}s}$. The determination of the angular coordinate, θ, requires an extra differential equation; this is the arc-length equation, which by virtue of the Pythagorean Theorem reads:

$$\frac{1}{R_0^2} \left(\mathrm{d}r^2 + r^2\, \mathrm{d}\theta^2 - \mathrm{d}s^2 \right) = 0. \tag{2.34}$$

The solution of the augmented Young-Laplace (2.32) is determined subject to the following, Neumann-type, boundary condition:

$$\frac{1}{R_0} \frac{\mathrm{d}r}{\mathrm{d}\theta} = 0 \quad \text{at} \quad s = 0, \tag{2.35}$$

which is equivalent to Eq. 2.22 and prescribes the axial symmetry around the z-axis (see Fig. 2.14). In addition, the Young contact angle boundary condition (2.23) is now replaced by the following Neumann-type condition:

$$\frac{1}{R_0} \frac{\mathrm{d}r}{\mathrm{d}\theta} = 0 \quad \text{at} \quad s = s_{\max}, \tag{2.36}$$

which prescribes the axial symmetry around the z-axis, at the droplet base. Moreover, the following, Dirichlet-type, boundary condition singles out the arc-length equation (2.34):

$$\theta = 0 \quad \text{at} \quad s = 0. \tag{2.37}$$

The constraint prescribing the droplet volume, V_{droplet}, now reads (starting from Eq. 2.24):

$$\int_0^{s_{\max}} \left(\frac{r}{R_0} \right)^3 \sin\theta\, \theta_s\, \mathrm{d}s = 2, \tag{2.38}$$

where, however, the maximum arc-length of the droplet surface, $s_{\max}$, which delimits the boundary of the computational domain, is unknown. The extra equation required to deal with the free boundary reads:

$$\frac{1}{R_0} r \sin\theta = 0, \quad \text{at} \quad s = s_{\max}. \tag{2.39}$$

Essentially, Eq. 2.39 is a condition that the liquid surface touches the z-axis at $s = s_{\max}$ (see Fig. 2.14).

In the case of translational symmetry (considering cylindrical droplets), the local mean

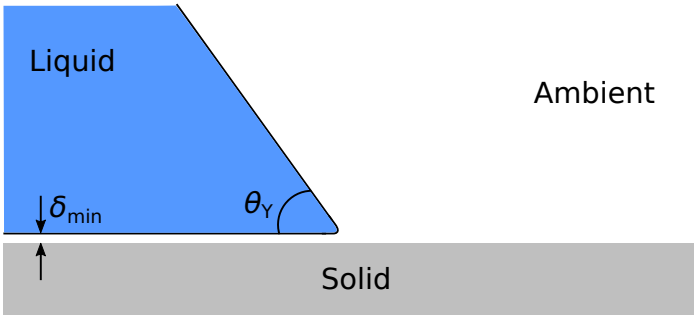

Figure 2.15: Schematic of the three-phase contact using the proposed unified conception (one equation for both the liquid-solid and the liquid-ambient interfaces). The liquid and the solid phases are considered to be separated by an intermediate layer (with thickness δ_{min}) which is the locus where the disjoining pressure acts.

curvature, as a function of the arc-length, s, reads:

$$C = \frac{1}{\sqrt{r^2\,\theta_s^2 + r_s^2}}\left[\theta_s + \frac{\mathrm{d}}{\mathrm{d}s}\arctan\left(\frac{r\,\theta_s}{r_s}\right)\right]. \tag{2.40}$$

In addition, Eq. 2.38 must now be replaced by a constraint prescribing the droplet cross-sectional area, A_{droplet}. In particular, starting from Eq. 2.28, yields:

$$\int_0^{s_{\max}} \left(\frac{r}{R_0}\right)^2 \theta_s^2\,\mathrm{d}s = \pi, \tag{2.41}$$

which singles out the solution of the augmented Young-Laplace equation in the case of translational symmetry. The rest of the equations (Eqs. 2.34, 2.35, 2.36, 2.37 and 2.39) are identical for both cylindrical (translational symmetry) and spherical (axial symmetry) droplets.

We note that, in contrast with the conventional Young-Laplace equation, the expression of the augmented Young-Laplace is not affected by the shape of the solid structure. In particular, the structure shape was explicitly introduced in the conventional Young-Laplace equation, through the Young contact angle boundary condition (Eq. 2.23), as well as through the volume (or area) constraint (Eq. 2.26 or Eq. 2.29), respectively. In the proposed formulation, however, we do not have any explicit boundary condition at the solid surface while the effect of the solid structure is implicitly incorporated in the disjoining pressure term, p^{LS}, as will be discussed in the following Section.

2.2.4.b Disjoining (or Derjaguin) pressure

The concept of the disjoining pressure was initially introduced by Derjaguin in order to represent the molecular interactions between surfaces [69]. In particular, the disjoining pressure is defined as the pressure in excess of the external pressure that must be applied to a fluid between two plates to maintain a given separation, that is essentially, the force

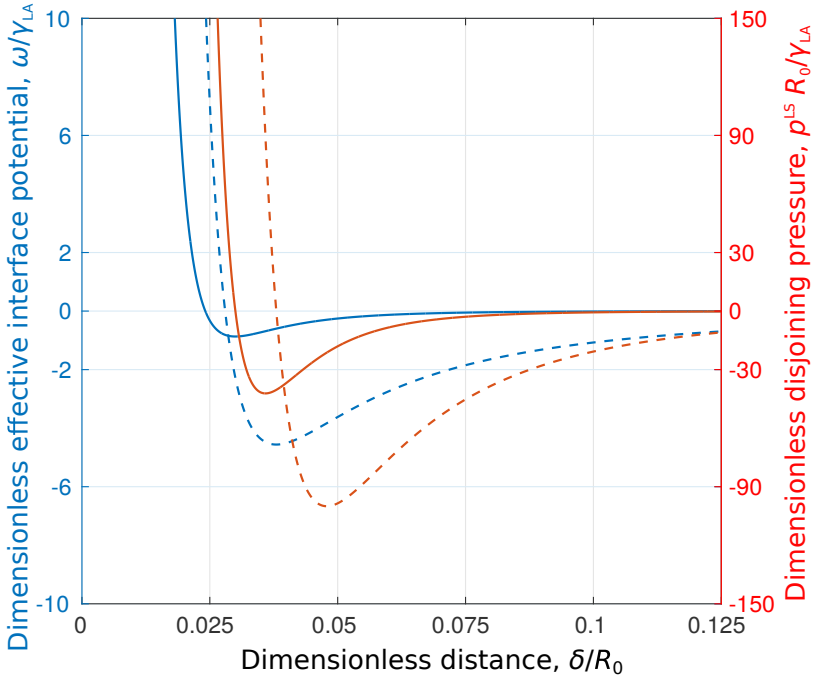

Figure 2.16: Profiles of the dimensionless disjoining pressure, $\frac{R_0}{\gamma_{LA}} p^{LS}$ (red lines), and of the corresponding dimensionless effective interface potential (blue lines), $\frac{\omega}{\gamma_{LA}}$, as a function of the liquid-solid dimensionless distance, $\frac{\delta}{R_0}$. The above profiles are evaluated for two sets of parameters: (i) solid lines for $\sigma = 3.8 \times 10^{-2}$, $C_1 = 8$, $C_2 = 6$, $\epsilon = 8 \times 10^{-3}$, $w^{LS} = 4 \times 10^2$ and (ii) dashed lines for $\sigma = 3.8 \times 10^{-2}$, $C_1 = 6$, $C_2 = 3$, $\epsilon = 0$, $w^{LS} = 4 \times 10^2$.

of attraction or repulsion between the plates per unit area. Here, the disjoining pressure term, p^{LS}, essentially expresses the excess pressure in the region between the liquid and the solid phases, due to molecular interactions (including van der Waals, electrostatic and steric forces [68]). Such point of view differs from the conventional description, where the disjoining pressure is raised within a thin liquid film that precedes the three-phase contact line [68].

We formulate the disjoining pressure according to the following expression:

$$\frac{R_0}{\gamma_{LA}} p^{LS} = w^{LS} \left[\left(\frac{\sigma}{\delta/R_0 + \epsilon} \right)^{C_1} - \left(\frac{\sigma}{\delta/R_0 + \epsilon} \right)^{C_2} \right], \tag{2.42}$$

which resembles a Lennard-Jones type potential (see Eq. 2.30). Alternative formulations for the disjoining pressure could also be employed, as demonstrated in [70]. In Eq. 2.42, the depth of the potential well is proportional to a wetting parameter, w^{LS}, which is directly related with the solid wettability (an increase of w^{LS} results in a deeper well of the potential, indicating stronger liquid-solid affinity). In addition, the exponents C_1 (in the repulsive term of Eq. 2.42) and C_2 (in the attractive term of Eq. 2.42) control the range of the molecular interactions (large C_1 and C_2 reduce the range within which these interactions are active, as can be observed in the disjoining pressure profiles plotted in Fig. 2.16). The distance, δ, between the liquid and the solid surface determines whether

the disjoining pressure is attractive (modeling van der Waals interactions, for relatively large δ) or repulsive (modeling steric forces and electrostatic interactions determined by an overlapping of the electrical double layers, for small δ) [68]. In the case of a perfectly flat solid surface, the distance, δ, is defined as the vertical distance of the liquid surface from the solid boundary. For non-flat, rough, solid surfaces, the definition of distance, δ, requires special consideration. Here, we take δ as the Euclidean distance from the solid. This quantity is obtained from the solution of the Eikonal equation [71], which expresses the signed distance from a boundary (even arbitrarily shaped). The solution of the Eikonal equation is discussed in Section A.3 of the Appendix A. As previously argued, in our formulation we consider that the liquid and the solid phases are separated by an intermediate layer (with thickness $\delta_{\min}$) which is stabilized by the presence of the disjoining pressure (see Fig. 2.15). In particular at $\delta = \delta_{\min}$ the repulsive and attractive forces balance each other; further reduction of the intermediate layer thickness, below $\delta_{\min}$, would generate strong repulsion. The minimum allowed liquid-solid distance $\delta_{\min}$ is determined by the constants σ and ϵ. Specifically, for $\delta = \delta_{\min} \Leftrightarrow p^{\mathrm{LS}} = 0 \Rightarrow \delta_{\min} = R_0(\sigma - \epsilon)$. We note that the presented formulation is still valid even with a zero value of the ϵ parameter (see e.g. a disjoining pressure profile with $\epsilon = 0$ in Fig. 2.16), however, ϵ has a small finite value in all of the demonstrated results in this Thesis, in order to avoid any numerical singularities as δ approaches zero.

A common description of the attractive term (van der Waals component) of the disjoining pressure ($\left[-\frac{\gamma_{\mathrm{LA}}}{R_0}\left(\frac{\sigma}{\delta/R_0+\epsilon}\right)^{C_2}\right]$ in Eq. 2.42) can be given in terms of the so-called Hamaker constant, H_{a} [72]. In particular, the van der Waals interactions are usually modeled as [72]: $\left[-\frac{H_{\mathrm{a}}}{6\,\pi\,\delta^3}\right]$, with $H_{\mathrm{a}} > 0$. By equating this common description with our disjoining pressure formulation, considering that $C_2 = 3$ and $\epsilon = 0$, yields:

$$H_{\mathrm{a}} = 6\,\pi\,\gamma_{\mathrm{LA}}\,{R_0}^2\,\sigma^3. \tag{2.43}$$

Since the typical values of the Hamaker constant of liquids is about 10^{-19} J [72], then Eq. 2.43 yields that the disjoining pressure parameter, σ, must be of the order of 10^{-5}, for a water droplet ($\gamma_{\mathrm{LA}} = 0.072$ N/m) with a nominal radius $R_0 = 1$ mm. This results to a minimum liquid-solid distance, $\delta_{\min} = R_0(\sigma - \epsilon) \sim 10^{-8}$ m. Unfortunately, the modeling of such multiple length scales between the disjoining pressure (nm scale) and the interfacial tension (μm to mm scale) would be infeasible in a continuum-level approach. Thus, we can either consider droplets with very small nominal radius (of the order of μm) or, for the shake of computational efficiency, we can use a $\delta_{\min}$ quite larger than $\sim 10^{-8}$ m. Even in the latter case, though, our formulation can efficiently capture several equilibrium and dynamic phenomena, as will be demonstrated in the following Chapters (from 4 to 7). Decreasing liquid-solid distance to the realistic value of the order of 10^{-8} m, while simulating millimeter-sized droplets, would require a multiscale modeling approach. In this case, the interaction phenomena at nanometer scale should be linked with the macroscopic droplet behavior at a millimeter scale. Such a scale linking is a subject of ongoing research and will be discussed in the Section 9.4 of Chapter 9.

The molecular interactions, which are lumped into the disjoining pressure term, result to an additional contribution to the surface free energy, referred as effective interface potential, ω. The effective interface potential essentially expresses the cost of free energy per unit area to maintain a distance, δ, between the solid and the liquid phases ($\omega \rightarrow 0$ when $\delta \rightarrow \infty$) and is expressed in terms of the disjoining pressure, p^{LS}, according to [68]:

$$p^{\mathrm{LS}} = -\frac{\mathrm{d}\omega}{\mathrm{d}\delta}, \tag{2.44}$$

which yields:

$$\frac{\omega}{\gamma_{\mathrm{LA}}} = w^{\mathrm{LS}} \left(\frac{\delta}{R_0} + \epsilon\right) \left[\frac{\left(\frac{\sigma}{\delta/R_0+\epsilon}\right)^{C_2}}{1-C_2} - \frac{\left(\frac{\sigma}{\delta/R_0+\epsilon}\right)^{C_1}}{1-C_1}\right]. \tag{2.45}$$

Characteristic profiles of the disjoining pressure and the effective interface potential, as a function of the liquid-solid distance, δ, are presented in Fig. 2.16. Starting from Eq. 2.4, the surface free energy of the droplet now reads:

$$E = \gamma_{\mathrm{LS}}\, A_{\mathrm{LS}} + \gamma_{\mathrm{SA}}\, A_{\mathrm{SA}} + \gamma_{\mathrm{LA}}\, A_{\mathrm{LA}} + \omega_{\mathrm{min}}\, A_{\mathrm{LS}}, \tag{2.46}$$

where ω_{min} is the absolute minimum of the effective interface potential, ω (see Fig. 2.16). In the above, we have considered that the contribution of ω in the free surface energy is significant only along the liquid-solid interface, i.e. when the liquid phase is at the minimum distance from the solid phase ($\delta = \delta_{\mathrm{min}}$). At this energetically favored distance, where $p^{\mathrm{LS}} = 0$, Eq. 2.44 gives $\frac{\mathrm{d}\omega}{\mathrm{d}\delta} = 0 \;\Rightarrow \omega = \omega_{\mathrm{min}}$. Thus by substituting $\delta = \delta_{\mathrm{min}} = R_0\,(\sigma - \epsilon)$ in Eq. 2.45 yields:

$$\frac{\omega_{\mathrm{min}}}{\gamma_{\mathrm{LA}}} = -\frac{w^{\mathrm{LS}}\,\sigma\,(C_1 - C_2)}{(C_1 - 1)\,(C_2 - 1)}. \tag{2.47}$$

In an analogy to the theory of adhesion [35], introduced by Dupré, ω_{min} can be also treated as the work of adhesion between liquid and solid phases which is given by [35]:

$$\omega_{\mathrm{min}} = \gamma_{\mathrm{SA}} + \gamma_{\mathrm{LA}} - \gamma_{\mathrm{LS}}, \tag{2.48}$$

representing the work necessary to separate a unit area of the liquid-solid interface into two liquid-ambient and solid-ambient interfaces.

Since the Young contact angle, θ_{Y}, is not imposed explicitly in the simulation (both liquid-ambient and liquid-solid interfaces are treated in a consolidated framework), a correlation between the liquid-solid affinity, expressed via the wetting parameter, w^{LS}, and Young's contact angle is deemed necessary. In particular, such a correlation yields by combining Eq. 2.48 with the Young equation (2.6):

$$\cos\theta_{\mathrm{Y}} = \frac{\omega_{\mathrm{min}}}{\gamma_{\mathrm{LA}}} - 1. \tag{2.49}$$

The above is known as Frumkin-Derjaguin equation and is widely used in the literature

(see [73, 68]) to calculate contact angle values in the presence of a disjoining pressure, replacing the Young equation (2.6). Finally, by using Eq. 2.47 we can construct an one-to-one correlation between the Young contact angle and the wetting parameter ($w^{\mathrm{LS}} = w^{\mathrm{LS}}(\theta_{\mathrm{Y}})$) which reads:

$$w^{\mathrm{LS}} = \frac{(C_1 - 1)(C_2 - 1)(1 + \cos\theta_{\mathrm{Y}})}{\sigma(C_1 - C_2)}. \tag{2.50}$$

A validation of the above formula is presented in Chapter 4 (Fig. 4.2), by calculating the Young contact angle with circular fitting on the equilibrium droplet profiles, in the absence of any gravitational field.

We note that the computational cost of the Augmented Young-Laplace equation is similar to that of the conventional form, however, it exhibits a plethora of advantages such as modeling of droplets with multiple and reconfigurable three-phase contact lines and independence of the equations form from the solid topography (in contrast with the conventional Young-Laplace equation, the substrate geometry is not incorporated explicitly in the augmented Young-Laplace equation).

The overall problem is solved as follows: the augmented Young-Laplace (2.32) and the arc-length (2.34) equations, along with the constraints 2.38 (or 2.41 for a cylindrical droplet) and 2.39, are discretized using the finite element method, accounting for the boundary conditions 2.35, 2.36 and 2.37. The resulting set of non-linear dimensionless equations is solved iteratively (with Newton-Raphson method) with an in-house code for the droplet surface coordinates $r(s)$ and $\theta(s)$, the maximum arc-length, $s_{\max}$, and the reference pressure, K. We note that the solution of the Eikonal equation is performed only once for a particular solid geometry (see Section A.3 of the Appendix A), thus it is not included in the above iterative procedure. Computational results of the augmented Young-Laplace equation, along with the Galerkin residuals of the finite element method, when deemed necessary, are presented in Part II of the Thesis. Following is a discussion regarding the modeling of dynamic wetting phenomena.

CHAPTER 3

Dynamics

In this Chapter we discuss the importance of the three-phase contact line motion for various technological processes. We present the current modeling approaches for predicting the three-phase contact line dynamics as well as the emerging limitations arising either from the tedious implementation of the Young contact angle boundary condition or from the high computational needs. We, then, apply our previously presented continuum level, sharp interface approach, based on the unified conception of the liquid-ambient and liquid-solid interfaces, in order to predict the dynamics of wetting on heterogeneous substrates (chemically or geometrically textured). Our formulation enables the computationally efficient treatment of multiple, dynamic contact lines, eliminating the need to apply any explicit boundary condition at the three-phase contact line.

3.1 Contact line motion

Consider that a droplet is placed on a solid surface, far from its equilibrium state. What follows is that the three-phase contact line will set in motion until the equilibrium contact angle, θ_{Y}, is reached. The evolving macroscopic contact angle, until the equilibrium state, is called dynamic contact angle, θ_{d} (see Fig. 3.1). The dynamic behavior of the three-phase contact is of utmost importance for various technological applications such as coating of solids by liquid films, inkjet printing and fluid motion in lab-on-a-chip devices. The contact line velocity, for example, determines whether air bubbles can be entrapped underneath the liquid film in coating processes. This is a crucial limiting factor for the smoothness and adhesion of the coating. Due to their significance in such applications, wetting dynamics has been studied extensively, both theoretically and experimentally [74, 75, 37, 76].

What renders the dynamic wetting phenomena more complicated than the equilibrium is the presence of viscous forces, in a length scale starting from molecular size to the capillary length, $\lambda_\kappa = \sqrt{\frac{\gamma_{\mathrm{LA}}}{\rho g}}$, and inertial forces at larger scales. Therefore, the contact line motion as well as the apparent dynamic contact angle of the droplet are now governed by viscous, inertial and capillary forces as well as by molecular phenomena interplay.

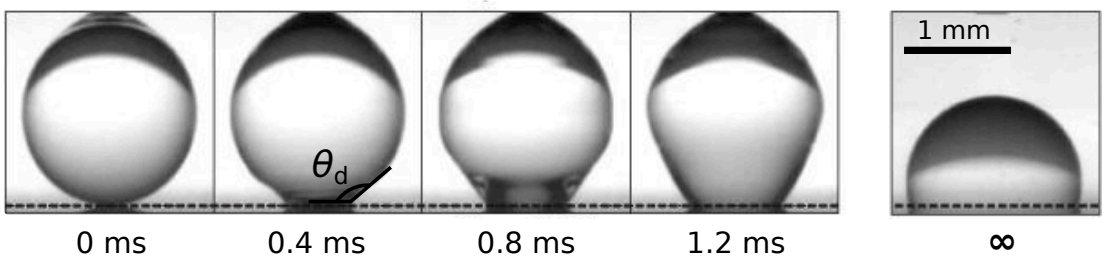

Figure 3.1: Different time instances of a water droplet spreading on a solid surface with θ_Y = 117°. The last image shows the equilibrium droplet shape (reprinted from [77]).

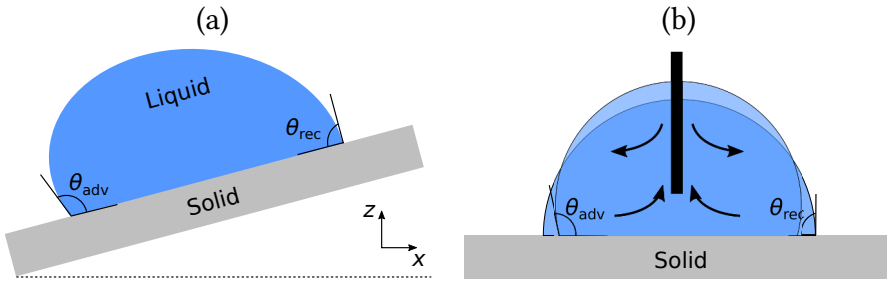

Figure 3.2: Schematic presentation of the advancing (θ_{adv}) and receding (θ_{rec}) contact angles in the case of (a) a sliding droplet on a tilted substrate and (b) a droplet which is slowly pumped or drawn, on a horizontal substrate.

The relative importance between the liquid-ambient interfacial tension, γ_{LA}, and viscosity, μ, is given by the capillary number:

$$\mathrm{Ca} = \frac{u_{cl}\,\mu}{\gamma_{LA}}, \tag{3.1}$$

where u_{cl} is the velocity scale (usually the contact line velocity). Several complex phenomena originate from the presence of viscosity during the contact line motion. In particular, it has been observed that the dynamic contact angle at the front of a sliding droplet (advancing contact angle, θ_{adv}) differs from the rear one (receding contact angle, θ_{rec}) as much as tens of degrees [37, 76] (see Fig. 3.2a). A typical technique to measure the advancing and receding dynamic contact angles is to add and withdraw liquid from a droplet by using a needle, as demonstrated in Fig. 3.2b. In particular, the variation of the dynamic contact angle, as a function of the droplet volume, is presented in Fig. 3.3. This phenomenon of contact angle hysteresis (CAH) can also be substantially enhanced by surface roughness and chemical heterogeneities, however, it has also been observed in molecularly smooth free liquid films [78].

Apart from viscous forces, the inertial forces are also significant in wetting dynamics, especially in the case where the droplet impacts a solid surface with an initial velocity (see Fig 3.4). The dimensionless quantity which determines the relative importance between the inertial forces and the interfacial tension is the Weber number:

$$\mathrm{We} = \frac{\rho\,{u_0}^2\,D_0}{\gamma_{LA}}, \tag{3.2}$$

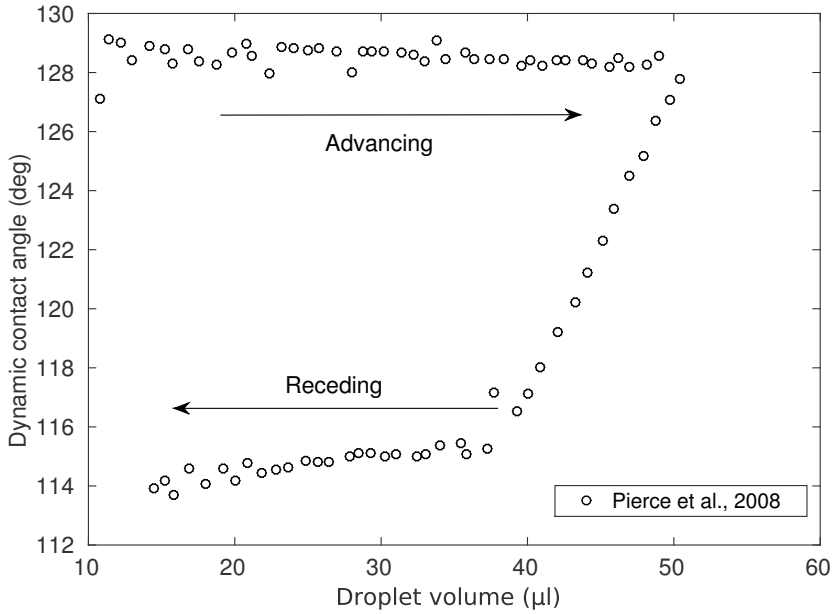

Figure 3.3: Typical advancing and receding contact angle measurements of a water droplet on a fluorinated silicon substrate [80].

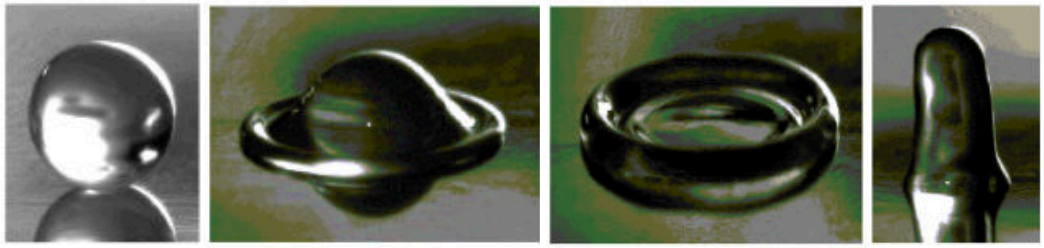

Figure 3.4: Different time instances of a water droplet impacting on a wax solid surface with θ_Y = 93.5° and We = 58 (reprinted from [81]).

where ρ is the fluid density, D_0 is the nominal droplet diameter ($D_0 = 2\,R_0$) and u_0 is a characteristic velocity (usually, in the case of an impacting droplet, the velocity just before the collision). Droplet impact with high velocities can lead to unusual droplet formations (see Fig 3.4), accompanied with ejection of small satellite droplets (splashing). The influence of solid texture is also crucial since it can lead to a complete droplet rebound after the impact on a superhydrophobic surface [79], like the self-cleaning lotus leaf. Definitely, in order to design and optimize the functional substrates that are described in Section 1.2, a detailed model for the droplet dynamic behavior on heterogeneous surfaces is deemed necessary.

The current prevailing modeling approaches to simulate dynamic wetting phenomena are the hydrodynamic model (HD) [82] and the molecular kinetic theory (MKT) [83]. According to the hydrodynamic approach, the viscous friction is assumed to be the only significant dissipative force during liquid motion. On the other hand, molecular kinetic theory derives a theoretical dependence of the dynamic contact angle on the velocity

of the contact line, by balancing the capillary forces with a liquid-solid friction and neglecting any viscous dissipation. A combined description was also proposed by Petrov and Petrov [84], intending to exploit the advantages of the both approaches. We note, however, that despite the huge amount of work published in the last thirty years, the appropriate modeling of contact lines under dynamic conditions is yet a controversial issue since both hydrodynamic model and the molecular kinetic theory exhibit discrepancies from several sets of experiments [85]. In addition, in case we select the hydrodynamic model to predict the behavior of a droplet on a geometrically structured substrate, a contact angle boundary condition has to be applied to multiple three-phase contact lines, unknown in number. Such a task would be infeasible by using the conventional sharp-interface formulations of the hydrodynamic model.

Other approaches for predicting the contact line dynamics include fine-scale methods (molecular dynamics and mesoscopic lattice Boltzmann models) which are described in Section 2.2.3. These methodologies can handle cases with multiple contact lines, however, they suffer from severe computational limitations when realistic-sized systems are examined (i.e. millimeter-sized droplets). In the next Section, we initially discuss the hydrodynamic and the molecular kinetic approaches as well as their restrictions that prevent us from performing efficient dynamic simulations on structured geometries. We then reformulate the hydrodynamic model, by applying the proposed unified, sharp-interface approach and incorporating molecular phenomena (liquid-solid interactions via a disjoining pressure term) in order to address the previously referred limitations.

3.2 Modeling of dynamic wetting phenomena

3.2.1 Hydrodynamic model

In the hydrodynamic approach, the viscous dissipation determines the liquid motion on a solid surface. Unlike the augmented Young-Laplace equation presented in Chapter 2, we note that the variety of the dynamic wetting problems which are examined in the current Thesis renders the definition of particular characteristic quantities complicated and thus we prefer to present the following mathematical formulation in dimensional form. In particular, the dynamics of a fluid are modeled by the incompressible Navier-Stokes equations [86]:

$$\rho\left(\frac{\mathrm{d}\boldsymbol{u}}{\mathrm{d}t}+\boldsymbol{u}\cdot\nabla\boldsymbol{u}\right)=-\nabla p+\mu\,\nabla^2\boldsymbol{u}+\boldsymbol{G}, \tag{3.3a}$$

$$\nabla\cdot\boldsymbol{u}=0, \tag{3.3b}$$

where, ρ, is the fluid density, μ, is the viscosity, $\boldsymbol{u}=(u_x,u_z)$ and p are the fluid velocity field and pressure, respectively; $\boldsymbol{G}$ is a body force expressing the effect of gravity ($\boldsymbol{G}=\rho\boldsymbol{g}$, where the vector, $\boldsymbol{g}$, is the gravitational acceleration). The fluid dynamics at the

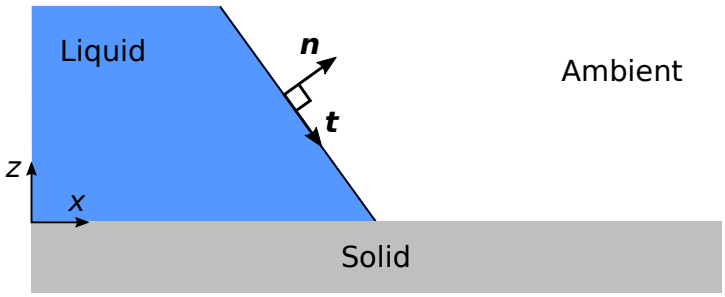

Figure 3.5: Unit normal, $\boldsymbol{n}$, and the unit tangent, $\boldsymbol{t}$, vectors of the liquid-ambient interface.

droplet surface requires special consideration. In particular, the following stress balance holds at liquid-ambient interface [86]:

$$\boldsymbol{s}(\boldsymbol{n})|_{\text{liquid}} - \boldsymbol{s}(\boldsymbol{n})|_{\text{ambient}} + \nabla_s \gamma_{\text{LA}} - \gamma_{\text{LA}}\, C\, \boldsymbol{n} = 0, \tag{3.4}$$

where $\boldsymbol{s}$ is the total stress tensor and $\boldsymbol{n}$ the unit normal of the liquid-ambient interface (see Fig. 3.5). In the absence of surfactant adsorption on the droplet surface [87, 88] or temperature gradients along the solid substrate (thermocapillary phenomena) [89, 90], the interfacial tension gradient ($\nabla_s \gamma_{\text{LA}}$) can be neglected from Eq. 3.4. Phenomena with interfacial tension gradients are out of the scope of this Thesis. Therefore, resolving Eq 3.4 into normal and tangential components gives [86]:

$$\Delta p + \tau_{\text{nn}}|_{\text{ambient}} - \tau_{\text{nn}}|_{\text{liquid}} - \gamma_{\text{LA}}\, C = 0, \tag{3.5a}$$

$$\tau_{\text{nt}}|_{\text{ambient}} - \tau_{\text{nt}}|_{\text{liquid}} = 0, \tag{3.5b}$$

where τ_{nn} is the normal and τ_{nt} the shear stress, respectively. In particular, $\tau_{\text{nn}} = \boldsymbol{n} \cdot \boldsymbol{\tau} \cdot \boldsymbol{n}$ and $\tau_{\text{nt}} = \boldsymbol{n} \cdot \boldsymbol{\tau} \cdot \boldsymbol{t}$, where $\boldsymbol{\tau}$ is the viscous stress tensor ($\boldsymbol{\tau} = \mu \left[\nabla \boldsymbol{u} + (\nabla \boldsymbol{u})^{\text{T}}\right]$) and $\boldsymbol{t}$ the unit tangent of the liquid-ambient interface (see Fig. 3.5). It is also notable that, for static fluids, Eq. 3.5a reduces to the Young-Laplace equation (2.20).

Considering that the liquid-ambient interface is explicitly tracked as a boundary of the physical domain (sharp-interface scheme), the computational mesh must be capable of following the droplet deformations. Such boundary conforming meshes are generated by mapping the physical domain (x, y coordinates) into a geometrically simple domain ($\xi_{\text{c}}, \eta_{\text{c}}$ coordinates). One of the simplest algorithms is the conformal mapping [91, 92], where the mesh is generated by solving a pair of Laplace's equations:

$$\nabla^2 \xi_{\text{c}} = 0, \tag{3.6a}$$

$$\nabla^2 \eta_{\text{c}} = 0, \tag{3.6b}$$

accounting for the following kinematic boundary condition along the liquid-ambient interface:

$$(\boldsymbol{u}_{\text{mesh}} - \boldsymbol{u}) \cdot \boldsymbol{n} = 0, \tag{3.7}$$

where $\boldsymbol{u}_{\text{mesh}}$ is the velocity of the mesh at the interface.

The typical boundary condition for the Navier-Stokes equations at the solid boundary is the no-slip boundary condition, which in the case a flat solid surface reads:

$$u_x = 0, \tag{3.8}$$

where u_x is the horizontal component of the velocity field. The above boundary condition, however, is problematic since it creates a stress singularity at the three-phase contact line. The breakdown of the standard hydrodynamic model at the three-phase contact line was initially reported by Huh and Scriven in 1971 [82]. In particular, they predicted a singularity for the shear stress which leads to a divergence in the energy dissipation rate. Worth mentioning their famous quote: "*not even Herakles could sink a solid if the physical model were entirely valid, which it is not*", referring to the above paradox. This problem has been resolved by introducing a slip boundary condition, where the tangential component of the velocity appears to have a finite value at the contact line [93, 94]. The slip boundary condition that replaces Eq. 3.8 at the liquid-solid interface has the following form in the case a flat solid surface:

$$u_x = L_\mathrm{s} \frac{\mathrm{d}u_x}{\mathrm{d}z}, \tag{3.9}$$

where L_s is a constant called slip length. The slip length essentially denotes the fictitious depth within the solid at which u_x would reach zero [86].

The three-phase contact line is a moving boundary, and therefore additional information is needed in order to determine its evolution. Since the detailed physics very close to the contact line is not clear yet, several theoretical correlations between the contact line velocity and the dynamic contact angle, θ_d, imposed at the contact line, have been developed. In particular, by assuming that the viscous friction is the only significant dissipative force at the contact line, Cox [94] proposed the following formula:

$$\mathrm{Ca} = \left[\ln(\epsilon_c)^{-1} - \frac{Q_1}{f_c(\theta_\mathrm{d})} + \frac{Q_2}{f_c(\theta_\mathrm{Y})}\right]^{-1} [g_c(\theta_\mathrm{d}) - g_c(\theta_\mathrm{Y})] + O\left[\frac{1}{\ln(\epsilon_c)^{-1}}\right]^3, \tag{3.10}$$

where, θ_d is the dynamic contact angle, ϵ_c is a small dimensionless parameter related with the slip region around the contact line, Q_1, Q_2 and f_c, g_c are parameters and functions of the model [94]. The majority of the current modeling approaches of the dynamic contact angle are based on the above general expression, which correlates the velocity of the contact line (u_cl, included in the capillary number) with the dynamic (θ_d) and the Young contact angle (θ_Y). One of the most famous working simplification of Eq. 3.10 reads:

$$u_{cl} = c_\mathrm{T} \left(\theta_\mathrm{d} - \theta_\mathrm{Y}\right)^{n_\mathrm{T}} \tag{3.11}$$

where c_T is an empirical constant called mobility exponent and n_T usually takes values in the range of $1 \leqslant n_\mathrm{T} \leqslant 3$. This functional dependence has been used by several researchers to model contact line motion [95, 96, 97]. We also note that similar correlations

have been also derived from molecular dynamics simulations (see e.g. the work of Ren and E [98]) indicating that despite its phenomenological nature, Eq. 3.11 can adequately describe the physics of contact line motion.

The above sharp-interface hydrodynamic model does succeed in removing the singularity arising in the motion of the contact line, however, it does not have general applicability on a geometrically patterned solid surface since the change in the droplet topology demands a reconfiguration of the contact lines. In particular, the contact angle boundary condition has to be applied in *a priori* unknown cardinality of contact lines hindering the simulation of the physical system. An attempt to overcome this restriction was performed by Savva and Kalliadasis [99] by treating the contact line of a two-dimensional droplet as a set of two points, at the droplet edges. The applicability of this methodology is however limited only for slow flows and small contact angles. In addition, the experimentally observed entrapment of the ambient phase under the droplet [100] is totally neglected.

An alternative approach to alleviate the stress singularity at the moving contact line is to use diffuse-interface formulations of the hydrodynamic model. Such examples are the level-set methods (LSM) [101], the volume of fluid (VOF) [102] and the phase-field methods (PFM) [103] which can compute the interface motion and deformation on a fixed computational mesh by using implicit functions to represent separate phases. In these methods, the Navier-Stokes equations (3.3) are modified by the addition of a term representing the effect of interfacial tension.

In the level-set methods the interface is defined as the zero level-set of a distance function, ϕ_{LSM}, from the interface. The motion of the interface is then performed by convecting the distance function with the velocity field:

$$\frac{\mathrm{d}\phi_{\mathrm{LSM}}}{\mathrm{d}t} = \boldsymbol{u} \cdot \nabla \phi_{\mathrm{LSM}}. \tag{3.12}$$

Level-set methods have been widely used in wetting phenomena simulations, due to their ease of implementation (see [104, 105]), however they suffer from loss of mass problems in case where the interface is highly deformed.

In the case of VOF methods, a color function, ϕ_{VOF}, is employed indicating the fractional amount of fluid present at every cell in the computational grid ($\phi_{\mathrm{VOF}} = 0$ for an empty cell and $\phi_{\mathrm{VOF}} = 1$ for a cell filled with the traced fluid). The evolution of the interface is again predicted by Eq. 3.12. In this case, however, apart from the value of the color function, the interface orientation has also to be determined from the gradient of ϕ_{VOF}. Typically, VOF methods do not suffer from loss of mass problems like level-set [106, 107], however, there are still drawbacks compared to the sharp-interface schemes (e.g. loss of accuracy due to numerical diffusion).

In the phase-field methods, the diffusion of the interface is assumed to be proportional

to the chemical potential, F_{PFM}, gradient:

$$\frac{\mathrm{d}\phi_{\mathrm{PFM}}}{\mathrm{d}t} = \kappa_{\mathrm{PFM}} \nabla^2 F_{\mathrm{PFM}}, \tag{3.13}$$

where, ϕ_{PFM}, is the color function, κ_{PFM}, is model constant which is called mobility and $F_{\mathrm{PFM}} = \frac{\mathrm{d}E^{\mathrm{PFM}}}{\mathrm{d}\phi_{\mathrm{PFM}}}$, with $\mathrm{d}E^{\mathrm{PFM}}$ the free energy of the phase concerned. Phase-field models, have been extensively used to simulate wetting phenomena, since they can effectively model liquid interactions with complex solid geometries [108, 109], however, they also suffer from limitations such as the relatively large width of the interfaces.

Overall, diffuse interface formulations can handle cases with multiple dynamic contact lines on complex surfaces, however, they exhibit drawbacks compared to sharp-interface hydrodynamic formulations (e.g. limited accuracy for highly deformed interfaces, mass conservation problems, numerical diffusion, large width of the interface). The conceptually different (since it neglects any viscous dissipation phenomena) modeling approach of molecular kinetic theory is also presented in the next Section.

3.2.2 Molecular kinetic theory

According to the molecular kinetic theory, proposed by Blake and Haynes [83], the dependence of the dynamic contact angle on the contact line velocity is determined by the balance of the capillary force ($\gamma_{\mathrm{LA}}(\cos\theta_{\mathrm{Y}} - \cos\theta_{\mathrm{d}})$) and a friction force in the three-phase contact line, neglecting any viscous dissipation. Molecular kinetic theory is based on the activated rate theory of Eyring [110], assuming that the movement of the contact line is determined by the cumulative dynamics of the individual molecules within a region close to the three-phase contact line. In particular, Blake and Haynes assume that the wetting kinetics is a process of desorption of the molecules of the receding fluid and adsorption of those of the advancing one onto adsorption sites of the solid surface. They concluded that the contact line finally moves with a velocity [83]:

$$u_{cl} = 2\, K_0\, \lambda_b \sinh\left[\frac{\lambda_b^2\, \gamma_{\mathrm{LA}}}{2\, k_B\, T_B}\,(\cos\theta_{\mathrm{Y}} - \cos\theta_{\mathrm{d}})\right], \tag{3.14}$$

where, K_0, is the equilibrium frequency of molecular displacement between adsorption sites, λ_b, is the average distance between the adsorption sites of the solid surface and $k_B\, T_B$ is the thermal energy.

The molecular kinetic theory can predict the liquid motion in some systems (see e.g. [111]), however, it does not have universal applicability and exhibits discrepancies from other experimental data [85]. Moreover, it does not account for the exact solid geometry near the contact line as well as it neglects any viscous dissipation phenomena.

Here we suggest to apply the previously presented unified conception of the liquid-ambient and the liquid-solid interfaces (see Section 2.2.4) to the sharp-interface hydro-

dynamic model. This way, we would bypass the implementation of any explicit boundary condition at the contact line (e.g. Eq. 3.11) and enable the simulation of multiple dynamic contact lines on geometrically structured surfaces. The reformulation (augmentation) of the hydrodynamic model is presented in the next Section. We note that the incorporation of molecular interactions in the Navier-Stokes equations is not unusual in the literature. In particular, an extra body force, representing the van der Waals interactions, has been used in a plethora of publications studying liquid films rapture [112, 113]. Moreover, there are several examples where the lubrication approximation has been used, taking account of a disjoining pressure term acting in a precursor liquid film [114]. Such models, however, neglect the ambient phase entrapment and are limited to small contact angle values.

3.2.3 Augmented hydrodynamic model

According to the unified conception (see Fig.2.14 in Chapter 2), the solution of the Navier-Stokes equations (Eq. 3.3) must by determined subject to a single stress balance boundary condition applied at the whole droplet surface, referred from now on as the liquid-ambient interface. The behavior of this unified interface is governed by Eq. 3.4, which, due to the absence of any explicit boundary condition at the contact line, should now be augmented with liquid-solid interactions. As described previously (see Section 2.2.4), the liquid-solid interactions are lumped in a disjoining pressure term, p^{LS} (see Eq. 2.42), which will now be included in the normal component of the interface force balance (Eq. 3.4). In particular Eq. 3.5a will now read:

$$\Delta p + \tau_{\mathrm{nn}}|_{\mathrm{ambient}} - \tau_{\mathrm{nn}}|_{\mathrm{liquid}} - \gamma_{\mathrm{LA}}\, C - p^{\mathrm{LS}} = 0, \tag{3.15}$$

which describes the interplay between capillary and molecular forces. Note that the disjoining pressure term is active only in the vicinity of solid surface. For static fluids, the above equation reduces to the augmented Young-Laplace equation (2.32). Regarding the tangential stress component along the liquid surface (Eq. 3.5b), we will now use a Navier slip model with an effective slip coefficient, β_{eff}, active only in close proximity to the solid:

$$\tau_{\mathrm{nt}}|_{\mathrm{ambient}} - \tau_{\mathrm{nt}}|_{\mathrm{liquid}} + \beta_{\mathrm{eff}}\,(\boldsymbol{t}\cdot\boldsymbol{u}) = 0, \tag{3.16}$$

In the above we consider a uniform interfacial tension along the interface ($\nabla_s \gamma_{\mathrm{LA}} = 0$). In order to activate the above slip model only in the vicinity of the solid surface, we formulate the effective slip coefficient, β_{eff} (Eq. 3.16), as follows:

$$\beta_{\mathrm{eff}} = \frac{\mu\,\beta_{\mathrm{LS}}}{R_0}\left(1 - \tanh\left[p_{\mathrm{trs}}\left(\frac{\delta}{\delta_{\mathrm{min}}} - 1\right)\right]\right), \tag{3.17}$$

where the dimensionless slip parameter, β_{LS} (i.e. scaled inverse slip length), regulates the adhesion strength of the liquid on the solid surface. The above formulation is a

simple way to denote in a continuous manner the transition from a shear-free boundary condition, applied on the liquid-ambient interface, to a partial slip boundary condition along the liquid-solid interface. In particular, in the limit $\delta \approx \delta_{\min}$, Eq. 3.17 reduces to $\beta_{\text{eff}} = \mu\beta_{\text{LS}}/R_0$, whereas for $\delta > \delta_{\min}$, Eq. 3.17 yields $\beta_{\text{eff}} = 0$. The parameter, p_{trs}, ensures a sharp transition between these two regimes. We note that, in the computations presented in this Thesis, we assume $p_{\text{trs}} = 5$. Finally, we consider that typical values of the dimensionless slip parameter, β_{LS}, are of the order of the scaled inverse minimum distance ($R_0/\delta_{\min}$).

Overall, the Navier-Stokes (Eq. 3.3) and the elliptic mesh generation equations (3.6) are discretized using the finite element method accounting for the boundary conditions 3.15, 3.16 and 3.7. In addition, by assuming axial symmetry around the z-axis (or translational symmetry along a direction perpendicular to the xz-plane), the model becomes two-dimensional. The resulting set of discrete equations is integrated in time using the implicit Euler method. The above model has been implemented in COMSOL Multiphysics® commercial software. We note that, similar to the static case, the liquid-solid distance, δ, is obtained from the solution of the Eikonal equation. The latter is solved only once for a particular solid geometry (see Section A.3 of the Appendix A), thus it is not included in the above iterative procedure. Computational results of the augmented hydrodynamic model are presented in Part III of the Thesis.

References

[1] W. Barthlott and C. Neinhuis. “Purity of the sacred lotus, or escape from contamination in biological surfaces”. In: *Planta* 202.1 (1997), pp. 1–8.

[2] R. Helbig, J. Nickerl, C. Neinhuis, and C. Werner. “Smart skin patterns protect springtails”. In: *PLOS ONE* 6.9 (2011), e25105.

[3] R. Hensel, C. Neinhuis, and C. Werner. “The springtail cuticle as a blueprint for omniphobic surfaces”. In: *Chemical Society Reviews* 45.2 (2016), pp. 323–341.

[4] J. Bico, C. Marzolin, and D. Quéré. “Pearl drops”. In: *Europhysics Letters* 47.2 (1999), p. 220.

[5] T Liu and C. Kim. “Turning a surface superrepellent even to completely wetting liquids”. In: *Science* 346.6213 (2014).

[6] B. Bhushan. “Biomimetics: lessons from nature–an overview”. In: *Philosophical Transactions of the Royal Society of London A: Mathematical, Physical and Engineering Sciences* 367.1893 (2009), pp. 1445–1486.

[7] J. W. Bush and D. L. Hu. “Walking on water: biolocomotion at the interface”. In: *Annual Review of Fluid Mechanics* 38 (2006), pp. 339–369.

[8] G. S. Watson, D. W. Green, L. Schwarzkopf, X. Li, B. W. Cribb, S. Myhra, and J. A. Watson. “A gecko skin micro/nano structure–A low adhesion, superhydrophobic, anti-wetting, self-cleaning, biocompatible, antibacterial surface”. In: *Acta Biomaterialia* 21 (2015), pp. 109–122.

[9] A. R. Parker and C. R. Lawrence. “Water capture by a desert beetle”. In: *Nature* 414.6859 (2001), pp. 33–34.

[10] A. R. Parker. “Natural photonics for industrial inspiration”. In: *Philosophical Transactions of the Royal Society of London A: Mathematical, Physical and Engineering Sciences* 367.1894 (2009), pp. 1759–1782.

[11] K.-C. Park, P. Kim, A. Grinthal, N. He, D. Fox, J. C. Weaver, and J. Aizenberg. “Condensation on slippery asymmetric bumps”. In: *Nature* (2016).

[12] J. Ju, H. Bai, Y. Zheng, T. Zhao, R. Fang, and L. Jiang. “A multi-structural and multi-functional integrated fog collection system in cactus”. In: *Nature Communications* 3 (2012), p. 1247.

[13] H. F. Bohn and W. Federle. “Insect aquaplaning: Nepenthes pitcher plants capture prey with the peristome, a fully wettable water-lubricated anisotropic surface”. In: *Proceedings of the National Academy of Sciences of the United States of America* 101.39 (2004), pp. 14138–14143.

[14] K.-C. Park, S. S. Chhatre, S. Srinivasan, R. E. Cohen, and G. H. McKinley. “Optimal design of permeable fiber network structures for fog harvesting”. In: *Langmuir* 29.43 (2013), pp. 13269–13277.

[15] B. White, A. Sarkar, and A.-M. Kietzig. “Fog-harvesting inspired by the Stenocara beetle—An analysis of drop collection and removal from biomimetic samples with wetting contrast”. In: *Applied Surface Science* 284 (2013), pp. 826–836.

[16] C. Liu, J. Ju, Y. Zheng, and L. Jiang. “Asymmetric ratchet effect for directional transport of fog drops on static and dynamic butterfly wings”. In: *ACS Nano* 8.2 (2014), pp. 1321–1329.

[17] W. Barthlott, T. Schimmel, S. Wiersch, K. Koch, M. Brede, M. Barczewski, S. Walheim, A. Weis, A. Kaltenmaier, A. Leder, et al. "The Salvinia paradox: superhydrophobic surfaces with hydrophilic pins for air retention under water". In: *Advanced Materials* 22.21 (2010), pp. 2325–2328.

[18] J. A. Callow and M. E. Callow. "Trends in the development of environmentally friendly fouling-resistant marine coatings". In: *Nature Communications* 2 (2011), p. 244.

[19] M. Schultz, J. Bendick, E. Holm, and W. Hertel. "Economic impact of biofouling on a naval surface ship". In: *Biofouling* 27.1 (2011), pp. 87–98.

[20] G. McHale, M. I. Newton, and N. J. Shirtcliffe. "Immersed superhydrophobic surfaces: Gas exchange, slip and drag reduction properties". In: *Soft Matter* 6.4 (2010), pp. 714–719.

[21] A. K. Balasubramanian, A. C. Miller, and O. K. Rediniotis. "Microstructured hydrophobic skin for hydrodynamic drag reduction". In: *AIAA Journal* 42.2 (2004), pp. 411–414.

[22] J. Genzer and K. Efimenko. "Recent developments in superhydrophobic surfaces and their relevance to marine fouling: a review". In: *Biofouling* 22.5 (2006), pp. 339–360.

[23] M. J. Mayser and W. Barthlott. "Layers of air in the water beneath the floating Fern Salvinia are exposed to fluctuations in pressure". In: *Integrative and Comparative Biology* (2014), icu072.

[24] Y. Zheng, X. Gao, and L. Jiang. "Directional adhesion of superhydrophobic butterfly wings". In: *Soft Matter* 3.2 (2007), pp. 178–182.

[25] F. K. Balagaddé, L. You, C. L. Hansen, F. H. Arnold, and S. R. Quake. "Long-term monitoring of bacteria undergoing programmed population control in a microchemostat". In: *Science* 309.5731 (2005), pp. 137–140.

[26] G. M. Whitesides. "The origins and the future of microfluidics". In: *Nature* 442.7101 (2006), pp. 368–373.

[27] R. B. Fair. "Digital microfluidics: is a true lab-on-a-chip possible?" In: *Microfluidics and Nanofluidics* 3.3 (2007), pp. 245–281.

[28] F. Lapierre, M. Jonsson-Niedziolka, Y. Coffinier, R. Boukherroub, and V. Thomy. "Droplet transport by electrowetting: lets get rough!" In: *Microfluidics and Nanofluidics* 15.3 (2013), pp. 327–336.

[29] R. S. Subramanian. "Thermocapillary migration of bubbles and droplets". In: *Advances in Space Research* 3.5 (1983), pp. 145–153.

[30] I. Wagner, E.-M. Materne, S. Brincker, U. Süßbier, C. Frädrich, M. Busek, F. Sonntag, D. A. Sakharov, E. V. Trushkin, A. G. Tonevitsky, et al. "A dynamic multi-organ-chip for long-term cultivation and substance testing proven by 3D human liver and skin tissue co-culture". In: *Lab on a Chip* 13.18 (2013), pp. 3538–3547.

[31] E. Gogolides, K. Ellinas, and A. Tserepi. "Hierarchical micro and nano structured, hydrophilic, superhydrophobic and superoleophobic surfaces incorporated in microfluidics, microarrays and lab on chip microsystems". In: *Microelectronic Engineering* 132 (2015), pp. 135–155.

[32] A. Cavalli, P. Bøggild, and F. Okkels. "Parametric optimization of inverse trapezoid oleophobic surfaces". In: *Langmuir* 28.50 (2012), pp. 17545–17551.

[33] E Bormashenko, A Musin, G Whyman, Z Barkay, and M Zinigrad. "Revisiting the fine structure of the triple line". In: *Langmuir* 29.46 (2013), pp. 14163–14167.

[34] N. J. Mlot, C. A. Tovey, and D. L. Hu. "Fire ants self-assemble into waterproof rafts to survive floods". In: *Proceedings of the National Academy of Sciences* 108.19 (2011), pp. 7669–7673.

[35] A. W. Adamson and A. P. Gast. *Physical Chemistry of Surfaces*. Wiley, 1997.

[36] P.-G. De Gennes, F. Brochard-Wyart, and D. Quéré. *Capillarity and wetting phenomena: drops, bubbles, pearls, waves*. Springer Science & Business Media, 2013.

[37] D. Bonn, J. Eggers, J. Indekeu, J. Meunier, and E. Rolley. "Wetting and spreading". In: *Reviews of Modern Physics* 81.2 (2009), p. 739.

[38] T. Onda, S. Shibuichi, N. Satoh, and K. Tsujii. "Super-water-repellent fractal surfaces". In: *Langmuir* 12.9 (1996), pp. 2125–2127.

[39] K. Bewig and W. Zisman. "The wetting of gold and platinum by water". In: *The Journal of Physical Chemistry* 69.12 (1965), pp. 4238–4242.

[40] C. W. Extrand. "Origins of Wetting". In: *Langmuir* 32.31 (2016), pp. 7697–7706.

[41] D. Quéré. "Wetting and roughness". In: *Annual Review of Materials Research* 38 (2008), pp. 71–99.

[42] R. N. Wenzel. "Resistance of solid surfaces to wetting by water". In: *Industrial & Engineering Chemistry* 28.8 (1936), pp. 988–994.

[43] T. S. Meiron, A. Marmur, and I. S. Saguy. "Contact angle measurement on rough surfaces". In: *Journal of Colloid and Interface Science* 274.2 (2004), pp. 637–644.

[44] A. Cassie and S Baxter. "Wettability of porous surfaces". In: *Transactions of the Faraday Society* 40 (1944), pp. 546–551.

[45] A. Lafuma and D. Quéré. "Superhydrophobic states". In: *Nature Materials* 2.7 (2003), pp. 457–460.

[46] C. Extrand. "Contact angles and hysteresis on surfaces with chemically heterogeneous islands". In: *Langmuir* 19.9 (2003), pp. 3793–3796.

[47] H. Y. Erbil and C. E. Cansoy. "Range of Applicability of the Wenzel and Cassie- Baxter Equations for Superhydrophobic Surfaces†". In: *Langmuir* 25.24 (2009), pp. 14135–14145.

[48] L. Gao and T. J. McCarthy. "How Wenzel and Cassie were wrong". In: *Langmuir* 23.7 (2007), pp. 3762–3765.

[49] L. Gao and T. J. McCarthy. "An attempt to correct the faulty intuition perpetuated by the Wenzel and Cassie "laws"". In: *Langmuir* 25.13 (2009), pp. 7249–7255.

[50] Y. Wang and S. Chen. "Numerical study on droplet sliding across micropillars". In: *Langmuir* 31.16 (2015), pp. 4673–4677.

[51] G. McHale. "Cassie and Wenzel: were they really so wrong?" In: *Langmuir* 23.15 (2007), pp. 8200–8205.

[52] P. Papadopoulos, L. Mammen, X. Deng, D. Vollmer, and H.-J. Butt. "How superhydrophobicity breaks down". In: *Proceedings of the National Academy of Sciences* 110.9 (2013), pp. 3254–3258.

[53] P. Lv, Y. Xue, Y. Shi, H. Lin, and H. Duan. "Metastable states and wetting transition of submerged superhydrophobic structures". In: *Physical Review Letters* 112.19 (2014), p. 196101.

[54] O. Zienkiewicz, R. Taylor, and J. Zhu. *The Finite Element Method: Its Basis and Fundamentals*. Elsevier Science, 2005.

[55] E. Lobaton and T. Salamon. "Computation of constant mean curvature surfaces: Application to the gas–liquid interface of a pressurized fluid on a superhydrophobic surface". In: *Journal of Colloid and Interface Science* 314.1 (2007), pp. 184–198.

[56] J. De Coninck and T. Blake. "Wetting and molecular dynamics simulations of simple liquids". In: *Annual Review of Materials Research* 38 (2008), pp. 1–22.

[57] J.-Y. Park, M.-Y. Ha, H.-J. Choi, S.-D. Hong, and H.-S. Yoon. "A study on the contact angles of a water droplet on smooth and rough solid surfaces". In: *Journal of Mechanical Science and Technology* 25.2 (2011), pp. 323–332.

[58] E. S. Savoy and F. A. Escobedo. "Molecular simulations of wetting of a rough surface by an oily fluid: Effect of topology, chemistry, and droplet size on wetting transition rates". In: *Langmuir* 28.7 (2012), pp. 3412–3419.

[59] A Dupuis and J. Yeomans. “Modeling droplets on superhydrophobic surfaces: equilibrium states and transitions”. In: *Langmuir* 21.6 (2005), pp. 2624–2629.

[60] M. E. Kavousanakis, C. E. Colosqui, I. G. Kevrekidis, and A. G. Papathanasiou. “Mechanisms of wetting transitions on patterned surfaces: continuum and mesoscopic analysis”. In: *Soft Matter* 8.30 (2012), pp. 7928–7936.

[61] C. E. Colosqui, M. E. Kavousanakis, A. G. Papathanasiou, and I. G. Kevrekidis. “Mesoscopic model for microscale hydrodynamics and interfacial phenomena: Slip, films, and contact-angle hysteresis”. In: *Physical Review E* 87.1 (2013), p. 013302.

[62] Y. Liu, L. Moevius, X. Xu, T. Qian, J. M. Yeomans, and Z. Wang. “Pancake bouncing on superhydrophobic surfaces”. In: *Nature Physics* 10.7 (2014), pp. 515–519.

[63] X. Yong and L. T. Zhang. “Nanoscale wetting on groove-patterned surfaces”. In: *Langmuir* 25.9 (2009), pp. 5045–5053.

[64] N. Moradi, M. Gross, F. Varnik, G. Zikos, and I. Steinbach. “Morphologies of small droplets on patterned hydrophobic substrates”. In: *Modelling and Simulation in Materials Science and Engineering* 19.4 (2011), p. 045005.

[65] G. Saville. “Computer simulation of the liquid–solid–vapour contact angle”. In: *Journal of the Chemical Society, Faraday Transactions 2: Molecular and Chemical Physics* 73.7 (1977), pp. 1122–1132.

[66] R. J. Allen, C. Valeriani, and P. R. ten Wolde. “Forward flux sampling for rare event simulations”. In: *Journal of Physics: Condensed Matter* 21.46 (2009), p. 463102.

[67] C. K. Aidun and J. R. Clausen. “Lattice-Boltzmann method for complex flows”. In: *Annual Review of Fluid Mechanics* 42 (2010), pp. 439–472.

[68] V. M. Starov. “Surface forces action in a vicinity of three phase contact line and other current problems in kinetics of wetting and spreading”. In: *Advances in Colloid and Interface Science* 161.1 (2010), pp. 139–152.

[69] B. Derjaguin and N. Churaev. “Structural component of disjoining pressure”. In: *Journal of Colloid and Interface Science* 49.2 (1974), pp. 249–255.

[70] M. E. Kavousanakis, N. T. Chamakos, and A. G. Papathanasiou. “Connection of Intrinsic Wettability and Surface Topography with the Apparent Wetting Behavior and Adhesion Properties”. In: *The Journal of Physical Chemistry C* 119.27 (2015), pp. 15056–15066.

[71] B. Dacorogna and P. Marcellini. *Implicit partial differential equations, volume 37 of Progress in Nonlinear Differential Equations and their Applications*. 1999.

[72] J. N. Israelachvili. *Intermolecular and Surface Forces: revised third edition*. Academic Press, 2011.

[73] M Rauscher and S Dietrich. “Wetting phenomena in nanofluidics”. In: *Annual Review of Materials Research* 38 (2008), pp. 143–172.

[74] A. Oron, S. H. Davis, and S. G. Bankoff. “Long-scale evolution of thin liquid films”. In: *Reviews of Modern Physics* 69.3 (1997), p. 931.

[75] T. D. Blake. “The physics of moving wetting lines”. In: *Journal of Colloid and Interface Science* 299.1 (2006), pp. 1 –13. ISSN: 0021-9797.

[76] J. H. Snoeijer and B. Andreotti. “Moving contact lines: scales, regimes, and dynamical transitions”. In: *Annual Review of Fluid Mechanics* 45 (2013), pp. 269–292.

[77] L. Courbin, J. C. Bird, M. Reyssat, and H. Stone. “Dynamics of wetting: from inertial spreading to viscous imbibition”. In: *Journal of Physics: Condensed Matter* 21.46 (2009), p. 464127.

[78] D Platikanov, M Nedyalkov, and V Petkova. "Phospholipid black foam films: dynamic contact angles and gas permeability of DMPC bilayer films". In: *Advances in colloid and interface science* 100 (2003), pp. 185–203.

[79] A. Yarin. "Drop impact dynamics: splashing, spreading, receding, bouncing…" In: *Annual Review of Fluid Mechanics* 38 (2006), pp. 159–192.

[80] E Pierce, F. Carmona, and A Amirfazli. "Understanding of sliding and contact angle results in tilted plate experiments". In: *Colloids and Surfaces A: Physicochemical and Engineering Aspects* 323.1 (2008), pp. 73–82.

[81] C. Tropea and M. Marengo. "The impact of drops on walls and films". In: *Multiphase Science and Technology* 11.1 (1999).

[82] C. Huh and L. Scriven. "Hydrodynamic model of steady movement of a solid/liquid/fluid contact line". In: *Journal of Colloid and Interface Science* 35.1 (1971), pp. 85–101.

[83] T. Blake and J. Haynes. "Kinetics of liquidliquid displacement". In: *Journal of Colloid and Interface Science* 30.3 (1969), pp. 421–423.

[84] P Petrov and I Petrov. "A combined molecular-hydrodynamic approach to wetting kinetics". In: *Langmuir* 8.7 (1992), pp. 1762–1767.

[85] R. Fetzer, M. Ramiasa, and J. Ralston. "Dynamics of liquid- liquid displacement". In: *Langmuir* 25.14 (2009), pp. 8069–8074.

[86] W. M. Deen. *Analysis of transport phenomena (topics in chemical engineering)*. Vol. 3. Oxford Univ Press, 1998.

[87] R Miller, J. Li, M Bree, G Loglio, A. Neumann, and H Möhwald. "Interfacial relaxation of phospholipid layers at a liquid–liquid interface". In: *Thin Solid Films* 327 (1998), pp. 224–227.

[88] Y. Zhang, Z. An, G. Cui, and J. Li. "Stabilized complex film formed by co-adsorption of β-lactoglobulin and phospholipids at liquid/liquid interface". In: *Colloids and Surfaces A: Physicochemical and Engineering Aspects* 223.1 (2003), pp. 11–16.

[89] V. Pratap, N. Moumen, and R. S. Subramanian. "Thermocapillary Motion of a Liquid Drop on a Horizontal Solid Surface". In: *Langmuir* 24.9 (2008), pp. 5185–5193.

[90] G. Karapetsas, K. C. Sahu, K. Sefiane, and O. K. Matar. "Thermocapillary-driven motion of a sessile drop: effect of non-monotonic dependence of surface tension on temperature". In: *Langmuir* 30.15 (2014), pp. 4310–4321.

[91] J. F. Thompson, Z. U. Warsi, and C. W. Mastin. "Boundary-fitted coordinate systems for numerical solution of partial differential equations—a review". In: *Journal of Computational Physics* 47.1 (1982), pp. 1–108.

[92] K. Christodoulou and L. Scriven. "Discretization of free surface flows and other moving boundary problems". In: *Journal of Computational Physics* 99.1 (1992), pp. 39–55.

[93] V Dussan et al. "The moving contact line: the slip boundary condition". In: *Journal of Fluid Mechanics* 77.04 (1976), pp. 665–684.

[94] R. Cox. "The dynamics of the spreading of liquids on a solid surface. Part 1. Viscous flow". In: *Journal of Fluid Mechanics* 168 (1986), pp. 169–194.

[95] P. J. Haley and M. J. Miksis. "The effect of the contact line on droplet spreading". In: *Journal of Fluid Mechanics* 223 (1991), pp. 57–81.

[96] S. W. Benintendi and M. K. Smith. "The spreading of a non-isothermal liquid droplet". In: *Physics of Fluids (1994-present)* 11.5 (1999), pp. 982–989.

[97] G. Karapetsas, R. V. Craster, and O. K. Matar. "On surfactant-enhanced spreading and superspreading of liquid drops on solid surfaces". In: *Journal of Fluid Mechanics* 670 (2011), pp. 5–37.

[98] W. Ren and W. E. "Boundary conditions for the moving contact line problem". In: *Physics of Fluids (1994-present)* 19.2 (2007), p. 022101.

[99] N. Savva and S. Kalliadasis. "Two-dimensional droplet spreading over topographical substrates". In: *Physics of Fluids (1994-present)* 21.9 (2009), p. 092102.

[100] A. Peters, C Pirat, M Sbragaglia, B. Borkent, M Wessling, D Lohse, and R. G. Lammertink. "Cassie-Baxter to Wenzel state wetting transition: Scaling of the front velocity". In: *The European Physical Journal E: Soft Matter and Biological Physics* 29.4 (2009), pp. 391–397.

[101] J. A. Sethian. *Level set methods and fast marching methods: evolving interfaces in computational geometry, fluid mechanics, computer vision, and materials science*. Vol. 3. Cambridge university press, 1999.

[102] C. W. Hirt and B. D. Nichols. "Volume of fluid (VOF) method for the dynamics of free boundaries". In: *Journal of Computational Physics* 39.1 (1981), pp. 201–225.

[103] D. Jacqmin. "Calculation of two-phase Navier–Stokes flows using phase-field modeling". In: *Journal of Computational Physics* 155.1 (1999), pp. 96–127.

[104] L. Zheng and H Zhang. "An adaptive level set method for moving-boundary problems: application to droplet spreading and solidification". In: *Numerical Heat Transfer: Part B: Fundamentals* 37.4 (2000), pp. 437–454.

[105] S. Tanguy and A. Berlemont. "Application of a level set method for simulation of droplet collisions". In: *International Journal of Multiphase Flow* 31.9 (2005), pp. 1015–1035.

[106] M van Sint Annaland, N. Deen, and J. Kuipers. "Numerical simulation of gas bubbles behaviour using a three-dimensional volume of fluid method". In: *Chemical Engineering Science* 60.11 (2005), pp. 2999–3011.

[107] T. Kékesi, G. Amberg, and L. P. Wittberg. "Drop deformation and breakup". In: *International Journal of Multiphase Flow* 66 (2014), pp. 1–10.

[108] G Pashos, G Kokkoris, and A. G. Boudouvis. "A modified phase-field method for the investigation of wetting transitions of droplets on patterned surfaces". In: *Journal of Computational Physics* 283 (2015), pp. 258–270.

[109] Q. Zhang, T.-Z. Qian, and X.-P. Wang. "Phase field simulation of a droplet impacting a solid surface". In: *Physics of Fluids (1994-present)* 28.2 (2016), p. 022103.

[110] S. Glasstone, K. Laidler, and H. Eyring. *The Theory of Rate Processes: The Kinetics of Chemical Reactions, Viscosity, Diffusion and Electrochemical Phenomena*. International Chemical Series. McGraw-Hill Book Company, Incorporated, 1941.

[111] H. Li, R. Sedev, and J. Ralston. "Dynamic wetting of a fluoropolymer surface by ionic liquids". In: *Physical Chemistry Chemical Physics* 13.9 (2011), pp. 3952–3959.

[112] E. Ruckenstein and R. K. Jain. "Spontaneous rupture of thin liquid films". In: *Journal of the Chemical Society, Faraday Transactions 2: Molecular and Chemical Physics* 70 (1974), pp. 132–147.

[113] M. B. Williams and S. H. Davis. "Nonlinear theory of film rupture". In: *Journal of Colloid and Interface Science* 90.1 (1982), pp. 220–228.

[114] J. Eggers. "Contact line motion for partially wetting fluids". In: *Physical Review E* 72.6 (2005), p. 061605.

PART II

Simulation of statics of wetting

CHAPTER 4

Wetting transitions on structured surfaces

In this Chapter, we validate the proposed augmented Young-Laplace equation against the conventional formulation, as well as against mesoscopic lattice-Boltzmann simulations, for simple solid surface geometries. Moreover, we demonstrate accurate and efficient computations of equilibrium shapes of entire millimeter sized droplets on complex, geometrically patterned, surfaces. Our computations reveal the existence of multiple meta-stable states including Cassie-Baxter, Wenzel, as well as intermediate wetting states. The calculation of the energy barriers separating these states, which can be performed by our method with negligible computational cost, would be very important for designing and realizing surfaces with fully tunable wetting properties.

4.1 Introduction: Meta-stable wetting states

As presented in Chapter 2, the wetting state where the droplet is sitting on top of the protrusions (Cassie-Baxter state of "fakir" state, due to its similarity with a fakir sitting on a bed of nails) is usually meta-stable, since the droplet can undergo a collapse transition to a Wenzel state, by impaling the solid protrusions. Unlike the Cassie-Baxter state, the Wenzel state features strong pinning on the substrate [1]. Such dynamic modification of the adhesion properties of a solid surface would be highly advantageous in many applications, for example micro-channels with intelligent adhesion switching and controllable release of chemicals in lab-on-a-chip micro-reactors [2].

The Cassie-Baxter to the Wenzel wetting transition has been observed by increasing the liquid pressure [3] or by vibrating the solid surface [4]. However, a more versatile tool to examine wetting transitions is electrowetting phenomenon, where the material wettability (Young's contact angle) is electrostatically enhanced. Krupenkin et al, [5], by performing electrowetting experiments on structured surfaces, reported that collapse transitions occur when certain wettability thresholds are surpassed. They also observed that the reverse transition could not be realized by switching off the electric actuation. Further experimental studies reveal that strong external actuations (e.g., thermal heating) are required in order to induce de-wetting transitions [6]. From a thermodynamic point of view Cassie-Baxter and Wenzel states correspond to distinct minima of the free

energy landscape suggesting the existence of at least one intermediate unstable state which corresponds to a local maximum of the free energy. The difference between the saddle of the free energy landscape and the local minima determine the energy barrier for a wetting or a de-wetting transition. In this direction, recent publications argue that reversible wetting transitions can be facilitated by minimizing the energy barriers which separate the distinct wetting states through proper design of the solid surface roughness [7, 8]. The majority of theoretical studies, however, provide analytical expressions for such energy barrier computations based on significant simplifications regarding the actual shape of the droplet and/or the solid surface [9, 10]. For an accurate determination of the wetting transition energy barriers, the computation of all admissible states on a heterogeneous surface is deemed necessary. Such a task can be readily performed by our proposed modeling methodology. In particular, in this Chapter, we employ the proposed augmented Young-Laplace equation (2.32) in order to simulate equilibrium wetting phenomena of smooth as well as rough solids where multiple and reconfigurable three-phase contact lines are formed.

4.2 Results and discussion

4.2.1 Flat solid surface

We initially present computational predictions of the proposed augmented Young-Laplace equation (2.32) for the equilibrium of cylindrical sessile droplets (assuming translational symmetry along a direction perpendicular to the xz-plane in Fig. 2.10) on flat and smooth solid surfaces. The effect of gravity is neglected in the computations presented here ($N_g = 0$ in Eq. 2.32) since the initial droplet radius is considered smaller than the capillary length. More details about the discretization of Eq. 2.32 and in particular the Galerkin residuals, $\boldsymbol{R}$, are presented in the Section B.1 of Appendix B. As described in the previous Chapter (2), in our formulation the material wettability is determined by the wetting parameter value, w^{LS}, without imposing any explicit boundary condition at the three-phase contact lines. The disjoining pressure parameters (see Eq. 2.42) are chosen here as $\sigma = 3.8 \times 10^{-2}$, $C_1 = 8$, $C_2 = 6$ and $\epsilon = 8 \times 10^{-3}$. The above parameters result to a disjoining pressure profile depicted in Fig. 4.1, for $w^{LS} = 4 \times 10^2$. According to Eq. 2.50 in Chapter 2 which reads: $cos\theta_Y = \frac{w^{LS}(C_1-C_2)\sigma}{(C_1-1)(C_2-1)} - 1$, the above w^{LS} value corresponds to a Young contact angle $\theta_Y \approx 100^o$. In order, however, to test the validity of this equation, we also calculate the Young contact angle value by performing circular fitting to the liquid-ambient interface, considering that the droplet forms a spherical cap in the absence of any gravitational field. The circular fitting on the droplet profile is performed with least squares fitting at a level, beyond which the liquid-solid interactions are of negligible magnitude, and a constant curvature of the droplet is to be expected. The Young contact angle is then evaluated analytically from:

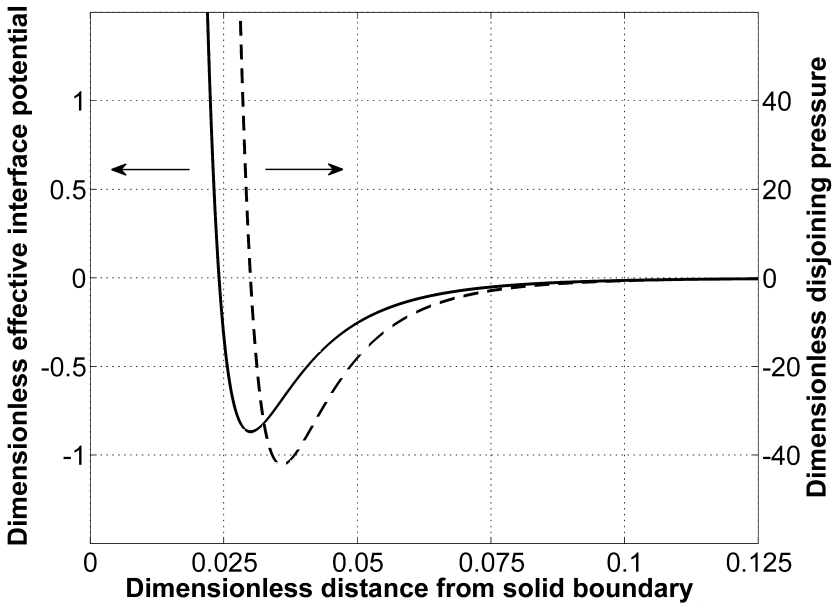

Figure 4.1: Profiles of the dimensionless disjoining pressure, $\frac{R_0}{\gamma_{\mathrm{LA}}} p^{\mathrm{LS}}$ (dashed line), and of the corresponding dimensionless effective interface potential (solid line), $\frac{\omega}{\gamma_{\mathrm{LA}}}$, as a function of the dimensionless liquid-solid distance, $\frac{\delta}{R_0}$, for $\sigma = 3.8 \times 10^{-2}$, $C_1 = 8$, $C_2 = 6$, $\epsilon = 8 \times 10^{-3}$ and $w^{\mathrm{LS}} = 4 \times 10^2$.

$$\theta_{\mathrm{Y}} = \operatorname{acos}\left(1 - \frac{z_{\max}}{R}\right), \tag{4.1}$$

where R is the radius of fitting circle and $z_{\max}$ the droplet height. The comparison is presented in Fig. 4.2 where we observe that the results obtained by circular fitting are in agreement with Eq. 2.50, except for extremely low wetting parameter values ($w^{\mathrm{LS}} \to 0$), which, however, do not correspond to realistic systems.

What is also interesting here is to present the variation of the local mean curvature, C, along the surface of the droplet. The above is depicted in Fig. 4.3, for a solid wettability which corresponds to $\theta_{\mathrm{Y}} = 120^{\mathrm{o}}$. In Fig. 4.3, we can distinguish three interfacial regions:

(I) The liquid-ambient interface region, where the curvature is constant, consistent with the circular profile,

(II) an intermediate region, in the vicinity of the fictitious three-phase contact line, with sharply increasing curvature, and

(III) the liquid-solid interface region where the curvature is equal with the curvature of the solid surface (zero for flat surfaces).

The conventional Young-Laplace equation treats only the region (I) up to the three-phase contact line, where the Young boundary condition is applied. On the other hand, the augmented Young-Laplace equation accounts for the entire droplet surface, including regions where liquid-solid interactions are active ((II) and (III)). In the inset of Fig. 4.3, we can also observe the thin layer that separates the liquid and solid phases. In particular,

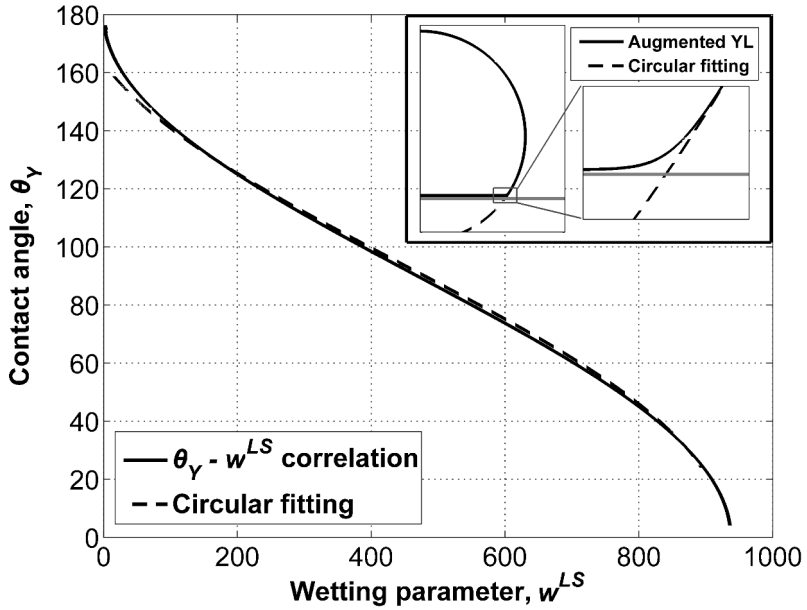

Figure 4.2: Young's contact angle, θ_{Y}, for a droplet on a flat surface as a function of the w^{LS}. The solid line is obtained from the application of Eq. 2.50; the dashed line is produced by circular fitting to the liquid-ambient interface - Embedded figure: Droplet profile and circular fitting at the interface.

as described in Chapter 2, the repulsive interactions between the liquid and the solid phases induce a minimum distance, δ_{min}, between the droplet and the solid boundary. When $\delta = \delta_{\mathrm{min}}$, then the disjoining pressure, $p^{\mathrm{LS}} = 0$ and Eq. 2.42 yields:

$$\frac{\gamma_{\mathrm{LA}}}{R_0} w^{\mathrm{LS}} \left[\left(\frac{\sigma}{\delta_{\mathrm{min}}/R_0 + \epsilon} \right)^{C_1} - \left(\frac{\sigma}{\delta_{\mathrm{min}}/R_0 + \epsilon} \right)^{C_2} \right] = 0 \;\Rightarrow \quad \frac{\delta_{\mathrm{min}}}{R_0} = \sigma - \epsilon, \tag{4.2}$$

where in this case, $\frac{\delta_{\mathrm{min}}}{R_0} = 3 \times 10^{-2}$. We note that for a droplet with e.g., cross-sectional area, $A_{\mathrm{droplet}} = 5\,\mathrm{mm}^2$, the characteristic length is $R_0 = \left(A_{\mathrm{droplet}}/\pi \right)^{1/2} = 1.262\,\mathrm{mm}$ and the minimum liquid-solid distance is $\delta_{\mathrm{min}} = 3.7 \times 10^{-2}$ mm.

It is also interesting here to examine the small region where the local mean curvature of the droplet profile reaches its maximum value ((II) in Fig. 4.3). At this region, the droplet profile essentially bends, thus from the augmented YL equation (2.32) yields that the dijoining pressure, p^{LS}, reaches its absolute minimum value (since the reference pressure, K, is constant along the whole interface). The distance, δ, at this point will be denoted as δ_{TPL}, and can be calculated as:

$$\frac{\mathrm{d}p^{\mathrm{LS}}}{\mathrm{d}\delta_{\mathrm{TPL}}} = 0 \;\Rightarrow\; \frac{\delta_{\mathrm{TPL}}}{R_0} = \frac{2\sqrt{3}\,\sigma}{3} - \epsilon. \tag{4.3}$$

This is a crucial point since it separates the region where liquid-solid interactions are

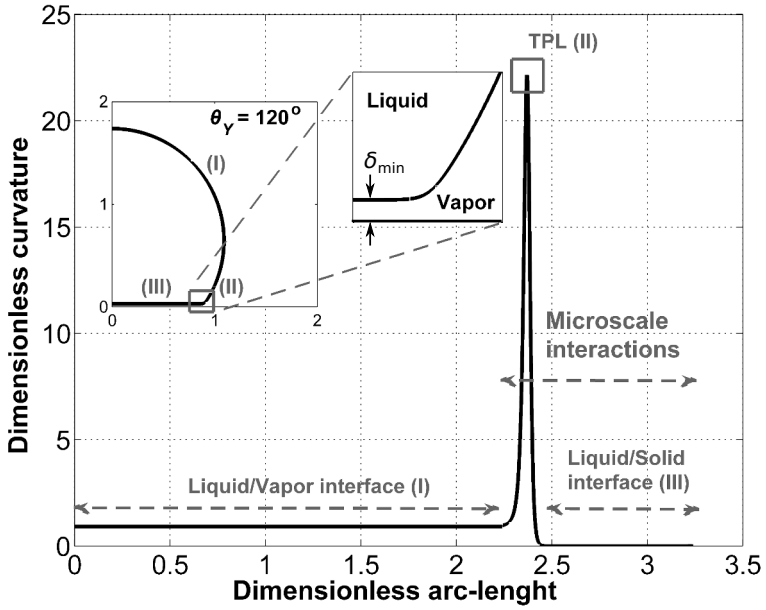

Figure 4.3: Dimensionless local mean curvature, $\widehat{C} = C\,R_0$, variation along the dimensionless arc-length, $\widehat{s} = s/R_0$, of the droplet surface ($\theta_Y = 120^o$).

strong (for $\delta \leqslant \delta_{TPL}$) from the region where the disjoining pressure fades and the local mean curvature is constant ($\delta > \delta_{TPL}$) (see Fig. 4.3). Thus, since the droplet surface is treated uniformly in our formulation, δ_{TPL} can be used as an artificial limit in order to to distinguish the liquid-ambient from the liquid-solid interface. This is important in cases where the calculation the liquid-solid and the liquid-ambient surface areas is required (see e.g. Section 4.2.5). We note that δ_{TPL} equals 4.5×10^{-2} mm, for a droplet with cross-sectional area $A_{droplet} = 5\,mm^2$.

In the next Section we perform simulations on geometrically structured substrates. Such solid surface cases are more interesting, in terms of potential applications, since they can sustain meta-stable wetting states (Cassie-Baxter, Wenzel and intermediate states) with different adhesion behaviors, as also experimental observed by Lafuma and Quéré [3].

4.2.2 Single-stripe structured surfaces

Our first step here is to test the validity of the augmented Young-Laplace equation by comparing its predictions against the ones obtained from the conventional Young-Laplace equation (2.20), for a single-stripe structured solid surface (see Fig. 4.4). This is a quite simple solid surface geometry that, however, can sustain meta-stable solutions, which can also be predicted by the conventional Young-Laplace equation, as shown in [11]. Such a task requires a throughout exploration of the solution space by using parameter continuation methods. On of the most common methods is the pseudo arc-length continuation technique [12], which enables the computation of stable and unstable steady state solutions (see Section B.2 of the Appendix B). The stability of the com-

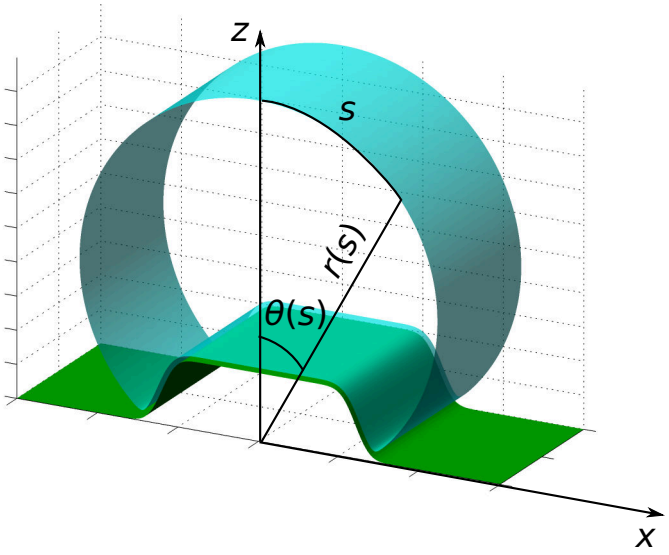

Figure 4.4: Cylindrical droplet (by assuming translational symmetry along the direction perpendicular to the xz-plane) on a single-stripe structured solid surface ($p_1 = 0.6$, $p_2 = 10$, $p_3 = 5$ in Eq. 4.4).

puted solutions is quantified by solving the eigenvalue problem of the Jacobian matrix (the matrix of all first-order partial derivatives of the residual vector, $\boldsymbol{R}$). One solution is stable when the real part of all eigenvalues of the Jacobian matrix is negative; when at least one eigenvalue has a positive real part, the solution is characterized as unstable [13].

In this simplified single-structured case, the dimensionless height of the geometry is given by:

$$\widehat{z} = \frac{1 - \mathrm{erf}\left[(\widehat{x} - p_1)p_2\right]}{p_3}, \tag{4.4}$$

where, erf, denotes the error function. The parameters p_1, p_2 and p_3 determine the geometric features of the stripe: p_1 regulates the width of the stripe at its top surface, p_2 controls the curvature of the lateral walls and p_3 determines the maximum height. The bifurcation diagram in Fig. 4.5 shows the dependence of the dimensionless droplet height on the material wettability, θ_Y. For the augmented Young-Laplace equation the bifurcation parameter is the wetting parameter, w^{LS}, which can be correlated with the Young's contact angle, θ_Y, through Equation 2.50. One can observe that both formulations predict, with exceptional agreement, an S-shaped curve with unstable wetting states (dashed lines) linking the branches of stable wetting states (solid lines) at the two turning points ((A) and (C)). This bifurcation diagram shows that transitions -induced by wettability modification- between suspended (upper stable branch) and collapsed states (lower stable branch) are hysteretic. Starting with a hydrophobic material (point (D)) and gradually enhancing material wettability (e.g., through electrowetting), then a drop collapse occurs at turning point (A) ($\theta_Y \approx 79^o$) i.e., the drop collapses following the route (D) $\rightarrow$ (A) $\rightarrow$ (B).

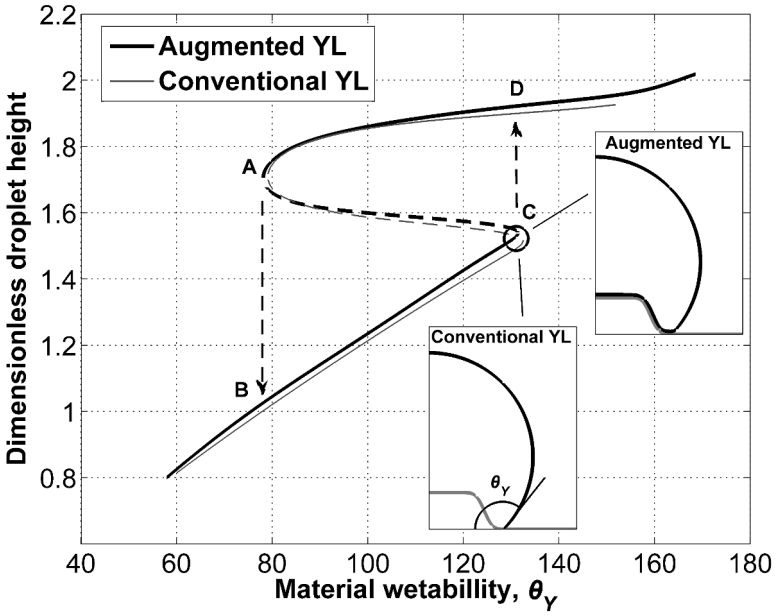

Figure 4.5: Dependence of the dimensionless droplet height, $z_{\max}/R_0$, on the material wettability, θ_Y, for a single-striped solid surface structure (p_1 = 0.6, p_2 = 10, p_3 = 5). The thick line corresponds to the results obtained from the augmented Young-Laplace equation, whereas the thin line corresponds to the conventional Young-Laplace equation results.

In a reverse experiment, where wettability is decreased, the droplet undergoes a de-wetting transition at turning point (C). For this particular geometry, this lifting transition would require lowering of wettability of as much as $\theta_Y \approx 130^o$. This suggests that de-wetting through wettability modification cannot be realized, considering that common hydrophobic materials do not exhibit $\theta_Y > 120^o$ (e.g. for Teflon® AF 1600, $\theta_Y = 120^o$). In experimental practice the range of tunable wettability is limited; e.g., when wettability is electrostatically enhanced (electrowetting), θ_Y has an upper limit set by the material chemistry [14] and a lower one due to the contact angle saturation phenomenon [15]. The physical origins of the contact angle saturation, where a limiting contact angle value is achieved (usually 60^o for a water droplet in air ambient) even at very large applied voltages, has been elucidated for some cases where electric charge is trapped in the solid substrate [16, 17]. A universal theory, however, must incorporate a variety of other synergistic phenomena, like ambient phase ionization [18] and liquid instabilities resulting in ejection of micro-droplets [19].

Next, we validate the augmented Young-Laplace equation, for the case of a droplet resting on a more complex substrate, against the conventional formulation (see Section 2.2.2) and the exceptionally different mesoscopic lattice-Boltzmann method which is described in Section 2.2.3).

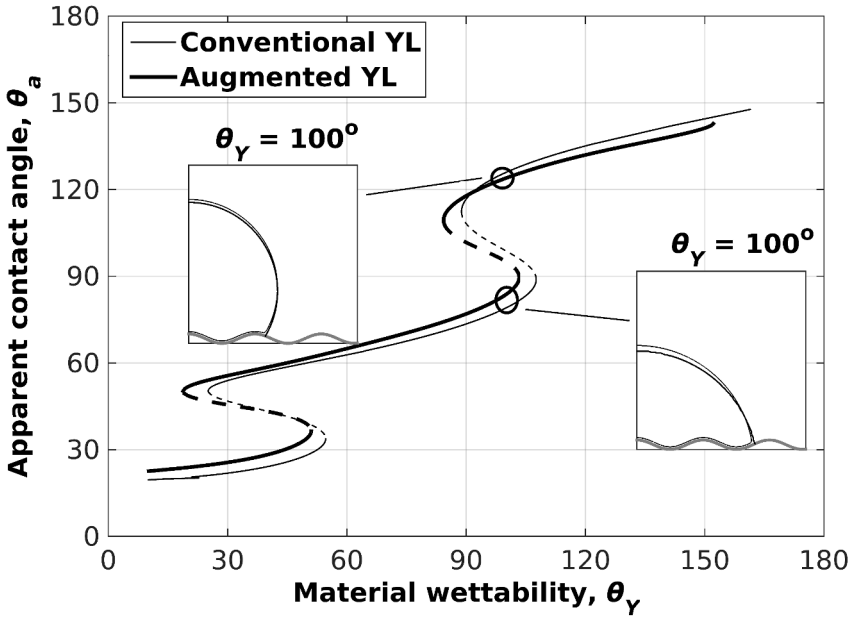

Figure 4.6: Dependence of the apparent contact angle of the droplet on the material wettability, θ_{Y}, for a wave-like stripe patterned surface ($p_4 = 4$, $p_5 = 3$ in Eq. 4.5). The thick line corresponds to the results obtained from the augmented Young-Laplace equation, whereas the thin line corresponds to the conventional Young-Laplace equation results.

4.2.3 Wave-like patterned surfaces

4.2.3.a Validation against the conventional Young-Laplace

The augmented Young-Laplace formulation can also be easily applied for a more complex, multi-striped solid surface. Here, we further test the validity of our method by comparing its results against the ones obtained from conventional Young-Laplace equation. In this case, the solid surface is structured with wave-like stripes, the height of which is described by:

$$\widehat{z} = \left[\frac{cos(p_4\,\widehat{x})}{p_5}\right]^2, \tag{4.5}$$

where the parameters p_4 and p_5 determine the geometric characteristics of the solid surface: p_4 controls the wavelength period and p_5 regulates the maximum height. We note that for a droplet with e.g., cross-sectional area: $A_{\mathrm{droplet}} = 5\,\mathrm{mm}^2$, the maximum height of the stripes corresponds to 0.389 mm and the wave-length period equals 1.325 mm.

In Fig. 4.6 we present the dependence of the apparent contact angle of the droplet, θ_{a}, as a function of the material wettability, θ_{Y}, where θ_{a} is calculated by fitting a circle to the liquid-ambient interface above the solid surface asperities. We observe that both the augmented and the conventional Young-Laplace equations can successfully capture the non-trivial behavior of the droplet on this wave-like stripe patterned surface. The reason that the conventional Young-Laplace equation is still valid here is that the surface roughness is relatively small (no air inclusions are formed below the droplet). In a

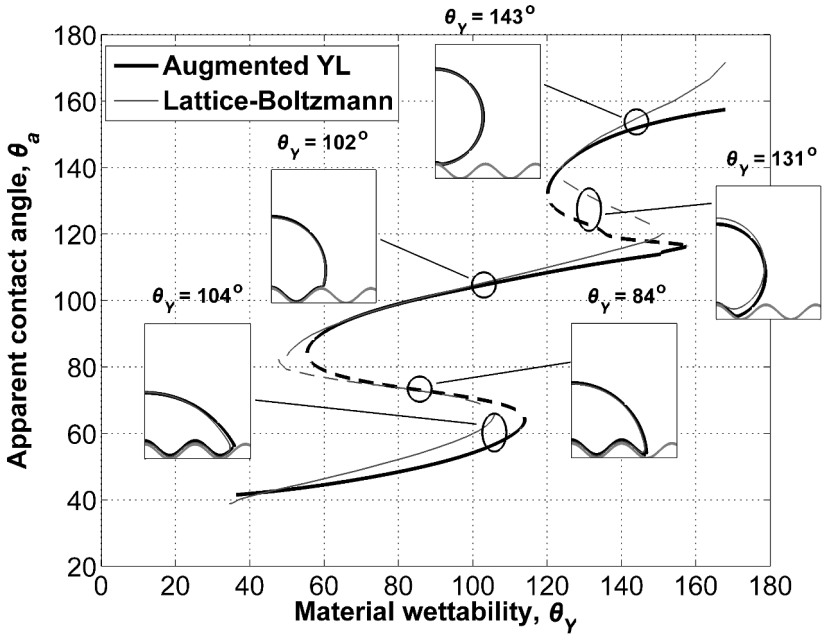

Figure 4.7: Dependence of the apparent contact angle of the droplet on the material wettability, θ_{Y}, for a patterned surface (p_4 = 3, p_5 = 1.8 in Eq. 4.5). The thick line corresponds to the results obtained from the augmented Young-Laplace equation, whereas the thin line corresponds to lattice-Boltzmann based computations.

more complex solid substrate case (such as a solid with increased roughness presented in the Section 4.2.4), however, the utilization of the conventional Young-Laplace equation would be unfeasible. Such a complex solid substrate requires the application of the Young's contact angle boundary condition to an unknown number of three-phase contact lines.

4.2.3.b Validation against mesoscopic lattice-Boltzmann

The predictions of the proposed methodology are also compared with the ones obtained from mesoscopic lattice-Boltzmann simulations (see also Section 2.2.3). A detailed description of the employed lattice-Boltzmann model can be found in [20]. In particular, the employed model accounts for non-trivial microscopic effects (e.g. disjoining pressure, partial wetting) through the application of liquid-solid pseudo-potential interactions. The liquid-solid interactions include an attractive part modeling van der Waals forces, and a repulsive component associated with double-layer interactions and in direct analogy with DLVO theory [21]. Fluid-fluid interactions are defined to ensure constant compressibility in both phases, with a density ratio of 10 : 1 and a compressibility ratio of 15.625 : 1 when the system reaches phase equilibrium.

The dependence of the apparent contact angle, θ_{a}, on the material wettability, θ_{Y}, is depicted in Fig. 4.7 by using both approaches: the continuum-level augmented Young-Laplace and the mesoscopic lattice-Boltzmann model. The droplet interface, obtained

from the lattice-Boltzmann model, is defined by the density contour corresponding to $\rho_{\text{interface}} = (\rho + \rho_{\text{ambient}})/2$, where ρ_{ambient} is the density of the ambient bulk phase. Even though that the Young-Laplace and the lattice-Boltzmann are conceptually different descriptions of wetting phenomena (continuum- level and mesoscopic), they both capture, with satisfactory agreement, the non-trivial macroscopic behavior of a droplet wetting a striped structure. The observed discrepancies are attributed to the diffuse liquid-solid and liquid-ambient interfaces modeled in the lattice-Boltzmann description, as well as the different formulation of the liquid-solid interactions.

As a summary, we report that both approaches can successfully capture the droplet behavior, however, the augmented Young-Laplace description deals with the solution of a one-dimensional problem, as opposed to the two dimensional lattice-Boltzmann formulation. The computational benefits of the proposed continuum-level analysis are significant; indicatively we report that a Newton–Raphson iteration utilizing lattice-Boltzmann runs requires approximately 10 minutes ($\sim 6 \times 10^4$ lattice-Boltzmann time steps plus the required time for the initialization of each lattice-Boltzmann run), whereas the augmented Young-Laplace model requires about 1 second, when all computations are performed on the same CPU (Intel® Core™ i7 @3.07 GHz). This computational advantage of the augmented Young-Laplace equation is obtained without implementing any adaptive mesh technique for automatic refinement in regions of high interface curvature, which highlights the efficiency of our proposed method.

4.2.4 Multi-stripe patterned surfaces

The proposed formulation is now used to compute the admissible equilibrium wetting states on a stripe-patterned solid surface of increased roughness (see Fig. 4.8). Definitely, the conventional Young-Laplace formulation cannot be used here since the cardinality of the formed contact lines (where the Young contact angle boundary condition has to be applied) is unknown. In this example, the topography of the solid surface is given by the following relation:

$$\widehat{z} = 1 - \frac{\operatorname{erf}\left[p_6 \cos(p_7\, \widehat{x})\right]}{p_8}. \tag{4.6}$$

The geometric features of the solid surface are defined by the parameters p_6, p_7, and p_8, which determine the stripe edge sharpness, the wavelength period and the maximum height of the stripes, respectively. The parameter values are given in the caption of Fig. 4.8. The unit cell of this solid surface structure is a stripe (see Eq. 4.4) with $p_1 = 4.31\times10^{-2}$, $p_2 = 43.88$, $p_3 = 21.16$. In the case of a droplet with cross-sectional area: $A_{\text{droplet}} = 5\,\text{mm}^2$, the maximum height of the stripes equals 0.125 mm and the wavelength period is 0.121 mm. The roughness factor (ratio of the actual over the apparent surface area), r_f, is 1.52 as opposed to 1.19 for the solid surface presented in the previous Section (4.2.3.b). It is worth mentioning that the application of bifurcation analysis utilizing lattice-Boltzmann simulations, for this case study, requires a substantial amount of com-

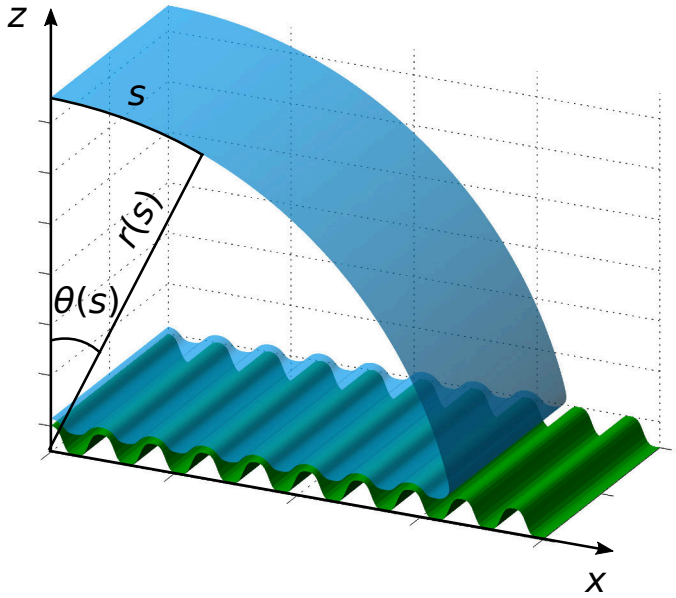

Figure 4.8: Cylindrical droplet profile (by assuming translational symmetry along the direction perpendicular to the xz-plane) on a stripe-patterned surface ($p_6 = 1.3$, $p_7 = 33$, $p_8 = 20$ in Eq. 4.6).

putational time and resources. However, the solution of the augmented Young-Laplace equation sustains its computational needs at very low levels.

In Fig. 4.9 we present the dependence of the apparent contact angle, θ_a, on the material wettability, quantified by the Young contact angle, θ_Y. The diagram exhibits multiple S-shaped curves, which are directly associated with the number of stripes of the solid surface. Multiple wetting steady states are computed (i.e. satisfy the governing equations of equilibrium) within large θ_Y value intervals, e.g. 9 equilibrium states for a solid material with $\theta_Y = 104^o$. Wetting or de-wetting transitions induced by material wettability modification set on at the turning point values of θ_Y. One can observe that de-wetting transitions for this particular solid surface would demand a material wettability of $\theta_Y > 120^o$ (θ_Y value at the lower right side turning point) which is not feasible with the common hydrophobic materials.

Each stable branch (solid line) extends over a finite interval of θ_Y values, the maximum of which corresponds to droplets suspended on the surface protrusions trapping air beneath it (see local magnification of the droplet shape corresponding to state (T2) at Fig. 4.10); the lower end of this interval corresponds to wetting states being immersed in the asperities of the surface (see local magnification of the droplet shape corresponding to state (T1) at Fig. 4.10) retaining the number of wetted stripes. It is observed that the material wettability modification, along a stable branch, does not result in significant change of the apparent wettability. Indicatively, the difference in the apparent contact angle ($\Delta\theta_a$) between states (T2) and (T1) is 9^o, whereas the material wettability modification required is far greater ($\Delta\theta_Y$ (T2 $\rightarrow$ T1) = 69^o). This change, along the same stable branch, is not usually observed in experiments because the apparent contact angle vari-

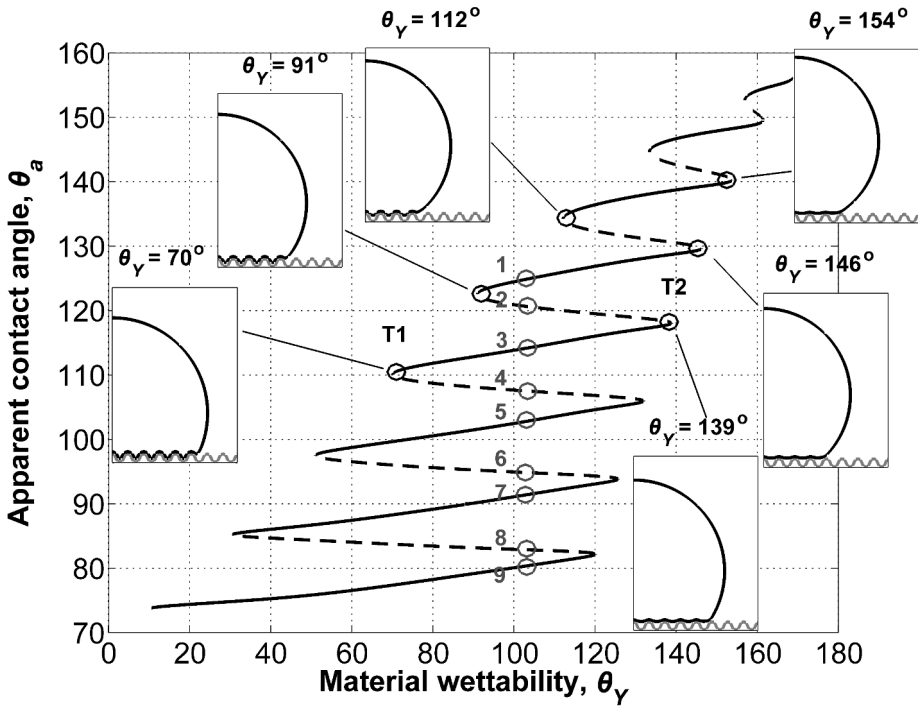

Figure 4.9: Dependence of the apparent contact angle, θ_a, on the material wettability, θ_Y, for a patterned solid surface (p_6 = 1.3, p_7 = 33, p_8 = 20 in Eq. 4.6).

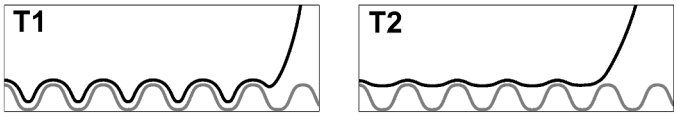

Figure 4.10: Local magnification of the droplet shapes corresponding to points (T1) and (T2) of Figure 4.9.

ation is small.

On the other hand, transitions between co-existing states, wetting a different number of stripes (e.g. from point (3) to (7) at Fig. 4.9) lead to substantial apparent contact angle change ($\Delta\theta_a$ (3 → 7) = 23°) without modifying the wettability properties ($\Delta\theta_Y$ (3 → 7) = 0°). Thereafter, the experimentally observed significant apparent wettability modification (e.g. at a Cassie-Baxter to Wenzel transition) is attributed to the variation in the number of stripes covered by the liquid, which can be triggered, e.g., by mechanical actuation [22].

In Fig. 4.11 we illustrate nine co-existing droplet profiles (five stable and four unstable) for a hydrophobic material with θ_Y = 104° covering a large interval of apparent wetting behaviour types, i.e. from hydrophilic to super-hydrophobic. In particular, the apparent contact angle, θ_a, of the droplet ranges from 80° up to 125°. In experimental practice, a super-hydrophobic state is attained when the droplet is gently deposited on the protrusions of the surface, whereas impaled states require forced droplet deposition (droplet impacts the surface).

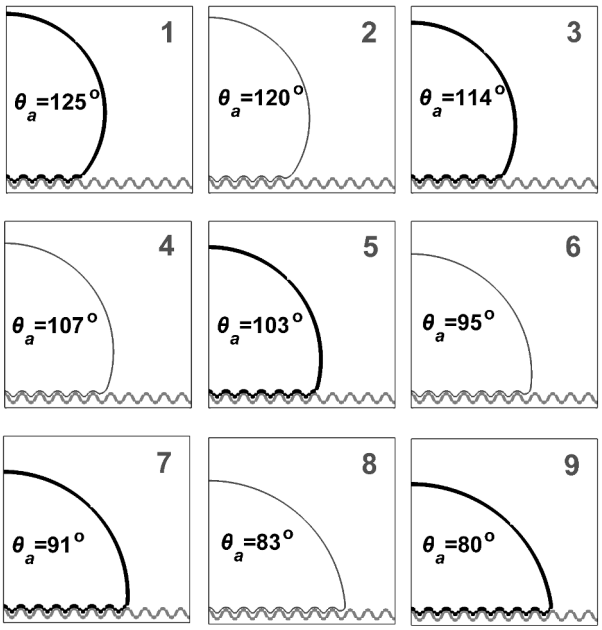

Figure 4.11: Droplet profiles corresponding to points (1) - (9) in Fig. 4.9. Profiles drawn with thick line correspond to stable wetting states, whereas those with thin line correspond to unstable ones. All states computed correspond to material wettability, $\theta_Y = 104^o$.

From a thermodynamic point of view, a wetting transition, e.g. between states (1) and (3) in Fig. 4.9, requires a minimum amount of energy (energy barrier), set by an intermediate unstable state (2) (see Fig. 4.12). The computation of energy barriers, separating meta-stable wetting states, has been performed by Savoy et al. [23], by using molecular dynamics, in, however, non-realistic systems (nano-droplets). In addition, continuum-level computations of wetting transitions have only been presented, up to now, on a unit cell of the structured surface [24]. Such computations disregard the pinning/ de-pining effect of the droplet contact lines, when more stripes are wetted, as it actually happens between states (1) and (3) in Fig. 4.9. According to our knowledge, this is the first time that energy barrier computations are performed by using a continuum-level methodology and accounting for the whole droplet surface. These computations will be presented in the following Section.

4.2.5 Energy barrier computations

The computation of wetting or de-wetting energy barriers separating co-existing stable wetting states for a certain material wettability can be computed as the difference in surface free energy, given in Eq. 2.46, between each state and the unstable intermediate one. Thus, by substituting Young's equation, $\gamma_{SA} = \gamma_{LS} + \gamma_{LA} \cos\theta_Y$ (Eq. 2.6), into Eq. 2.46,

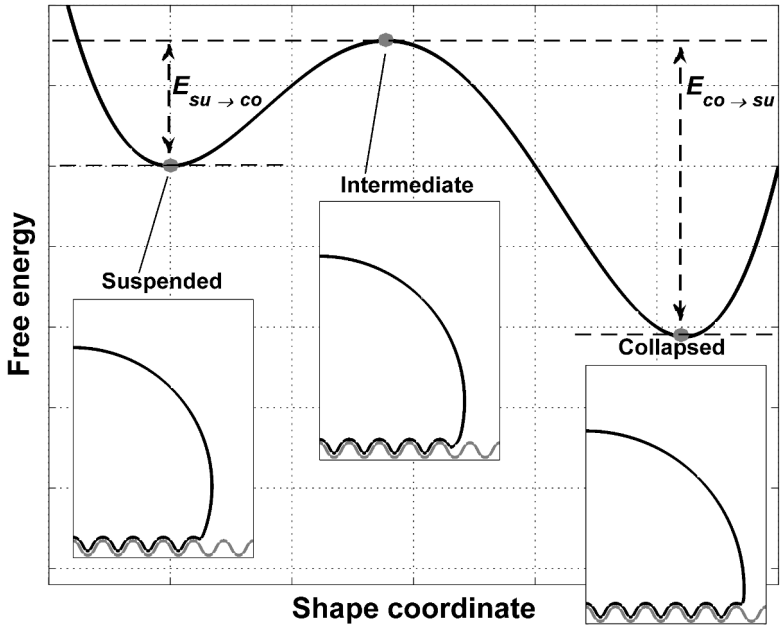

Figure 4.12: Schematic of a segment of the surface free energy profile for a textured solid surface and constant Young's contact angle, θ_Y.

the free surface energy reads:

$$E = \gamma_{LA}\,(A_{LA} - \cos\theta_Y\, A_{LS}) + \omega_{min}\, A_{LS} + \gamma_{SA}\, A_S, \tag{4.7}$$

where, $A_S = A_{LS} + A_{SA}$ is the total, constant, area covered by the solid surface. If we denote with E_{su}, E_{co} and E_{un} the surface free energy of the stable suspended (su), stable collapsed (co) and unstable (un) - intermediate wetting states (Fig. 4.12), which can be admitted on a textured solid surface with a constant Young's contact angle, θ_Y, then the wetting (or the suspended to collapsed, su $\rightarrow$ co) energy barrier can be computed from:

$$\begin{aligned} &E_{su\to co} = E_{un} - E_{su} \;\Rightarrow \\ &\frac{E_{su\to co}}{\gamma_{LA}} = (A_{LA,un} - A_{LS,su}) - \cos\theta_Y (A_{LS,un} - A_{LS,su}) \\ &\qquad\qquad + \frac{\omega_{min}}{\gamma_{LA}}\,(A_{LS,un} - A_{LS,su})\,. \end{aligned} \tag{4.8}$$

The surface area of the interfaces in Eq. 4.8 can be calculated as: $A = SL$, where S is the corresponding arc-length of the interface (S_{LA} and S_{LS}) and L expresses the depth along the direction perpendicular to the xz-plane; because of the translational symmetry of the droplet, we set $L = R_0$. The energy barrier for a de-wetting transition, $E_{co\to su}$, is computed similarly.

In Fig. 4.13 we present the energy barriers (using Eq. 4.8) for wetting and de-wetting transitions on a hydrophobic material with $\theta_Y = 104^o$. The admissible stable states,

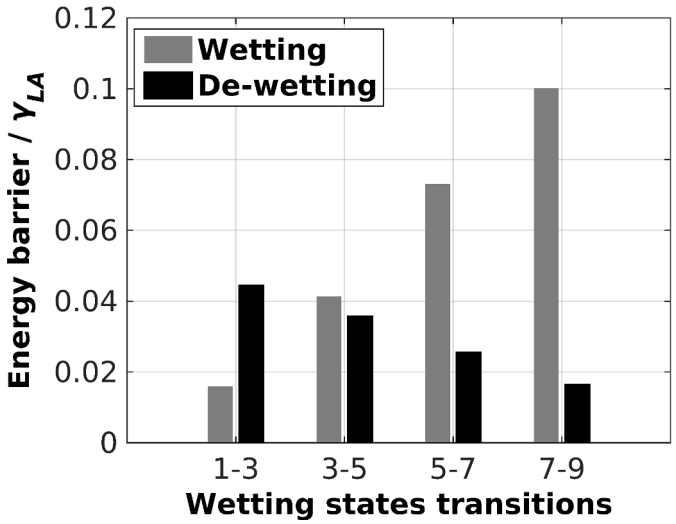

Figure 4.13: Energy barriers computed for the wetting and de-wetting transitions between the stable wetting states corresponding to points (1), (3), (5), (7), (9) of Fig. 4.9.

between which transitions can occur, are shown in Fig. 8: (1) → (3) → (5) → (7) → (9) for wetting, and (9) → (7) → (5) → (3) → (1) for de-wetting. It is found that the energy barriers increase as the number of the wetted stripes increases. Notice that $E_{(1)\to(3)} < E_{(3)\to(5)} < E_{(5)\to(7)} < E_{(7)\to(9)}$. On the contrary, for de-wetting transitions the energy barriers increase as the number of the wetted stripes decreases. It is worth mentioning that the presented methodology can be straightforwardly paired with optimization algorithms in order to design surface structures that resist impalement transitions or facilitate switching between certain wetting states.

4.3 Summary and conclusions

In this Chapter we initially validated the augmented YL equation against the conventional form for droplets equilibrating solid surfaces with simple topography. Moreover, a comparison with the conceptually different lattice-Boltzmann approach showed satisfactory agreement between the two different methodologies. We then demonstrated the efficiency of the proposed methodology to compute all admissible wetting states on a more complex, stripe-patterned solid surface. In particular, by performing parametric continuation methods, we computed multiple equilibrium wetting states and studied their relative stability. Finally, the calculation of the free energy difference of the metastable wetting states enabled the computation of the minimum energy required to induce certain wetting transitions (energy barrier).

To our knowledge, this is the first time that a one-dimensional continuum-level model is able to predict Cassie-Baxter and Wenzel wetting states by simulating the entire droplet profile and not a unit cell. In addition to the results presented here, concerning cases with translational symmetry, we also demonstrate similar computations for axisymmet-

ric droplets in Chapter B.3 of the Appendix B. We note that our methodology can also be extended beyond one spatial dimension, preserving its computational merits, however, in this case, further investigation is required in order to properly parameterize the two-dimensional droplet surface. Such an attempt has been recently performed by Pashos et al. [25], by using the augmented YL methodology proposed here, simulating, however, only the bottom region and not the entire two-dimensional droplet surface. We also note that fine-scale simulators (e.g. lattice-Boltzmann or molecular dynamics) utilized for the same task required substantial computational resources, especially when real millimeter-sized droplets are studied, as also discussed in Section 2.2.3 of Chapter 2.

The study of the dependence of the computed energy barriers on various geometric features of a rough surface would strongly impact the design of surfaces with addressable wetting properties in terms of high resistance in impalement transitions or efficient switching between wetting states. The wetting properties of a solid material can be modified with a variety of techniques (electric, thermal, pressure). Among the different choices, electrowetting [5] (electrostatical enhancement of solid wettability) combines a lot of advantages (rapid switchability, reliability) and is commonly used in recent applications. The equilibrium droplet shape on a structure solid surface, under the effect of electric field is studied in the next Chapter (5).

CHAPTER 5

Electrowetting on structured dielectric surfaces

In this chapter we employ the previously proposed augmented Young-Laplace equation, accounting also for an electric stress term along the droplet surface, in order to simulate the electrowetting phenomenon (i.e. the electrostatical enhancement of wetting by applying a voltage). Without making any simplification concerning the droplet shape or the field distribution, our formulation goes beyond the limitations of the classic theoretical models (Lippmann equation), while it is relieved from the implementation of the Young contact angle boundary condition. This way, electric field singularities (arising in the conventional modeling) are bypassed, allowing for accurate and efficient simulations, in terms of computational time and recourses. We initially examine the effect of the electric field strength (controlled by the voltage magnitude as well as the solid dielectric thickness) on both macroscopic (apparent contact angle) and microscopic (Young's contact angle) droplet shape characteristics. Next, by applying our methodology to patterned dielectrics we compute all admissible droplet equilibrium droplet profiles, including Cassie-Baxter, Wenzel and mixed wetting states.

5.1 Theory and modeling of electrowetting phenomenon

As previously discussed, miniaturization of devices renders electrowetting (EW) as the most convenient tool for manipulating droplets in lab-on-a-chip systems [26], optofluidic devices [27, 28] and even in more exotic systems such as energy harvesters using reverse electrowetting [29]. In a typical electrowetting-on-dielectric (EWOD) setup (see Fig. 5.1), a droplet of a conductive liquid (usually an aqueous solution) is deposited on a dielectric layer coating a flat base electrode. We note that the ambient medium must be an insulating fluid. By applying a voltage, V, between the base electrode and the conductive droplet, electric charge accumulates in the liquid-solid interface. The resulting decrease in the corresponding interfacial energy is observed as a decrease of the apparent contact angle i.e., as an enhancement of the wettability of the solid by the liquid [30, 15, 31].

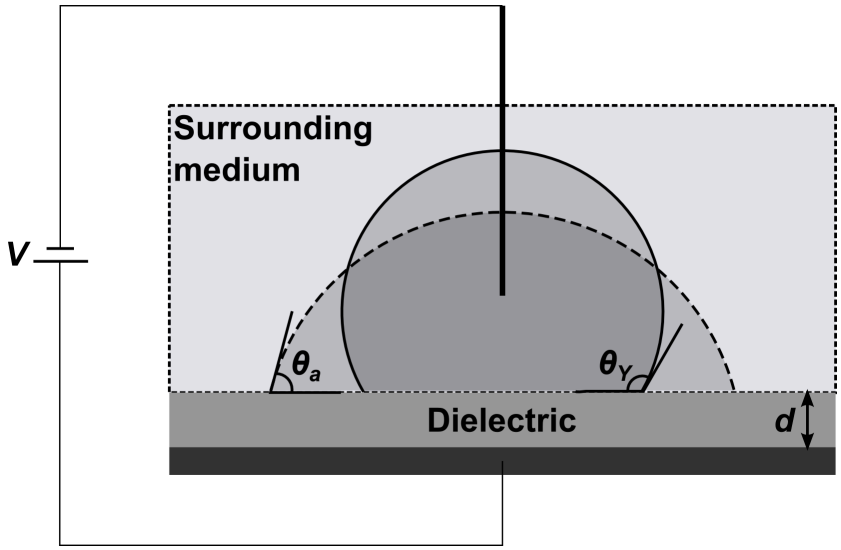

Figure 5.1: Schematic of the electrowetting-on-dielectric (EWOD) setup illustrating a drop at zero voltage (solid line) and its new profile when voltage is applied (dashed line).

A simple mathematical description of the apparent contact angle, θ_{a}, dependence on the applied voltage, V, is provided by the so-called Lippmann equation [31]:

$$\cos\theta_{\mathrm{a}} = \cos\theta_{\mathrm{Y}} + \frac{\epsilon_0\,\epsilon_r\,V^2}{2\,d\,\gamma_{\mathrm{LA}}} \Rightarrow \cos\theta_{\mathrm{a}} = \cos\theta_{\mathrm{Y}} + \eta, \tag{5.1}$$

where d is the thickness of the solid dielectric, ϵ_0 is the vacuum permittivity ($\epsilon_0 = 8.854 \times 10^{-12}$ F/m) and ϵ_r is the dielectric constant of the solid. The dimensionless EW number, η, in Eq. 5.1 expresses the relative strength of the electrostatic over the surface tension forces in the system, assuming a uniform electric field at the liquid-solid interface (ideal parallel plate capacitor). Despite its simplicity, the Lippmann equation provides accurate predictions in many EW configurations [32, 18], for low applied voltages and flat dielectrics; however, when higher voltages are applied the Lippmann equation fails to accurately predict the apparent contact angle since it neglects the electric fringe fields close to the three phase contact line (TPL), where the three different phases meet. In addition, the Lippmann equation predicts a steep monotonic decrease of the apparent contact angle (up to complete wetting) as the voltage increases. This contradicts the experimentally observed contact angle saturation phenomenon, where the contact angle variation slows down at high voltages, before reaching total wetting [30, 15]. The physical origins of contact angle saturation have not yet been completely explained in all cases, however, its onset is closely connected with the electric field distribution close to the TPL [16]. Furthermore, Lippmann equation does not account for the solid structure effect on the droplet shape, which would by particularly important in electrowetting applications on superhydrophobic [6] and generally heterogeneous solid surfaces. Thus, for a more accurate description of the EW phenomenon, accurate modeling approaches, without making any assumptions regarding the droplet shape, are required. Such an approach has been realized by solving the equations of capillary electrohydrostatics [33, 17]. In

particular, the droplet shape is given by the conventional Young-Laplace equation (2.20), augmented with the electric stress term accounting for the electric forces exerted on the droplet surface. If such a modeling is applied to structured surfaces, however, it would suffer from the previous discussed vulnerability of imposing the Young contact angle boundary condition to an unknown in number three-phase contact lines. In addition, the capillary electrohydrostatics equations are also limited from electric field singularities arising at the sharp wedge liquid shape, assumed at a three-phase contact line. The above limitations can be overcome by using the previously proposed augmented Young-Laplace formulation while incorporating the effect of the electric field on the equilibrium droplet shape.

In particular, in this Chapter we utilize the augmented YL formulation in order to reformulate the capillary electrohydrostatics equations and efficiently model, for a first time, the electrowetting phenomenon on textured solid dielectric surfaces. As previously discussed, our formulation does not require any pinning boundary condition, thus enabling the computation of wetting states with multiple and reconfigurable contact lines. In addition, the emerging electrohydrostatics equations will not suffer from the electric field singularities that arise from the sharp wedge shape of the liquid at the TPL. The droplet profile solutions obtained from the augmented YL formulation do no longer form wedges, allowing for a more accurate computation of the curvature of the liquid surface and of the field distribution close to the TPL. The reformulated (augmented) electrohydrostatics equations are presented in the following Section.

5.1.1 Augmented electrohydrostatics equations

Here, the electric field effect is incorporated in the augmented Young-Laplace equation as an electric stress term [34]. In particular, starting from Eq. 2.32, the dimensionless augmented Young-Laplace equation accounting for the electric stress term (and neglecting the effect of gravity) reads:

$$\frac{R_0}{\gamma_{\mathrm{LA}}} p^{\mathrm{LS}} + C = K + \frac{N_{\mathrm{e}} \widehat{E}^2}{2}, \tag{5.2}$$

where $N_{\mathrm{e}} = \frac{\epsilon_0 V^2}{\gamma_{LA} R_0}$ is the electric Bond number and $\widehat{E}$ the dimensionless electric field strength ($\widehat{E} = \frac{E R_0}{V}$). The latter is calculated along the droplet surface by solving the equations of electrostatics (Gauss law for electricity) for both the ambient phase and the dielectric material (see Fig. 5.2.):

$$\nabla \cdot (\epsilon_r \nabla \widehat{u}) = 0, \tag{5.3}$$

where $\widehat{u}$ is the dimensionless electric potential ($\widehat{u} = \frac{u}{V}$), and $\widehat{E} \equiv \| \nabla \widehat{u} \|$. The permittivity, ϵ_r, is denoted by ϵ_s for the ambient phase (insulating medium) and ϵ_d for the solid dielectric, respectively. Eq. 5.3 is solved accounting for the following dimensionless boundary

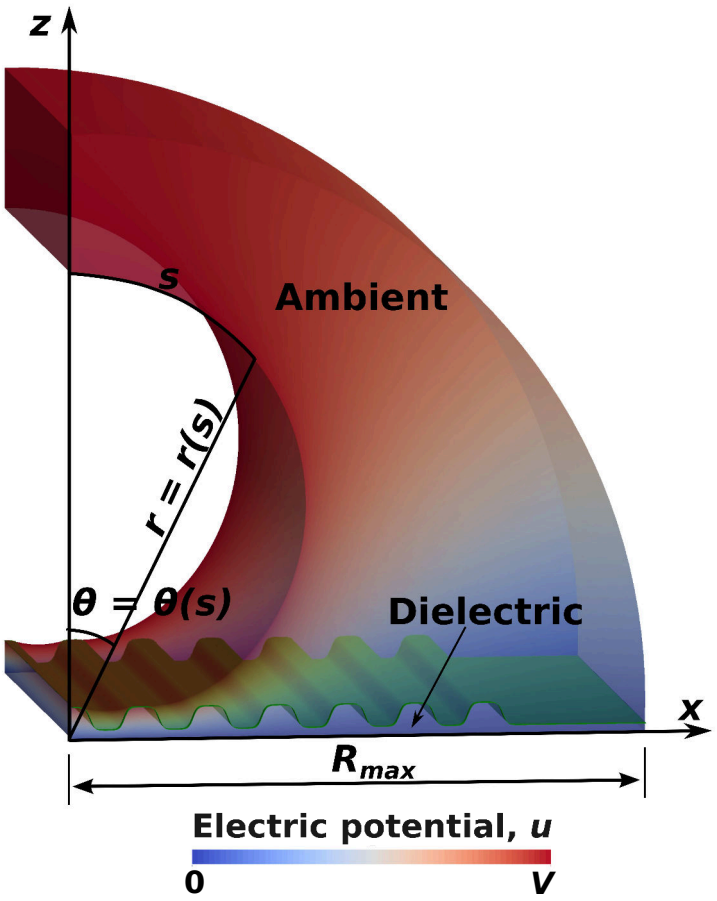

Figure 5.2: Electrowetting of a cylindrical drop on a stripe patterned solid dielectric. The droplet shape is obtained by solving the augmented Young-Laplace Equation (5.2).

conditions:

$$\frac{u}{V} = 1 \text{ at } (x,z) \in \sqrt{x^2+z^2} = r(s), \tag{5.4}$$

$$\frac{u}{V} = 0 \text{ at } z = 0, \tag{5.5}$$

$$\frac{R_0}{V}\frac{\mathrm{d}u}{\mathrm{d}x} = 0 \text{ at } x = 0, \tag{5.6}$$

$$\frac{1}{R_0\, V}\nabla u \cdot \boldsymbol{n}_\mathrm{b} = 0 \text{ at } (x,z) \in \sqrt{x^2+z^2} = R_\mathrm{max}, \tag{5.7}$$

where $\boldsymbol{n}_\mathrm{b}$ is the unit vector normal to the boundary of the computational domain, $\sqrt{x^2+z^2} = R_\mathrm{max}$ (see Fig. 5.2). Here we assume that the droplet is perfectly conductive; however, in the case of a dielectric liquid or a liquid with finite conductivity, the equations of electrostatics should also be solved in the interior of the droplet, and the electric stresses in the Eq. 5.2 should also be modified in order to account for the non-zero electric field inside the droplet.

In our computations, we study droplets with translational symmetry along the direction perpendicular to the xz-plane (cylindrical droplets). In order to capture both the liquid-solid and the liquid-ambient interface, the droplet profile, which is defined in cylindrical

coordinates (r, θ), is parameterized in terms of the arc-length, s, of the effectively one-dimensional droplet surface (see Fig. 5.2). More details about the arc-length parameterization are presented in Section 2.2.4.a of Chapter 2. The sought droplet shape affects the electric field distribution, u, and vice versa constituting a coupled non-linear and free boundary problem, which can be solved iteratively as presented in Section B.4 of the Appendix B.

5.2 Results and discussion

5.2.1 Apparent contact angle calculation

In this Section, we present computations of the dependence of the apparent contact angle, θ_a, on the applied voltage, V, for a cylindrical aqueous droplet in silicone oil ambient (AK 5, Wacker). Such insulating oils are commonly used as an ambient phase in experimental practice [35, 36]. For the selected ambient phase, the Young contact angle of the aqueous droplet on a Teflon® (PTFE) [37] flat surface is approximately 170° (corresponding to a wetting parameter, w^{LS} = 84, from Eq. 2.50). The disjoining pressure parameters, used here, are: $\sigma = 9 \times 10^{-3}$, $C_1 = 12$, $C_2 = 10$, $\epsilon = 8 \times 10^{-3}$. The selected characteristic length, R_0 = 0.62 mm, corresponds to a droplet with cross-sectional area $A_{droplet} = \pi {R_0}^2$ = 1.21 mm^2. The same configuration is used for the derivation of all results presented in this Chapter.

The electric stresses, developed along the droplet surface in an electrowetting simulation, result to an additional contribution to the surface free energy. This contribution can be included in a modified effective interface potential, ω^*. In particular, ω^* must incorporate both the molecular interactions (disjoining pressure, p^{LS}) and the electric field effect (expressed as an electrostatic pressure, $p_{el} = \frac{\epsilon_0 V^2 \widehat{E}^2}{2 R_0^2}$ [38]):

$$p^{LS} - \frac{\epsilon_0 V^2 \widehat{E}^2}{2 R_0} = \frac{d\omega^*}{d\delta}. \tag{5.8}$$

In the above, the electric field strength, E, is not constant but is evaluated along the droplet surface, expressed as a function of the distance, δ, i.e., $E = E(\delta)$. Furthermore, in an analogy to Eq. 2.48, the absolute minimum of ω^* which appears at the liquid-solid interface (for $\delta = \delta_{min}$, where δ_{min} is the minimum value of the liquid-solid distance) can be expressed as:

$$\omega^*_{min} = \gamma_{SA} + \gamma_{LA} - \gamma^{eff}_{LS}, \tag{5.9}$$

where γ^{eff}_{LS} is an effective liquid-solid interfacial tension (incorporating electrostatic forces) [38], with $\gamma^{eff}_{LS} < \gamma_{LS}$. By using the above equation, we can derive a Frumkin-Derjaguin type theoretical formula (similar to Eq. 2.49) for the prediction of the apparent contact angle of the droplet in the presence of a disjoining pressure and electric field.

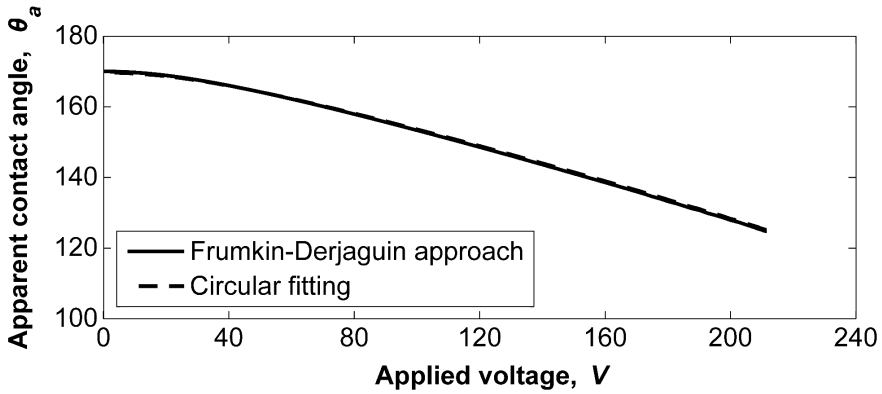

Figure 5.3: Apparent contact angle dependence on the applied voltage; θ_a is calculated following the Frumkin-Derjaguin approach (Eq. 5.11), as well as by circular fitting on the liquid-ambient interface (ϵ_d = 2.1 (PTFE), ϵ_s = 2.58 (AK 5, Wacker), θ_Y = 170°, γ_{LA} = 0.038 N/m, d = 10 μm).

In particular, by using a modified Young's equation (2.6), where γ_{LS} is replaced with the effective γ_{LS}^{eff} and the Young contact angle, θ_Y, with the apparent one, θ_a:

$$\gamma_{LS}^{eff} + \gamma_{LA}\cos\theta_a = \gamma_{SA}, \tag{5.10}$$

and by combining Eq. 5.9 with Eq. 5.10, finally yields:

$$cos\theta_a = \frac{\omega^*_{min}}{\gamma_{LA}} - 1. \tag{5.11}$$

In the above, the modified effective interface potential is computed from the integral:

$$\omega^* = \int_{\delta_{min}}^{\delta} \left[p^{LS}(\delta') - \frac{\epsilon_0 V^2 \widehat{E}^2(\delta')}{2 R_0^2} \right] d\delta'. \tag{5.12}$$

We can observe that in order to compute the apparent contact angle from Eq. 5.11, apart from the exact droplet shape, we also need the electric field distribution along the droplet surface, which definitely is not convenient for a quick calculation of θ_a (it requires the solution of the augmented electrohydrostatics equations described in Section 5.1.1). We note, however, that the above relation can be used to validate our computations, by comparing its predictions against the θ_a derived from circular fitting. In particular, in Fig. 5.3, we show the dependence of the apparent contact angle value on the applied voltage, for a PTFE substrate with thickness d = 10 μm, as computed from the Frumkin-Derjaguin type formula (Eq. 5.11) and by performing a circular fitting on the computed liquid-ambient (here water-oil) interface (more details about the circular fitting are presented in Section 4.2.1). We observe that the two lines are optically indistinguishable, which strengthens the validity of our computations. We note that similar findings also hold for different dielectric thicknesses. Eq. 5.11 could also be used by assuming simplifications regarding the electric field distribution (e.g. neglecting the effect of fringe fields around the contact line), in order to make quick estimations of the apparent contact angle. The

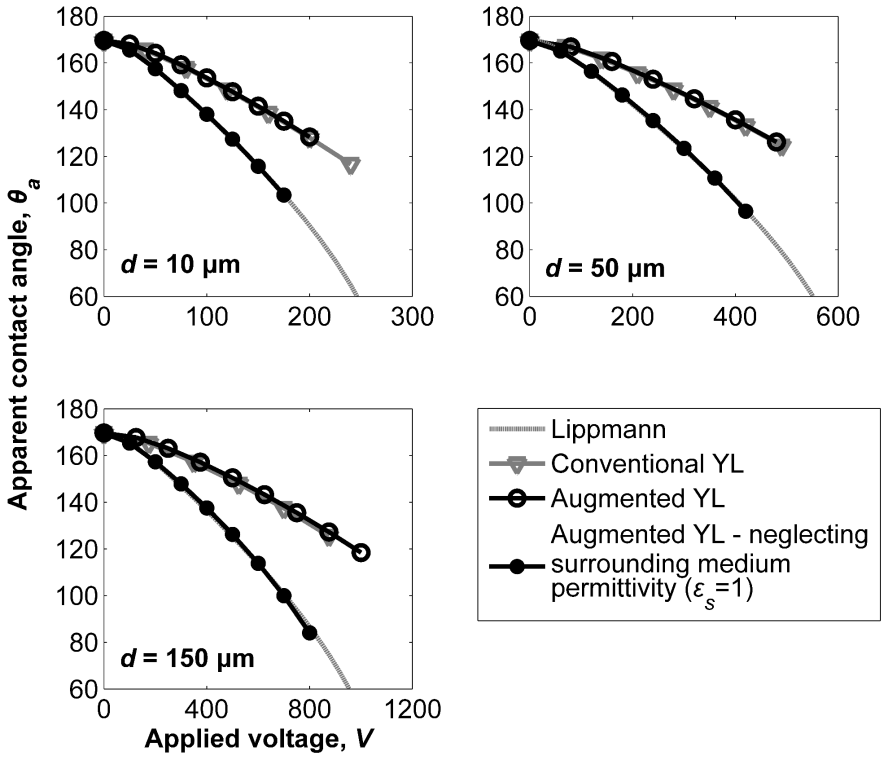

Figure 5.4: Dependence of the apparent contact angle on the applied voltage, V, for d = 10 μm, 50 μm and 150 μm PTFE, calculated from the conventional YL, the augmented YL (Eq. 5.2) and the Lippmann equation (5.1).

accuracy of such assumption, however, would be low, leading to erroneous estimations of θ_a. Next, we further validate our proposed methodology by comparing the predictions of the augmented YL equation, against those from the conventional one, which explicitly imposes the Young contact angle boundary condition. The latter model is analytically described in the work of Drygiannakis et al. [17].

5.2.2 Validation against the conventional Young-Laplace

The results obtained from the electro-capillary augmented YL equation (5.2) are compared with those obtained from the conventional electrohydrostatics formulation (described in detail in [17]) for flat solid dielectrics (PTFE foils) of variable thickness (d = 10 μm, 50 μm and 150 μm). The apparent contact angle presented in Fig. 5.4 is obtained by circular fitting at the liquid-ambient interface. The comparison between the results obtained from the two different formulations shows excellent agreement for all dielectric thicknesses tested. However, the predicted contact angle values obtained by the Lippmann equation are systematically smaller. This deviation is expected, and has been reported in the literature [33], since the Lippmann equation accounts only for the electrostatic energy stored within the dielectric layer between the droplet and the flat

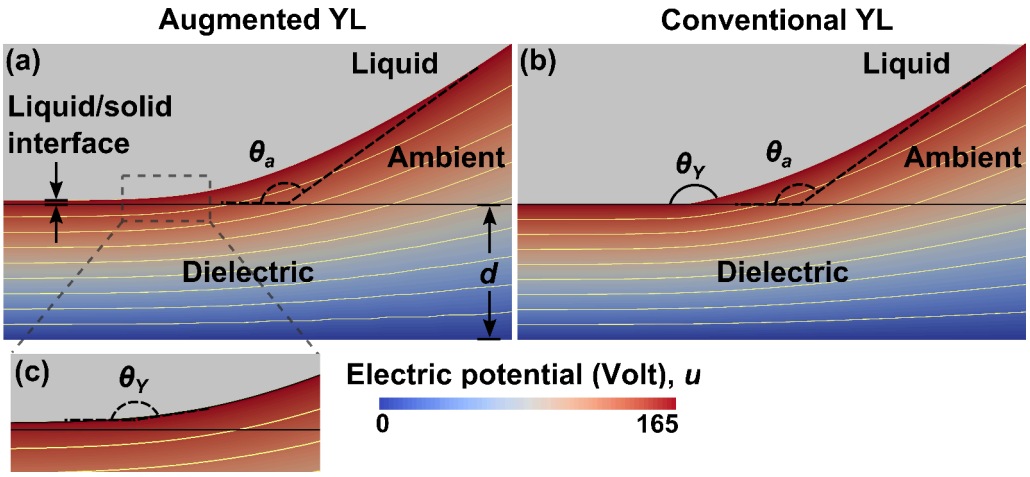

Figure 5.5: Electric potential distribution in the vicinity of the TPL computed from the solution of (a) the augmented and (b) the conventional YL equation. The Young contact angle boundary condition in the conventional formulation creates a wedge-shaped geometry at the TPL. The equipotential lines are depicted with light yellow (d = 10 μm PTFE, η = 0.67, V = 165 Volt).

electrode, neglecting the corresponding energy of the ambient medium. Indeed, if we neglect the surrounding medium permittivity (i.e., assuming $\epsilon_s = 1$) our computations agree with the Lippmann equation (see Fig. 5.4).

In Fig. 5.5, the droplet profiles and the electric potential distribution are shown at the TPL region. In the case of the conventional YL equation, the Young contact angle is explicitly imposed as a boundary condition assuming a wedge-shaped liquid-ambient interface profile at the TPL. This geometric assumption is not necessary when solving the augmented YL equation. In this case, and in order to implicitly obtain the Young contact angle, we perform high order (sixth) polynomial fitting to the droplet profile close to the TPL. The Young contact angle emerges within the range of action of the microscale interactions (disjoining pressure) (see Fig. 5.5(c)). The augmented YL equation governs also the liquid-solid interface, defined as the part of the droplet interface, which is at a minimum distance, $\delta_{\min}$, from the solid boundary. This minimum distance, $\delta_{\min}$, corresponds to the thickness of the liquid-solid diffuse interface. Indicatively, when the characteristic length is R_0 = 0.62 mm, $\delta_{\min}$= 3.25 × 10^{-4}mm.

It should be also noted that the proposed augmented YL formulation can provide a more detailed picture of the droplet surface shape and of the field distribution close to the TPL, compared to the conventional formulation; in the latter case, the field strength theoretically reaches an infinite value due to the singularity induced by the wedge-shaped droplet profile at the TPL.

Theoretical studies of Buehrle et al. [39], based on the local balancing of electrostatic and capillary forces at the TPL, suggest that the Young contact angle is independent of the applied voltage. Experimental studies [35], however, show a variation of the Young contact angle with the applied voltage, especially when the thickness of the solid dielectric is small ($\leqslant$ 10 μm). Below, we examine whether a change of the dielectric thickness

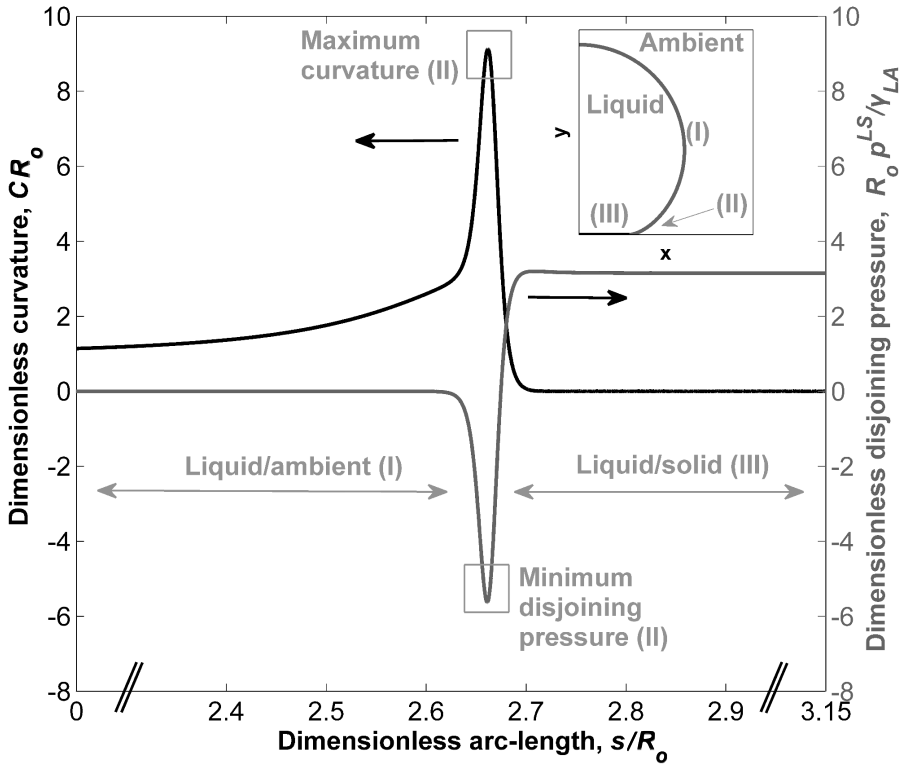

Figure 5.6: Dimensionless local mean curvature ($C\,R_0$) and disjoining pressure ($R_0\,p^{\mathrm{LS}}/\gamma_{\mathrm{LA}}$) distribution along the droplet surface (d = 10 µm PTFE, η = 0.5, V = 319.7 Volt).

has an effect on the Young contact angle value, which in the augmented YL formulation arises implicitly from the combined action of microscale and capillary forces.

5.2.3 Influence of the dielectric thickness on Young's contact angle

In this section we investigate a possible link between the dielectric thickness and the Young contact angle value as well as the liquid surface curvature in the vicinity of the TPL. Initially, in Fig. 5.6, we present the liquid surface curvature and the disjoining pressure distribution along the droplet interface profile for electrowetting number, η = 0.5. For a computed droplet equilibrium profile, the curvature distribution is evaluated from Eq. 2.40. In Fig. 5.6, we distinguish three interfacial regions corresponding to:

(I) the liquid-ambient interface where the curvature is constant and the disjoining pressure is virtually absent,

(II) the region close to the TPL where the curvature increases sharply up to a maximum finite value while the dimensionless disjoining pressure has reached a minimum value, and

(III) the liquid-solid interface where the curvature equals to that of the solid surface (zero for a flat dielectric) and the dimensionless disjoining pressure has a virtually

constant value ($R_0\, p^{\mathrm{LS}}\, \gamma_{\mathrm{LA}} = K + N_{\mathrm{e}}\, \widehat{E}^2/2$, from Eq. 5.2).

Overall, the droplet shape is mainly determined by the capillary forces along the liquid-ambient interface whereas the microscale forces (disjoining pressure) prevail along the TPL and the liquid-solid interface. The force balance at three-phase contact line region is also affected by the electric field, resulting in an increase of the apparent wettability with the applied voltage. The electric stresses effect on the force balance at the TPL has been investigated in numerous publications [40, 39, 35]. In particular, two different approaches have been proposed in the literature: the electrochemical approach, where the electric field affects the interfacial energies resulting in a reduction of the Young contact angle, and the electromechanical approach, where the electric stresses result in a net force acting on the droplet. In the latter case, the Young contact angle remains unaffected as the droplet deforms. Here, since the Young contact angle derives implicitly in our formulation (see Section 2.2.4), it is critical to examine the effect of the electric field strength (by modifying the applied voltage and the thickness of the solid dielectric) on the Young contact angle value and consequently on the curvature of the droplet in the vicinity of the three-phase contact line.

In Fig. 5.7, we present important shape features of the droplet surface for different solid dielectric thicknesses of PTFE (d = 10 μm, 50 μm and 150 μm), over a range of electrowetting numbers ($\eta \in [0, 1]$). In particular, we compute the dependence of the apparent contact angle, θ_{a}, the Young contact angle, θ_{Y}, and the dimensionless maximum local mean curvature of the surface as a function of the electrowetting number, η. For the computation of the Young contact angle, a sixth order polynomial fitting is applied on the droplet surface in the vicinity of the TPL. Initially, in Fig. 5.7a, it is observed that the macroscopic droplet shape (i.e. the apparent contact angle, θ_{a}) is not affected by the thickness of the solid dielectric. Note that, however, the applied voltage is considerably higher in the case of the thick dielectric, in order to achieve the same electrowetting number (e.g. for η = 0.5, V = 101 V for thin dielectric (d = 10 μm) and V = 392 V for the thick one (d = 150 μm)). Regarding the microscopic characteristics of the droplet, in Fig. 5.7b, it is observed that the Young contact angle variates in the case of the thin dielectric (d = 10 μm). In particular, θ_{Y} is reduced from 170° to ∼ 156° for η = 1. Such a behavior is not observed in the case of thick dielectrics (d = 50, 150 μm), where the Young contact angle appears to be insensitive to the electrowetting number. The maximum droplet curvature, at the (fictitious in our model) three-phase contact line, behaves in a similar fashion, as observed in Fig. 5.7c. Thus, the maximum curvature, in the case of the thin dielectric (d = 10 μm), is considerable increased with the applied voltage, contrary to the thick dielectrics cases (d = 50, 150 μm).

Similar trends have been presented in the experimental work of Mugele and Buehrle [35]. In particular they performed electrowetting experiments of a water droplet, in a silicone oil ambient (AK 5, Wacker), on solid dielectrics (PTFE) of various thicknesses (d = 10, 50 and 150 μm). They found that Young's contact angle decreases with the applied voltage only in the case of the thin dielectric (d = 10 μm). A direct comparison of the

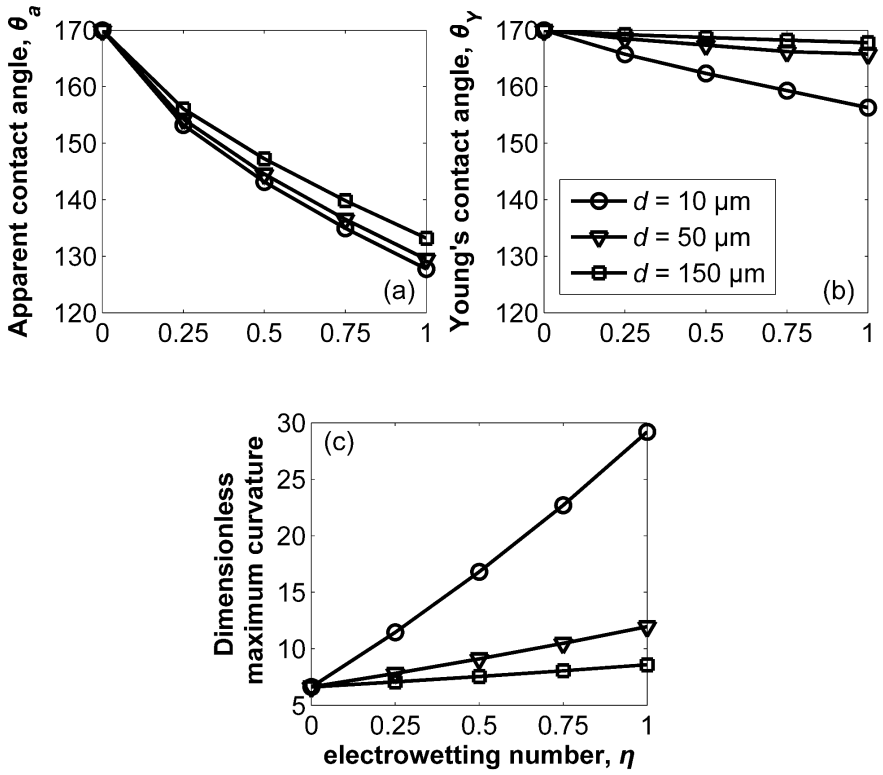

Figure 5.7: Dependence of (a) the apparent contact angle, θ_a, (b) the Young contact angle, θ_Y, and (c) the dimensionless maximum curvature of the droplet surface on the electrowetting number, η, for different dielectric thicknesses (d = 10 µm, 50 µm and 150 µm).

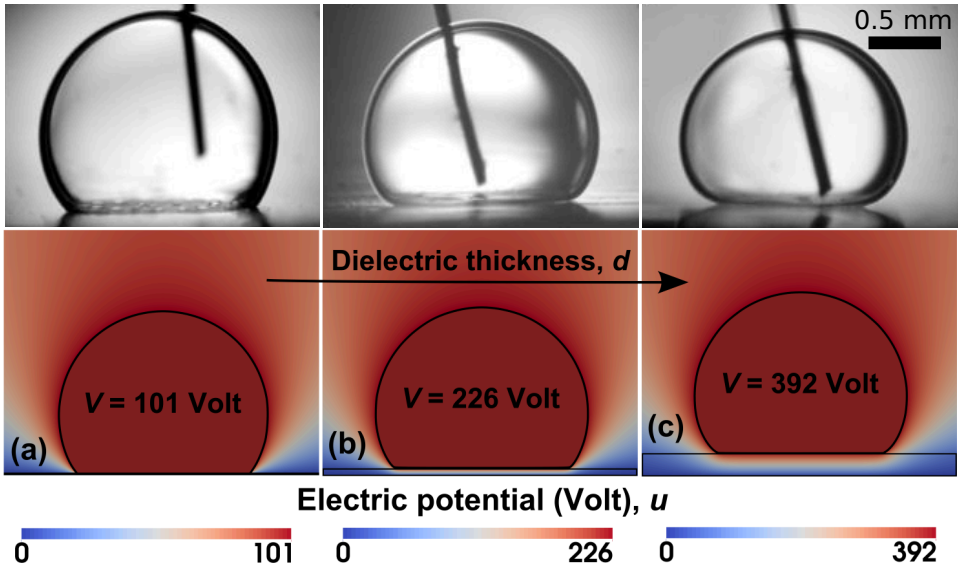

Figure 5.8: Comparison between experimental (upper part of the figure, reprinted from [35]) and computed droplet shapes (lower part of the figure) for different dielectric (PTFE) thicknesses (d = 10 µm, 50 µm and 150 µm) at η = 0.5. The aqueous droplets are immersed in a silicone oil bath (AK 5, Wacker). The variation of the local curvature (in the vicinity of the TPL) with the dielectric thickness can be easily observed in both experiments and simulations. We note that the computed apparent contact angle is virtually the same for all these cases (see also Fig. 5.7a).

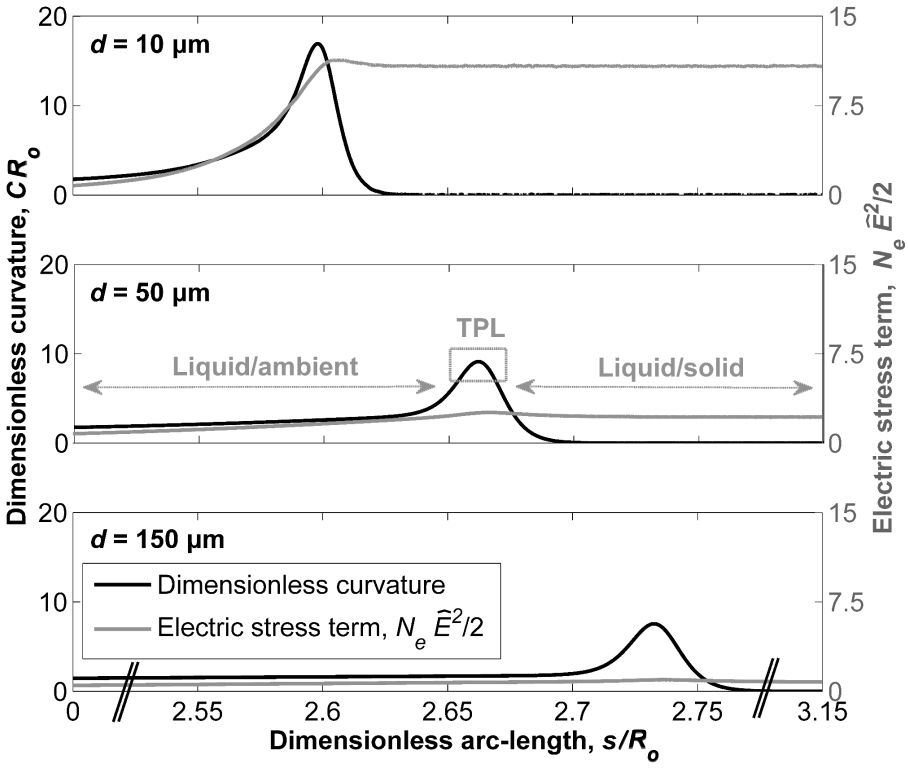

Figure 5.9: Variation of the dimensionless local mean curvature ($C\,R_0$) and the electric stress term ($N_e\,\widehat{E}^2/2$) of the augmented YL equation along the droplet surface for different dielectric thicknesses (η = 0.5).

droplet shapes between the experiments of Mugele and Buehrle and our simulations is depicted in Fig. 5.8. In these experiments, the variation of the Young contact angle value measured for thin dielectrics was attributed to the finite and limited optical resolution of their setup to resolve the details of the droplet profile; measuring curvature values in experimental practice involves high order polynomial fitting of the droplet interface, a process highly sensitive to the optical resolution. According to our perspective, the Young contact angle variation is not really a resolution issue, but is related with the electric field distribution along the droplet surface, which strongly depends on the thickness of the dielectric. The investigation of the dielectric thickness effect on the electric stress term of the augmented YL equation would provide more evidence on the link between the Young contact angle and the electric field strength at the TPL.

In Fig. 5.9, we present the variation of the curvature and the electric stress term of the augmented YL, along the droplet surface for different PTFE thicknesses and for a fixed electrowetting number (in this case η = 0.5). We observe that for the case of the thin dielectric (d = 10 μm) the strength of electric stress term increases sharply at the TPL and then reaches a constant value along the liquid-solid interface. For thicker dielectrics (see Fig. 5.9, d = 50 μm and 150 μm), the maximum electric stress value is reduced and its effect extends over a wider region around the TPL (as compared to the case of the thin dielectric with d = 10 μm in Fig. 5.9).

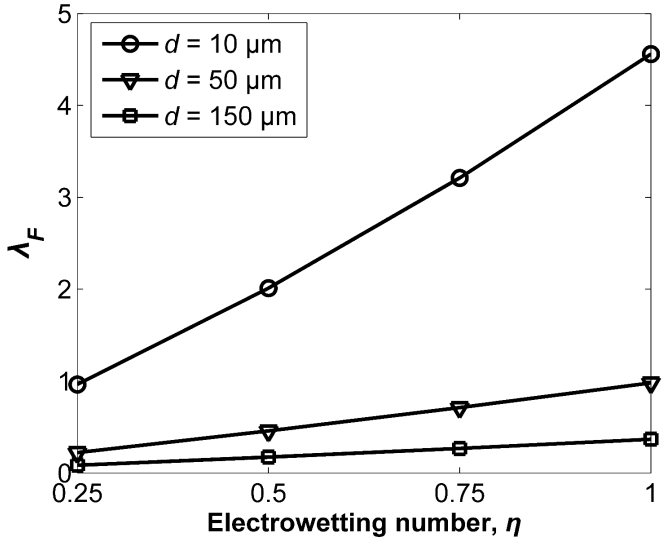

Figure 5.10: Dependence of the relative strength, λ_F, of the electric stress term ($N_e\ \widehat{E}^2/2$) over the disjoining pressure ($R_0\ p^{LS}/\gamma_{LA}$) of the augmented YL (Eq. 5.2), at the TPL, on the electrowetting number for different dielectric thicknesses: d = 10 μm, 50 μm and 150 μm.

As a summary, the observed variations of the computed maximum curvature value (as well as the Young contact angle) for thin dielectrics can be attributed to the higher electric stresses developed within the action range of the microscale forces (disjoining pressure). In Fig. 5.10, we present the relative strength, λ_F, of the electric stress term, of the augmented YL equation, over the disjoining pressure in the vicinity of the TPL for different dielectric thicknesses and electrowetting numbers. The electric stress term is of lower magnitude compared to the disjoining pressure in all studied cases of electrowetting numbers, when the dielectric thickness is 50, and 150 μm. However, in thinner dielectric thickness cases (d = 10 μm) the electric field effect is significantly enhanced especially at high electrowetting numbers; the magnitude of the developed electric stresses exceeds the disjoining pressure causing an increase of the local curvature and a concomitant decrease in the Young contact angle. Similar results can be obtained using different forms of the disjoining pressure isotherm as presented in Section B.5 of the Appendix B. The above argument is extremely important for realizing reversible wetting transitions on superhydrophobic surfaces, by controlling the droplet surface curvature at the TPL, as will be demonstrated in Section 9.1 of Chapter 9.

Apart from the previously presented curvature and electric field computations on smooth solid surfaces, the main advantage of the proposed methodology is the ability to model electrowetting on geometrically patterned solid dielectric surfaces, where multiple and reconfigurable TPLs arise. Existing fine-scale electrowetting modeling approaches, e.g., molecular dynamics [41, 23] and mesoscopic lattice-Boltzmann models [42, 11, 20] suffer from severe computational limitations (especially when real millimeter sized droplets are studied), whereas continuum-level models are based on significant simplifications regarding the actual shape of the droplet and the field distribution [43]

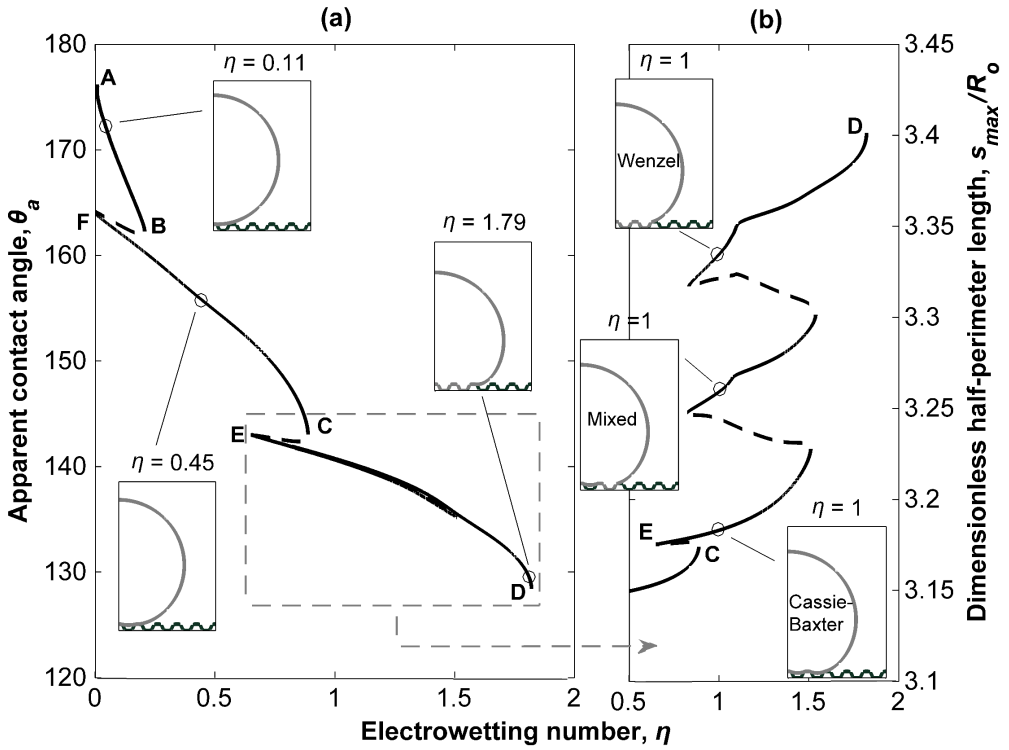

Figure 5.11: Dependence of (a) the apparent contact angle, θ_a, and (b) the dimensionless half perimeter length, s_{max}/R_0, on the electrowetting number, η, for a patterned solid dielectric surface.

at the TPL.

5.2.4 Electrowetting on geometrically patterned dielectric surfaces

In our illustrative example we model electrowetting on a multi-striped dielectric (see Fig. 5.2). The height (h_d) and the width (w_d) of the protrusions are 62.03 µm and 93.05 µm, respectively. The minimum thickness of the dielectric (PTFE) is: d_{min} = 25 µm, and the maximum thickness is $d_{max} = h_d + d_{min}$ = 87.03 µm. For the computation of the electrowetting number (see Eq. 5.1), we select: $d = d_{max} = h_d + d_{min}$ in order to account for the non-uniformity of the dielectric thickness.

As reported above, geometrically patterned dielectrics can admit multiple droplet equilibrium profiles ranging from Cassie-Baxter to Wenzel wetting states. By utilizing parameter continuation techniques, all the admissible wetting states (stable and unstable) can be traced. In particular, in Fig. 5.11, we present the dependence of the apparent contact angle (calculated by fitting a circle to the liquid-ambient interface above the solid surface asperities) and the dimensionless half-perimeter length of the droplet, s_{max}/R_0, on the electrowetting number. The different solution branches correspond to distinct wetting states. In particular, the stable solution branch AB corresponds to droplets wetting a single stripe, while the stable solution branch FC corresponds to Cassie-Baxter

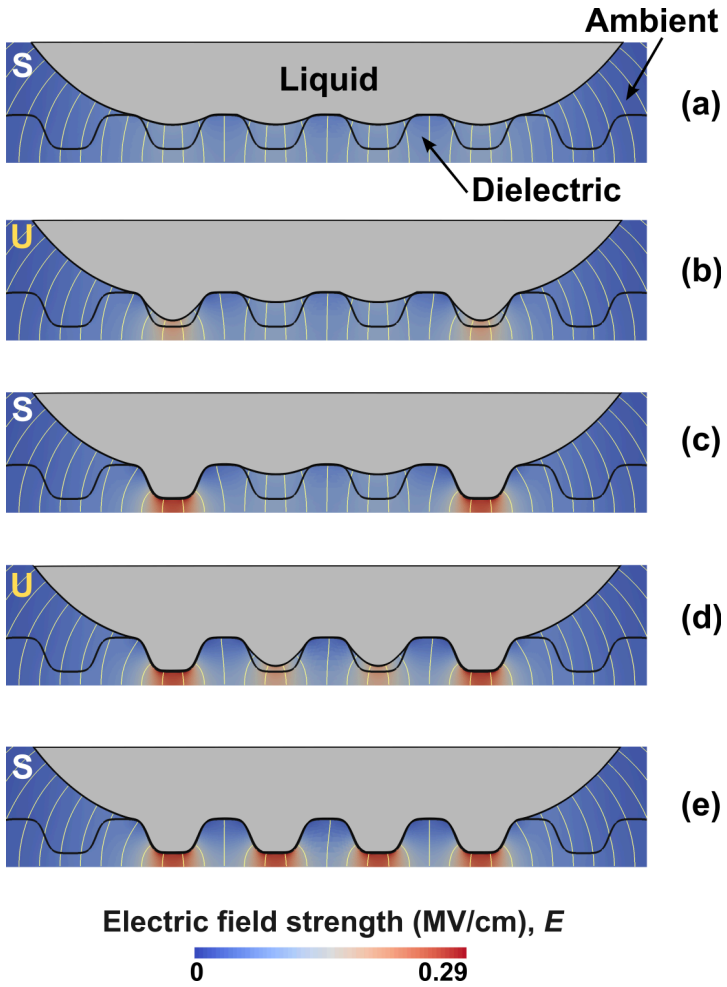

Figure 5.12: Electric field distribution around co-existing wetting states on a stripe patterned dielectric for η = 1.19, in the vicinity of the solid surface. The streamlines of the electric field are depicted with light yellow. The stable wetting states are denoted with "S", and the unstable ones with "U".

states wetting three stripes (taking into account the reflection symmetry about the vertical plane (θ = 0)). Several solution branches intervene between points E and D exhibiting approximately the same apparent wettability for the same electrowetting number, and correspond to:

1. Cassie-Baxter states wetting five stripes (see Fig. 5.11b, η = 1 (Cassie-Baxter)),
2. fully collapsed Wenzel states wetting the same number of stripes (see Fig. 5.11b, η = 1 (Wenzel)) and
3. mixed wetting states where the liquid has partially penetrated into the solid roughness (see Fig. 5.11b, η = 1 (Mixed)).

We also observe that the electrostatically induced wetting transitions on the patterned dielectric under study are hysteretic. When no voltage is applied, a "fakir" droplet sits on the top of protrusions (see Fig. 5.11, point A for η = 0, θ_a = 177^o). By quasi-statically increasing the applied voltage, the apparent wettability is enhanced (the apparent contact

angle reduces from 177° to 128°) and the liquid gradually penetrates the solid surface roughness following the route: A → B → C → D along the stable solution branches (solid lines in Fig. 5.11a). By decreasing the applied voltage, the droplet de-wets the solid surface following a different route: D → E → F (see Fig. 5.11a). The range of hysteresis is determined by the range of the intermediate unstable branches (dashed lines in Fig. 5.11). We also note that the initial "fakir" droplet with θ_a = 177° cannot be recovered by switching off the applied voltage; the wetting transition is irreversible, and the highest apparent contact angle that can be recovered through voltage reduction is 164°.

Interestingly enough, the intervening stable solution branches between points E and D in Fig. 5.11 correspond to wetting states exhibiting nearly identical macroscopic characteristics (same apparent wettability for the same applied voltage), yet with significantly different fractions of the solid surface area wetted by the liquid. In Fig. 5.12, we present the electric field distribution in the vicinity of the solid surface for five co-existing wetting states (stable and unstable) with $\theta_a \approx 139.3°$ and the same electrowetting number (η = 1.19). Apart from the stable Cassie-Baxter (Fig. 5.12a), and Wenzel (Fig. 5.12e) wetting states, the patterned dielectric can also admit mixed stable states (Fig. 5.12c), where only two of the four oil pockets of the solid surface are filled with water. We remark that the intermediate unstable equilibrium states depicted in Fig. 5.12b and Fig. 5.12d cannot be tracked experimentally. The sequence of equilibrium profiles in Fig. 5.12b-d illustrates the intermediate states of a minimum energy path connecting the Cassie-Baxter state (Fig. 5.12a) and Wenzel state (Fig. 5.12e); impalement originates from the outer side of the droplet and succeeds in the center for the particular solid surface geometry.

5.3 Summary and conclusions

In this Chapter, after validating the presented methodology against the predictions of the conventional Young-Laplace equation (which imposes the Young contact angle boundary condition) we studied the effect of dielectric thickness on the liquid surface curvature distribution, and on the Young contact angle for different electrowetting numbers. We found that by increasing the applied voltage in adequately thin dielectrics, results in variations in the droplet shape both macroscopically (apparent contact angle), and microscopically (Young's contact angle). Such a dependence of the Young contact angle on the applied voltage has also been reported previously in the literature [35], however not theoretically supported.

The advantage of the proposed modeling approach is its ability to perform electrowetting computations on geometrically structured dielectric surfaces. To our knowledge, this is the first time that a continuum-level model can predict Cassie–Baxter, Wenzel, and mixed wetting states by simulating the entire droplet and not a small part of it, like a unit cell. Continuum-level studies of wetting transitions on geometrically patterned surfaces have been previously presented in the literature, however they do not take into account

the pinning/de-pinning effects of the droplet at the protrusion edges, performing the analysis at a unit cell of the texture [44, 45]. Under this assumption, no mixed states can be predicted (since the outer stripes are equivalent with the inner ones) and thus there is no information concerning the energetics of the mechanism of the wetting transition. The multiplicity of the wetting states, computed here for a relatively simple patterned geometry is indicative of the wealth of equilibrium states expected to be computed when smaller scale or of arbitrary roughness (i.e., without any symmetry assumption) solid surfaces are studied.

References

[1] P. S. Forsberg, C. Priest, M. Brinkmann, R. Sedev, and J. Ralston. "Contact line pinning on microstructured surfaces for liquids in the Wenzel state". In: *Langmuir* 26.2 (2009), pp. 860–865.

[2] T. Sun, G. Wang, L. Feng, B. Liu, Y. Ma, L. Jiang, and D. Zhu. "Reversible switching between superhydrophilicity and superhydrophobicity". In: *Angewandte Chemie* 116.3 (2004), pp. 361–364.

[3] A. Lafuma and D. Quéré. "Superhydrophobic states". In: *Nature Materials* 2.7 (2003), pp. 457–460.

[4] E. Bormashenko, R. Pogreb, G. Whyman, Y. Bormashenko, and M. Erlich. "Vibration-induced Cassie-Wenzel wetting transition on rough surfaces". In: *Applied Physics Letters* 90.20 (2007), p. 201917.

[5] T. N. Krupenkin, J. A. Taylor, T. M. Schneider, and S. Yang. "From rolling ball to complete wetting: the dynamic tuning of liquids on nanostructured surfaces". In: *Langmuir* 20.10 (2004), pp. 3824–3827.

[6] T. N. Krupenkin, J. A. Taylor, E. N. Wang, P. Kolodner, M. Hodes, and T. R. Salamon. "Reversible wetting-dewetting transitions on electrically tunable superhydrophobic nanostructured surfaces". In: *Langmuir* 23.18 (2007), pp. 9128–9133.

[7] R. J. Vrancken, H. Kusumaatmaja, K. Hermans, A. M. Prenen, O. Pierre-Louis, C. W. Bastiaansen, and D. J. Broer. "Fully reversible transition from Wenzel to Cassie- Baxter states on corrugated superhydrophobic surfaces". In: *Langmuir* 26.5 (2009), pp. 3335–3341.

[8] C. Ran, G. Ding, W. Liu, Y. Deng, and W. Hou. "Wetting on nanoporous alumina surface: transition between Wenzel and Cassie states controlled by surface structure". In: *Langmuir* 24.18 (2008), pp. 9952–9955.

[9] N. A. Patankar. "Transition between superhydrophobic states on rough surfaces". In: *Langmuir* 20.17 (2004), pp. 7097–7102.

[10] C Ishino, K Okumura, and D Quéré. "Wetting transitions on rough surfaces". In: *Europhysics Letters* 68.3 (2004), p. 419.

[11] M. E. Kavousanakis, C. E. Colosqui, I. G. Kevrekidis, and A. G. Papathanasiou. "Mechanisms of wetting transitions on patterned surfaces: continuum and mesoscopic analysis". In: *Soft Matter* 8.30 (2012), pp. 7928–7936.

[12] H. Keller. "Lectures on numerical methods in bifurcation problems". In: *Applied Mathematics* 217 (1987), p. 50.

[13] M. W. Hirsch, S. Smale, and R. L. Devaney. *Differential equations, dynamical systems, and an introduction to chaos*. Academic Press, 2012.

[14] D. Y. Kwok and A. W. Neumann. "Contact angle measurement and contact angle interpretation". In: *Advances in Colloid and Interface Science* 81.3 (1999), pp. 167–249.

[15] F. Mugele. "Fundamental challenges in electrowetting: from equilibrium shapes to contact angle saturation and drop dynamics". In: *Soft Matter* 5.18 (2009), pp. 3377–3384.

[16] A. Papathanasiou and A. Boudouvis. "Manifestation of the connection between dielectric breakdown strength and contact angle saturation in electrowetting". In: *Applied Physics Letters* 86.16 (2005), p. 164102.

[17] A. I. Drygiannakis, A. G. Papathanasiou, and A. G. Boudouvis. "On the connection between dielectric breakdown strength, trapping of charge, and contact angle saturation in electrowetting". In: *Langmuir* 25.1 (2008), pp. 147–152.

[18] M. Vallet, M. Vallade, and B. Berge. "Limiting phenomena for the spreading of water on polymer films by electrowetting". In: *The European Physical Journal B-Condensed Matter and Complex Systems* 11.4 (1999), pp. 583–591.

[19] F. Mugele and S. Herminghaus. "Electrostatic stabilization of fluid microstructures". In: *Applied Physics Letters* 81.12 (2002), pp. 2303–2305.

[20] C. E. Colosqui, M. E. Kavousanakis, A. G. Papathanasiou, and I. G. Kevrekidis. "Mesoscopic model for microscale hydrodynamics and interfacial phenomena: Slip, films, and contact-angle hysteresis". In: *Physical Review E* 87.1 (2013), p. 013302.

[21] V. M. Starov. "Surface forces action in a vicinity of three phase contact line and other current problems in kinetics of wetting and spreading". In: *Advances in Colloid and Interface Science* 161.1 (2010), pp. 139–152.

[22] E. Bormashenko, R. Pogreb, G. Whyman, and M. Erlich. "Resonance Cassie-Wenzel wetting transition for horizontally vibrated drops deposited on a rough surface". In: *Langmuir* 23.24 (2007), pp. 12217–12221.

[23] E. S. Savoy and F. A. Escobedo. "Molecular simulations of wetting of a rough surface by an oily fluid: Effect of topology, chemistry, and droplet size on wetting transition rates". In: *Langmuir* 28.7 (2012), pp. 3412–3419.

[24] A. Giacomello, S. Meloni, M. Müller, and C. M. Casciola. "Mechanism of the Cassie-Wenzel transition via the atomistic and continuum string methods". In: *The Journal of chemical physics* 142.10 (2015), p. 104701.

[25] G Pashos, G Kokkoris, A. Papathanasiou, and A. Boudouvis. "Wetting transitions on patterned surfaces with diffuse interaction potentials embedded in a Young-Laplace formulation". In: *The Journal of Chemical Physics* 144.3 (2016), p. 034105.

[26] R. B. Fair. "Digital microfluidics: is a true lab-on-a-chip possible?" In: *Microfluidics and Nanofluidics* 3.3 (2007), pp. 245–281.

[27] S. Kuiper and B. Hendriks. "Variable-focus liquid lens for miniature cameras". In: *Applied physics letters* 85.7 (2004), pp. 1128–1130.

[28] B. Berge and J. Peseux. "Variable focal lens controlled by an external voltage: An application of electrowetting". In: *The European Physical Journal E* 3.2 (2000), pp. 159–163.

[29] T. Krupenkin and J. A. Taylor. "Reverse electrowetting as a new approach to high-power energy harvesting". In: *Nature Communications* 2 (2011), p. 448.

[30] C. Quilliet and B. Berge. "Electrowetting: a recent outbreak". In: *Current Opinion in Colloid and Interface Science* 6.1 (2001), pp. 34–39.

[31] F. Mugele, M. Duits, and D. Van den Ende. "Electrowetting: a versatile tool for drop manipulation, generation, and characterization". In: *Advances in Colloid and Interface Science* 161.1 (2010), pp. 115–123.

[32] H. Moon, S. K. Cho, R. L. Garrell, et al. "Low voltage electrowetting-on-dielectric". In: *Journal of Applied Physics* 92.7 (2002), pp. 4080–4087.

[33] K. Adamiak. "Capillary and electrostatic limitations to the contact angle in electrowetting-on-dielectric". In: *Microfluidics and Nanofluidics* 2.6 (2006), pp. 471–480.

[34] K. H. Kang. "How electrostatic fields change contact angle in electrowetting". In: *Langmuir* 18.26 (2002), pp. 10318–10322.

[35] F Mugele and J Buehrle. "Equilibrium drop surface profiles in electric fields". In: *Journal of Physics: Condensed Matter* 19.37 (2007), p. 375112.

[36] M. Dhindsa, S. Kuiper, and J. Heikenfeld. "Reliable and low-voltage electrowetting on thin parylene films". In: *Thin Solid Films* 519.10 (2011), pp. 3346–3351.

[37] H. Liu, S. Dharmatilleke, D. K. Maurya, and A. A. Tay. "Dielectric materials for electrowetting-on-dielectric actuation". In: *Microsystem Technologies* 16.3 (2010), pp. 449–460.

[38] F. Mugele and J.-C. Baret. "Electrowetting: from basics to applications". In: *Journal of Physics: Condensed Matter* 17.28 (2005), R705.

[39] J. Buehrle, S. Herminghaus, and F. Mugele. "Interface profiles near three-phase contact lines in electric fields". In: *Physical Review Letters* 91.8 (2003), p. 086101.

[40] T. B. Jones. "On the relationship of dielectrophoresis and electrowetting". In: *Langmuir* 18.11 (2002), pp. 4437–4443.

[41] J.-Y. Park, M.-Y. Ha, H.-J. Choi, S.-D. Hong, and H.-S. Yoon. "A study on the contact angles of a water droplet on smooth and rough solid surfaces". In: *Journal of Mechanical Science and Technology* 25.2 (2011), pp. 323–332.

[42] A Dupuis and J. Yeomans. "Modeling droplets on superhydrophobic surfaces: equilibrium states and transitions". In: *Langmuir* 21.6 (2005), pp. 2624–2629.

[43] V. Bahadur and S. V. Garimella. "Electrowetting-based control of static droplet states on rough surfaces". In: *Langmuir* 23.9 (2007), pp. 4918–4924.

[44] J. Oh, G Manukyan, D Van den Ende, and F Mugele. "Electric-field–driven instabilities on superhydrophobic surfaces". In: *Europhysics Letters* 93.5 (2011), p. 56001.

[45] Y. C. Jung and B. Bhushan. "Wetting transition of water droplets on superhydrophobic patterned surfaces". In: *Scripta Materialia* 57.12 (2007), pp. 1057–1060.

PART III

Simulation of dynamics of wetting

CHAPTER 6

Modeling of droplet spreading on rough surfaces

The conventional hydrodynamic model suffers from severe limitations when modeling the wetting dynamics on textured substrates due to the tedious implementation of the boundary condition to an unknown number, and reconfigurable, contact lines. In order to resolve these limitations, we apply the proposed hydrodynamic model formulation (see Section 3.2.3), in which no explicitly boundary condition is required at the three-phase contact lines. The validity of our approach is initially tested against experimental data of a droplet impacting on an arbitrary roughened solid surface. In our simulations, we observe that the viscous dissipation on the solid surface roughness gives rise to an effective no-slip boundary condition, although it is not explicitly imposed. The study of the early spreading phase on hierarchically structured, as well as on chemically patterned, solid substrates reveal an inertial regime where the contact radius grows according to a universal power law, perfectly agreeing with recently published experimental findings. Finally, we also investigate the droplet dynamics under the effect of electric field (electrospreading). Electrostatically assisted spreading is commonly observed in practice, in lab-on-a-chip devices.

6.1 Spreading dynamics

As experimentally observed [1, 2] for low viscosity fluids on smooth substrates, the contact radius of a spreading droplet, R_s (see Fig. 6.1), grows with time according to the power law:

$$\frac{R_s}{R_0} = K_s \left(\frac{t}{t_c}\right)^{\alpha}, \tag{6.1}$$

where K_s is the power law prefactor, α is a spreading exponent and t_c is the inertio-capillary time ($t_c = \sqrt{\frac{\rho R_0^3}{\gamma_{\mathrm{LA}}}}$), defining the time scale where the flow is inertia-dominated. Bird et al. [2] demonstrated that $\alpha = 0.3$ for a water droplet on a solid substrate with $\theta_{\mathrm{Y}} = 120^{\mathrm{o}}$, whereas it increases to $\alpha = 0.5$ for a fully wetted substrate ($\theta_{\mathrm{Y}} \approx 0^{\mathrm{o}}$). As spreading continues, the viscous friction inside in the droplet becomes the main dissipation mech-

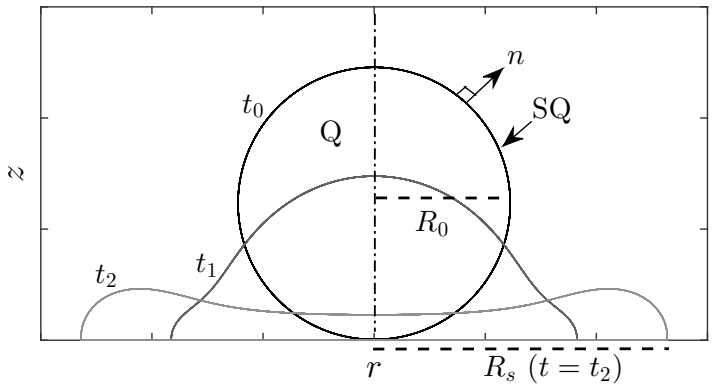

Figure 6.1: Snapshots of an axisymmetric droplet at different time instances ($t_0 < t_1 < t_2$) after impacting on a flat solid substrate.

anism and $\alpha = 0.1$, with another constant K'. Thus, in order to accurately simulate of a droplet impinging and spreading on solid surface, one needs to take into account both the inertial and viscous forces, as well as the friction that the liquid exhibits at the three-phase contact lines. The latter is usually incorporated through the Navier slip boundary condition (Eq. 3.9). In addition, since an amount of roughness is always present, even in macroscopically flat substrates, the viscous friction on the solid micro-structure must also be included in the modeling. Such a study, however, would be infeasible with the conventional formulation of the hydrodynamic model (see Section 3.2.1). In this Chapter, we utilize the proposed augmented hydrodynamic model formulation (see Section 3.2.3) to perform dynamic simulations of axisymmetric droplets spreading on solid substrates covered with arbitrary asperities, in air ambient. Contrary to the conventional hydrodynamic model, in our proposed formulation the relative velocity between the solid and the liquid is not directly imposed with a boundary condition, thus allowing the throughout study of the solid roughness effect on the spreading dynamics.

In particular, in order to highlight the role of the solid surface micro-structure in the energy dissipation, in this Chapter we neglect any tangential stresses along the liquid surface ($\beta_{\text{eff}} = 0$, in Equation 3.16). What we expect is that the roughness will enhance the viscous dissipation in the vicinity of the solid surface, resulting to an effective tangential stress. Such an argument was initially introduced by Richardson [3] and Jansons [4] who concluded that the energy dissipation taking place on the intrinsic roughness can approximate, macroscopically, a no-slip boundary condition, even when the solid material is microscopically perfectly slipping. This assertion was later mathematically proved for a three dimensional flow by Casado-Diaz et al. [5], however, a throughout investigation of the solid micro-structure effect on the flow characteristics (e.g. contact radius and apparent contact angle versus time) has not yet been performed. In the following Section, we initially validate the computational results (i.e. contact radius and dynamic contact angle of the droplet against time) against experimental measurements and we discuss the influence of surface roughness geometric characteristics on the spreading dynamics.

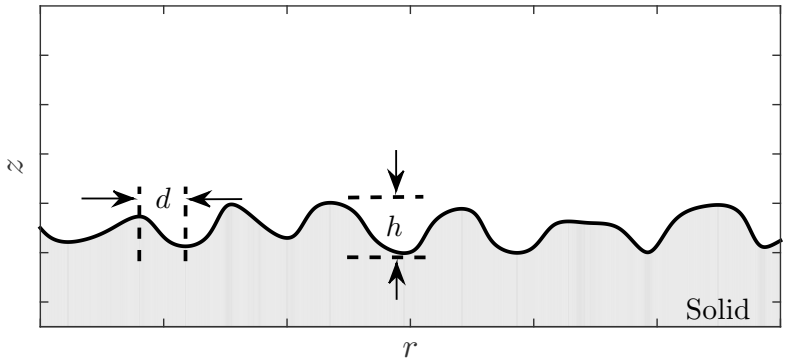

Figure 6.2: Geometric parameters of the solid surface intrinsic roughness.

6.2 Results and discussion

6.2.1 Spreading dynamics: Validation with experimental data

The proposed "boundary-condition-free" approach is implemented to model the dynamics of a droplet impacting and spreading on a horizontal surface (see Fig. 6.1). In order to validate our predictions, the results are compared with experimental data [6] of a glycerin/water mixture droplet (85 % of glycerin) spreading on a wax solid surface (see also Section C.2 of the Appendix C for a pure water droplet). Since the viscosity of the surrounding phase (air ambient) in our system is negligible compared to that of the droplet, the flow problem is solved only for the droplet interior (Q in Fig. 6.1) and thus the total stress tensor of the ambient phase, $\boldsymbol{s}(\boldsymbol{n})|_{\text{ambient}} = 0$, in the stress balance boundary condition (Eq 3.4). In the studied experiment, the droplet impacts and then spreads on a solid surface with an initial vertical speed of u_0 = 1.04 m/s. This corresponds to a Weber number, We = 51.2, and a Reynolds number, Re = 26.8 (We = $\frac{\rho {u_0}^2 2R_0}{\gamma_{\text{LA}}}$ and Re = $\frac{\rho u_0 2R_0}{\mu}$, where ρ = 1220 kg/m^3, R_0 = 1.225 mm, γ_{LA} = 0.063 N/m and μ = 116 mPa s). Furthermore, the gravitational force, $\boldsymbol{G}$, in the Navier-Stokes equation (3.3) is neglected since the initial droplet radius, R_0, is smaller than the capillary length, λ_κ ($\lambda_\kappa = \sqrt{\frac{\gamma_{\text{LA}}}{\rho g}}$ = 2.294 mm for the used glycerin/water mixture droplet). Finally, the wettability of the wax substrate corresponds to a Young contact angle, θ_{Y} = 93.5$^{\text{o}}$, which is equivalent to a wetting parameter $w^{\text{LS}} = 5.16 \times 10^3$, given from Eq. 2.50 for C_1 = 12, C_2 = 10, $\sigma = 9 \times 10^{-3}$ and $\epsilon = 8 \times 10^{-3}$. We note that a sensitivity analysis regarding the value of the disjoining pressure parameters is presented in Section C.3.1 of Appendix C.

There are previous studies [7, 8] where the conventional hydrodynamic model has been utilized to simulate the same experiments. Although they do succeed in capturing some of the experimental trends, the above approaches are case sensitive since *ad hoc* correlations are used to model the dynamic contact angle and the shear stresses at the contact lines. In particular, in the first study [7] Sikalo et al. use a semi-empirical correlation given by Kistler [9], whereas in the latter [8] a time variation of the contact angle, based

on experimental measurements, is employed. Here, by using the suggested hydrodynamic formulation, the effective shear stresses have to arise macroscopically due to the micro-scale roughness of the solid surface (note that disjoining pressure induces only normal forces to the liquid-ambient interface (see Eq. 3.15)). Aiming to mimic the intrinsic roughness of the wax surface, we employ an arbitrary roughness topography, which is characterized by two length parameters: a maximum amplitude of the protrusions, h, and an average distance between two neighboring extrema of the surface, d (see Fig. 6.2). The solid surface topography is produced with the following procedure: Initially, an array of random scalars, representing the local extrema of the substrate profile, is drawn from the standard uniform distribution on the interval $(0, h)$ and the distance between them is set equal to d. Next, the final form of the solid topography is obtained by performing a piecewise cubic interpolation [10] on the random extrema of the substrate, ensuring that the substrate profile and its derivatives are continuous. In order to quantify the non-uniform, arbitrary pattern of the solid protrusions we also introduce the surface roughness factor, r_f, which is defined as the ratio of the actual over the apparent surface area ($r_f \geq 1$). The effect of the roughness factor on the spreading dynamics is examined in the following Section.

6.2.1.a The effect of the micro-scale roughness factor

In the cases under study, the intrinsic roughness factor of the modeled surface varies from $r_f = 1$ (for an ideally smooth surface) to $r_f = 1.2$ (for the most roughened solid surface). In the following Sections, when referring, for brevity, to a "smooth" surface we mean an ideally smooth and flat substrate. The solid surface rugosity is parametrized by the average distance of the inhomogeneities, d, (0.012 mm $\leq d \leq 0.06$ mm), and by their maximum height, h, (0.012 mm $\leq h \leq 0.055$ mm). Note that the ratio of the smallest roughness height ($h = 0.012$ mm) over the initial droplet diameter, $2R_0$, is $\frac{1}{204}$.

In Fig. 6.3, we present the temporal evolution of the normalized contact radius, R_s/R_0 (see also Fig. 6.1), for different solid surface roughness cases. In particular, we consider that the contact radius is the position of the outer (or macroscopic) contact line which is defined as the intersection of the droplet surface with a horizontal baseline just above the substrate ($z \approx 4 \times 10^{-3} R_0$). The initial frame, i.e. $t = 0$, is the instance of the droplet impact. The time is presented in dimensionless form and the characteristic time is tu_0/R_0. The surface roughness factor, here, is increased either by decreasing the average distance between the surface inhomogeneities while keeping fixed their maximum amplitude (see Fig. 6.3a), or by increasing their maximum amplitude by fixing their distance constant (see Fig. 6.3b).

Our results show that the spreading behavior is not similar for the different surface roughness cases. The spreading evolves in three stages (see Fig. 6.3):

(I) An early spreading stage, where the radius sharply increases with time (notice the

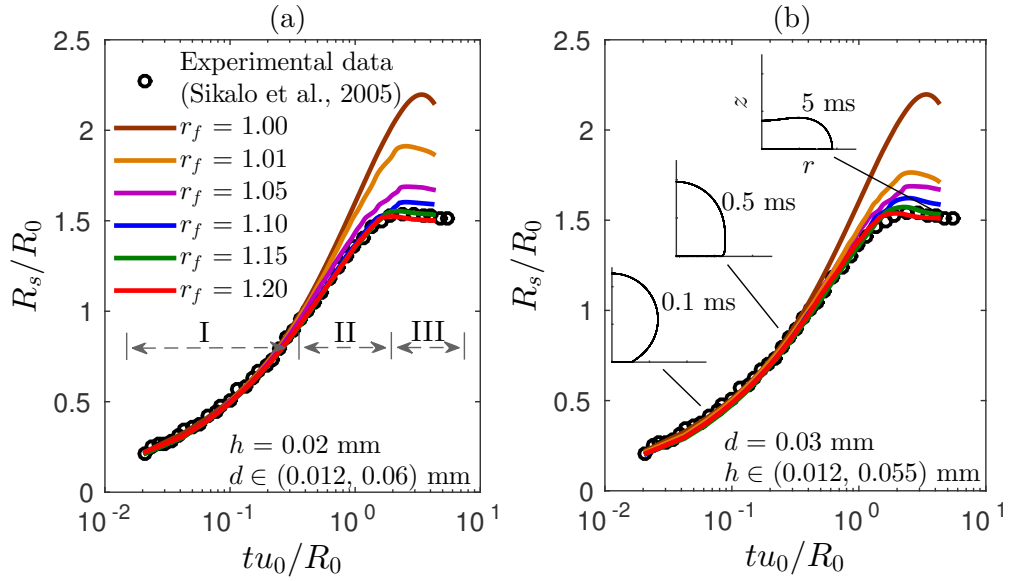

Figure 6.3: Temporal evolution of the normalized contact radius of a glycerin/water mixture droplet impacting on wax surface: simulations against experimental data from Sikalo et al. [6] for different roughness factor cases. The roughness is increased by: (a) reducing the average distance of the inhomogeneities, d, or (b) enlarging the protrusions amplitude, h.

concave part of the curve). At this stage the spreading evolution does not depend on the roughness factor.

(II) An intermediate stage, where an almost linear dependence of the normalized contact radius on the logarithmic characteristic time can be observed. At the end of this stage the effect of the roughness factor is visible. As it can be seen, the more roughened the substrate, the slower the contact radius evolution.

(III) A recoiling stage, where the droplet begins to recede and the contact radius slightly reduces after reaching a maximum value. This effect is particularly visible in the case of the perfectly smooth surface. As it can be observed, at the recoiling stage, the positions of the outer contact line for the smooth and the rough substrate cases significantly differ.

Interestingly enough, the computational results converge to the experimental data, regardless of the geometric details of the substrate, above a certain roughness factor threshold (here for $r_\mathrm{f} > 1.15$). The minor effect of the exact roughness topography (for $r_\mathrm{f} > 1.15$) on the impact dynamics, is an indication that the assumption of the axially-symmetric substrate does not play a key role in the obtained results. We also note that a sensitivity analysis regarding the size of the computational mesh is presented in Section C.4.1 of Appendix C.

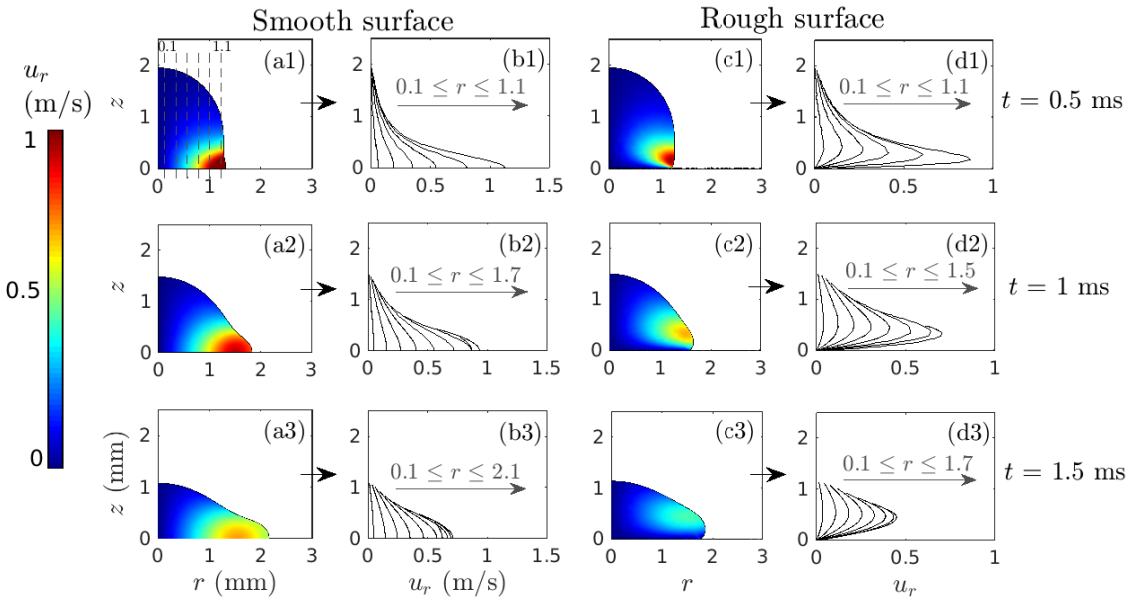

Figure 6.4: Visualization of the r-component of the droplet velocity, u_r, for different roughness factor cases: (a) $r_f = 1$ and (c) $r_f = 1.2$, at various time instances ($t \in [0.5$ ms, 1.5 ms$]$). The u_r distribution is also plotted along vertical, equidistant cut lines (with a δr step of 0.2 mm) for (b) smooth and (d) rough substrate cases.

6.2.1.b Recovering the no-slip boundary condition

Aiming to unravel the effect of the solid substrate roughness on the flow dynamics, we visualize in Fig. 6.4 the r-component of the velocity, u_r, for a droplet spreading on a smooth and a rough solid surface. By plotting the u_r distribution along equidistant cut lines of constant r (see Fig. 6.4d1-d3), it can be observed that the velocity considerably decreases and reaches almost zero, especially very close to the substrate (for $z \to 0$), in the case of the rough surface. This indicates that small variations in the velocity direction, as the fluid slips on the solid asperities, dissipates a considerable amount of energy. Clearly, the total dissipation in the roughness vicinity can approximate a no-slip boundary condition, without imposing directly any shear interaction between the liquid and the solid surfaces. On the contrary, in the absence of an intrinsic surface roughness, the velocity has a finite value on the wall since the energy dissipation is negligible (see Fig. 6.4b1-b3). Note that such a free-slip case is non-realistic since a microscopic slip length has been observed (in molecular dynamics simulations) even for molecularly smooth surfaces due to the discrete nature of the lattice structure of the solids [11]. Here, however, we use this case in order to highlight that the no-slip boundary condition can occur as a solely geometric effect, even at a molecular level. The above is in line with the work of Richardson [3] and Jansons [4].

A magnification of the droplet profile in the vicinity of the solid surface, shown in Fig. 6.5, provides a detailed view of the droplet deformation during the initial spreading stages ($t < 0.5$ ms). The discrepancy between the contact radius at the smooth (Fig. 6.5a) and the rough solid surface (Fig. 6.5b) is visible, especially on the last frame ($t = 0.5$ ms).

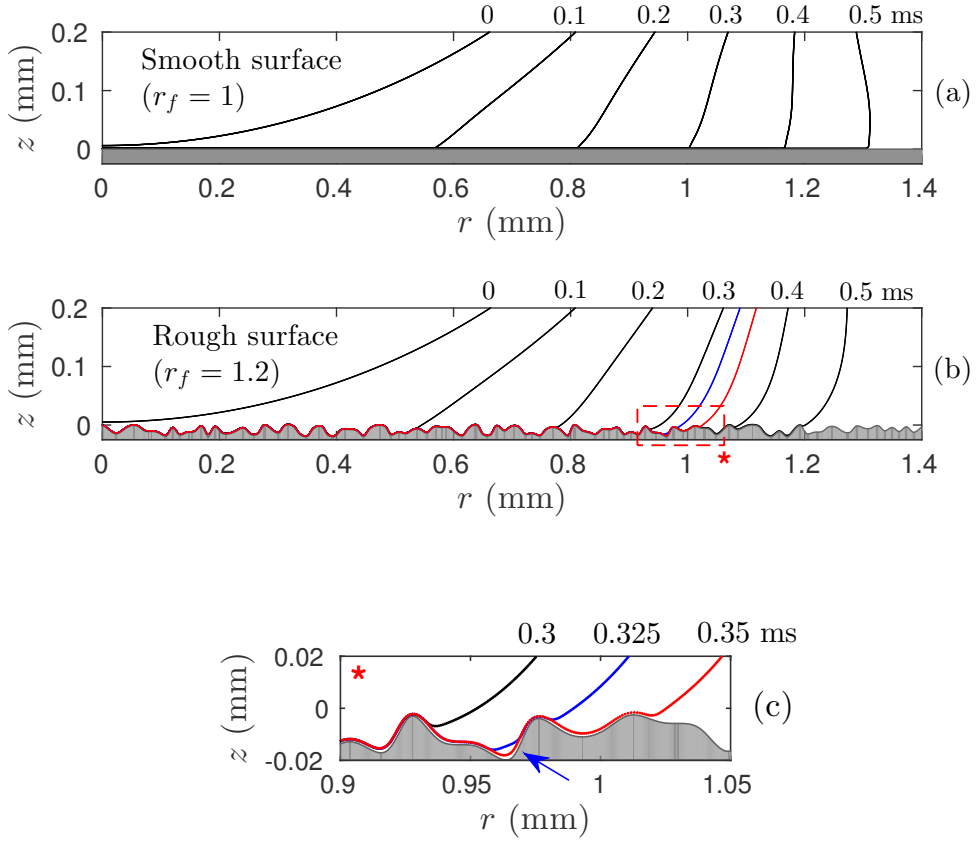

Figure 6.5: Droplet profiles in the vicinity of: (a) a perfectly smooth (r_f = 1) and (b) a rough solid surface (r_f = 1.2) during the initial spreading stages ($t \leq 0.5$ ms). A magnification of the droplet shape, for the area outlined in (b), is depicted in (c) for $t \in [0.3$ ms, 0.35 ms]; changes in the droplet topology (marked by the arrow) can be effectively handled by using our proposed formulation.

The inherent capability of our formulation to handle changes in the droplet topology is presented in Fig. 6.5c. In particular, the formation (t = 0.325 ms) as well as the destruction (t = 0.35 ms) of contact lines can be observed, as the droplet slips on the corrugated substrate. Regarding the evolution of the contact angle, it is noticeable that the two cases (perfectly smooth and roughened substrate) exhibit large differences. We note here that the apparent (or macroscopic) dynamic contact angle, in the conventional hydrodynamic models, is set as a function between the equilibrium (Young's) contact angle and the capillary number, Ca (Ca = $u_{cl}\mu/\gamma_{\mathrm{LA}}$, where u_{cl} is the fluid velocity magnitude at the outer contact line) (see e.g. Eq. 3.10 in Chapter 3), however, in our modeling approach it emerges "naturally" as a result of the local interplay of viscous, capillary and liquid-solid interaction forces. Indicatively, in Fig. 6.6 we present the dynamic contact angle value, θ_{d}, of the droplet for a smooth (r_{f} = 1) and a rough (r_{f} = 1.2) solid surface cases, as a function of time. Unfortunately, as Sikalo et al. [6] claim, the dynamic contact angle measurements are at limited accuracy (the measured values depend on the experience of the experimentalist). Here, we apply their measurement technique in our computational

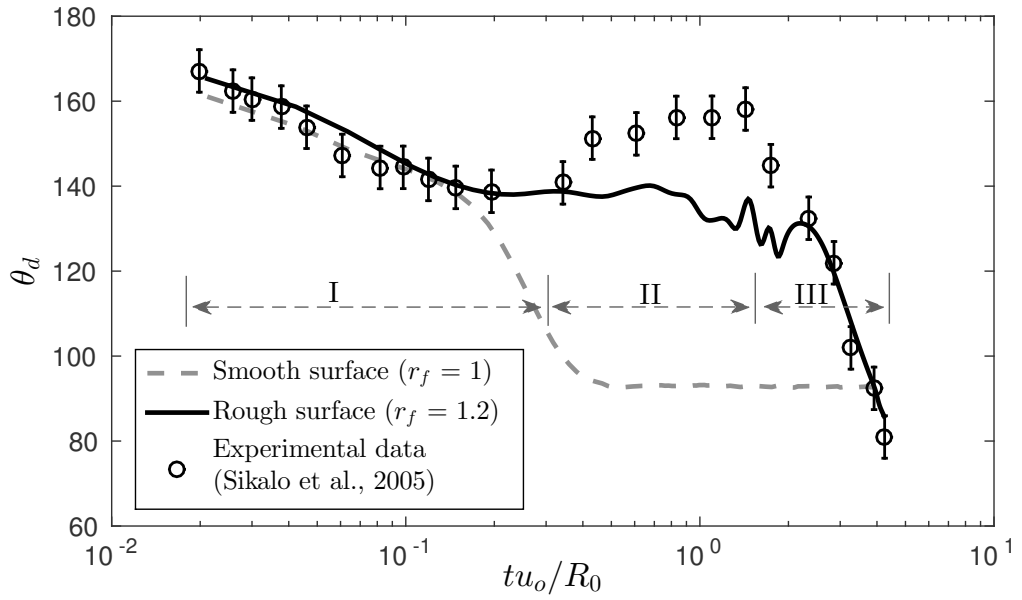

Figure 6.6: Dynamic contact angle, θ_{d}, of a glycerin/water mixture droplet impacting on wax surface: Computations, on a smooth (r_{f} = 1) and a rough (r_{f} = 1.2) solid substrate, are tested against experimental data from Sikalo et al. [6]

predictions (namely to obtain the contact angle from the computed droplet profiles) in order to directly compare them with the experimental measurements. In particular, the slope of the droplet surface is evaluated, against the horizontal plane, at a fixed distance from the substrate ($z \approx 8 \times 10^{-3} R_0$) where the action of the disjoining pressure has been effectively vanished (region III in Fig. C.4b, Section C.3.1).

Our results in Fig. (6.6) show that the early spreading (I) and the recoiling (III) stages are adequately captured, for the case of rough solid substrate. During the intermediate stage (II), however, our results predict fluctuations around a plateau value of the contact angle which can be attributed to the pinning-depinning of the contact lines on the substrate corrugations. This contrasts to Sikalo et al. [6] measurements, where a local maximum of the dynamic contact angle is observed. To our opinion the discrepancy is caused by the relative large height of the roughness protrusions, compared to the droplet size, which highly distorts the droplet shape at the outer contact line. Further decrease of the protrusions length scale, resulting in more realistic roughness structures (e.g. the documented average roughness amplitude for the wax surface is 0.3×10^{-3} mm [6]), although it is feasible in our formulation, it requires extensive computational resources sacrificing the efficiency of the continuum-level modeling. Such a study is beyond the scope of this particular work. When the substrate is ideally smooth, the dynamic contact angle coincides with the Young contact angle ($\theta_{\mathrm{d}} \approx \theta_{\mathrm{Y}} = 93.5^{\mathrm{o}}$) shortly after the droplet impact, indicating again that an amount of roughness is essential in our modeling approach.

Aiming to obtain more insight of the viscous effects resisting the droplet spreading, we next investigate the dissipation of energy during the droplet impact. In particular, we focus on the differences at the energy loss between the case of the ideally smooth and a

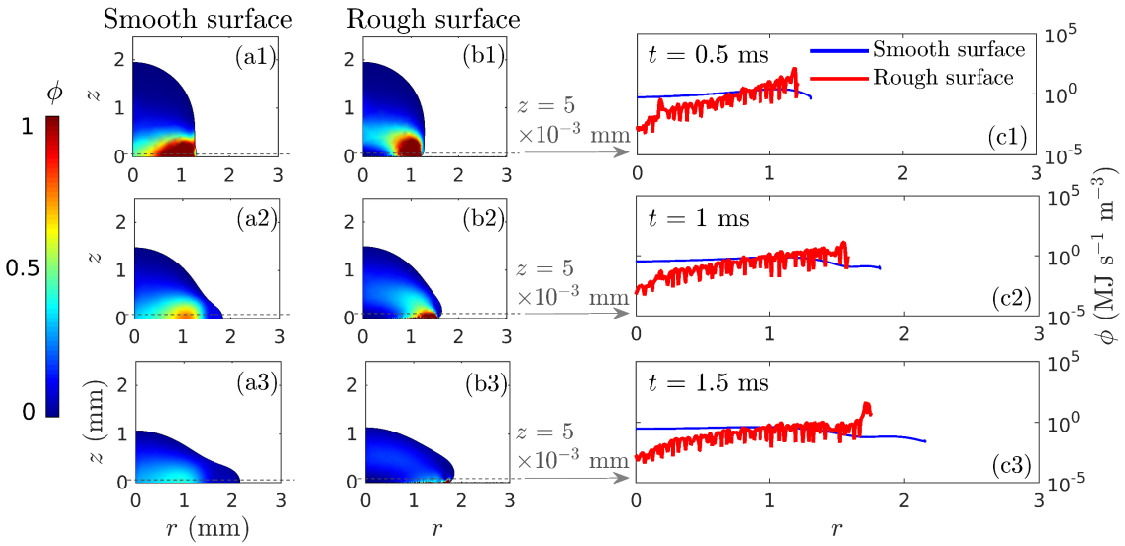

Figure 6.7: Rate of energy dissipation per unit volume, ϕ (given in units $\frac{\text{MJ}}{\text{s m}^3}$), during the impact process on: (a) a smooth solid surface ($r_f = 1$) and (b) a rough solid surface ($r_f = 1.2$), at different time instances ($t \in [0.5\text{ ms}, 1.5\text{ ms}]$). The distribution of ϕ along a line with constant height ($z = 5 \times 10^{-3}$ mm) above the substrate is depicted in the right panel of the figure (c).

roughened solid substrate.

6.2.1.c *Quantifying the rate of energy dissipation*

The energy dissipation can be quantified by calculating the viscous dissipation function, ϕ [12]:

$$\phi = \boldsymbol{\tau} : \nabla \boldsymbol{u}. \tag{6.2}$$

By evaluating the double-dot product and utilizing the symmetry arguments, Eq. 6.2 in cylindrical coordinates, reads:

$$\phi = 2\,\mu \left[\left(\frac{\mathrm{d}u_r}{\mathrm{d}r}\right)^2 + \left(\frac{\mathrm{d}u_z}{\mathrm{d}z}\right)^2 + \left(\frac{u_r}{r}\right)^2 + \frac{1}{2}\left(\left(\frac{\mathrm{d}u_z}{\mathrm{d}r}\right)^2 + \left(\frac{\mathrm{d}u_r}{\mathrm{d}z}\right)^2 + 2\frac{\mathrm{d}u_z}{\mathrm{d}r}\frac{\mathrm{d}u_r}{\mathrm{d}z} \right) \right], \tag{6.3}$$

where u_z represents the z-component of the fluid velocity. In Fig. (6.7), we plot the spatial distribution of ϕ, which practically expresses the rate of energy dissipation per unit volume of the fluid. It is observed that during the spreading process, the initial droplet energy for the rough surface, is mainly dissipated in the vicinity of solid boundary. By examining the distribution of ϕ along a line with constant height $z = 5 \times 10^{-3}$ mm (see Fig. 6.7c1-c3), we find a considerable energy dissipation close to the outer contact line (note that the ϕ values are presented on a logarithmic scale on the right panel of Fig. 6.7). This means that the energy loss, responsible for the spreading deceleration in the rough surface, predominantly occurs at the outer contact line region as a fluid passes over the substrate irregularities. We note that the fluctuations, observed in dissipation function distribution in Fig. 6.7c1-c3, are attributed to the highly inhomogeneous

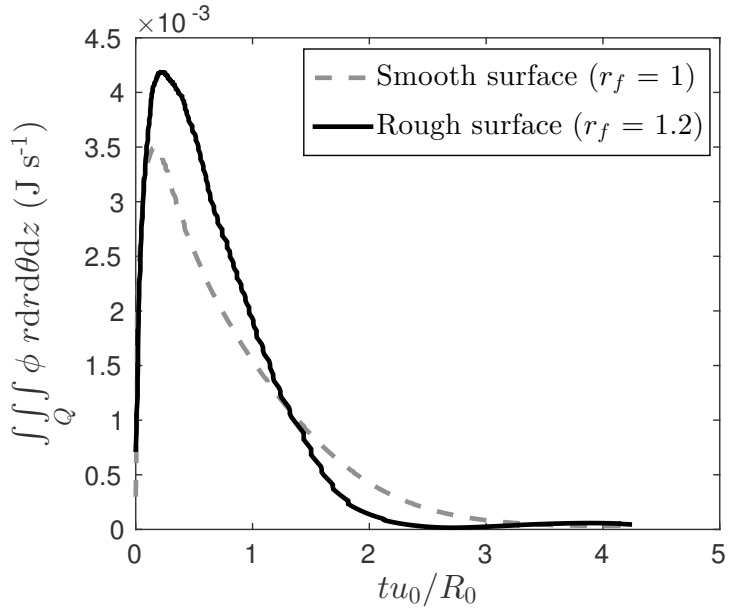

Figure 6.8: Volume integral of the dissipation function in cylindrical coordinates, $\iiint_Q \phi \, \mathrm{d}V_{\text{droplet}} = \iiint_Q \phi \, r\mathrm{d}r\mathrm{d}\theta\mathrm{d}z$, during the spreading process for a perfectly smooth (r_f =1) and a rough (r_f = 1.2) solid surface case. In the expression of the volume element, $r\mathrm{d}r\mathrm{d}\theta\mathrm{d}z$, θ represents the cylindrical azimuthal coordinate ($\theta \in [0, 2\pi)$).

geometrical features of the substrate. Away from the outer contact line, as observed in Fig. 6.7b1-b3, the rate of dissipation is negligible due to the low liquid velocity. When the droplet is spreading on a perfectly smooth and slippery substrate, the energy dissipation is attributed only to the inertial forces resisting the fluid movement. In this case, as demonstrated in Fig. 6.7c1-c3, the dissipation function, ϕ, does not exhibit extreme values along the line parallel to the solid surface at height $z = 5 \times 10^{-3}$ mm, since the effect of the solid substrate is insignificant.

The integration of ϕ over the entire droplet's volume, V_{droplet}, presented in Fig. 6.8, also highlights the differences in the evolution of energy dissipation, for the rough and the smooth substrates, respectively. Specifically, in the rough surface, the overall rate of dissipation is high during the early spreading stages ($\frac{t\,u_0}{R_0} < 1$) followed by a sharp decrease. In the case of smooth surface the energy dissipation is milder. Although the rate of dissipation over time differs significantly between the two cases, a question arises about the relative ratio of the total amount of energy dissipated. Up to the time where the dissipation rate asymptotically gets very small (at $\frac{t\,u_0}{R_0} \approx 4$ or $t = 4.7$ ms) we calculate that the total energy consumed is: $E_{\text{diss}} = \int_0^{4.7\text{ms}} \iiint_Q \phi \, \mathrm{d}V\mathrm{d}t = 4.72 \times 10^{-6}$ J for the rough substrate, and $E_{\text{diss}} = 4.35 \times 10^{-6}$ J for the smooth substrate. The first corresponds to the 75.3 % of the initial droplet energy before impact, E_t, and the latter to the 69.3 %

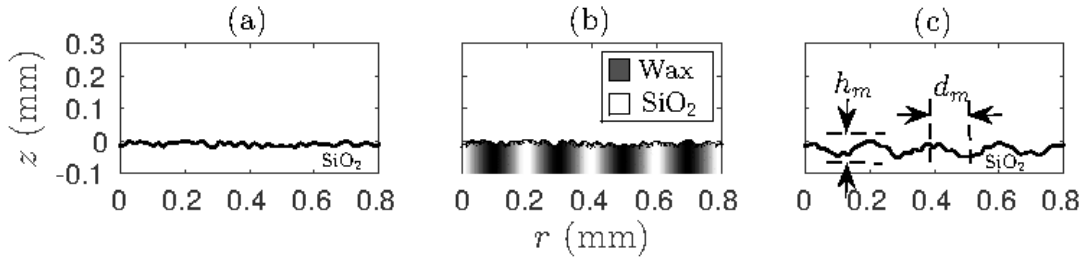

Figure 6.9: Solid substrates featuring: (a) micro-scale textures (r_f = 1.15), (b) micro-scale textures accompanied with chemical heterogeneities and (c) hierarchical roughness with micro- and macro-scale textures.

respectively, where E_t is calculated as:

$$\begin{aligned} E_t = E_k + E_s = \frac{1}{2} M_{\text{droplet}}\, u_0^2 + S_{\text{droplet}}\, \gamma_{\text{LA}} \;\Rightarrow \\ E_t = \rho\, \frac{2}{3} \pi\, R_0^3\, u_0^2 + 4\,\pi\, R_0^2\, \gamma_{\text{LA}} = 6.27 \times 10^{-6}\ \text{J}, \end{aligned} \tag{6.4}$$

with E_k the initial kinetic energy, E_s the initial surface energy, M_{droplet} the droplet's mass and S_{droplet} the surface area of droplet at t = 0. From the above, we conclude that although the overall energy loss is virtually the same, the major differences observed in the spreading behavior on a rough and on a smooth solid surface, are mainly attributed to the locally dissimilar distribution of ϕ close to the outer contact line.

We believe that such an analysis can provide important information for the understanding of energy dissipating phenomena taking place at the contact lines and would contribute in extending our understanding regarding the underlying complex physical mechanism. Finally, we note that the corresponding experimental measurement, of the dissipated energy during the spreading process, is until now unfeasible. In the following Section, we perform computations of droplets spreading on chemically patterned and hierarchical roughened solid surfaces (where an intrinsic surface roughness is superimposed on larger structures) in order to examine a recently proposed argument [13] of a universal droplet evolution regime at the early spreading stages, regardless of the underlying substrate.

6.2.2 Early spreading universality on complex surfaces

6.2.2.a Spreading on different types of surface complexity

The proposed modeling approach can be used to examine the effect of any kind of complex geometrical structure of the substrate (even hierarchical patterned solid surfaces) on the spreading dynamics - an arduous task for the conventional hydrodynamic models. Early time spreading phenomena, on partially or fully wetted substrates, are far from being fully understood [14], since the droplet behavior is affected by inertia, viscous and

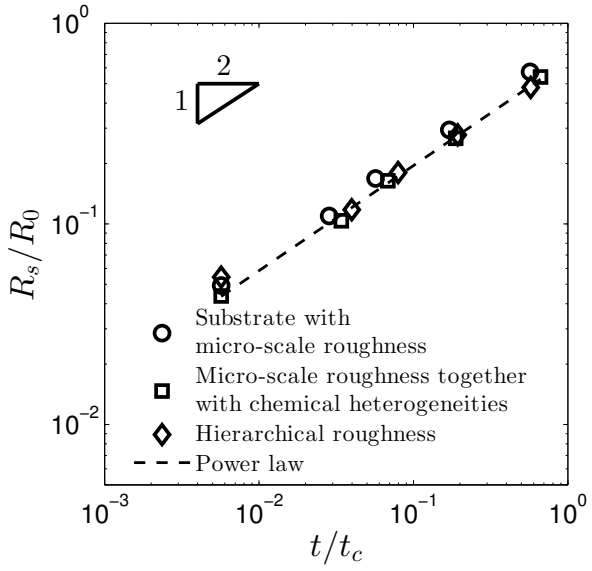

Figure 6.10: Normalized contact radius, R_s/R_0, as a function of dimensionless time from impact, t/t_c, for three different types of solid substrates featuring topographical and chemical inhomogeneities (see Fig. 6.9).

contact line friction effects; for later times, the energy dissipation mechanism is simplified and the dynamics can be adequately captured by the well-established Tanner's law [15], which is also recovered by our model (see C.1 of the Appendix C). In a recent work, Stapelbroek et al. [13], argued that the initial spreading dynamics of low viscosity fluids obey to a universal power law, independently of the geometric or chemical complexity of the solid substrate. Aiming to verify this argument, i.e. the insensitivity of the early spreading dynamics on the substrate's details, we next perform droplet impact computations on different types of solid surfaces, featuring topographical, as well as chemical heterogeneities.

For a perfectly wetting substrate, it has been experimentally observed that the spreading exponent, α, equals to 1/2 [1, 2]. In particular, Eq. 6.1 reads:

$$\frac{R_s}{R_0} = K_s \left(\frac{t}{t_c}\right)^{1/2}. \tag{6.5}$$

The above applies for $t/t_c < 1$, where the dynamics are inertia-dominated. Stapelbroek et al. [13] experimentally demonstrated that the geometrical morphology and the chemical heterogeneities of the substrate are unimportant during the early spreading case. In particular, even if the final equilibrium profiles are different, they argue that there exist an ubiquitous inertial regime where the power law (Eq. 6.5) is applicable. Here, in order to demonstrate this inertial spreading universality, we perform computations of the previously examined glycerin/water mixture droplet spreading on different types of solid surfaces. Indicatively, we examine the effect of geometrical, in conjunction with chemical heterogeneities, on the droplet motion on silicon dioxide (SiO_2) substrates (see

Fig. 6.9). In the first solid substrate case (see Fig. 6.9a), the selected micro-scale (intrinsic) geometrical complexity corresponds to a roughness factor of 1.15, which equals to the minimum roughness required to match the experimental measurements in the case of spreading on a horizontal wax surface (see Fig. 6.3).

Chemical patterns are introduced in the second solid surface case, by alternating the hydrophilic SiO_2 substrate with wax patches (see Fig. 6.9b). Indicatively, the wetting parameter, w^{LS}, varies along the spatial r coordinate, ranging from a minimum (SiO_2) to a maximum value (wax) with a wavelength of 0.2 mm. Note that the wettability of the SiO_2 corresponds to a $\theta_{\mathrm{Y}} = 5^{\mathrm{o}}$, and $\theta_{\mathrm{Y}} = 93.5^{\mathrm{o}}$ for the wax substrate. Lastly, a hierarchical roughened solid surface (see Fig. 6.9c), where the micro-scale intrinsic roughness is superimposed on larger sinusoidal structures (macro-scale roughness), is also investigated. Regarding the hierarchical patterned surface (Fig. 6.9c), the ratio of first to second level roughness amplitude is $\frac{h_m}{h} = 1.7$, whereas the distance of the respective inhomogeneities correspond to a ratio $\frac{d_m}{d} = 6.8$ ($h_m = 0.033$ mm and $d_m = 0.1$ mm). The impact velocity of the droplet is now neglected since the approach speed at the corresponding experiments is extremely low ($u_0 < 20 \times 10^{-6}$ m/s) [13]. Overall, as demonstrated in Fig. 6.10, the evolution of the normalized contact radius, R_s/R_0 is indeed identical for the different types of surface complexity during the early stage of spreading ($t/t_c < 1$). The results are plotted in logarithmic scale so as to demonstrate the power law (Eq. 6.5) growth dynamics of the early spreading inertial regime.

6.2.2.b Universal spreading mechanism

In order to interpret the minor role of the underlying substrate to the spreading dynamics, we examine the normal component of the stress balance along the liquid-ambient interface (Eq. 3.4) which reads:

$$\Delta p = \tau_{\mathrm{nn}}|_{\mathrm{liquid}} + 2\,\gamma_{\mathrm{LA}}\,\kappa + p^{\mathrm{LS}} = 0, \tag{6.6}$$

where $\kappa = \frac{C}{2}$. By disregarding the viscous stress components of the above equation, due to the negligible impact velocity, the stress balance along the droplet surface (Eq. 6.6) for the early spreading stage can be approximated by:

$$\Delta p \approx 2\,\gamma_{\mathrm{LA}}\,\kappa + p^{\mathrm{LS}}. \tag{6.7}$$

When the droplet equilibrates, the pressure difference between the liquid and the ambient medium, Δp, is maintained constant along the effectively one-dimensional droplet surface. In our case, however, the calculation of the right hand side of Eq. 6.7, $2\,\gamma_{\mathrm{LA}}\,\kappa + p^{\mathrm{LS}}$, along the entire droplet profile at the time instance just after impact ($t = 5 \times 10^{-2}$ ms), shows a significant deviation from a constant value, localized in the vicinity of the solid surface. This results to a local pressure drop, close to the solid substrate region, as illustrated in Fig. 6.11. Namely, the highly negative disjoining pressure value

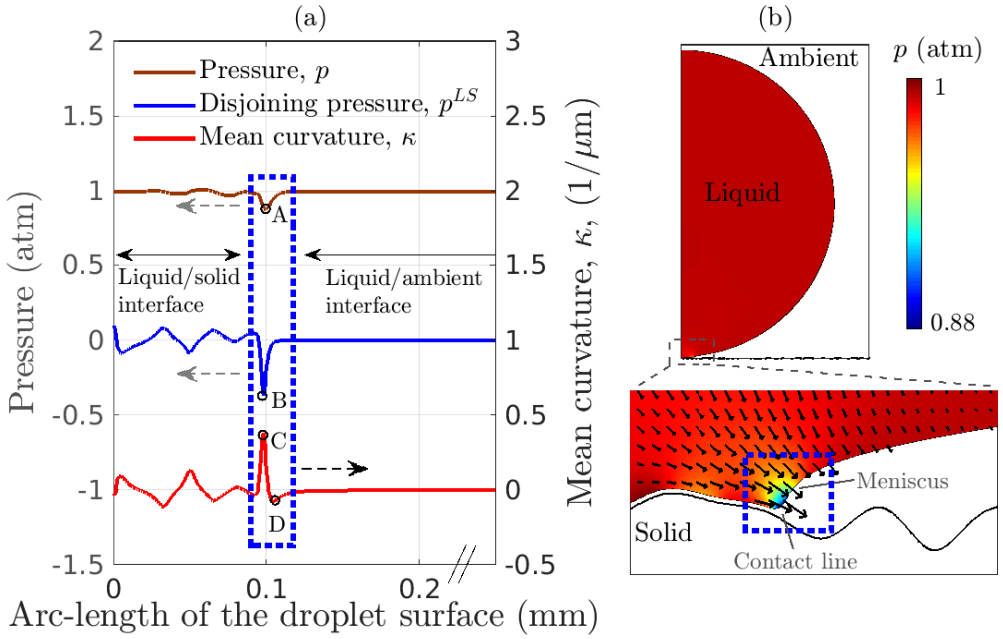

Figure 6.11: (a) Mean curvature, κ, (right axis) and pressure (left axis) values along the effectively one-dimensional droplet surface just after the contact ($t = 5 \times 10^{-2}$ ms) with a rough ($r_f = 1.15$) SiO_2 substrate. (b) Visualization of the pressure, p, distribution for the entire droplet and a magnified region close to the outer contact line. The arrows at the latter sub-figure represent the fluid velocity field, $\boldsymbol{u}$.

at the outer contact line (equals to the depth of the Lennard-Jones potential well; see Eq. 2.42) (point B in Fig. 6.11a) is not compensated by the surface tension forces, $2\,\gamma_{LA}\,\kappa$, even though κ reaches a peak value (point C in Fig. 6.11a). This unbalanced surface force generates a pressure gradient inside the droplet (see point A in Fig. (6.11a)), which drives the initial liquid motion over topographical or chemical inhomogeneities, annihilating the role of the substrate. At equilibrium, the pressure difference between the liquid (p) and the surrounding medium (p_0), $\Delta p = p - p_0$, should approach zero since the extremely small Young contact angle ($\theta_Y = 5^o$) drives the droplet into a liquid film. This yields to: $p^{LS} = -2\,\gamma_{LA}\,\kappa$, at SQ, from Eq. 6.7. Previous theoretical attempts to explain the spreading insensitivity on the roughness structure [16, 13] suggest that the strong curvature induced at the liquid meniscus, connecting the droplet and the substrate (see Fig. 6.11b), is the origin of the pressure difference. However, in our detailed analysis, by examining the entire droplet surface, we conclude that the curvature of the meniscus does not have a major contribution; contrariwise the key factor is the increased curvature at the three-phase outer contact line. Specifically, we calculate that just after the droplet contacts the substrate ($t = 5 \times 10^{-2}$ ms), the absolute curvature value of the liquid meniscus equals to 7.8×10^{-2} μm^{-1} (point D in Fig. 6.11a) whereas the corresponding value at the outer contact line is larger and equal to 38×10^{-2} μm^{-1} (point C in Fig. 6.11a).

As previously discussed, experimental studies show that the spreading exponent α and the prefactor K_s in Eq. 6.1 depend on the fluid properties and the solid wettability [2]. Due to the recent development of lab-on-a-chip devices though, there is a need to influ-

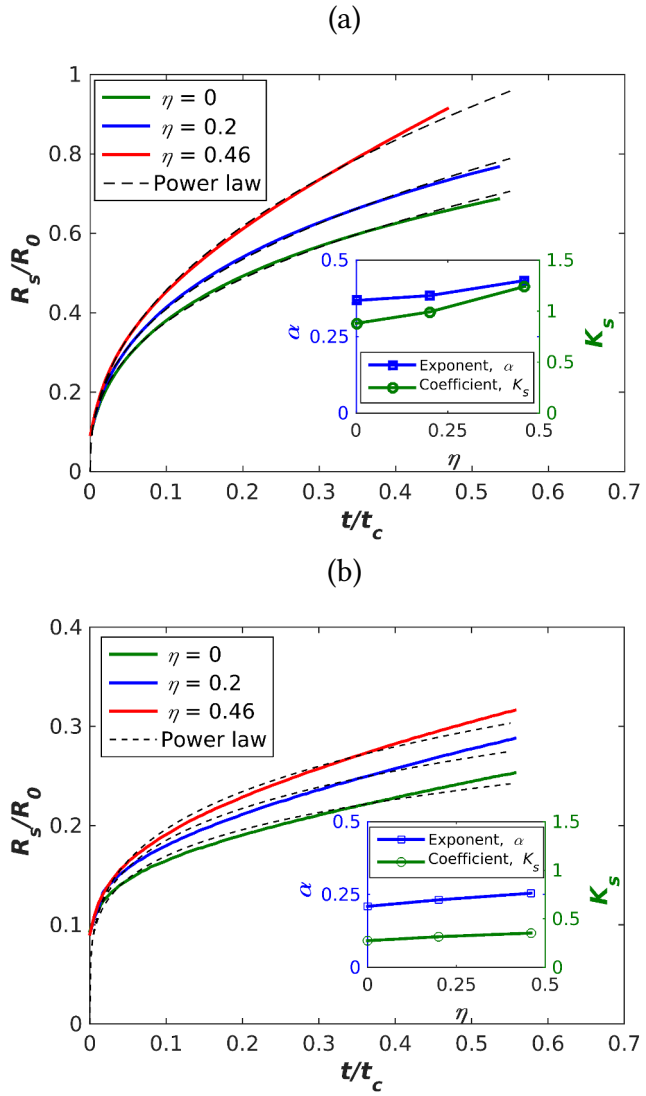

Figure 6.12: Temporal evolution of the normalized contact radius of (a) a water and (b) a glycerin droplet spreading, under the influence of electrostatic forces, on a hydrophobic substrate (θ_Y = 114°). The spreading exponent, α, and the power law prefactor, K_s, (of Eq. 6.1) vs the electrowetting number, η, are presented in the insets.

ence these parameters in order to control the spreading dynamics. The use of an external potential (e.g. electrowetting phenomenon which is described in Chapter 5) can overcome these limits, offering a more precise control on the spreading dynamics. Next, we perform a systematic study of such electrospreading dynamics of axisymmetric droplets on smooth as well as structured solid surfaces.

6.3 Electrostatically assisted spreading

In this Section, we study the electrostatically assisted spreading (by utilizing the electrowetting phenomenon) of conductive (aqueous) droplets on smooth as well as structured (even with arbitrary roughness) hydrophobic surfaces (θ_Y = 114°). The effect of the

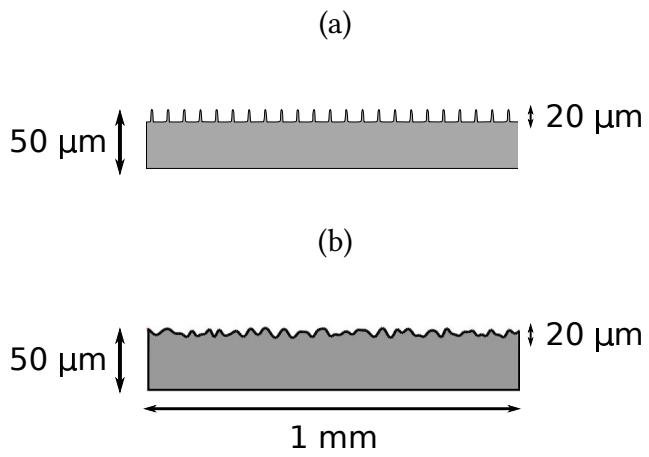

Figure 6.13: Geometric characteristics of (a) a concentric rings-structured and (b) an arbitrary roughened topography. The roughness factor corresponds to $r_f = 2.21$ for (a) and $r_f = 1.21$ for (b), respectively.

electric field is incorporated through an electrostatic pressure term, p_{el} (see Section 5.2.1), which acts on the liquid surface, with a negative contribution to the total pressure [17]. The modified normal stress component of the interface force balance (Eq. 3.4) then would read:

$$\Delta p = \tau_{nn}|_{liquid} + \gamma_{LA}\, C + p^{LS} - p_{el} = 0. \tag{6.8}$$

In the above, the electrostatic pressure, $p_{el} = \frac{\epsilon_0 E^2}{2}$, is calculated from the solution of the electrostatics equations (5.3) in the air ambient and the solid dielectric, by accounting for the boundary conditions 5.4-5.7 and without making any simplification regarding the droplet shape. Finally, similarly to the solution procedure presented in Section 3.2.3, the set of Eqs. 3.3, 5.3 and 3.6 is discretized using the finite element method and integrated in time using the implicit Euler method. The extra unknown here is the electric field distribution, u, around the droplet, as also described in the static electrowetting simulations in Chapter 5. The above model has been implemented in COMSOL Multiphysics® commercial software.

6.3.1 Glycerin droplet on a smooth substrate

We initially study the electrospreading dynamics of an conductive droplet on a smooth solid dielectric substrate. In Fig. 6.12 we depict the normalized spreading radius just after contact with the surface, R_s/R_0, of (a) a water (ρ = 1000 kg/m^3, R_0 = 1.25 mm, γ_{LA} = 0.072 N/m and μ = 1.002 mPa s) and (b) a glycerin droplet (ρ = 1261 kg/m^3, R_0 = 1.25 mm, γ_{LA} = 0.063 N/m and μ = 1.412 Pa s). The thickness of the dielectric material (Teflon® coated silicon dioxide) is d = 50 μm and ϵ_d = 4.2 for both cases. By fitting Eq. 6.1 to the computational results presented in Fig. 6.12, we observe that the spreading exponent, α, and the prefactor, K_s, get higher values by increasing the electric potential difference between the drop and the base electrode. Such an argument is in qualitative agreement with electrospreading experiments of aqueous droplets on both hydrophilic

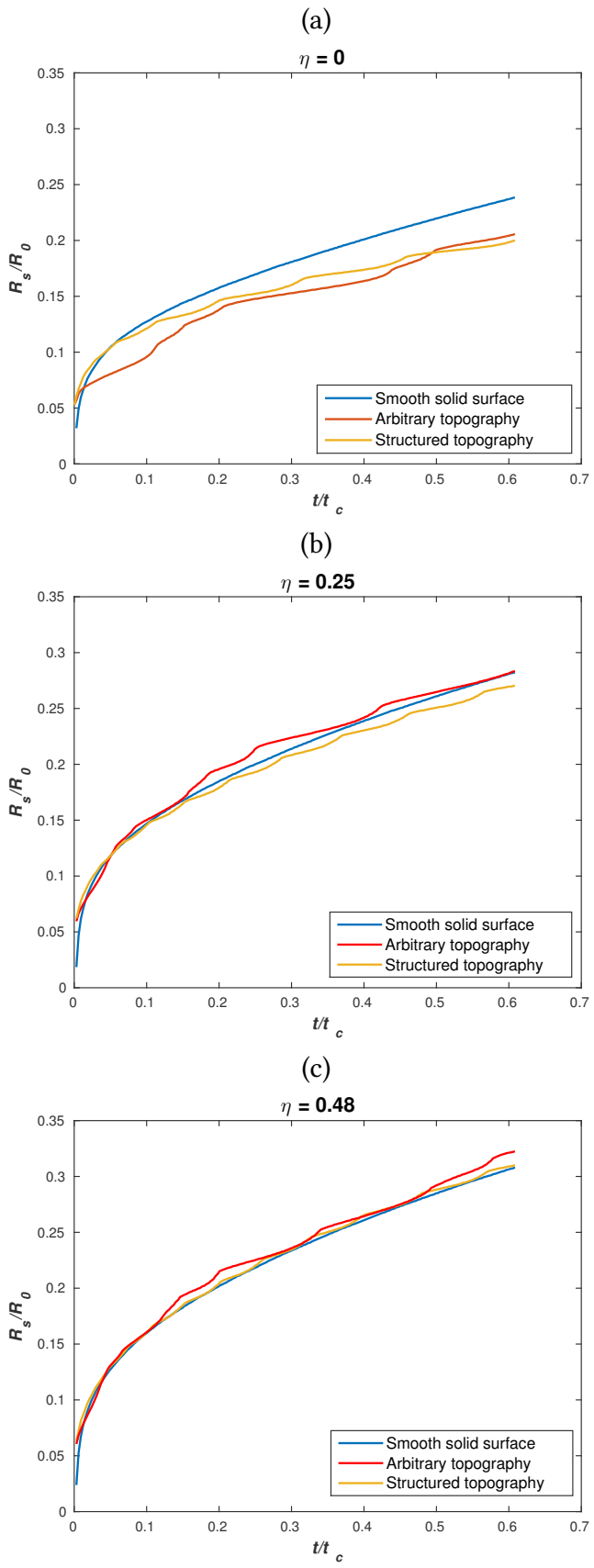

Figure 6.14: Temporal evolution of the normalized contact radius of a glycerin droplet on different kind of hydrophobic substrates (smooth with the blue line, arbitrary roughened with the red line and concentric rings-structured with the orange line) (see also Figure 6.13) for various electrowetting numbers (η = 0, 0.25 and 0.48).

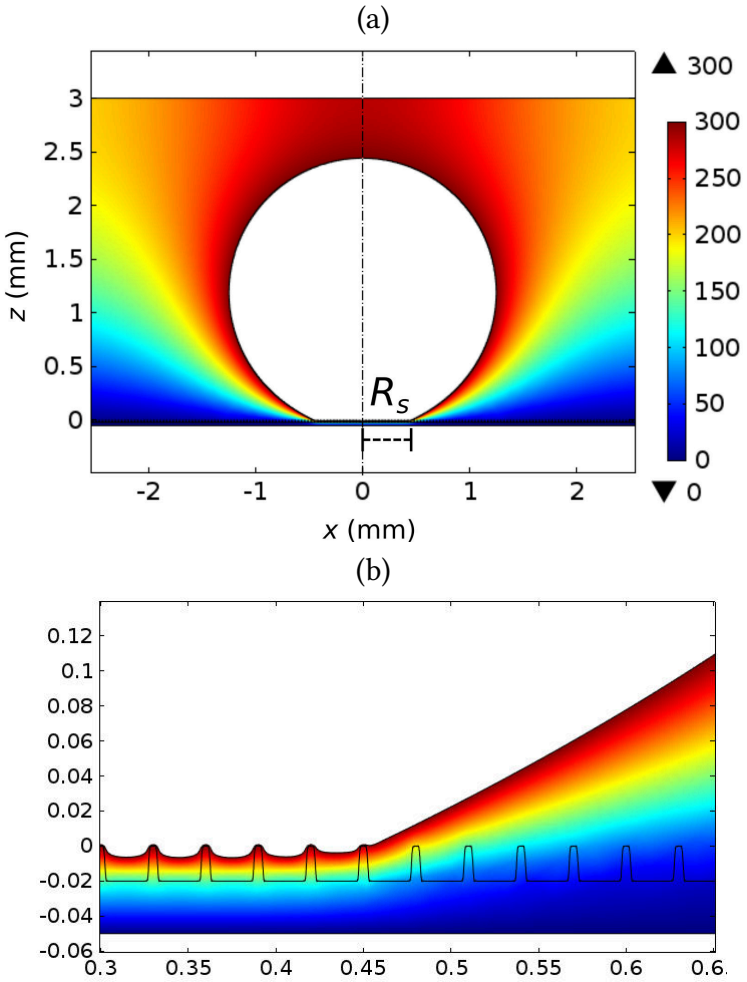

Figure 6.15: (a) Electric potential, u, distribution of a spreading glycerin droplet on a concentric rings-structured solid surface (at t = 5 ms in Fig 6.14c, with V = 300 V). A magnification of the droplet profile in the vicinity of the solid surface is presented in (b).

and hydrophobic solid surfaces [18, 19].

6.3.2 Glycerin droplet on rough substrates

In this section we examine the electrospreading dynamics on concentric rings-structured as well as arbitrary roughened solid surfaces. The geometric details of these two cases are demonstrated in Fig. 6.13. Our results, in Fig. 6.14, show that the topography of the substrate strongly affects the capillary spreading dynamics (for $\eta = 0$). In particular, the spreading on rough solid surfaces is found to be slower as compared to the spreading on a flat solid surface due to viscous dissipation on the roughness protrusions. When voltage is applied ($\eta > 0$), the role of the substrate morphology is downgraded since the electrostatically enhancement of the liquid momentum lowers the effect of viscous dissipation. Finally, the profile of an glycerin droplet spreading under the effect of electric field, as well as a detailed view of the droplet shape close to the solid protrusions, at t = 5 ms is presented in Fig. 6.15.

6.4 Summary and conclusions

Aiming to validate our augmented hydrodynamic model formulation (presented in Section 3.2.3), we examined the dynamic behavior of a axisymmetric droplets spreading on a horizontal surface. We found that when enhancing the micro-scale intrinsic roughness of the solid surface, our results gradually converge to the experimental measurements. Interestingly enough we demonstrated that local viscous forces, which are generated at the solid surface roughness length scale, give rise to effective (macroscopic) shear stresses resisting the droplet deformation. The above is accompanied with a substantial energy loss at the outer contact line in the case of a roughened substrate, contrary to an ideally smooth solid surface, as noticed by visualizing the local rate of energy dissipation.

By studying the initial spreading behavior of a droplet on highly complex -hierarchically and/or chemically patterned- solid surfaces, we found that there always exists an inertia-dominated, initial stage, where the contact radius evolution is independent of the underlying solid substrate complexity. During this time interval, the spreading dynamics can be well approximated by a universal power law (Eq. 6.5). This argument is in remarkable agreement with experimental observations performed by Stapelbroek et al. in a recently published work[13]. After the initial spreading stage, the only factor that limits the dynamics is the viscosity of the liquid; this slow spreading regime can also be captured by our model, in agreement with Tanner's law [15]. The contact line dynamics of a droplet spreading under the influence of electric field (by using the electrowetting phenomenon) has been also examined. In particular, we observed that an increase in the voltage between the base electrode and the droplet induces a growth in the spreading exponent of the power law (Eq 6.1), in qualitative agreement with experimental findings [19]. We also, for a first time, investigated the effect of the solid roughness on electrospreading dynamics. We found that the effect of solid topography on the spreading dynamics is important at low voltages, however, the droplet motion is insensitive to the geometric details of the substrate at high voltages.

Regarding the future perspectives of modeling, we note that our computations would enable the derivation of an overall energy dissipation term (including all the micro-scale dissipation phenomena taking place on the solid roughness) as a function of the outer contact line velocity. Such a phenomenological approach, which is a subject of ongoing research, could greatly simplify the computations since the complex roughness geometry could be replaced by a flat boundary featuring the same friction properties; different roughness scales can also be simulated in this way. These kind of approximations are already used in modified hydrodynamic models [20] as well as in phase-field computations [21, 22], where the microscopic interactions at a contact line are incorporated through a single friction parameter. The proposed modeling approach is however advantageous over these methodologies when dealing with complex surface topographies.

CHAPTER 7

Passive droplet motion on asymmetrically patterned surfaces

Asymmetrically patterned surfaces appear in many living organisms. An interesting example is the ratchet-like structures of the Morpho aega butterfly wings which help to keep water droplets away from its body, thus enhancing the flying stability. Here, we investigate the mechanisms of droplet motion on inclined as well as oscillated (horizontally or vertically) asymmetrically structured substrates. Our results show that the imbalance of capillary forces leads to a preferential direction of motion. In particular, the directionality is regulated by the ratios of capillary retention forces (that impede movement) in opposing directions. We demonstrate that the solid structure asymmetry can be exploited in order to passively transfer droplets in miniaturized devices and we also perform a parametric study, by varying the roughness parameters, in order to maximize the migration velocity.

7.1 Droplet actuation on asymmetric surfaces

As discussed in Section 1.2.3, the selection of the optimal actuation type for handling a sessile droplet in lab-on-a-chip devices is of utmost importance for modern applications. Several techniques have been proposed like the electrowetting effect [23] (see also Chapter 5), thermocapillary convection [24], the Leidenfrost phenomenon (where a droplet can levitate on a cushion of vapor when brought in contact with a hot solid) [25, 26] or even acoustic fields [27]. In addition, droplet handling can be achieved by a combination of vertical and horizontal substrate vibrations which result, due to their phase difference, in the breaking of the droplet axial symmetry [28, 29, 30, 31]. Recently, it has also been demonstrated that the uni-directional droplet transport can be facilitated on surfaces featuring anisotropic wettability (with asymmetric micro-structures), even if the micro-device is operating under non-stationary conditions [32, 33, 34, 35]. The latter case actually requires only one driving oscillation, since the symmetry breaking occurs due to the anisotropy of the solid substrate.

The concept of fabricating surfaces with anisotropic wettability originates from living organisms. In particular, Zheng et al., in a milestone work [36], found that the wings of

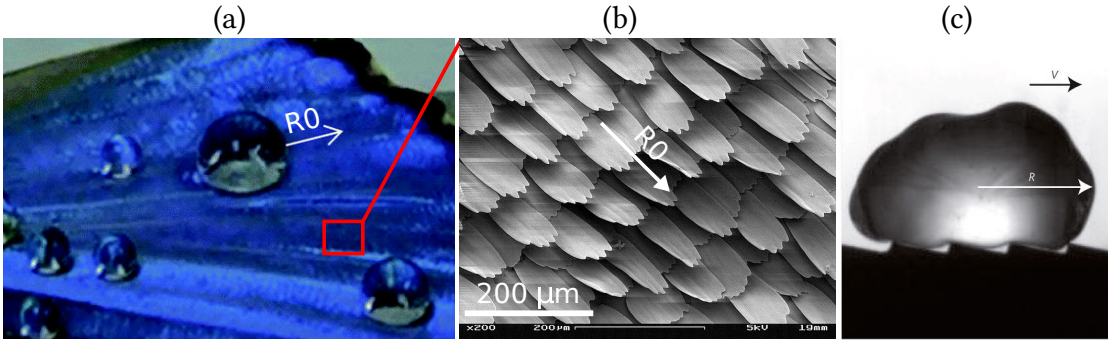

Figure 7.1: (a) Directional droplet motion (along the direction toward the corrugations tilt, RO) on superhydrophobic butterfly wings (reprinted from [45]). Details of the asymmetric solid structure are presented in (b) (CC BY-SA 3.0). (c) Self-propelling ethanol droplet (with a radius R = 3 mm), moving in the direction opposing the corrugations tilt, on a hot ratchet (with temperature 350°C) (reprinted from [25]). The latter is known as Leidenfrost phenomenon, where the droplet levitates on a cushion of its own vapor.

the *Morpho aega* butterfly are covered by asymmetric ratchet-like structures, exhibiting directionally biased wetting. The above causes droplets deposited on the wings to roll off along the outward direction (and not toward its body), providing flying stability for the butterfly, which lives in the humid rainforest. A plethora of similar structure morphologies, that can directionally control the movement of droplets, have been also discovered in living nature (e.g. shark and lizard skin, spider silk) [37, 38, 39], inspiring the design of asymmetrically structured substrates in order to handle small amounts of liquid [40, 41, 42, 43, 44], as also discussed in Section 1.2.3 of Chapter 1.

Determining the preferable motion direction on an asymmetrically patterned surface is, however, still an ambiguous issue in the literature, since it is affected by the local forces applied in the vicinity of the contact lines. In particular, a droplet moves to the direction toward the corrugations tilt on the butterfly wings [46] (see Fig. 7.1a, b) whereas it self-propels to the opposite direction when deposited on a hot ratchet due to the vapor escape below the droplet (Leidenfrost phenomenon [25]) (see Fig. 7.1c). In addition, opposing motion directions of droplets on asymmetrically structured, vibrating substrates were considered in published experiments [33] and simulations [35]. From the above it is clear that different driving forces may exist, originating from competing mechanisms.

In this Chapter, we aim to extend our understanding regarding the driving mechanism and the dynamic behavior of a droplet on asymmetrically micro-structured substrates, by using the proposed sharp-interface, continuum-level formulation. In particular, we provide predictions regarding the migration velocity and the (dynamic) contact angle hysteresis under the effect of gravity (by tilting the solid surface, as depicted in Fig 7.2a) or a periodic force induced by oscillating the bottom plate either in the vertical (see Fig 7.2b) or horizontal direction (see Fig 7.2c). The effect of the solid structure length scale on the droplet motion is also investigated. Our goal here is to maximize the migration velocity of the droplet by understanding the role of the structure asymmetry on the liquid transfer process. Such a task has a great practical importance in designing and

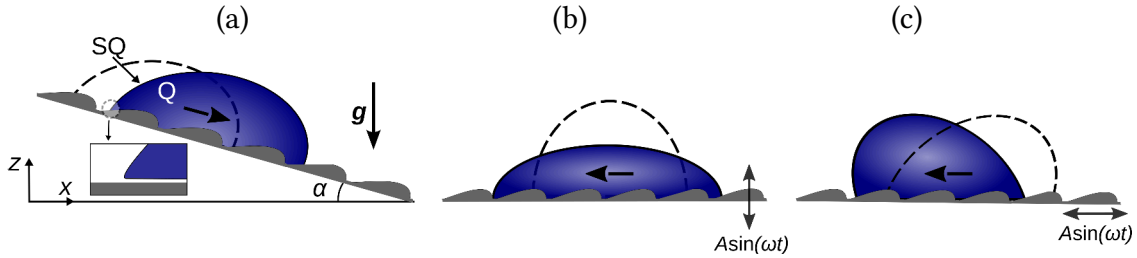

Figure 7.2: Schematic of a droplet: (a) sliding, and moving on a (b) vertically, or (c) horizontally oscillated, asymmetrically structured substrate, where, A, is the oscillation amplitude and ω the angular frequency (notice that droplet and surface features are not shown in the same scale).

optimizing modern miniaturized devices (see also Section 1.2.3 of Chapter 1).

7.2 Results

We begin our study by examining the flow dynamics of a glycerin/water mixture droplet (85% of glycerin, ρ = 1275 kg/m^3, R_0 = 1.5 mm, γ_{LA} = 0.07 N/m and μ = 116 mPa s) sliding on inclined surfaces with different topographies (both symmetrically and asymmetrically structured). Then we study the effect of solid vibration on the movement of droplets on asymmetrically structured surfaces. Here, we consider translational symmetry along a direction perpendicular to the xz-plane (see Fig. 7.2). Moreover, similarly to the previous Chapter 6, the flow problem is solved only for the droplet interior (Q in Fig. 7.2). We have selected the glycerin/water mixture droplets (instead of water droplets) so as to minimize the inertial effect and highlight the role of the solid surface asymmetric structure. Considering that the disjoining pressure parameters (see Eq. 2.42) do not significantly affect the obtained results (the details of the disjoining pressure profile have a negligible effect on the droplet shape, as discussed in the sensitivity analysis presented in Section C.3.2 and C.3.3 of Appendix C), we selected their values in accordance with the previous Chapters (see 4 and 5), namely: C_1 = 12, C_2 = 10, $\sigma = 9 \times 10^{-3}$ and $\epsilon = 8 \times 10^{-3}$. In addition, in order to account for the liquid-solid friction, even on macroscopically smooth solid surfaces, we have selected a slip parameter value (see Eq. 3.17) of the order of the scaled inverse minimum distance (R_0/δ_{min}), as also discussed in Section 3.2.3 of Chapter 3. Specifically, $\beta_{LS} = 10^3$. We note that the flow dynamics remain practically unaffected beyond this large β_{LS} value, as demonstrated in [47] (in an analogy to the converging curves of the spreading radius versus time, by increasing the roughness factor in Fig. 6.3).

The heterogeneity of problems which are examined in the current Chapter (involving sliding, and vibrated droplets) renders difficult the definition of particular characteristic quantities and thus we prefer to present the results of our simulations in dimensional form. This is by no means restrictive since dimensionless groups are introduced where deemed necessary to draw conclusions on the importance of different physical mechanisms. Finally, we note that a sensitivity analysis regarding the size of computational

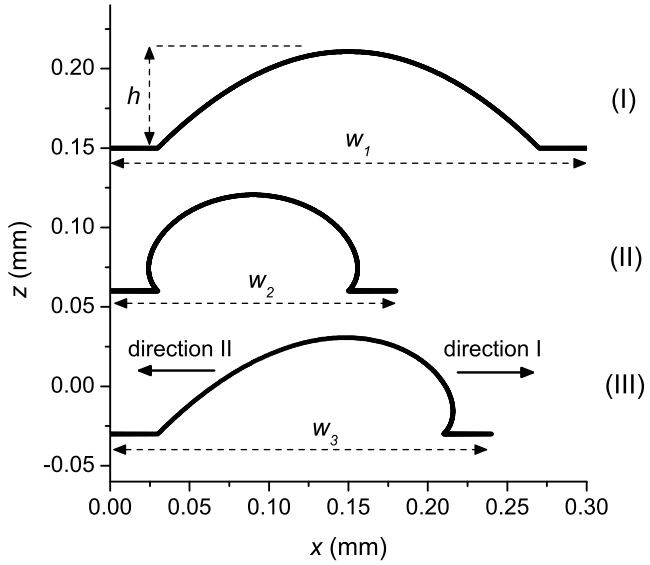

Figure 7.3: Unit structure of the different substrate cases. The elementary corrugation of the asymmetric surface (III) is a combination of the basic structure of the two symmetric surfaces (I, II).

mesh can also be found in Section C.4.2 of Appendix C.

7.2.1 Droplet sliding on inclined structured surfaces

We initially examine the mobility of a droplet on two kinds of textured substrates, favoring either the Wenzel (the droplet fully penetrates the micro-structure [48]) or the Cassie-Baxter (air pockets are trapped in the micro-structure [48]) wetting state. In particular, as observed in Fig. 7.3, we consider:

1. a symmetrically structured striped surface (symmetric surface I) featuring smooth protrusions of width $w_1 = 0.3$ mm that favors the Wenzel wetting state,
2. a symmetrically structured striped surface (symmetric surface II) with mushroom like cross-sectional shape that promotes the Cassie-Baxter wetting state. In this case the width of the stripes, w_2, is 0.18 mm.

The roughness factor, defined as the ratio of the actual over the apparent surface area, is evaluated to be approximately equal to $r_f = 1.12$ for the symmetric surface I and and $r_f = 1.49$ symmetric surface II, respectively. Our main objective, however, is to study the droplet dynamic behavior on an asymmetrically structured surface. The asymmetric surface is formed by merging the halves of each symmetric unit structure studied in our previous work. Then a hybrid structure of width, $w_3 = 0.24$ mm, arises (III in Fig. 7.3). The height of the protrusions is identical for the three structures, $h = 0.06$ mm; Note that the ratio of the height, h, over the initial droplet diameter, $2R_0$, is $\frac{1}{50}$. We also consider that the solid material is hydrophobic ($\theta_Y = 130^o$).

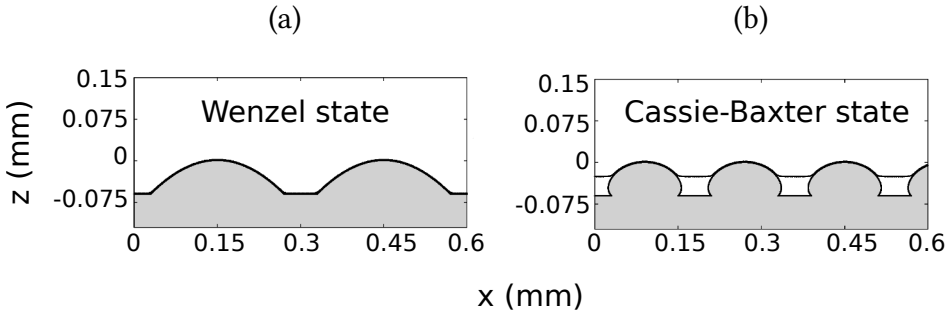

Figure 7.4: Magnification of an equilibrium droplet profile on a solid substrate which promotes (a) the Wenzel wetting state (symmetric surface I) and (b) the Cassie-Baxter wetting state (symmetric surface II).

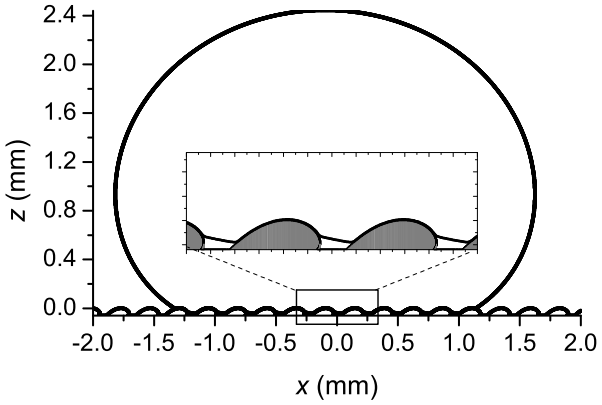

Figure 7.5: Equilibrium profile of a glycerin/water mixture droplet on an asymmetrically patterned surface with $\theta_Y = 130^o$.

Our computations showed that the liquid has impaled the solid roughness in the case of symmetric surface II (see a magnification of the equilibrium droplet profile in Fig. 7.4a), whereas the droplet sits on top of the protrusions minimizing the contact between the liquid and the solid surface in the case of symmetric surface II (see Fig. 7.4b). Regarding the asymmetric surface, we observe that the droplet rests on a Cassie-Baxter state (see Fig. 7.5), where, however, the liquid meniscus between the protrusions is inclined (see the inset of Fig. 7.5).

We continue by investigating the behavior of a droplet sliding on an inclined symmetrically structured substrate. In particular, in a virtual experiment, starting from the equilibrium state (at $t = 0$ the inclination angle is $\alpha = 0^o$) the droplet is inclined at $\alpha = 60^o$. Naively, one would expect that the droplet mobility would decrease in the case of high r_f value since we would expect that viscous dissipation would be more enhanced on a rougher surface. However, in Fig 7.6 we observe that the presence of air pockets trapped in the solid structure (Cassie-Baxter wetting state) leads to an increased mobility of the droplet as it slides on the inclined symmetric surface II. The above argument was also in qualitative agreement with experimental observations [49]. Additionally, we also examine the dynamic behavior of a droplet sliding in the different directions of an asymmetrically structured surface. In particular, we now tilt the left end of the substrate either

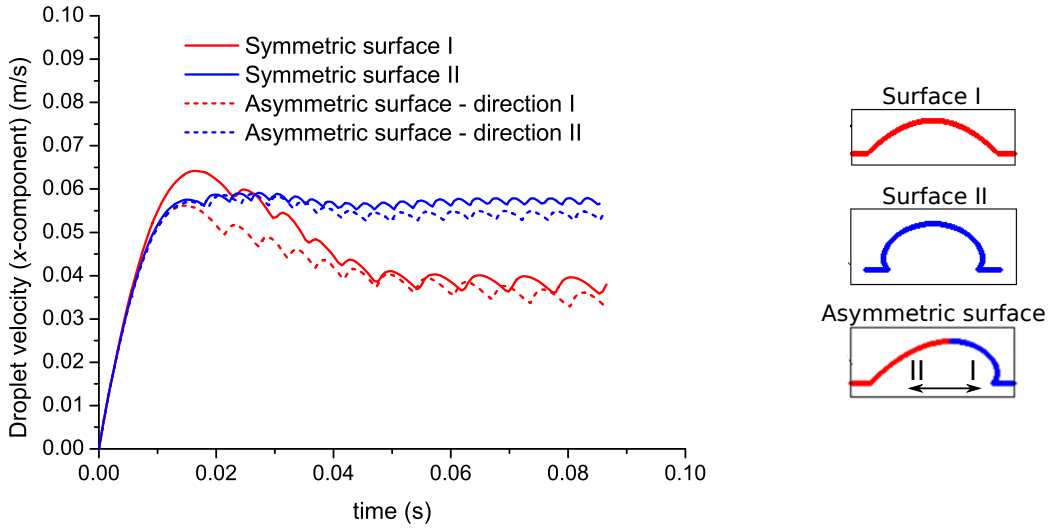

Figure 7.6: Temporal evolution of the average x-component of the velocity for a glycerin/water mixture droplet on different kinds of solid surfaces. The two different motion directions for the asymmetric solid surface are presented with dashed lines of different color (red - direction I, blue - direction II). The unit structure of the different surfaces is depicted in the right part of the figure. We note that the absolute value of the velocity is used in the case where the droplet is moving in the negative direction (II).

upwards or downwards, as presented in Fig. 7.7. In the first case (for inclination angle α = 60^o) the droplet moves to the right (toward the direction of the corrugations tilt), defined as direction I, whereas in the latter case (α = -60^o) the droplet moves to the left (opposite to the direction of the corrugations tilt), which is defined as direction II (see also Fig. 7.3). Interestingly enough, in Fig 7.6 it is observed that the droplet exhibits different migration velocities, according to the direction of motion on the asymmetrically structured substrate. An illustrative example is presented in Fig. 7.7, where, for the same period of time (t = 0.1 s), the droplet has covered larger distance when moving in the direction II. In particular, the droplet's center of mass has been displaced by 5.25 and 6.35 mm when moving in the direction I and II, respectively.

By returning at Fig. 7.6, which presents the droplet migration velocity on the different solid substrate cases (symmetric surface I, II and asymmetric surface), we notice an acceleration phase (sharp increase of the velocity) at early times (for t < 0.02 s) whereas for later times (t > 0.07 s) the migration velocity reaches a plateau value. The observed fluctuations of the velocity around the plateau value can be attributed to the pinning and de-pinning of the contact lines on the substrate corrugations. In more detail, we observe that the asymmetric surface behaves in a similar fashion with the symmetric surface I (exhibiting stronger adhesion) when the droplet advances in the direction I, whereas the dynamics compare to the ones of the symmetric surface II (facilitating the droplet sliding) when the fluid moves in the direction II.

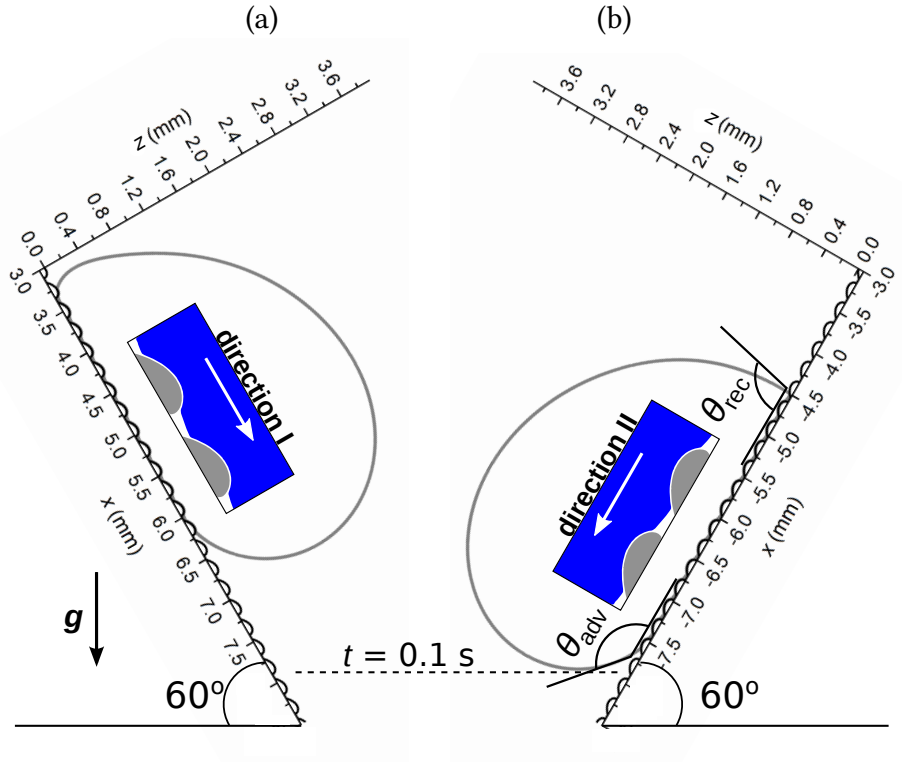

Figure 7.7: Profiles (at t = 0.1 s) of a glycerin/water mixture droplet, sliding on two different directions (a: forward and b: against the corrugations tilt) of an asymmetrically structured inclined substrate.

7.2.1.a Preferable motion direction

In the previous Section, we have attributed the difference in the migration velocity, between the two symmetrically structured surfaces, to the presence of trapped air pockets in the Cassie-Baxter state. However, in the case of asymmetric texturing the droplet is always in the Cassie-Baxter state no matter whether it moves in the direction I or II (see Fig. 7.7) and therefore the contact area between liquid and solid remains roughly the same. Thus the preference in the motion direction has to arise due to the local forces applied in the vicinity of the solid surface. A study regarding the capillary retention forces developed at the outer contact line of a droplet on asymmetric features has been performed by Extrand [50]. In particular, it is calculated that the force resisting the droplet motion, originated by the interfacial tension acting at the outer contact line of a sessile droplet, is defined as:

$$F_{\mathrm{i}} = k\, R_0\, \gamma_{\mathrm{LA}} (\cos\theta_{\mathrm{rec}} - \cos\theta_{\mathrm{adv}}), \tag{7.1}$$

where k is a prefactor which depends on the shape of the outer contact line, θ_{adv} and θ_{rec} are the macroscopically observed advancing and receding contact angles of the droplet, respectively (see Fig. 7.7). In our simulation the capillary forces are predominant against the viscous forces (the capillary number is below unity, $\mathrm{Ca} = \frac{\mu u^*}{\gamma_{\mathrm{LA}}} = 0.2$, where $u^* = \sqrt{\|\boldsymbol{g}\| R_0}$ is a characteristic velocity) therefore the capillary net force that resists the droplet motion on the different directions should be critical. Furthermore, the

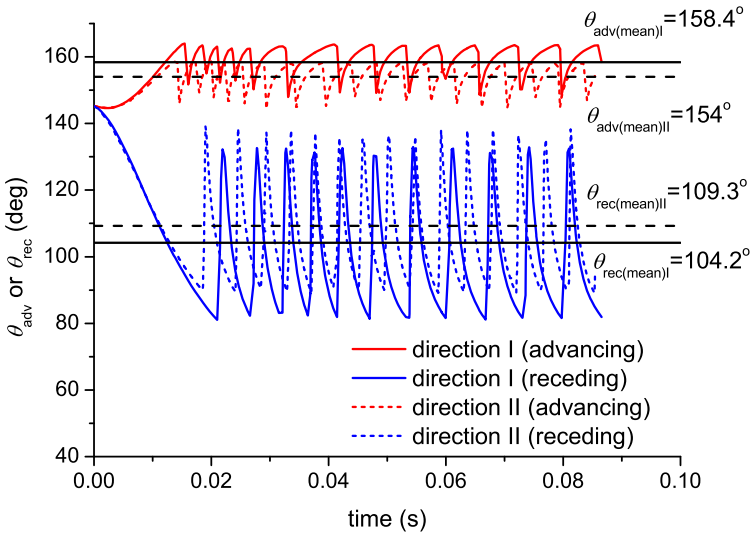

Figure 7.8: Advancing and receding contact angles of a glycerin/water mixture droplet sliding on an inclined (α = 60°) asymmetrically structured surface. The solid lines correspond the direction coinciding the corrugations tilt (I) whereas the dashed lines correspond to the opposite direction of motion (II). The mean value for each advancing and receding contact angles is also presented.

advancing and receding contact angles can be easily predicted by our proposed scheme as shown in Fig. 7.8. In particular, the slope of the droplet surface is evaluated, against the inclined plane, at a fixed distance ($y = 1 \times 10^{-2} R_0$) from the substrate, where the action of the disjoining pressure has been effectively vanished (see also Fig. C.6, of Appendix C.3.2, for the advancing and receding contact angles of the symmetrically structured surfaces I and II). Even though the dynamic contact angles exhibit fluctuations (due to the pinning-depinning of contact lines on the substrate corrugations), our results show that the mean contact angle hysteresis, $\Delta\theta$ (the difference between the advancing and the receding contact angles) is smaller when the droplet slides in the slippery direction (II). In particular $\Delta\theta_{\rm I} = \theta_{\rm adv(mean)I} - \theta_{\rm rec(mean)I}$ = 158.4° - 104.2° = 54.2°, whereas $\Delta\theta_{\rm II} = \theta_{\rm adv(mean)II} - \theta_{\rm rec(mean)II}$ = 154° - 109.3° = 44.7°. Therefore, the retention capillary force in direction I, $F_{\rm I}$, significantly exceeds the one in the opposite direction, $F_{\rm II}$, and their ratio is $\frac{F_{\rm I}}{F_{\rm II}} = 1.23$ (the values of $F_{\rm I}$, $F_{\rm II}$ are calculated by using Eq. 7.1). We note that the preferred motion direction predicted here is in line with the theoretical work of Extrand [50], as well as the experimental works of Buguin et al. [33] who studied droplets moving on vibrated asymmetrically structured substrates, and Contraires et al. [51] who considered droplets growing asymmetrically on asymmetric asperities.

7.2.1.b Surfactant-bearing droplet

According to the above, it would be expected that a change in the capillary forces magnitude (e.g. by using a surfactant to lower the surface tension) would affect the preferable motion direction of the droplet on the asymmetrically structured substrate. It order

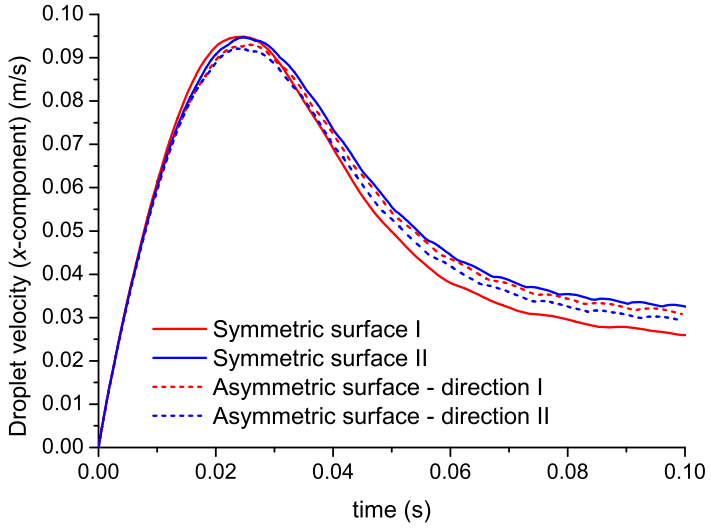

Figure 7.9: Temporal evolution of the average x-component of the velocity for a surfactant-bearing glycerin/water mixture droplet on different kinds of solid surfaces.

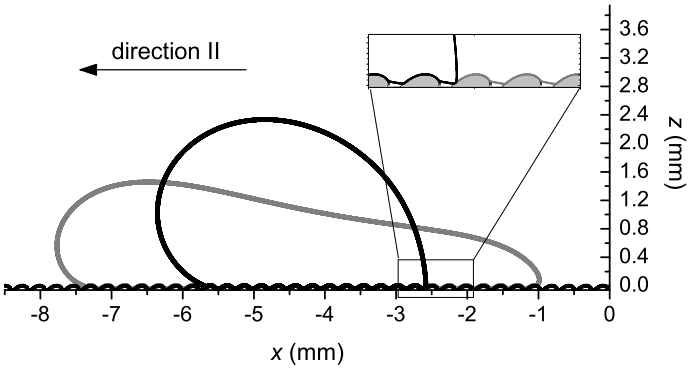

Figure 7.10: Snapshots of a surfactant-bearing (gray line) versus a normal (black line) glycerin/water mixture droplet, sliding (α = -60°) in the direction II of the asymmetric surface, at $t = 8.5 \times 10^{-2}$ s.

to examine this situation, we calculate the migration velocity of a surfactant-bearing droplet (γ_{LA} = 0.014 N/m, which corresponds to a capillary number, Ca $\approx$ 1) sliding on each of the previously studied substrates (the symmetric I, II and the asymmetric one). Specifically, in Fig. 7.9 we plot the temporal evolution of the average x-component of the droplet velocity. Interestingly enough, we observe that the migration velocity is virtually the same for all the substrate cases. The above argument cannot be attributed to the change of the wetting state (i.e. from Cassie-Baxter to Wenzel state) since the liquid, on the asymmetrically patterned surface, is still suspended above the solid protrusions, as can be observed in Fig. 7.10. Such a conclusion is important for selecting suitable liquids in cases where a directional droplet motion is required. In particular, a low surface tension liquid seems to be inappropriate.

7.2.2 Droplet on a vibrated asymmetrically structured surface

Although that transferring droplets on tilted substrates has a practical importance in some applications (e.g. fog harvesting [52]), the active control of the droplet migration velocity (e.g. in lab-on-a-chip devices) requires an external stimuli. Such an actuation can be achieved by applying horizontal or vertical forced oscillations on the solid substrate.

7.2.2.a Effect of the vibration frequency

The effect of several parameters (frequency, direction, amplitude of the oscillation, length scale of the solid texture) on the droplet motion is investigated in this Section. We initially consider a droplet on an asymmetrically structured substrate subjected to a forced sinusoidal vibration either at the vertical or the horizontal direction. The position of the solid substrate for each of the two cases is described by the following equations:

$$z = z_0 - A\sin(\omega t), \tag{7.2a}$$

$$x = x_0 - A\sin(\omega t), \tag{7.2b}$$

where x_0, y_0 are the positions at $t = 0$; A is the oscillation amplitude and, ω, denotes the angular frequency. In order to maximize the effect of vibration on the liquid droplet motion and to minimize the energy damping, it is reasonable to set the frequency, $f = \omega/2\pi$, to the resonance frequency of the system [53]. It is well known that the resonance frequency strongly depends on the droplet size and the liquid properties [54]. Moreover, in the case of a supported droplet on a structured substrate the resonance frequency depends on the detailed equilibrium droplet shape on the corrugated surface (it has been demonstrated that several equilibrium droplet shapes can be accommodated on a certain structured substrate [55]). The above requires detailed computations of the statics and dynamics of the droplet on such a complex solid surface.

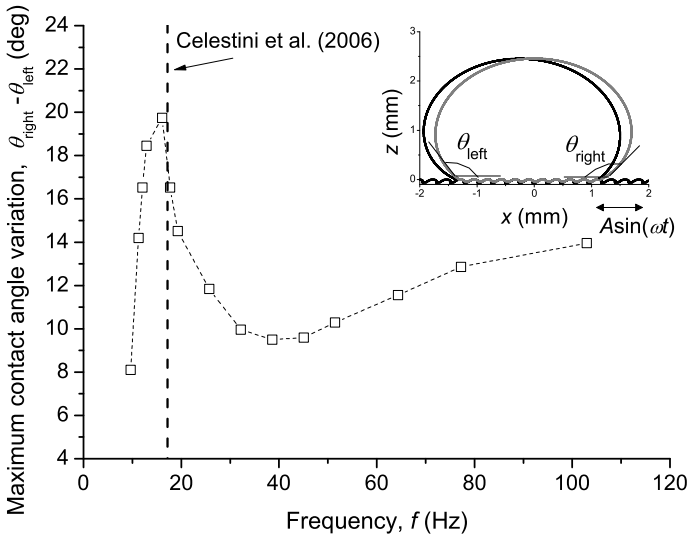

Figure 7.11: Maximum contact angle variation as a function of the frequency of the horizontal vibration. The semianalytical prediction of Celestini et al. [56] for the resonance frequency is presented with the dashed line (see Eq. 7.3).

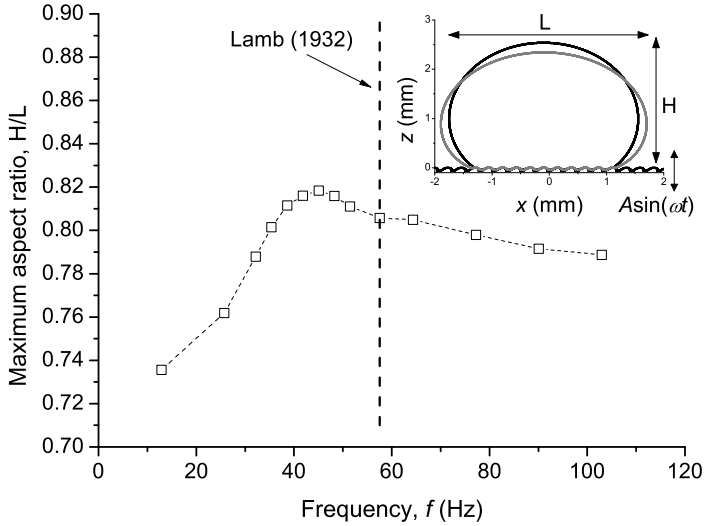

Figure 7.12: Maximum aspect ratio of the droplet profile as a function of the frequency of the vertical vibration. An analytical prediction for the resonance frequency, proposed by Lamb [57], is depicted with the dashed line (see Eq. 7.4).

Here, we detect the resonance by computing the dependence of the deformation of the droplet on the applied frequency. A simple measure of the deformation for the horizontal oscillations is the maximum difference between the right and the left contact angles (see Fig. 7.11); for vertical oscillations we select the aspect ratio of the droplet profile (see Fig. 7.12). Therefore, by using a small oscillation amplitude (A = 0.075 mm) we calculate that the maximum deformation appears at $f_{\mathrm{res,\,h}}$ = 16.1 Hz for the horizontal and $f_{\mathrm{res,\,v}}$ = 45.05 Hz for the vertical vibrations. At this point, it would be interesting to test our predictions against the existing theoretical models.

For predicting the resonance frequency of horizontally vibrated droplets Celestini et al. [56] proposed a semianalytical expression. In particular, by using a simple oscillator analogy they concluded that the resonance angular frequency of a two-dimensional droplet under the influence of horizontal vibrations is estimated by:

$$\omega_0 = \sqrt{\frac{6\,\gamma_{\mathrm{LA}}\,h(\theta_{\mathrm{Y}})}{\rho\,(1-\cos\theta_{\mathrm{Y}})\,(2+\cos\theta_{\mathrm{Y}})}}\,R_0^{-3/2}, \tag{7.3}$$

where the function $h(\theta_{\mathrm{Y}})$, which is computed by static simulations, incorporates the effect of droplet deformation [56]. The agreement between our simulation and the prediction of Celestini et al. (see Fig. 7.11) corroborates to the reliability and accuracy of our scheme. Unfortunately, there is no such formula for the vertical vibrations case, however, our results can be roughly compared with a general expression, proposed by Lamb [57], for the n-tn vibration mode of a three-dimensional free liquid droplet:

$$\omega_n = \sqrt{\frac{n\,(n-1)\,(n+2)\,\gamma_{\mathrm{LA}}}{\rho\,{R_0}^3}}. \tag{7.4}$$

The fundamental frequency (n = 2) predicted by Eq. 7.4 deviates from our computations (see Fig. 7.12) due to the contribution of pinning effects of the contact lines that were obviously not taken into account in the theoretical work of Lamb [57].

7.2.2.b Effect of the vibration direction

We have already shown that the asymmetric structure may set a preferential direction of motion in the case of gravity driven droplet migration. A question that may arise is whether it is possible to exploit the asymmetric features in order to set a droplet to motion by applying either vertical or horizontal vibrations. In Fig. 7.13 we present the temporal evolution of the droplet's center of mass (the horizontal position), x_{cm}, as a function of oscillation direction and amplitude. The forced frequency for each case corresponds to the resonance (f_{res}), as calculated in the previous Section for a glycerin/water mixture droplet. Note that in order to depict both cases of horizontal and vertical vibrations in a single graph, and given that the oscillation frequency differ (16.1 Hz for the horizontal and 45.05 Hz for the vertical vibrations, respectively), time is expressed

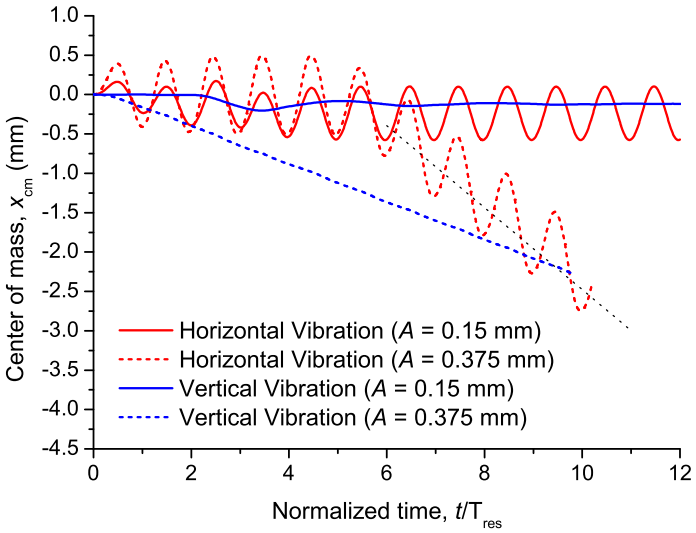

Figure 7.13: Temporal evolution of the droplet's center of mass (the horizontal position), x_{cm}, for different vibration directions (horizontal and vertical) and magnitudes, A. The normalized time is defined as t/T_{res} where T_{res} is the oscillation period which corresponds to the resonance ($T_{\mathrm{res}} = \frac{1}{f_{\mathrm{res}}}$). An average value of the droplet's center of mass , for A = 0.375 mm in the case of horizontal vibrations, is presented by the black dotted line.

here in dimensionless units. It is observed that for small oscillation amplitude (A = 0.15 mm) the droplet deforms but does not move along the substrate (see Fig. 7.13). However, for a vibration amplitude larger than the width of the solid protrusions (A = 0.375 mm > w_3 = 0.24 mm) the liquid moves to the direction opposing the corrugations tilt (direction II). The motion direction here conforms to the preferable sliding direction when the asymmetrically structured solid surface is tilted (see previous Section).

Although that the liquid moves to the same direction for both horizontal and vertical substrate oscillations, the dynamic behavior of the droplet changes significantly. In particular, as observed in Fig. 7.13, the displacement of the center of mass is smoother in the case of vertical oscillations, whereas it is distorted (exhibits fluctuations) when the substrate is vibrated horizontally. Moreover, in contrast with the vertical oscillation case where the droplet starts to migrate almost immediately at t = 0, the droplet starts to move after a certain time interval (e.g. $\sim$ 5 periods ($5T_{\mathrm{f}}$), for the specific solid structure) in the case of horizontal vibrations. Interesting observations can also be made by zooming at the droplet shape near the solid surface. In particular, in Fig. 7.14 we present different snapshots of the droplet (for $t = 7.5T_{\mathrm{f}}$ and $9T_{\mathrm{f}}$, where $T_{\mathrm{f}} = T_{\mathrm{res}}$ for each case) by applying horizontal and vertical forced vibrations. Note that in both time instances ($t = 7.5T_{\mathrm{f}}$ and $9T_{\mathrm{f}}$) the solid substrate is at the same position although the acceleration direction is opposite. It is observed that in the case of horizontal oscillations the droplet sits on top of the protrusions, minimizing the contact area between the liquid and the solid phases (Cassie-Baxter state). On the other hand, the picture is different for the vertical oscillations where the liquid fully penetrates the solid asperities (Wenzel state).

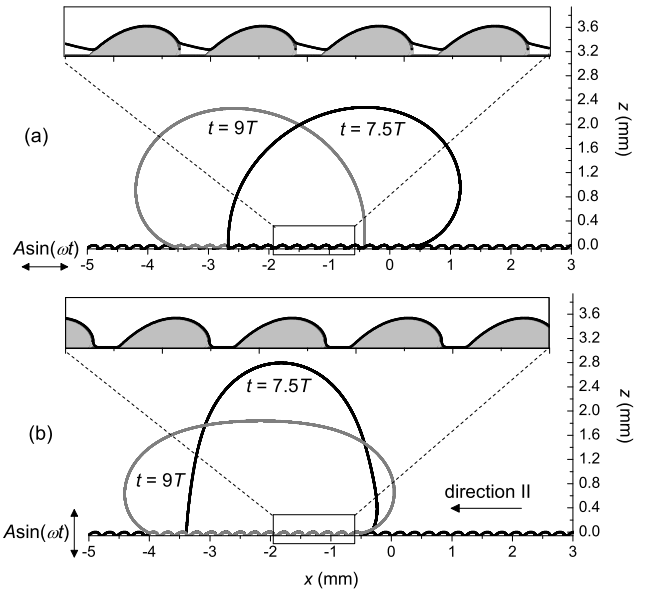

Figure 7.14: Snapshots of a glycerin/water mixture droplet moving on an asymmetrically structured solid surface which is vibrated (a) horizontally and (b) vertically on the resonance frequency for each case. A magnification of the droplet profiles, close to the solid surface, is presented in the insets.

In particular, the higher momentum developed in the y-direction facilitates the collapse from Cassie-Baxter to Wenzel state. The migration velocity is expected to be lower in this case since it is known that Wenzel wetting states exhibit high friction and thus low droplet mobility [49]. Such a behavior can be actually observed in Fig. 7.13, where the droplet migrates faster in the case of horizontal vibration (black dotted line). The different rate in the energy dissipation may also be responsible for this discrepancy (the droplet deforms to a greater extend in the case of vertical vibrations). A detailed analysis regarding the energy dissipation rate will be presented in the following Section.

7.2.2.c Effect of the vibration amplitude

We have shown that a droplet migrates uni-directionally on an asymmetrically structured surface when the oscillation amplitude is larger than a threshold value, however it is important to better understand the factors that affect the droplet migration velocity. In Fig. 7.15 we depict the mean value of the droplet migration velocity (computed in the interval of two oscillation periods) for different amplitudes. In particular, the mean velocity is estimated by $u_{\text{mean}} = \frac{\delta x_{\text{mean}}}{8T_{\text{f}}-6T_{\text{f}}}$, where δx_{mean} is the displacement of the droplet's center of mass in the time interval between the 6^{th} and the 8^{th} oscillation periods, when the droplet has reached a virtually constant velocity (see also Fig. 7.13).

As observed in Fig. 7.15, the mean droplet velocity is very sensitive to the vibration amplitude. In particular, we observe four different regimes:

(I) For low vibration amplitudes ($A < 0.2$ mm) the external force is not enough to

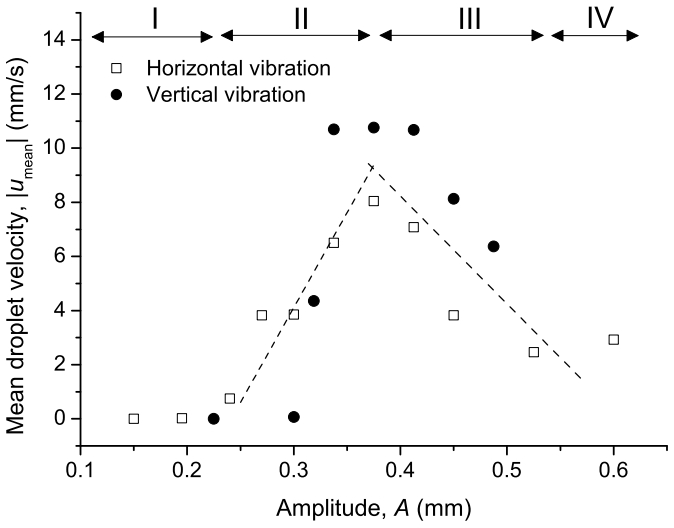

Figure 7.15: Absolute value of the average droplet migration velocity during two oscillation periods (from $6T_f$ to $8T_f$), as a function of the amplitude, A, for horizontal and vertical vibrations. The oscillation frequency corresponds to the resonance for each case. Dashed lines (linear fit to the computational data) are drawn as guide to the eye.

surpass the static hysteresis and thus no motion is detected.

(II) Exceeding a vibration amplitude threshold (A = 0.24 mm for the horizontal and 0.32 mm for vertical oscillations, respectively) the friction in direction II (opposing the corrugations tilt) is surpassed and the droplet migrates with a mean velocity, u_{mean}. The latter is observed to increase linearly with the amplitude.

(III) As the amplitude further increases, the vibration gets so intense that the contact angle hysteresis can be surpassed in both directions. The above results to a decrease in the average droplet velocity. The critical amplitude, A_{crit}, where the migration velocity is maximal, is equal to 0.375 mm for the horizontal vibration case. On the other hand it ranges from 0.34 mm to 0.41 mm for the vertical oscillations. A similar behavior, where the migration velocity is reduced for large vibration amplitudes, has also been reported experimentally [33] which strengthens the validity of our simulations.

(IV) Finally, the mean velocity is stabilized for larger vibration amplitudes.

Considering that during an oscillation period, T_f, the droplet moves along a number of solid unit cells, n_{uc}, the average velocity equals to: $u_{\text{mean}} = \frac{n_{\text{uc}}\, w_3}{T_f}$, where w_3 is the width of the unit cell structure of the asymmetric substrate (see Fig. 7.3). Consequently, when the migration velocity is maximal (8 mm/s for the horizontal and 10.8 mm/s for the vertical vibration) the droplet is shifted by two solid structure corrugations for the horizontal and one for the vertical oscillations. Given that the lateral displacement of the droplet by one corrugation requires overcoming an energy barrier [58] (constant for

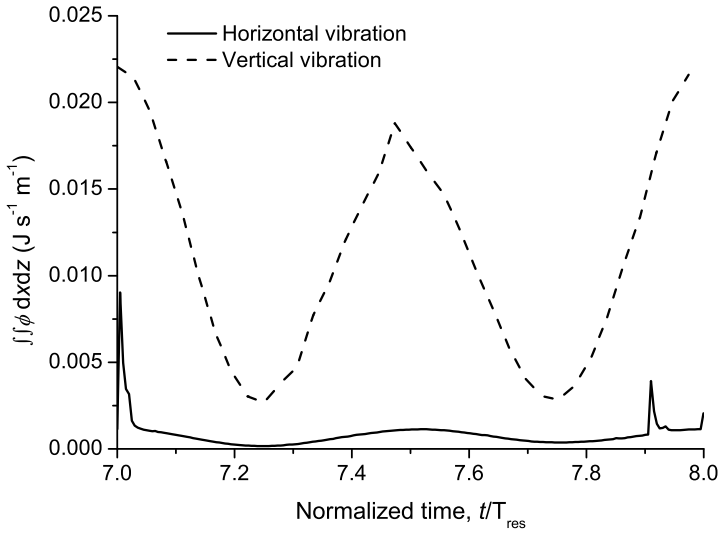

Figure 7.16: Surface integral of the energy dissipation function, ϕ, during an oscillation cycle (from $t = 7T_\mathrm{f}$ to $t = 8T_\mathrm{f}$), for both horizontal and vertical vibration cases.

both vibration cases), we would expect that the peak potential energy of the droplet is larger in the case of the horizontal vibration. This is not the case though: by evaluating the peak potential energy, E_{tot}, per unit mass, M_droplet, at $A = A_\mathrm{crit}$ and $f = f_\mathrm{res}$:

$$\frac{E_\mathrm{tot}}{M_\mathrm{droplet}} = \pi\, f_\mathrm{res}^2\, A_\mathrm{crit}^2, \tag{7.5}$$

we conclude that the peak energy of the vertical is considerable higher compared with the horizontal vibrations, $\frac{E_\mathrm{tot,\,ver}}{E_\mathrm{tot,\,hor}} = 7.83$ (we considered an average value of $A_\mathrm{crit} = 0.375$ mm for the vertical vibration case). The lateral displacement per cycle, however, is smaller in the first case. An explanation for this behavior can be derived by examining the energy dissipation for both vibration cases.

In Fig. 7.16 we present the surface integral, over the entire droplet cross-sectional area, A_droplet, of the dissipation function, ϕ, which reads in cartesian coordinates [12]:

$$\phi = \boldsymbol{\tau} : \nabla \boldsymbol{u} = 2\,\mu \left[\left(\frac{\mathrm{d}u_x}{\mathrm{d}x} \right)^2 + \left(\frac{\mathrm{d}u_z}{\mathrm{d}z} \right)^2 \right] + \mu \left[\left(\frac{\mathrm{d}u_x}{\mathrm{d}z} \right) + \left(\frac{\mathrm{d}u_z}{\mathrm{d}x} \right) \right]^2 . \tag{7.6}$$

It is clear, from our results, that the rate of dissipation is substantially larger in the case of vertical vibrations. This is also evident by looking at the droplet deformation for the two cases (see Fig. 7.14). In particular, the total energy, per unit depth of the droplet, consumed during a cycle is: $E_\mathrm{diss,\,hor} = \int_{7T_\mathrm{f}}^{8T_\mathrm{f}} \iint_{A_\mathrm{droplet}} \phi \,\mathrm{d}x\,\mathrm{d}z\,\mathrm{d}t = 5.05 \times 10^{-5}$ J/m and $E_\mathrm{diss,\,ver} = 2.34 \times 10^{-4}$ J/m for the horizontal and vertical oscillations, respectively.

7.2.2.d Effect of the structure length scale

Useful conclusions can be derived by proportionally modifying the size of the solid structure unit cell. In particular, in Fig. 7.17 we present the dependence of the mean droplet velocity on the texture scale factor, s. We consider that the basic case, studied in the previous Sections, where w_3 = 0.24 mm and h = 0.06 mm (see Fig. 7.3), corresponds to a scale factor, s = 1. In the studied cases, the width the asymmetric structure (w_3) ranges from 0.18 mm (s = 0.75) to 0.3 mm (s = 1.25) and the height (h) from 0.045 mm to 0.075 mm, respectively. The frequency of each vibration is set to the corresponding resonance which is evaluated as described in Section 7.2.2.a, for each case.

Initially, in the case of vertical forced vibrations (Fig. 7.17a) and small oscillation amplitudes, we observe that the mean velocity of the droplet increases with the scale factor of the solid structure. By further increasing the amplitude, we observe that the mean velocity is at first stabilized but then decreases sharply, for very high amplitude values. An interesting note here is that the interval of amplitudes, where the mean velocity of the droplet has a constant value, shrinks by increasing the structure scaling. Thus, the smaller the scale factor is, the more insensitive is the migration velocity to the oscillation amplitude. We also remark that the maximal migration velocity is higher for larger solid structure length scale.

On the other hand, in the case of horizontal vibrations (Fig. 7.17b), we detect a sharp maximum of the migration velocity at a specific amplitude value (for $A = A_{\text{crit}}$) (in contrast with the interval of possible amplitudes, observed at the vertical vibrations). Furthermore, we remark that this critical value of the amplitude (A_{crit}) is a non-linear function of the structure scaling (i.e. A_{crit} decreases from 0.725 mm to 0.375 mm as the texture scale grows from 0.75 to 1 and then increases again to 0.65 mm for the larger structure scale, s = 1.25). The above behavior can be attributed to the fact that the anisotropic wetting properties gradually fade when reducing the structure scaling, thus requiring a larger oscillation amplitude to start the droplet motion in a certain direction. The latter depends on the maximum difference between the right and the left contact angles (see Eq. 7.1) which is observed to reduce, for a static droplet, as the structure size is shrunk (from $\Delta\theta = 2^{\text{o}}$, at s = 1.25 to $\Delta\theta = 0.2^{\text{o}}$, at s = 0.75). In addition, large amplitude is also required when the structure scale is magnified, since the droplet needs to be deformed to a greater extend in order to migrate. Therefore, fine tuning the amplitude of the horizontal oscillations, for an effective droplet migration in experimental practice, seems to be a tedious task, unless a predictive model for the droplet behavior, as the one described here, is employed.

An overall picture can be obtained by plotting, in Fig. 7.18, the maximum migration velocity of the droplet, $|u_{\text{mean (max)}}|$, as a function of the solid structure length scale, s. Interestingly enough, it is observed that the migration velocity increases linearly with the texture scale factor for the vertical vibration case. The above behavior is attributed on one hand to the larger distance covered by the droplet during a cycle (since the space

(a)

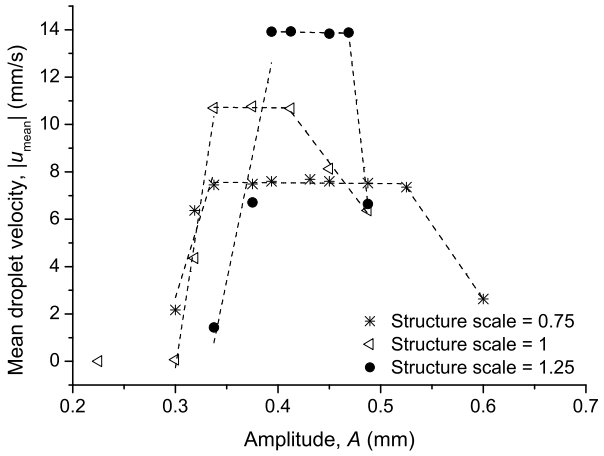

(b)

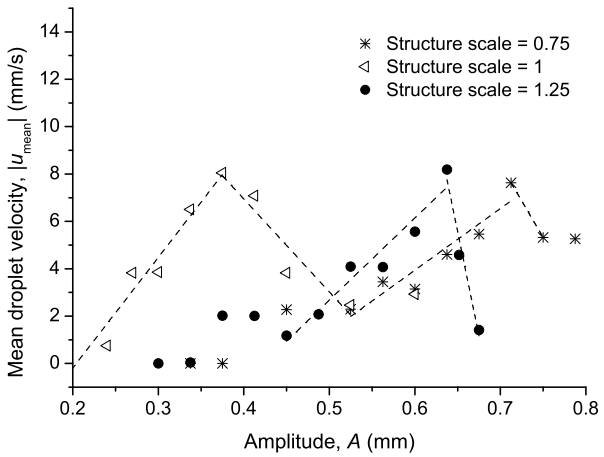

Figure 7.17: Absolute value of the average droplet migration velocity on substrates with different structure scale factor subjected to (a) vertical and (b) horizontal vibrations. The oscillation frequency corresponds to the resonance for each case. Dashed lines (linear fit to the computational data) are drawn as guide to the eye.

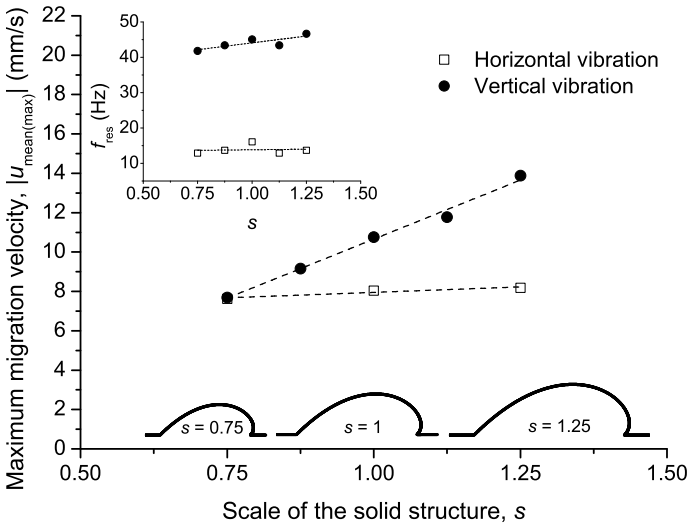

Figure 7.18: Maximum migration velocity as a function of the solid structure length scale, for both horizontal and vertical oscillations. The case where $s = 1$ corresponds to the initial unit structure presented in Fig. 7.3. The oscillation frequency and amplitude correspond to f_{res} and A_{crit}, respectively, for each case. The dependence of the resonance frequency on the structure scale factor is presented in the inset.

between the protrusions is increased), and on the other hand to the amplified effect of the unbalanced capillary retention force at the outer contact line. Furthermore, in the case of horizontal vibrations the migration velocity is not affected by changing the structure scale factor. Such a behavior may be attributed to the limited droplet deformation in this case, in contrast with the vertical vibrations (see also Fig. 7.14). The same analysis is performed for the resonance frequency (see the inset of Fig. 7.18) which also seems to change slightly with the length scale of the solid structure.

7.3 Summary and conclusions

In this Chapter, we focused on cases where the droplet motion was induced either by tilting or vibrating asymmetrically structured substrate. In the case of a sliding droplet, we demonstrated that an asymmetrically structured surface can reproduce two kinds of wetting behaviors: slippery behavior (resembling the Cassie-Baxter regime), when the substrate is tilted downward (for $\alpha < 0^{\text{o}}$) and sticky behavior (resembling the Wenzel regime), when the substrate is tilted upward (for $\alpha > 0^{\text{o}}$). This is attributed to the unbalanced capillary retention force at the outer contact line. Thus, in cases where the capillary effect is weakened (e.g. for a surfactant-bearing droplet) we observed that the anisotropic friction behavior fades.

We have also examined cases where the droplet movement is induced by a forced vibration of the solid substrate. Once again the droplet follows the direction prescribed

by the capillary forces (opposing the corrugations tilt), after a threshold value of the oscillation amplitude has been surpassed. Moreover, we have found that the migration velocity is maximal for a certain oscillation frequency and amplitude values (at $f = f_{\text{res}}$ and $A = A_{\text{crit}}$). Finally, we have demonstrated a link between the droplet migration velocity and the length scale of the solid structure. In particular, when applying vertical vibrations, the migration velocity is appeared to be a linear function of the texture scale factor. This is not the case, however, when the droplet is set to motion by horizontal vibrations. In the latter situation the migration velocity is not considerably affected by the structure scale factor.

Regarding the future perspectives, in order design more effective asymmetric structures that promote the uni-directional liquid motion, it would be extremely useful to evaluate the energy barriers (see Section 4.2.5) for the motion outset of a droplet in opposite directions (opposing and coinciding the corrugations tilt). Such a task requires to solve the augmented Young-Laplace equation (see Section 2.2.4) while, however, disregarding, due to the asymmetric substrate, any mirror symmetry conditions at the droplet's apex and base. More information about our ongoing research will also be presented in Chapter 9.

References

[1] A.-L. Biance, C. Clanet, and D. Quéré. “First steps in the spreading of a liquid droplet”. In: *Physical Review E* 69.1 (2004), p. 016301.

[2] J. Bird, S. Mandre, and H. Stone. “Short-Time Dynamics of Partial Wetting”. In: *Physical Review Letters* 100.23 (June 2008), p. 234501. ISSN: 0031-9007.

[3] S Richardson. “On the no-slip boundary condition”. In: *Journal of Fluid Mechanics* 59.04 (1973), pp. 707–719.

[4] K. M. Jansons. “Determination of the macroscopic (partial) slip boundary condition for a viscous flow over a randomly rough surface with a perfect slip microscopic boundary condition”. In: *Physics of Fluids (1958-1988)* 31.1 (1988), pp. 15–17.

[5] J. Casado-Dıaz, E. Fernández-Cara, and J. Simon. “Why viscous fluids adhere to rugose walls:: A mathematical explanation”. In: *Journal of Differential equations* 189.2 (2003), pp. 526–537.

[6] Š Šikalo, C Tropea, and E. Ganić. “Dynamic wetting angle of a spreading droplet”. In: *Experimental Thermal and Fluid Science* 29.7 (2005), pp. 795–802.

[7] Š Šikalo, H.-D. Wilhelm, I. Roisman, S Jakirlić, and C Tropea. “Dynamic contact angle of spreading droplets: experiments and simulations”. In: *Physics of Fluids (1994-present)* 17.6 (2005), p. 062103.

[8] S. F. Lunkad, V. V. Buwa, and K. Nigam. “Numerical simulations of drop impact and spreading on horizontal and inclined surfaces”. In: *Chemical Engineering Science* 62.24 (2007), pp. 7214–7224.

[9] S. F. Kistler. *"Hydrodynamics of Wetting", in Wettability*. edited by J. C. Berg, Marcel Dekker, New York, 1993, p. 311.

[10] F. N. Fritsch and R. E. Carlson. “Monotone piecewise cubic interpolation”. In: *SIAM Journal on Numerical Analysis* 17.2 (1980), pp. 238–246.

[11] J. Koplik, J. R. Banavar, and J. F. Willemsen. “Molecular dynamics of fluid flow at solid surfaces”. In: *Physics of Fluids A: Fluid Dynamics (1989-1993)* 1.5 (1989), pp. 781–794.

[12] Z. U. Warsi. *Fluid dynamics: theoretical and computational approaches*. CRC press, 2005.

[13] B. Stapelbroek, H. Jansen, E. Kooij, J. Snoeijer, and A Eddi. “Universal spreading of water drops on complex surfaces”. In: *Soft Matter* 10.15 (2014), pp. 2641–2648.

[14] A. Yarin. “Drop impact dynamics: splashing, spreading, receding, bouncing…” In: *Annual Review of Fluid Mechanics* 38 (2006), pp. 159–192.

[15] L. Tanner. “The spreading of silicone oil drops on horizontal surfaces”. In: *Journal of Physics D: Applied Physics* 12.9 (1979), p. 1473.

[16] M. Wu, T. Cubaud, and C.-M. Ho. “Scaling law in liquid drop coalescence driven by surface tension”. In: *Physics of Fluids (1994-present)* 16.7 (2004), pp. L51–L54.

[17] F. Mugele and J.-C. Baret. “Electrowetting: from basics to applications”. In: *Journal of Physics: Condensed Matter* 17.28 (2005), R705.

[18] L. Courbin, J. C. Bird, M. Reyssat, and H. Stone. “Dynamics of wetting: from inertial spreading to viscous imbibition”. In: *Journal of Physics: Condensed Matter* 21.46 (2009), p. 464127.

[19] L. Chen, C. Li, N. F. van der Vegt, G. K. Auernhammer, and E. Bonaccurso. "Initial electrospreading of aqueous electrolyte drops". In: *Physical Review Letters* 110.2 (2013), p. 026103.

[20] W. Ren and W. E. "Boundary conditions for the moving contact line problem". In: *Physics of Fluids (1994-present)* 19.2 (2007), p. 022101.

[21] A. Carlson, G. Bellani, and G. Amberg. "Contact line dissipation in short-time dynamic wetting". In: *Europhysics Letters* 97.4 (2012), p. 44004.

[22] J. Wang, M. Do-Quang, J. J. Cannon, F. Yue, Y. Suzuki, G. Amberg, and J. Shiomi. "Surface structure determines dynamic wetting". In: *Scientific Reports* 5 (2015).

[23] F. Lapierre, M. Jonsson-Niedziolka, Y. Coffinier, R. Boukherroub, and V. Thomy. "Droplet transport by electrowetting: lets get rough!" In: *Microfluidics and Nanofluidics* 15.3 (2013), pp. 327–336.

[24] G. Karapetsas, K. C. Sahu, K. Sefiane, and O. K. Matar. "Thermocapillary-driven motion of a sessile drop: effect of non-monotonic dependence of surface tension on temperature". In: *Langmuir* 30.15 (2014), pp. 4310–4321.

[25] G. Lagubeau, M. Le Merrer, C. Clanet, and D. Quéré. "Leidenfrost on a ratchet". In: *Nature Physics* 7.5 (2011), pp. 395–398.

[26] D. Quéré. "Leidenfrost dynamics". In: *Annual Review of Fluid Mechanics* 45 (2013), pp. 197–215.

[27] A. Wixforth, C. Strobl, C. Gauer, A. Toegl, J. Scriba, and Z. Guttenberg. "Acoustic manipulation of small droplets". In: *Analytical and Bioanalytical Chemistry* 379.7 (2004), pp. 982–991.

[28] P Brunet, J Eggers, and R. Deegan. "Vibration-induced climbing of drops". In: *Physical Review Letters* 99.14 (2007), p. 144501.

[29] X. Noblin, R. Kofman, and F. Celestini. "Ratchetlike motion of a shaken drop". In: *Physical Review Letters* 102.19 (2009), p. 194504.

[30] K. John and U. Thiele. "Self-ratcheting Stokes drops driven by oblique vibrations". In: *Physical Review Letters* 104.10 (2010), p. 107801.

[31] R. Borcia, I. D. Borcia, and M. Bestehorn. "Can vibrations control drop motion?" In: *Langmuir* 30.47 (2014), pp. 14113–14117.

[32] O Sandre, L Gorre-Talini, A Ajdari, J Prost, and P Silberzan. "Moving droplets on asymmetrically structured surfaces". In: *Physical Review E* 60.3 (1999), p. 2964.

[33] A Buguin, L Talini, and P Silberzan. "Ratchet-like topological structures for the control of microdrops". In: *Applied Physics A* 75.2 (2002), pp. 207–212.

[34] T. A. Duncombe, E. Y. Erdem, A. Shastry, R. Baskaran, and K. F. Böhringer. "Controlling liquid drops with texture ratchets". In: *Advanced Materials* 24.12 (2012), pp. 1545–1550.

[35] N. Tretyakov and M. Müller. "Directed transport of polymer drops on vibrating superhydrophobic substrates: a molecular dynamics study". In: *Soft Matter* 10.24 (2014), pp. 4373–4386.

[36] Y. Zheng, X. Gao, and L. Jiang. "Directional adhesion of superhydrophobic butterfly wings". In: *Soft Matter* 3.2 (2007), pp. 178–182.

[37] K. Liu and L. Jiang. "Bio-inspired design of multiscale structures for function integration". In: *Nano Today* 6.2 (2011), pp. 155–175.

[38] J. Yong, Q. Yang, F. Chen, D. Zhang, G. Du, H. Bian, J. Si, and X. Hou. "Bioinspired superhydrophobic surfaces with directional Adhesion". In: *RSC Advances* 4.16 (2014), pp. 8138–8143.

[39] P. Comanns, G. Buchberger, A. Buchsbaum, R. Baumgartner, A. Kogler, S. Bauer, and W. Baumgartner. "Directional, passive liquid transport: the Texas horned lizard as a model for a biomimetic 'liquid diode'". In: *Journal of The Royal Society Interface* 12.109 (2015), p. 20150415.

[40] A. D. Stroock, R. F. Ismagilov, H. A. Stone, and G. M. Whitesides. "Fluidic ratchet based on Marangoni-Bénard convection". In: *Langmuir* 19.10 (2003), pp. 4358–4362.

[41] K.-H. Chu, R. Xiao, and E. N. Wang. "Uni-directional liquid spreading on asymmetric nanostructured surfaces". In: *Nature Materials* 9.5 (2010), pp. 413–417.

[42] P. Guo, Y. Zheng, C. Liu, J. Ju, and L. Jiang. "Directional shedding-off of water on natural/biomimetic taper-ratchet array surfaces". In: *Soft Matter* 8.6 (2012), pp. 1770–1775.

[43] A. Cavalli, M. L. Blow, and J. M. Yeomans. "Modelling unidirectional liquid spreading on slanted microposts". In: *Soft Matter* 9.29 (2013), pp. 6862–6866.

[44] B. Thiria and J. Zhang. "Ratcheting fluid with geometric anisotropy". In: *Applied Physics Letters* 106.5 (2015), p. 054106.

[45] G. D. Bixler and B. Bhushan. "Rice-and butterfly-wing effect inspired self-cleaning and low drag micro/nanopatterned surfaces in water, oil, and air flow". In: *Nanoscale* 6.1 (2014), pp. 76–96.

[46] C. Liu, J. Ju, Y. Zheng, and L. Jiang. "Asymmetric ratchet effect for directional transport of fog drops on static and dynamic butterfly wings". In: *ACS Nano* 8.2 (2014), pp. 1321–1329.

[47] G. Karapetsas, N. T. Chamakos, and A. G. Papathanasiou. "Efficient modelling of droplet dynamics on complex surfaces". In: *Journal of Physics: Condensed Matter* 28.8 (2016), p. 085101.

[48] D. Quéré. "Wetting and roughness". In: *Annual Review of Materials Research* 38 (2008), pp. 71–99.

[49] B. Bhushan, Y. C. Jung, and K. Koch. "Micro-, nano- and hierarchical structures for superhydrophobicity, self-cleaning and low adhesion". In: *Philosophical Transactions of the Royal Society of London A: Mathematical, Physical and Engineering Sciences* 367.1894 (2009), pp. 1631–1672.

[50] C. Extrand. "Retention forces of a liquid slug in a rough capillary tube with symmetric or asymmetric features". In: *Langmuir* 23.4 (2007), pp. 1867–1871.

[51] E. Contraires, J. Teisseire, E. Søndergård, and E. Barthel. "Wetting against the nap–how asperity inclination determines unidirectional spreading". In: *Soft Matter* 12.28 (2016), pp. 6067–6072.

[52] K.-C. Park, S. S. Chhatre, S. Srinivasan, R. E. Cohen, and G. H. McKinley. "Optimal design of permeable fiber network structures for fog harvesting". In: *Langmuir* 29.43 (2013), pp. 13269–13277.

[53] S. Daniel, M. K. Chaudhury, and P.-G. De Gennes. "Vibration-actuated drop motion on surfaces for batch microfluidic processes". In: *Langmuir* 21.9 (2005), pp. 4240–4248.

[54] E. D. Wilkes and O. A. Basaran. "Forced oscillations of pendant (sessile) drops". In: *Physics of Fluids (1994-present)* 9.6 (1997), pp. 1512–1528.

[55] M. E. Kavousanakis, N. T. Chamakos, and A. G. Papathanasiou. "Connection of Intrinsic Wettability and Surface Topography with the Apparent Wetting Behavior and Adhesion Properties". In: *The Journal of Physical Chemistry C* 119.27 (2015), pp. 15056–15066.

[56] F. Celestini and R. Kofman. "Vibration of submillimeter-size supported droplets". In: *Physical Review E* 73.4 (2006), p. 041602.

[57] H. Lamb. *Hydrodynamics*. Cambridge University Press, 1932.

[58] G. Pashos, G. Kokkoris, and A. G. Boudouvis. "Minimum energy paths of wetting transitions on grooved surfaces". In: *Langmuir* 31.10 (2015), pp. 3059–3068.

PART IV

Conclusions and future perspectives

CHAPTER 8

Concluding remarks

In this Chapter we summarize the research presented in the Thesis and we discuss the impact of this work in both fields of applied and theoretical research. Briefly, our original contribution to knowledge is a novel, continuum-level, sharp-interface modeling approach which gave us the ability to study a plethora of wetting phenomena, ranging from equilibrium wetting states to droplet motion, on structured solid surfaces. Such a study would have been infeasible, up to now, with the conventional modeling approaches which either are failing to adequately describe the complex behavior of a droplet on a rough substrate, or being too expensive, in terms of computational cost, for real-life applications with millimeter-sized droplets.

8.1 Summary of the Thesis

In this Thesis, we proposed a novel, continuum-level, sharp-interface modeling approach which has been shown to be particularly efficient in cases where the conventional formulations fail, i.e. in the modeling of multiple static or dynamic contact lines of entire droplets. In particular, the simplest and most efficient computational approach for the determination of equilibrium wetting states, i.e. the solution of the Young-Laplace equation [1, 2], is of limited applicability for the computation of droplets wetting geometrically heterogeneous surfaces. The same applies also for the dynamic simulations where the conventional models are based on the Cox equation [3] (a condition that relates the velocity of a contact line with the dynamic contact angle). The above limitations originate from the *a priori* unknown number and position of the three contact lines (where the three different phases, liquid, ambient, solid, meet), where the Young contact angle boundary condition has to be applied. The main advantage of our proposed methodology is that it avoids the implementation of any explicit boundary condition at the contact line(s) by treating the liquid-ambient and the liquid-solid interfaces of the droplet in a unified framework. The solid-liquid boundary condition has now been replaced by micro-scale liquid-solid interactions, via a disjoining (or Derjaguin) pressure term [4], which act in close proximity to the solid. By using the above formulation we can successfully model the statics and dynamics of entire droplets (e.g. the droplet shape, the

velocity of the contact line(s), the dynamic contact angle) on any kind of geometrically or chemically structured solid surface.

After validating our methodology against the conventional modeling approach for static cases (Young-Laplace equation) as well as against a conceptually different mesoscopic lattice-Boltzmann model, we have for a first time managed to effectively predict multiple meta-stable equilibrium wetting states on patterned substrates. Moreover, we have easily computed the energy barriers required for wetting transitions between the well-known Cassie-Baxter (where air pockets are trapped in the solid structure) and Wenzel (the liquid fully wets the solid structure) states (see Chapter 4 as well as the corresponding published works [5, 6]). We note that fine scale computational approaches, such as molecular dynamics [7, 8] and mesoscopic lattice-Boltzmann models [9, 10, 11], commonly used for the same task, demand prohibitively higher computational resources.

By solving the equations of electrostatics, along with the augmented Young-Laplace, we have also successfully simulated the electrowetting phenomenon (where the solid wettability is electrostatically enhanced) on structured substrates, deriving useful conclusions regarding the mechanism of Cassie-Baxter to Wenzel wetting transitions. The electric field effect is incorporated in this case through an electric stress term accounting for the electric forces exerted on the droplet surface. Our results indicate that the microscopic (Young) contact angle, as well as the local mean curvature of the droplet in the vicinity of the solid surface, vary with the applied voltage, for adequately thin ($\leqslant 10\,\mu m$) solid dielectrics (see Chapter 5 as well as the corresponding published work [12]). Based on the above conclusion, we have experimentally performed real-time tuning of the wettability on superhydrophobic surfaces, which will be demonstrated in the following Chapter (Section 9.1). To our opinion, the potential applications of such a technique are abundant in lab-on-a-chip devices.

The proposed formulation was also utilized to perform dynamic simulations of droplets spreading on geometrically complex substrates -an essentially tedious task for conventional hydrodynamic models- showing exceptional agreement with experimental measurements. In this case, we have also observed that the no-slip boundary condition derives implicitly due to the viscous dissipation on the solid asperities, even though no tangential forces are explicitly imposed. This conclusion is in accordance with the theoretical work of Richardson [13] and Jansons [14]. Moreover, the study of the early droplet spreading stage on hierarchically structured, as well as on chemically patterned, solid substrates revealed an inertial regime where the contact radius of the droplet with the solid grows according to a universal power law, in agreement with recently published experimental findings (see Chapter 6 as well as the corresponding published works [15, 16]). We have also studied the droplet dynamics under the effect of electric field (electrospreading), which is commonly observed in practice, in lab-on-a-chip devices.

Finally, we have investigated the uni-directional droplet motion mechanism on asymmetrically patterned surfaces, inspired by the wings of the *Morpho aega* butterfly [17].

We have found that the uni-directional motion is strongly connected with the capillary forces at the outer contact line, thus the anisotropic wetting properties vanish as we reduce the surface tension of the droplet. We demonstrated that the structure asymmetry can be exploited in order to passively transfer a droplet by vibrating the solid surface, either vertically or horizontally. In addition we have performed a full parameter space investigation in order to improve the efficiency of the droplet displacement (e.g. increase the migration velocity of the droplet) (see Chapter 7 as well as the corresponding published work [18]).

8.2 Impact on potential applications

As described in Chapter 1, the proper surface patterning design can dramatically change the wetting properties of a solid surface (e.g. can render a slightly hydrophobic material as super water-repellant like the lotus leaf). Thus when designing surfaces with desirable and even switchable wettability, the surface patterning is of great importance. There are several studies that deal with optimizing the solid surface structure shape in order to obtain desirable wetting properties (e.g. by utilizing lattice-Boltzmann [19, 20] of continuum-level modeling approaches [21, 22, 23]). Our proposed methodology, however, seem advantageous over these approaches, since the computational requirements are quite lower than the lattice-Boltzmann models while the disengagement from the contact angle boundary condition distinguish our method between the other continuum-level approaches. The presented methodology can be readily applied to any kind of solid surface topography (or even chemically patterned) for understanding the effect of geometric characteristics on static and dynamic wetting behavior. The study of the active control of the droplet motion, by utilizing electrowetting phenomenon, is also an important feature of the proposed methodology. Several other actuation techniques, used in microfluidic applications, can also be readily incorporated in our modeling approach (e.g. thermocapillary migration, magnetic forces) as will be discussed in Section 9.3. The proposed formulation can even become more realistic by studying droplets resting on three-dimensional structured surfaces (see also the Section in the following Chapter) and by using more precise formulations of disjoining pressure profiles, i.e. with experimental force-distance isotherms, obtained from atomic force microscopy (AFM) [24]. Note that, however, the macroscopic droplet behavior, predicted by our model, seems to be virtually insensitive to the exact value of the disjoining pressure parameters (e.g. C_1, C_2, σ and ϵ, from Eq. 2.42) beyond a certain threshold (see also the sensitivity analysis is Section C.3 of Appendix C).

The model proposed in this Thesis, paired with optimization algorithms (e.g. gradient methods [25] or genetic algorithms [26]), can suggest the proper surface roughness geometry, in order to obtain certain apparent wettability and friction properties for the substrate, to facilitate (or prevent) the switching between Cassie-Baxter and Wenzel

wetting states and to directionally transfer droplet in lab-on-a-chip devices. The rational design of novel synthetic surfaces could contribute to the facing of contemporary engineering challenges (see also Section 1.2 of Chapter 1), such as freshwater shortage in arid areas (by using optimized fog harvesting surfaces inspired by the desert beetle), fuel economy in marine and airline industry (by reducing the drag on ship and airplane hulls with micro-structures inspired by the *Salvinia molesta* leaf) as well as better diagnostic technologies in developing countries (by using inexpensive lab-on-a-chip medical devices).

8.3 Impact on theoretical research

Apart from the benefits in the technological applications discussed above, our detailed simulations can also shed light to several physical mechanisms and explain experimental findings that cannot be clarified by the conventional theoretical models. In particular, in Chapters 4 and 5 we demonstrated the existence of multiple meta-stable wetting states on structured solid surfaces. Although meta-stable equilibrium states had been experimentally observed [27], the systematic study of the solid structure topography on the energy barriers (the minimum amount of energy required of a transition between meta-stable states) could not be performed, up to now. Moreover the fact that the dynamic contact angle derives implicitly in our simulations, as a result of the viscous dissipation above the arbitrary roughness of a solid surface (see Chapter 6), is a more sensible and accurate mechanism than using an explicitly imposed friction at the three-phase contact line(s). Obviously, the latter does not account for the exact solid surface topography. In addition the results presented in Chapter 7 can be extremely important for illuminating the onset of droplet motion on asymmetrically structured substrates. We note that this topic is still unclear and controversial in the literature [28, 29]. The derivation of such results would of course not have been possible by using the conventional Young-Laplace and hydrodynamic modeling approaches.

CHAPTER 9

Directions for future work

In this Chapter, we present the future perspectives of our research which are focused on four directions: (a) experimental validation of our model's predictions (e.g. the real-time tuning of the wettability of structured surfaces, based on electrowetting simulations presented in Chapter 5), (b) simulation of 3D droplets, (c) modeling of alternative droplet actuation techniques (thermocapillary convection, magnetic forces) on patterned solid substrates and (d) multi-scale modeling approaches so as to incorporate more realistic liquid-solid interactions.

9.1 Reversible wetting transitions on supehydrophobic surfaces

9.1.1 Theoretical establishment

As mentioned in Chapter 5 electrowetting is only efficient when applied on horizontal-smooth surfaces, on which only a limited range of apparent wettabilities is attainable, due to the constraints imposed by the material wettability (not exceeding 120^o in common hydrophobic materials) and the contact angle saturation phenomenon [30], which prevents apparent contact angle values from dropping below a certain value ($\sim 60^o$). When electrowetting is applied on a structured surface it can be efficient only uni-directionally, and in particular inducing transitions from super-hydrophobicity to hydrophilicity [31]; however, driving the reverse de-wetting transition is not feasible through voltage reduction or even by completely switching off the voltage application, thus, strong external actuations (e.g., thermal shocks [32]) are often required. These irreversibilities occur when a droplet undergoes a collapse transition from a Cassie-Baxter state (where air inclusions are trapped between the droplet and the solid structure) to a Wenzel wetting state (where the liquid fully impales the solid roughness). The latter corresponds to a local minimum of the free energy landscape, suggesting that an energy barrier has to be surpassed for a reverse de-wetting transition [6].

Several attempts have been made to prevent collapse transitions (Cassie-Baxter to Wenzel) on a structured surface subjected to electrowetting. In particular, Lapierre et al.

[33] achieved a small ranged contact angle reversibility interval (160^o - 130^o) by using specially designed substrates covered by two layers of packed silicon nanowires. Nevertheless, their poor mechanical properties, as well as their fairly complex fabrication technique render these substrates inappropriate for applications outside the laboratory. Later, Barberoglou et al. [34] demonstrated an electrowetting induced reversible contact angle modification on structured surfaces, which have been produced by laser irradiation. Although the reversibility range appears to be slightly wider in this case (140^o - 108^o), it is obscure whether the droplet at the final (reverted) state exhibits high mobility, which is the second requirement for superhydrophobicity. The wettability modification cannot be termed reversible if the above criterion is not met.

Here, guided by the detailed computations presented in Chapter 5, we experimentally verify that a fully reversible wettability tuning on superhydrophobic surfaces is possible when the dielectric thickness is sufficiently large, regardless of the topography of the structured solid. In particular, it was shown, in Section 5.2.3, that the local mean curvature of the droplet profile at the contact line (the droplet has a single contact line in this case since the substrate is smooth) exhibits strong dependence on the applied voltage when the solid dielectric layer is relatively thin ($\leqslant 10\,\mu m$) (see Fig. 5.7). Dielectrics of such a thickness are typically used in electrowetting experiments. Surprisingly enough, it was also found that when using a thicker dielectric layer ($> 50\,\mu m$), the mean curvature of the droplet profile remains virtually unaffected as the applied voltage increases. This behavior can be explained considering that the electrostatic pressure, acting on the droplet surface with a local negative contribution to the total pressure, is active at a length scale proportional to the thickness of the dielectric layer. When the dielectric layer is thin, the electrostatic pressure contribution is concentrated at the vicinity of the contact line, leading to a significant increase of the droplet local curvature. On the other hand, in the case of a thick dielectric layer, the electrostatic pressure contribution is scattered, resembling droplet compression experiments where a pressing force is applied to the entire droplet captured between two parallel plates [35].

The above could interpret experimental observations where specially designed, highly wetting resistant structured surfaces (e.g. with inverse-trapezoidal structures), cannot resist to a collapse transition, when subjected to electrowetting experiments (see e.g. [31, 32]), since the localized increase in the droplet curvature results in the liquid impalement into the solid roughness. Instead, we suggest that scattering of the electrostatic force along the droplet surface by using thick dielectric layers, would prevent the increase of the local curvature at the contact lines, which concomitantly would inhibit the liquid impalement into the solid roughness. Such a finding, that the only important requirement for contact angle reversibility is the thickness of the dielectric layer, regardless the specifics of the solid structure geometry, can be significantly useful for lab-on-a-chip applications. The above argument is next experimentally verified by demonstrating reversible wettability transitions on superhydrophobic surfaces.

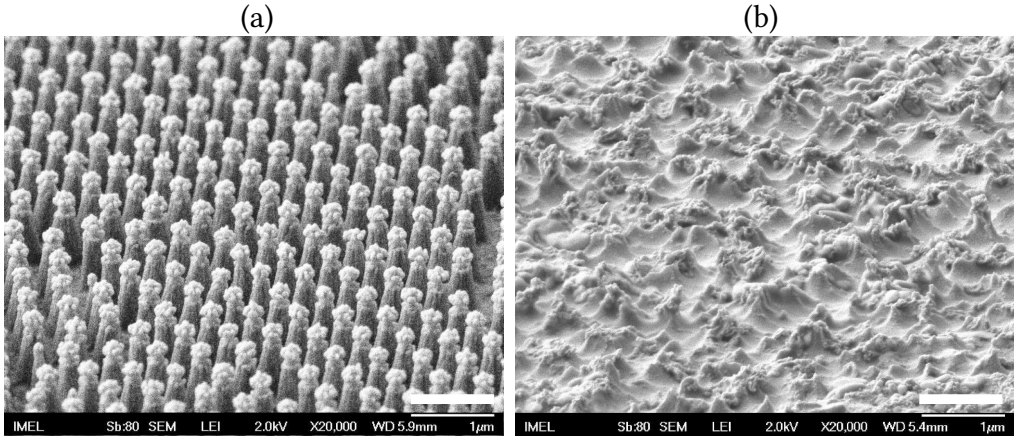

Figure 9.1: (a) SEM image of the solid surface topography displaying submicron (quasi-)ordered pillar arrays fabricated on the thin dielectric layer (400 nm TEOS and a 1 μm PMMA) and on the 75 μm SU8 film. (b) SEM image of the random micro-nanotextures fabricated on the 188 μm COP film. Scale bar = 1 μm.

9.1.2 Electrowetting experiments

Three different substrates (one thin and two thick) were used to test the effect of dielectric thickness on electrowetting behavior. First, we prepared one thin dielectric stack, consisting of a 400 nm tetraethoxysilane (TEOS) and a 1 μm poly(methyl methacrylate) (PMMA) layer, was assembled on a silicon wafer. Next, we prepared a 75 μm thick dielectric layer of SU8 photoresist. On top of these two stacks, submicron (quasi-)ordered pillar arrays were prepared, using a combination of colloidal lithography and plasma etching [36] (see Fig. 9.1a for a scanning electron micrograph of the topography). Finally, a random micro-nanostructure was fabricated on a 188 μm thick cyclic olefin copolymer (COP) film (see Fig. 9.1b). Details of the fabrication method are included in Appendix D. The apparent contact angle, θ_a, was measured using a real time image processing software that is developed in house and is based on drop shape analysis technique [30].

We initially conducted an electrowetting experiment on the thin dielectric substrate (1 um PMMA and 400 nm TEOS). Fig. 9.2a shows the dependence of the apparent contact angle, θ_a, on the electrowetting number, $\eta = \frac{cV^2}{2\gamma_{LA}}$, where c is the capacitance per unit area. The experimental setup is also demonstrated in the inset of Fig. 9.2a. In particular, the apparent wettability reduces by increasing the applied voltage, V, according the classic electrowetting model, given by an effective Lippmann equation [37] (solid line in Fig. 9.2a):

$$\cos\theta_a = \cos{\theta_a}^0 + \eta, \tag{9.1}$$

where ${\theta_a}^0$ is zero voltage apparent contact angle. When switching off the voltage application, however, we observe that the contact angle modification is irreversible for almost all the experimental points presented in Fig. 9.2a (with the exception of very low voltages, when $\eta < 5 \times 10^{-2}$). The apparent wettability reduction still follows the Lippmann

(a)

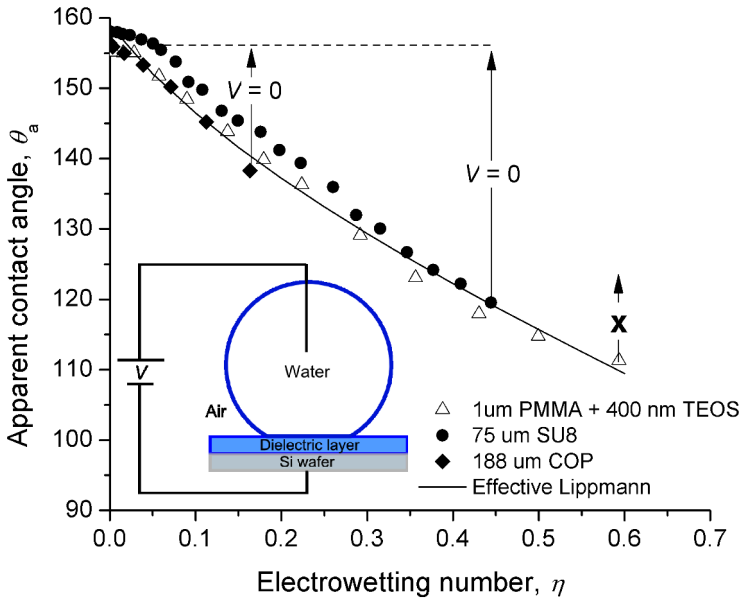

(b)

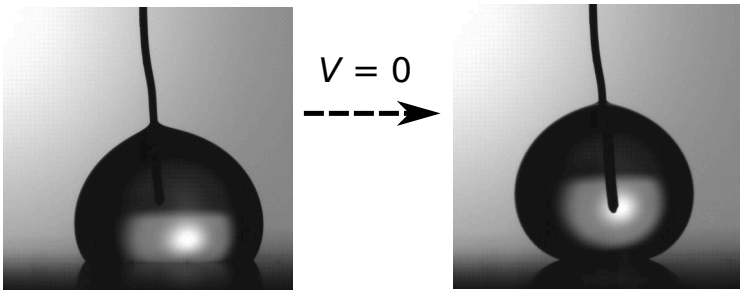

Figure 9.2: (a) Apparent contact angle vs electrowetting number, $\eta = \frac{c\,V^2}{2\,\gamma_{LA}}$, for a water droplet on structured surfaces featuring different dielectric thicknesses. The capacitance per unit area, $c = \frac{\epsilon_0 \epsilon_d}{d}$, is determined by fitting an effective Lippmann curve to the experimental measurements. In particular $c = 2 \times 10^{-5}$ F m^{-2} for the thin dielectric substrate (1 µm PMMA and 400 nm TEOS), $c = 3.1{\times}10^{-7}$ F m^{-2} for the 75 µm SU8 and $c = 7.8{\times}10^{-8}$ F m^{-2} for the 188 µm COP film, respectively. A schematic of the experimental setup is presented in the inset. (b) Snapshots demonstrating the contact angle reversibility (from 119° to 156°), when the voltage is switched off from 452 V, on a 75 µm thick SU8 substrate.

equation when performing the same electrowetting experiment on the thick dielectric substrates (75 um SU8 and 188 um COP). Surprisingly enough, when the applied voltage is removed in this case, the droplet retracts back almost to the initial superhydrophobic state from all the experimental points in Fig. 9.2a. Specifically, the maximum reversible contact angle modification observed is $\sim 37^o$, from 156^o to 119^o, in the case of SU8 (see Fig. 9.2b); this reversibility interval is considerably larger than any other relative experiment in the literature. We also remark that the above behavior has been successfully predicted by our previous computational analysis. Moreover, we note that the droplet mobility of the final state (when the voltage has been removed) has not been affected, indicating that the liquid has not impaled the solid roughness. In particular, the droplet still rolls-off easily, by tilting the substrate only by $\sim 2^o$.

Unfortunately, it was impossible to increase the apparent wettability up to complete wetting since the droplet shape exhibited instabilities for very high applied voltages. Thus, the minimum achieved apparent contact angle is 119^o for the SU8 and 138^o for the COP, respectively (see Fig. 9.2a). Specifically, in the conducted experiments, the droplet oscillates around the upper electrode, when approaching this wettability limit. The above limiting phenomenon cannot be attributed to the contact angle saturation [37] (see also Section 4.2.2 of Chapter 4) since the latter usually appears at $\sim 60^o$ for a water droplet in air ambient. A possible explanation is that the electric stresses along the outer three-phase contact line are unbalanced (the electric charge is not evenly distributed) due to infinitesimal dissimilarities of solid structure below the contact line, thus leading to a droplet bulk motion on the superhydrophobic surface. The above justifies why the wettability modification range is narrower in the case of the random micro-nanotextured substrate (COP film). We note that such a behavior is not observed in the thin dielectric case, due to the strong pinning of droplet on the solid structure (the liquid has impaled the solid roughness in this case).

Overall, considering that the two thick substrates (75 μm SU8 and 188 μm COP) have different surface topographies ((quasi-)ordered pillars and random micro-nanotextures) (see Fig. 9.1b) we conclude that the geometric details of the structure do not play a major role in the contact angle reversibility. Instead, we report that the electric field distribution along the droplet surface, which is controlled by the thickness of the dielectric layer, is the key factor, as shown in the computations in Chapter 5. Such a finding, that the contact angle reversibility is not connected with the solid structure detailed topography, opens new possibilities in manipulating micro-droplets, since the cost associated with the texture fabrication in miniaturized devices will be significantly reduced. We believe that the potential applications of the real-time tuning of the wettability on superhydrophobic surfaces, using electrowetting effect on a thick dielectric, are numerous and remain to be explored. The experimentally demonstrated contact angle reversibility opens new possibilities in manipulating micro-droplets, since the cost associated with the texture fabrication in miniaturized devices will be significantly reduced.

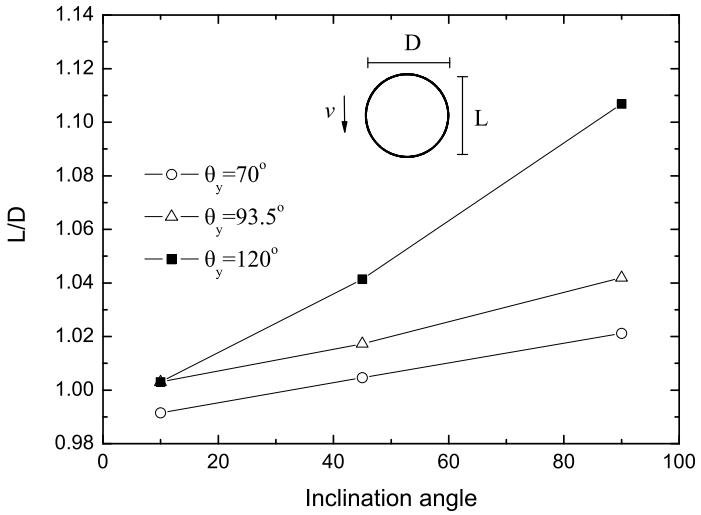

Figure 9.3: Footprint aspect ratio, of a glycerin/water mixture droplet, as a function of θ_{Y}; $\beta_{\mathrm{LS}} = 10^3$, $C_1 = 8$, $C_2 = 6$, $\sigma = 0.038$ and $\epsilon = 0.008$.

9.2 3D simulations

Despite that the two-dimensional simulations, presented in the previous Chapters, can effectively describe the static and dynamic droplet behavior in several cases, however, 3D simulations are crucial for understanding certain wetting phenomena (e.g the formation of oval droplets when sliding on an inclined solid surface [38]). In particular, in Fig. 9.3 we demonstrate the aspect ratio of a glycerin/water droplet's footprint as a function of the inclination angle for various material wettabilities, θ_{Y}, by using our proposed hydrodynamic model formulation (see Section 3.2.3). We note that, for the shake of computational efficiency, the above preliminary results have been obtained by considering an ideally smooth solid surface. It is interesting here that the droplet's aspect ratio increases with increasing hydrophobicity. Obviously, such a conclusion could not be derived by the previously presented 2D simulations.

Definitely, we can derive useful conclusions by performing 3D simulations on smooth solid surfaces, however, the solid topography has to be included in order to examine even more realistic cases (e.g. to investigate the viscous dissipation and friction of the contact lines on the roughness scale as well as the contact angle hysteresis). In this case, the computational cost may be considerably high, especially when the length scale of the solid structure is quite smaller than the nominal droplet radius. A methodology to reduce the computational requirements is to account for the solid roughness only in the vicinity of the outer three-phase contact line. The rest liquid-solid interfacial area, within the contact perimeter, can be considered as perfectly smooth, without any loss in the modeling accuracy (such an argument has been experimentally and computationally proved in recent studies [39, 40]). This work is among the subjects of our ongoing

research.

9.3 Modeling of alternative actuation techniques

9.3.1 Thermal actuation

When a temperature gradient is applied along a substrate (on which a droplet equilibrates) it induces surface tension gradients along the droplet surface, and in turn the presence of Marangoni stresses driving liquid flow from warmer to colder regions. The thermocapillary droplet migration has been the subject of several theoretical studies in the literature, which were mainly conducted under the thin film approximation [41, 42, 43]. Furthermore, several experimental studies of the droplet motion have been conducted [44, 45].

Recently, Dai et al. [46] investigated the influence of surface roughness and surface topography orientation and it was shown that the orientation of grinding scars may guide the motion direction of the droplet. To the best of our knowledge, however, the effect of the substrate topography has not been addressed theoretically in the literature due to the modeling limitations. Such a study can be easily performed by incorporating the Marangoni stresses at the stress balance along the droplet surface (Eq. 3.4) in our modeling approach. Such a work would be of great importance for thermocapillary-based microfluidic devices for trapping, sorting, mixing droplets, etc. [47].

9.3.2 Magnetic actuation

Alternatively, superparamagnetic droplets can also be effectively manipulated by using magnetic forces [48, 49]. In particular, as demonstrated in the literature, a magnetic field can actively actuate a droplet containing superparamagnetic nanoparticles and induce a Cassie-Baxter to Wenzel (and the reverse) wetting transition [50]. Once again the magnetic forces can be incorporating in our model, giving us the opportunity to study the physical phenomenon in detail, as well as to effectively design superparamagnetic droplet-based microfluidic devices.

9.4 Multiscale modeling

As discussed in Section 2.2.4, the exact modeling of the disjoining pressure action, would demand resolving multiple length scales, ranging from 10^{-9} m to 10^{-3} m. Such a task would be possible only by a multiscale modeling approach. In particular, simulations in the nanoscale (e.g. molecular dynamics) must be combined with the Navier-Stokes

equations. This is not a trivial work due to the tedious coupling of these very different descriptions of fluids, and in particular generating microscopic particle configurations from known macroscopic quantities such as density, momentum and energy. Although that several coupling schemes have been developed [51, 52, 53], the computational efficiency of such model is still relatively low.

In particular, Nie et al. [53] coupled the two descriptions by imposing continuity of fluxes at the boundaries of an overlap region. The mean particle velocities provide the boundary conditions for the Navier-Stokes solution at one side of the overlap region whereas a constrained dynamics algorithm forces the mean particle velocity to equal the continuum solution at the other side. We believe that such a multiscale approach, which is among the subjects of our ongoing research, will enable a more accurate description of the liquid-solid interactions, especially when simulating wetting on hierarchically structured superhydrophobic surfaces, where nano and/or micro-structures are superimposed on larger macro-structures.

References

[1] A. W. Adamson and A. P. Gast. *Physical Chemistry of Surfaces*. Wiley, 1997.

[2] P. Pujado, C. Huh, and L. Scriven. "On the attribution of an equation of capillarity to Young and Laplace". In: *Journal of Colloid and Interface Science* 38.3 (1972), pp. 662–663.

[3] R. Cox. "The dynamics of the spreading of liquids on a solid surface. Part 1. Viscous flow". In: *Journal of Fluid Mechanics* 168 (1986), pp. 169–194.

[4] V. M. Starov. "Surface forces action in a vicinity of three phase contact line and other current problems in kinetics of wetting and spreading". In: *Advances in Colloid and Interface Science* 161.1 (2010), pp. 139–152.

[5] N. T. Chamakos, M. E. Kavousanakis, and A. G. Papathanasiou. "Enabling efficient energy barrier computations of wetting transitions on geometrically patterned surfaces". In: *Soft Matter* 9.40 (2013), pp. 9624–9632.

[6] M. E. Kavousanakis, N. T. Chamakos, and A. G. Papathanasiou. "Connection of Intrinsic Wettability and Surface Topography with the Apparent Wetting Behavior and Adhesion Properties". In: *The Journal of Physical Chemistry C* 119.27 (2015), pp. 15056–15066.

[7] J.-Y. Park, M.-Y. Ha, H.-J. Choi, S.-D. Hong, and H.-S. Yoon. "A study on the contact angles of a water droplet on smooth and rough solid surfaces". In: *Journal of Mechanical Science and Technology* 25.2 (2011), pp. 323–332.

[8] E. S. Savoy and F. A. Escobedo. "Molecular simulations of wetting of a rough surface by an oily fluid: Effect of topology, chemistry, and droplet size on wetting transition rates". In: *Langmuir* 28.7 (2012), pp. 3412–3419.

[9] A Dupuis and J. Yeomans. "Modeling droplets on superhydrophobic surfaces: equilibrium states and transitions". In: *Langmuir* 21.6 (2005), pp. 2624–2629.

[10] M. E. Kavousanakis, C. E. Colosqui, I. G. Kevrekidis, and A. G. Papathanasiou. "Mechanisms of wetting transitions on patterned surfaces: continuum and mesoscopic analysis". In: *Soft Matter* 8.30 (2012), pp. 7928–7936.

[11] C. E. Colosqui, M. E. Kavousanakis, A. G. Papathanasiou, and I. G. Kevrekidis. "Mesoscopic model for microscale hydrodynamics and interfacial phenomena: Slip, films, and contact-angle hysteresis". In: *Physical Review E* 87.1 (2013), p. 013302.

[12] N. T. Chamakos, M. E. Kavousanakis, and A. G. Papathanasiou. "Neither Lippmann nor Young: Enabling Electrowetting Modeling on Structured Dielectric Surfaces". In: *Langmuir* 30.16 (2014), pp. 4662–4670.

[13] S Richardson. "On the no-slip boundary condition". In: *Journal of Fluid Mechanics* 59.04 (1973), pp. 707–719.

[14] K. M. Jansons. "Determination of the macroscopic (partial) slip boundary condition for a viscous flow over a randomly rough surface with a perfect slip microscopic boundary condition". In: *Physics of Fluids (1958-1988)* 31.1 (1988), pp. 15–17.

[15] N. T. Chamakos, M. E. Kavousanakis, A. G. Boudouvis, and A. G. Papathanasiou. "Droplet spreading on rough surfaces: Tackling the contact line boundary condition". In: *Physics of Fluids (1994-present)* 28.2 (2016), p. 022105.

[16] G. Karapetsas, N. T. Chamakos, and A. G. Papathanasiou. "Efficient modelling of droplet dynamics on complex surfaces". In: *Journal of Physics: Condensed Matter* 28.8 (2016), p. 085101.

[17] Y. Zheng, X. Gao, and L. Jiang. "Directional adhesion of superhydrophobic butterfly wings". In: *Soft Matter* 3.2 (2007), pp. 178–182.

[18] N. T. Chamakos, G. Karapetsas, and A. G. Papathanasiou. "How asymmetric surfaces induce directional droplet motion". In: *Colloids and Surfaces A: Physicochemical and Engineering Aspects* 511 (2016), pp. 180 –189.

[19] R. J. Vrancken, H. Kusumaatmaja, K. Hermans, A. M. Prenen, O. Pierre-Louis, C. W. Bastiaansen, and D. J. Broer. "Fully reversible transition from Wenzel to Cassie- Baxter states on corrugated superhydrophobic surfaces". In: *Langmuir* 26.5 (2009), pp. 3335–3341.

[20] M. E. Kavousanakis, C. E. Colosqui, and A. G. Papathanasiou. "Engineering the geometry of stripe-patterned surfaces toward efficient wettability switching". In: *Colloids and Surfaces A: Physicochemical and Engineering Aspects* 436 (2013), pp. 309–317.

[21] A. Cavalli, P. Bøggild, and F. Okkels. "Parametric optimization of inverse trapezoid oleophobic surfaces". In: *Langmuir* 28.50 (2012), pp. 17545–17551.

[22] A. Cavalli, P. Bøggild, and F. Okkels. "Topology optimization of robust superhydrophobic surfaces". In: *Soft Matter* 9.7 (2013), pp. 2234–2238.

[23] G Pashos, G Kokkoris, A. Papathanasiou, and A. Boudouvis. "Wetting transitions on patterned surfaces with diffuse interaction potentials embedded in a Young-Laplace formulation". In: *The Journal of Chemical Physics* 144.3 (2016), p. 034105.

[24] D. Bhatt, J. Newman, and C. Radke. "Equilibrium force isotherms of a deformable bubble/drop interacting with a solid particle across a thin liquid film". In: *Langmuir* 17.1 (2001), pp. 116–130.

[25] E. Polak. *Optimization: algorithms and consistent approximations*. Vol. 124. Springer Science & Business Media, 2012.

[26] M. Gen and R. Cheng. *Genetic algorithms and engineering optimization*. Vol. 7. John Wiley & Sons, 2000.

[27] E. Bormashenko, R. Pogreb, G. Whyman, and M. Erlich. "Resonance Cassie-Wenzel wetting transition for horizontally vibrated drops deposited on a rough surface". In: *Langmuir* 23.24 (2007), pp. 12217–12221.

[28] A Buguin, L Talini, and P Silberzan. "Ratchet-like topological structures for the control of microdrops". In: *Applied Physics A* 75.2 (2002), pp. 207–212.

[29] N. Tretyakov and M. Müller. "Directed transport of polymer drops on vibrating superhydrophobic substrates: a molecular dynamics study". In: *Soft Matter* 10.24 (2014), pp. 4373–4386.

[30] A. Papathanasiou, A. Papaioannou, and A. Boudouvis. "Illuminating the connection between contact angle saturation and dielectric breakdown in electrowetting through leakage current measurementsa)". In: *Journal of Applied Physics* 103.3 (2008), p. 034901.

[31] T. N. Krupenkin, J. A. Taylor, T. M. Schneider, and S. Yang. "From rolling ball to complete wetting: the dynamic tuning of liquids on nanostructured surfaces". In: *Langmuir* 20.10 (2004), pp. 3824–3827.

[32] T. N. Krupenkin, J. A. Taylor, E. N. Wang, P. Kolodner, M. Hodes, and T. R. Salamon. "Reversible wetting-dewetting transitions on electrically tunable superhydrophobic nanostructured surfaces". In: *Langmuir* 23.18 (2007), pp. 9128–9133.

[33] F. Lapierre, V. Thomy, Y. Coffinier, R. Blossey, and R. Boukherroub. “Reversible electrowetting on superhydrophobic double-nanotextured surfaces”. In: *Langmuir* 25.11 (2009), pp. 6551–6558.

[34] M. Barberoglou, V. Zorba, A. Pagozidis, C. Fotakis, and E. Stratakis. “Electrowetting properties of micro/nanostructured black silicon”. In: *Langmuir* 26.15 (2010), pp. 13007–13014.

[35] S.-J. Hong, T.-H. Chou, S. H. Chan, Y.-J. Sheng, and H.-K. Tsao. “Droplet compression and relaxation by a superhydrophobic surface: Contact angle hysteresis”. In: *Langmuir* 28.13 (2012), pp. 5606–5613.

[36] K. Ellinas, M. Chatzipetrou, I. Zergioti, A. Tserepi, and E. Gogolides. “Superamphiphobic Polymeric Surfaces Sustaining Ultrahigh Impact Pressures of Aqueous High-and Low-Surface-Tension Mixtures, Tested with Laser-Induced Forward Transfer of Drops”. In: *Advanced Materials* 27.13 (2015), pp. 2231–2235.

[37] F. Mugele, M. Duits, and D. Van den Ende. “Electrowetting: a versatile tool for drop manipulation, generation, and characterization”. In: *Advances in Colloid and Interface Science* 161.1 (2010), pp. 115–123.

[38] N. Le Grand, A. Daerr, and L. Limat. “Shape and motion of drops sliding down an inclined plane”. In: *Journal of Fluid Mechanics* 541 (2005), pp. 293–315.

[39] Y. Wang and S. Chen. “Numerical study on droplet sliding across micropillars”. In: *Langmuir* 31.16 (2015), pp. 4673–4677.

[40] C. W. Extrand. “Origins of Wetting”. In: *Langmuir* 32.31 (2016), pp. 7697–7706.

[41] F. Brochard. “Motions of droplets on solid surfaces induced by chemical or thermal gradients”. In: *Langmuir* 5.2 (1989), pp. 432–438.

[42] M. L. Ford and A. Nadim. “Thermocapillary migration of an attached drop on a solid surface”. In: *Physics of Fluids (1994-present)* 6.9 (1994), pp. 3183–3185.

[43] V. Pratap, N. Moumen, and R. S. Subramanian. “Thermocapillary Motion of a Liquid Drop on a Horizontal Solid Surface”. In: *Langmuir* 24.9 (2008), pp. 5185–5193.

[44] J. B. Brzoska, F. Brochard-Wyart, and F. Rondelez. “Motions of droplets on hydrophobic model surfaces induced by thermal gradients”. In: *Langmuir* 9.8 (1993), pp. 2220–2224.

[45] J. Z. Chen, S. M. Troian, A. A. Darhuber, and S. Wagner. “Effect of contact angle hysteresis on thermocapillary droplet actuation”. In: *Journal of Applied Physics* 97.1 (2005), p. 014906.

[46] Q. Dai, W. Huang, and X. Wang. “Surface roughness and orientation effects on the thermocapillary migration of a droplet of paraffin oil”. In: *Experimental Thermal and Fluid Science* 57 (2014), pp. 200–206.

[47] A. Karbalaei, R. Kumar, and H. J. Cho. “Thermocapillarity in Microfluidics—A Review”. In: *Micromachines* 7.1 (2016), p. 13.

[48] A. Papathanasiou and A. Boudouvis. “Wetting effects on magneto-hydrostatics of rotating ferrofluid drops: experimental and computational analysis”. In: *Journal of Magnetism and Magnetic Materials* 252 (2002), pp. 262–264.

[49] L. Mats, R. Young, G. T. Gibson, and R. D. Oleschuk. “Magnetic droplet actuation on natural (Colocasia leaf) and fluorinated silica nanoparticle superhydrophobic surfaces”. In: *Sensors and Actuators B: Chemical* 220 (2015), pp. 5 –12. ISSN: 0925-4005.

[50] Z. Cheng, H. Lai, N. Zhang, K. Sun, and L. Jiang. “Magnetically induced reversible transition between Cassie and Wenzel states of superparamagnetic microdroplets on highly hydrophobic silicon surface”. In: *The Journal of Physical Chemistry C* 116.35 (2012), pp. 18796–18802.

[51] S. T. O’Connell and P. A. Thompson. “Molecular dynamics–continuum hybrid computations: a tool for studying complex fluid flows”. In: *Physical Review E* 52.6 (1995), R5792.

[52] E. Flekkøy, G Wagner, and J Feder. “Hybrid model for combined particle and continuum dynamics”. In: *EPL (Europhysics Letters)* 52.3 (2000), p. 271.

[53] X. Nie, S. Chen, M. Robbins, et al. “A continuum and molecular dynamics hybrid method for micro-and nano-fluid flow”. In: *Journal of Fluid Mechanics* 500 (2004), pp. 55–64.

PART V

Appendices

APPENDIX A

A.1 Derivation of the Young-Laplace equation

We consider a small enough section of an arbitrary surface, that the two radii of curvature, R_1, R_2, are essentially constant (see Fig. A.1). If the surface is displaced by a small distance outward (dz), the change in the surface area will be: $(\lambda_1 + \mathrm{d}\lambda_1)(\lambda_2 + \mathrm{d}\lambda_2) - \lambda_1\lambda_2 = \lambda_1\mathrm{d}\lambda_1 + \lambda_2\mathrm{d}\lambda_2$. Thus, considering that there is a pressure difference, Δp, across the interface, the necessary work will be:

$$W = \gamma\,(\lambda_1\mathrm{d}\lambda_1 + \lambda_2\mathrm{d}\lambda_2) - \Delta p\lambda_1\lambda_2\mathrm{d}z, \tag{A.1}$$

where γ is the interfacial tension. Moreover, from a comparison of similar triangles (see Fig. A.1), it follows that:

$$\frac{\lambda_1 + \mathrm{d}\lambda_1}{R1 + \mathrm{d}z} = \frac{\lambda_1}{R_1} \;\Rightarrow \mathrm{d}\lambda_1 = \frac{\lambda_1\mathrm{d}z}{R_1}, \tag{A.2a}$$

$$\frac{\lambda_2 + \mathrm{d}\lambda_2}{R2 + \mathrm{d}z} = \frac{\lambda_2}{R_2} \;\Rightarrow \mathrm{d}\lambda_2 = \frac{\lambda_2\mathrm{d}z}{R_2}. \tag{A.2b}$$

In equilibrium state, Eq. A.1 equals to zero, thus by using Eqs. A.2a and A.2b for dλ_1 and dλ_2, yields [1]:

$$\Delta p = \gamma\left(\frac{1}{R_1} + \frac{1}{R_2}\right), \tag{A.3}$$

where the sum, $\frac{1}{R_1} + \frac{1}{R_2}$, corresponds to local mean curvature, $\frac{C}{R_0}$, of this small section of the surface (see also Section A.2). Eq. A.3 is the fundamental equation of capillarity (given in 1805 by Thomas Young and by Pierre-Simon Laplace), referred as the Young-Laplace equation [2]. We note that for the case of both radii being equal, Eq. A.3 simple reduces to Eq. 2.3.

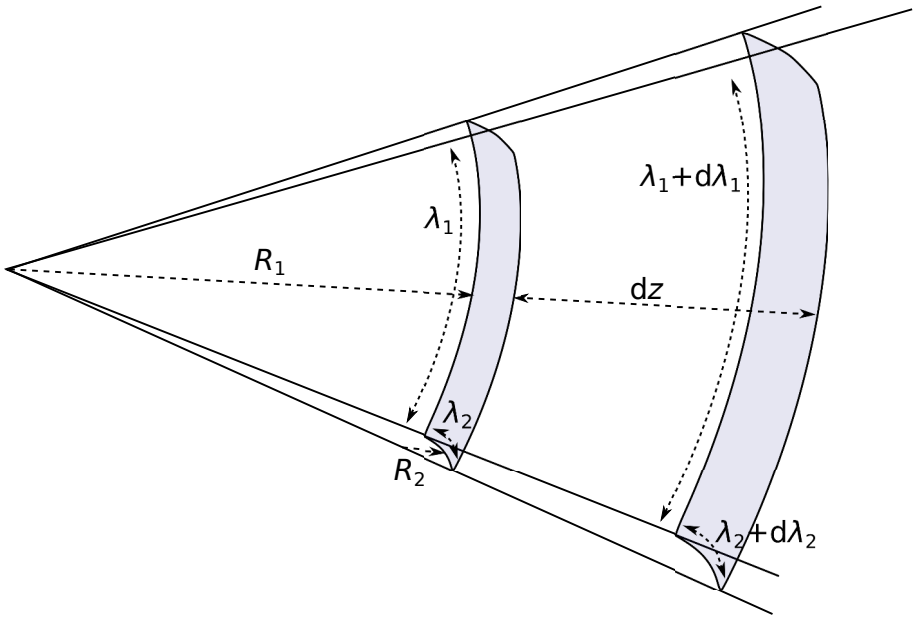

Figure A.1: Principal radii of curvature, R_1, R_2, of a small section of an arbitrary surface.

A.2 Evaluation of the local mean curvature

The local mean curvature of the droplet surface is evaluated as [3]:

$$C = \nabla_s \cdot \boldsymbol{n} = \frac{2PM - QN - GL}{H^2}, \tag{A.4}$$

where, $\boldsymbol{n}$ is the unit normal of the surface, ∇_s is the surface gradient operator ($\nabla_s = \nabla - \boldsymbol{n}(\boldsymbol{n} \cdot \nabla)$) and G, Q, P the first order magnitudes. The latter equal to:

$$G = \boldsymbol{p}^2 H^2, \tag{A.5}$$

$$Q = \boldsymbol{q}^2 H^2, \tag{A.6}$$

$$P = -\boldsymbol{p} \cdot \boldsymbol{q} H^2. \tag{A.7}$$

In the above, $H = \boldsymbol{n} \cdot (\boldsymbol{F}_{w1} \times \boldsymbol{F}_{w2})$, with $\boldsymbol{F}$ is the position vector of a point on the droplet surface (with $w1$, $w2$ the independent variables) and $\boldsymbol{n}$ the unit normal of the droplet surface ($\boldsymbol{n} = \frac{\boldsymbol{F}_{w1} \times \boldsymbol{F}_{w2}}{|\boldsymbol{F}_{w1} \times \boldsymbol{F}_{w2}|}$), $\boldsymbol{p} = \frac{\boldsymbol{F}_{w1} \times \boldsymbol{n}}{H}$ and $\boldsymbol{q} = \frac{\boldsymbol{n} \times \boldsymbol{F}_{w2}}{H}$. In addition, the second order magnitudes L, M, N equal to:

$$L = \boldsymbol{F}_{w1\ w1} \cdot \boldsymbol{n}, \tag{A.8}$$

$$M = \boldsymbol{F}_{w1\ w2} \cdot \boldsymbol{n}, \tag{A.9}$$

$$N = \boldsymbol{F}_{w2\ w2} \cdot \boldsymbol{n}. \tag{A.10}$$

where $\boldsymbol{F}_{w1} = \frac{\mathrm{d}\boldsymbol{F}}{\mathrm{d}w1}$, $\boldsymbol{F}_{w2} = \frac{\mathrm{d}\boldsymbol{F}}{\mathrm{d}w2}$, $\boldsymbol{F}_{w1w1} = \frac{\mathrm{d}^2\boldsymbol{F}}{\mathrm{d}w1^2}$ and $\boldsymbol{F}_{w2w2} = \frac{\mathrm{d}^2\boldsymbol{F}}{\mathrm{d}w2^2}$, $\boldsymbol{F}_{w1w2} = \frac{\mathrm{d}^2\boldsymbol{F}}{\mathrm{d}w1\mathrm{d}w2}$.

Next, we will demonstrate the evaluation of the local mean curvature of an axisymmetric droplet, parameterized in terms of the arc-length, s, of the intersection of the droplet

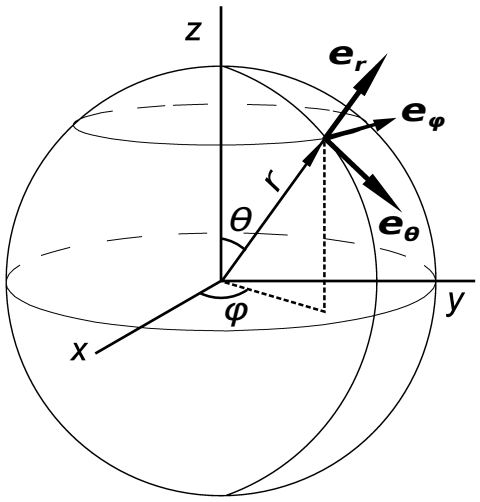

Figure A.2: Unit vectors, $\boldsymbol{e_r}$, $\boldsymbol{e_\theta}$, $\boldsymbol{e_\phi}$, of the spherical coordinate system.

surface with a vertical plane (see Section 2.2.4) and the azimuthal angle, ϕ, of the spherical coordinates (see Fig. A.2). In particular, a general formula of the position vector of a point on a surface, in Cartesian coordinates, reads:

$$\boldsymbol{F}(s,\phi) = x\boldsymbol{i} + y\boldsymbol{j} + z\boldsymbol{k}, \tag{A.11}$$

where $\boldsymbol{i}$, $\boldsymbol{j}$, $\boldsymbol{k}$ are the unit vectors of the Cartesian coordinate system in x, y and z direction, respectively. The above relation can be expressed in spherical coordinates, by using the following transformations:

$$x = r\sin\theta\cos\phi, \tag{A.12a}$$
$$y = r\sin\theta\sin\phi, \tag{A.12b}$$
$$z = r\cos\theta, \tag{A.12c}$$

and

$$\boldsymbol{i} = \sin\theta\cos\phi\boldsymbol{e_r} + \cos\theta\cos\phi\boldsymbol{e_\theta} - \sin\phi\boldsymbol{e_\phi}, \tag{A.13a}$$
$$\boldsymbol{j} = \sin\theta\sin\phi\boldsymbol{e_r} + \cos\theta\sin\phi\boldsymbol{e_\theta} + \cos\phi\boldsymbol{e_\phi}, \tag{A.13b}$$
$$\boldsymbol{k} = \cos\theta\boldsymbol{e_r} - \sin\theta\boldsymbol{e_\theta}, \tag{A.13c}$$

where, $\boldsymbol{e_r}$, $\boldsymbol{e_\theta}$, $\boldsymbol{e_\phi}$ are the unit vectors of the spherical coordinate system (see Fig A.2). Therefore, Eq. A.11 now reads:

$$\boldsymbol{F}(s,\phi) = r\boldsymbol{e_r}. \tag{A.14}$$

By assuming axial symmetry around the z-axis ($\frac{\mathrm{d}r}{\mathrm{d}\phi} = 0$, $\frac{\mathrm{d}\theta}{\mathrm{d}\phi} = 0$ and $\frac{\mathrm{d}\phi}{\mathrm{d}s} = 0$) (see Fig. A.2),

the unit normal on the droplet surface is then evaluated as:

$$\begin{aligned} \boldsymbol{n} &= \frac{\boldsymbol{F}_s \times \boldsymbol{F}_\phi}{|\boldsymbol{F}_s \times \boldsymbol{F}_\phi|} \Rightarrow \\ \boldsymbol{n} &= \frac{r\theta_s \boldsymbol{e_r} - r_s \boldsymbol{e_\theta}}{\sqrt{r^2\theta_s^2 + r_s^2}}, \end{aligned} \tag{A.15}$$

where $r_s = \frac{\mathrm{d}r}{\mathrm{d}s}$ and $\theta_s = \frac{\mathrm{d}\theta}{\mathrm{d}s}$. The scalar triple vector, H, is evaluated as:

$$\begin{aligned} H &= \boldsymbol{n} \cdot \left(\boldsymbol{F}_s \times \boldsymbol{F}_\phi\right) \Rightarrow \\ H &= r\sin\theta \sqrt{r^2\theta_s^2 + r_s^2}, \end{aligned} \tag{A.16}$$

and the vectors $\boldsymbol{p}, \boldsymbol{q}$ read:

$$\boldsymbol{p} = \frac{\boldsymbol{F}_\phi \times \boldsymbol{n}}{H} = \frac{r_s}{r^2\theta_s^2 + r_s^2}\boldsymbol{e_r} + \frac{r\theta_s}{r^2\theta_s^2 + r_s^2}\boldsymbol{e_\theta}, \tag{A.17a}$$

$$\boldsymbol{q} = \frac{\boldsymbol{n} \times \boldsymbol{F}_s}{H} = \frac{\boldsymbol{e_\phi}}{r\sin\theta}. \tag{A.17b}$$

We then compute the first order magnitudes G, Q, P:

$$G = r^2\sin^2\theta, \tag{A.18a}$$

$$Q = r^2\theta_s^2 + r_s^2, \tag{A.18b}$$

$$P = 0, \tag{A.18c}$$

and the second order magnitudes L, M, N:

$$L = \frac{\left(r_{ss} - r\theta_s^2\right) r\theta_s - \left(2r_s\theta_s + r\theta_{ss}\right) r_s}{\sqrt{r^2\theta_s^2 + r_s^2}}, \tag{A.19a}$$

$$M = 0, \tag{A.19b}$$

$$N = \frac{rr_s\sin\theta\cos\theta - r^2\sin^2\theta\theta_s}{\sqrt{r^2\theta_s^2 + r_s^2}}, \tag{A.19c}$$

where $F_{ss} = \left(r_{ss} - r\theta_s^2\right)\boldsymbol{e_r} + \left(2r_s\theta_s + r\theta_{ss}\right)\boldsymbol{e_\theta}$, $F_{s\phi} = \left(r_s\sin\theta + r\theta_s\cos\theta\right)\boldsymbol{e_\phi}$, $F_{\phi\phi} = -r\sin^2\theta\boldsymbol{e_r} - r\sin\theta\cos\theta\boldsymbol{e_\theta}$, $r_{ss} = \frac{\mathrm{d}^2r}{\mathrm{d}s^2}$ and $\theta_{ss} = \frac{\mathrm{d}^2\theta}{\mathrm{d}s^2}$. The local mean curvature is finally evaluated from Eq. A.4:

$$\begin{aligned} C &= \frac{2PM - QN - GL}{H^2} \Rightarrow \\ C &= \frac{1}{r\sin\theta\sqrt{r^2\theta_s^2 + r_s^2}}\left[2r\theta_s\sin\theta - r_s\cos\theta + r\sin\theta\frac{\mathrm{d}}{\mathrm{d}s}\arctan\left(\frac{r\theta_s}{r_s}\right)\right], \end{aligned} \tag{A.20}$$

as also presented in Section 2.2.4.

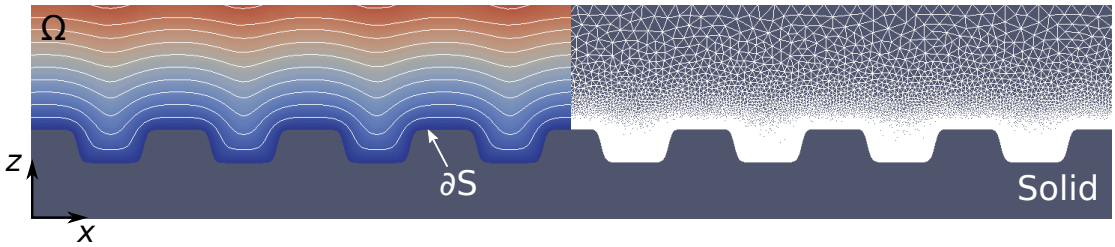

Figure A.3: Eikonal equation solution and contour lines of constant distance, δ, from a geometrically structured boundary (left side of the figure), along with the unstructured computational mesh, generated by the Gmsh software [6] (right side of the figure). The mesh is refined close to the solid boundary, ∂S, where high resolution is required.

A.3 Eikonal equation

As previously reported, the disjoining pressure, p^{LS}, is a function of the Euclidean distance from the solid boundary. In the case of geometrically structured surfaces, the liquid-solid distance is calculated from the solution of the Eikonal equation, which reads [4]:

$$\mid \nabla\delta(x,z) \mid = 1,\ x,z\ \in\ \Omega, \tag{A.21a}$$

$$\delta(x,z) = 0,\ x,z\ \in\ \partial S, \tag{A.21b}$$

where Ω denotes the two-dimensional computational domain and ∂S is the solid surface boundary (see Fig. A.3). The numerical solution of Eq. A.21a is a challenging task, and among the proposed solution schemes we adopt the vanishing viscosity method [5]:

$$\mid \nabla\delta \mid -\phi^{\mathrm{E}}\nabla^2\delta = 1,\ x,z\ \in\ \Omega, \tag{A.22}$$

where ϕ^{E} is a small scalar (numerical diffusion coefficient). When $\phi^{\mathrm{E}} \to 0$, Eq. A.22 yields the original formulation of the Eikonal equation (Eq. A.21a). The non-linear differential Eq. A.22 is discretized with the Finite Element Method (where the computational mesh is generated by using the Gmsh software [6] as shown Fig. A.3), accounting for the boundary condition A.21b and is solved with the iterative Newton-Raphson method in an in-house code.

We note that the solution $\delta(x,z)$ constitutes a $\mathbb{R}^2 \to \mathbb{R}$ mapping, i.e., for each point (x,z) of the two dimensional domain Ω, there exists a unique δ corresponding to the signed distance from the solid boundary ∂S. It is also notable that the added computational cost from the solution of the Eikonal equation is negligible, since a single Eikonal equation solution is required for a particular solid surface geometry.

APPENDIX B

B.1 Galerkin residuals

In the Galerkin finite element method [7], the solution of a differential equation is approximated by a finite sum of basis functions (usually first or second-order polynomials). The approximate solution is then the coefficient value of each of the basis function. The latter is found by minimizing the error between the linear combination of basis functions and actual solution (Galerkin residuals).

The Galerkin residuals, $\boldsymbol{R}$, of the dimensionless augmented Young-Laplace equation, in arc-length parameterization (i.e., $\widehat{r}(\widehat{s})$, $\theta(\widehat{s})$), are built by multiplying Eq. 2.32 by each of the basis functions, ϕ^{k}, and integrating the product over the entire droplet domain:

$$\boldsymbol{R} = \int_0^{\widehat{y}_{\max}} \int_0^{\widehat{s}_{\max}} \phi^{\mathrm{k}} \left(\frac{R_0}{\gamma_{\mathrm{LA}}} p^{\mathrm{LS}} + C - K \right) \sqrt{\widehat{r}^2 \, \widehat{\theta}_s^{\,2} + \widehat{r}_s^{\,2}} \, \mathrm{d}\widehat{s} \mathrm{d}\widehat{y}, \tag{B.1}$$

where $\widehat{r} = r/R_0$, $\widehat{s} = s/R_0$, $\widehat{y} = y/R_0$, $\widehat{r}_s = \mathrm{d}\widehat{r}/\mathrm{d}\widehat{s}$, $\widehat{\theta}_s = \mathrm{d}\theta/\mathrm{d}\widehat{s}$, $\widehat{y}_{\max}$ is the dimensionless width of the cylindrical droplet (see Fig. 4.4) and $\sqrt{\widehat{r}^2 \, \widehat{\theta}_s^{\,2} + \widehat{r}_s^{\,2}} \, \mathrm{d}\widehat{s} \, \mathrm{d}\widehat{y}$ is free surface area element (dimensionless), by considering a translationally symmetric case. For the shake of simplicity, in the following relations we have omitted the hat symbol ($\widehat{\ }$) from the dimensionless quantities. Next, we perform integration by parts of the curvature term in order to reduce the second-order derivatives to a first-order. This step is required so as to introduce the first-order derivative boundary conditions (2.35 and 2.36) in the

Galerkin residuals. In particular:

$$\boldsymbol{R} = \int_0^{s_{\max}} \phi^{\mathrm{k}} \left(\frac{R_0}{\gamma_{\mathrm{LA}}} p^{\mathrm{LS}} + C - K \right) \sqrt{r^2\,\theta_s^2 + r_s^2}\; y_{\max}\,\mathrm{d}s \xrightarrow{y_{\max}=1}$$

$$\boldsymbol{R} = \int_0^{s_{\max}} \phi^{\mathrm{k}} \left(\frac{R_0}{\gamma_{\mathrm{LA}}} p^{\mathrm{LS}} + C - K \right) \sqrt{r^2\,\theta_s^2 + r_s^2}\,\mathrm{d}s \xrightarrow{\text{Eq. 2.40}}$$

$$\boldsymbol{R} = \int_0^{s_{\max}} \phi^{\mathrm{k}}\,\theta_s\,\mathrm{d}s + \int_0^{s_{\max}} \phi^{\mathrm{k}} \frac{\mathrm{d}}{\mathrm{d}s} \left[\arctan\left(\frac{r\,\theta_s}{r_s} \right) \right] \mathrm{d}s$$

$$- \int_0^{s_{\max}} \phi^{\mathrm{k}}\,K \sqrt{r^2\,\theta_s^2 + r_s^2}\,\mathrm{d}s + \int_0^{s_{\max}} \phi^{\mathrm{k}} \frac{R_0}{\gamma_{\mathrm{LA}}} p^{\mathrm{LS}} \sqrt{r^2\,\theta_s^2 + r_s^2}\,\mathrm{d}s \Rightarrow$$

$$\boldsymbol{R} = \int_0^{s_{\max}} \phi^{\mathrm{k}}\,\theta_s\,\mathrm{d}s - \int_0^{s_{\max}} \phi^{\mathrm{k}} K \sqrt{r^2\,\theta_s^2 + r_s^2}\,\mathrm{d}s + \int_0^{s_{\max}} \phi^{\mathrm{k}} \frac{R_0}{\gamma_{\mathrm{LA}}} p^{\mathrm{LS}} \sqrt{r^2\,\theta_s^2 + r_s^2}\,\mathrm{d}s$$

$$- \int_0^{s_{\max}} \frac{\mathrm{d}\phi^{\mathrm{k}}}{\mathrm{d}s} \arctan\left(\frac{r\,\theta_s}{r_s} \right) \mathrm{d}s + \left[\phi^{\mathrm{k}} \arctan\left(\frac{r\,\theta_s}{r_s} \right) \right]_0^{s_{\max}}. \tag{B.2}$$

The boundary conditions (2.35 and 2.36) are then incorporated in the latter term as follows:

$$\left[\phi^{\mathrm{k}} \arctan\left(\frac{r\,\theta_s}{r_s} \right) \right]_0^{s_{\max}} = \frac{\pi}{2}\Big|_{s=s_{\max}} - \frac{\pi}{2}\Big|_{s=0}. \tag{B.3}$$

Thus, by using Eq. B.3 and Eq. 2.42, Eq. B.2 reads:

$$\begin{aligned} \boldsymbol{R} = & \int_0^{s_{\max}} \phi^{\mathrm{k}}\,\theta_s\,\mathrm{d}s - \int_0^{s_{\max}} \phi^{\mathrm{k}}\,K \sqrt{r^2\,\theta_s^2 + r_s^2}\,\mathrm{d}s \\ & + \int_0^{s_{\max}} \phi^{\mathrm{k}}\,w^{\mathrm{LS}} \left[\left(\frac{\sigma}{\delta+\epsilon} \right)^{C_1} - \left(\frac{\sigma}{\delta+\epsilon} \right)^{C_2} \right] \sqrt{r^2\,\theta_s^2 + r_s^2}\,\mathrm{d}s \\ & - \int_0^{s_{\max}} \frac{\mathrm{d}\phi^{\mathrm{k}}}{\mathrm{d}s} \arctan\left(\frac{r\,\theta_s}{r_s} \right) \mathrm{d}s - \frac{\pi}{2}\Big|_{s=0} + \frac{\pi}{2}\Big|_{s=s_{\max}}, \end{aligned} \tag{B.4}$$

where the last two terms are included only at the first ($s = 0$) and the last ($s = s_{\max}$) residual, respectively. Similarly, the Galerkin weighted residuals of the augmented Young-Laplace equation in the case of an axially symmetric droplet read:

$$\begin{aligned} \boldsymbol{R} = & \int_0^{s_{\max}} 4\,\pi \phi^{\mathrm{k}}\,r\,\theta_s \sin\theta\,\mathrm{d}s - \int_0^{s_{\max}} 2\,\pi\,\phi^{\mathrm{k}}\,u_s \cos\theta\,\mathrm{d}s \\ & - \int_0^{s_{\max}} 2\,\pi \frac{\mathrm{d}\phi^{\mathrm{k}}}{\mathrm{d}s} r \sin\theta \arctan\left(\frac{r\,\theta_s}{r_s} \right) \mathrm{d}s - \int_0^{s_{\max}} 2\,\pi\,\phi^{\mathrm{k}}\,r_s \sin\theta \arctan\left(\frac{r\,\theta_s}{r_s} \right) \mathrm{d}s \\ & - \int_0^{s_{\max}} 2\,\pi\,\phi^{\mathrm{k}}\,r \cos\theta \arctan\left(\frac{r\,\theta_s}{r_s} \right) \mathrm{d}s - \int_0^{s_{\max}} 2\,\pi\,\phi^{\mathrm{k}}\,K\,r \sin\theta \sqrt{r^2\,\theta_s^2 + r_s^2}\,\mathrm{d}s \\ & + \int_0^{s_{\max}} 2\,\pi\,\phi^{\mathrm{k}}\,w^{\mathrm{LS}} \left[\left(\frac{\sigma}{\delta+\epsilon} \right)^{C_1} - \left(\frac{\sigma}{\delta+\epsilon} \right)^{C_2} \right] r \sin\theta \sqrt{r^2\,\theta_s^2 + r_s^2}\,\mathrm{d}s, \end{aligned} \tag{B.5}$$

where the free surface area element of the droplet is $r \sin\theta \sqrt{r^2\,\theta_s^2 + r_s^2}\,\mathrm{d}s\,\mathrm{d}\phi$ in this case

(ϕ is the azimuthal angle). Details about the discretization of the conventional Young-Laplace equation (2.20) can be found in [8].

B.2 Pseudo arc-length continuation

The dependence of the droplet shape on parameter value, e.g. the wetting parameter, w^{LS}, is of utmost importance for the studied problems. At some critical values of w^{LS} parameter, however, the solution stability changes (see e.g. the turning points in Fig. B.3) and the ordinary parameter continuation fails. In particular, in the general case, the discretization of a boundary value problem (e.g., with the finite element method), produces a set of non-linear equations which is solved iteratively by the Newton-Raphson algorithm. In the turning points, however, the Jacobian matrix (the matrix of all first-order partial derivatives of the residual vector, $\boldsymbol{R}$) becomes singular and the Newton-Raphson method fails to converge. To overcome this failure we apply special parameter continuation techniques such as the pseudo arc-length continuation [9]. In this method, a new monotonically increasing parameter -the arc-length of the solution branch, s_{cont}- is introduced and the solution vector, in the case of the augmented YL equation, $\boldsymbol{U} = [r\ \theta]^{\mathrm{T}}$, as well as the wetting parameter, w^{LS}, are expressed as functions of this new parameter: $\boldsymbol{U} = \boldsymbol{U}(s_{\mathrm{cont}})$, $w^{\mathrm{LS}} = w^{\mathrm{LS}}(s_{\mathrm{cont}})$. In addition, the system of equations is augmented with an extra constraint that determines the value of s_{cont}, which reads [9]:

$$\| \boldsymbol{U}(s_{\mathrm{cont}}) - \boldsymbol{U}(s_{\mathrm{cont,0}}) \|^2 + \left[w^{\mathrm{LS}}(s_{\mathrm{cont}}) - w^{\mathrm{LS}}(s_{\mathrm{cont,0}}) \right]^2 = \left(s_{\mathrm{cont}} - s_{\mathrm{cont,0}} \right)^2, \tag{B.6}$$

where $s_{\mathrm{cont,0}}$ is the previous value of the parameter. Finally, the augmented system of equations becomes:

$$\begin{bmatrix} \frac{\mathrm{d}\boldsymbol{R}}{\mathrm{d}\boldsymbol{U}} & \frac{\mathrm{d}\boldsymbol{R}}{\mathrm{d}s_{\mathrm{cont}}} \\ \frac{\mathrm{d}R_{\mathrm{cont}}}{\mathrm{d}\boldsymbol{U}} & \frac{\mathrm{d}R_{\mathrm{cont}}}{\mathrm{d}s_{\mathrm{cont}}} \end{bmatrix} \begin{bmatrix} \delta\boldsymbol{U} \\ \delta s_{\mathrm{cont}} \end{bmatrix} = - \begin{bmatrix} \boldsymbol{R} \\ R_{\mathrm{cont}} \end{bmatrix}, \tag{B.7}$$

where $\boldsymbol{R}$ is the Galerkin residuals vector and R_{cont} the residual of the augmenting equation (B.6). The above scheme, which is solved with the Newton-Raphson method, enables the suppression of turning points and, thus, the tracing of entire branches of solution families, as demonstrated in Chapter 4.

B.3 Axisymmetric droplets

B.3.1 Single-pillar structured surface

Similarly to the cylindrical droplet case presented in Chapter 4, we initially test the validity of the augmented YL equation by comparing its predictions against the results

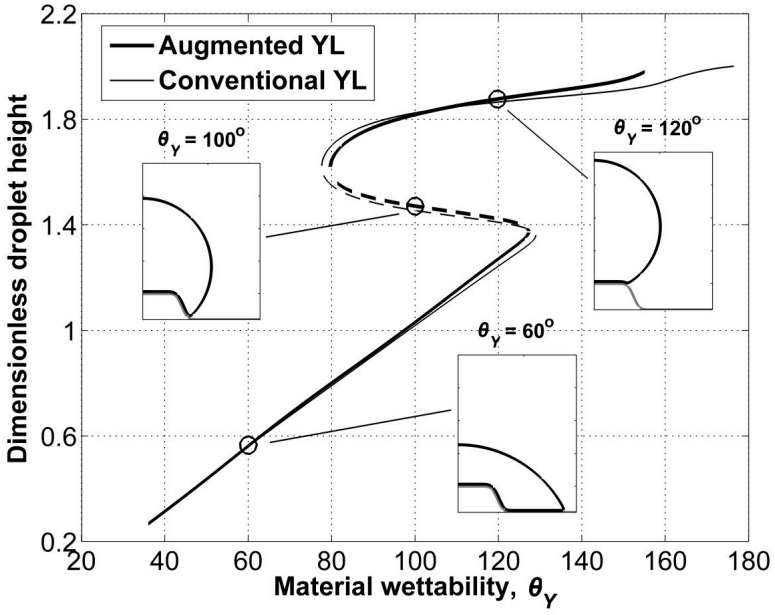

Figure B.1: Dependence of the dimensionless droplet height, $z_{\max}/R_0$, on the material wettability, θ_{Y}, for a single-pillared solid surface structure (Eq. 4.4 with $p_1 = 0.6$, $p_2 = 10$, $p_3 = 5$).

obtained from the conventional form for an axisymmetric droplet wetting a single-pillar structured solid surface; the pillar intersection with the vertical xz-plane is given by Eq. 4.4. We note that the expression of the local mean curvature, C, as well as the constraint equation that singles out the YL, differ in the cylindrical and spherical droplet cases (see the corresponding expressions in Section 2.2.4.a of Chapter 2).

The bifurcation diagram in Fig. B.1 depicts the dependence of the dimensionless droplet height, $z_{\max}/R_0$, on the material wettability, θ_{Y}. As expected, it is observed that both the augmented and the conventional YL equations produce nearly identical results. Furthermore, similarly to the cylindrical droplet case (see Fig. 4.5), the transition between the upper and the lower stable branch is also hysteretic. In the following Section we present equilibrium computations for the case of a droplet resting on a more complex solid surface.

B.3.2 Concentric rings-patterned surface

The proposed methodology can also be applied to a spherical droplet wetting a more complex, concentric rings-patterned solid surface (see Fig. B.2). The intersection of this solid surface with the vertical xz-plane is given by Eq. 4.5. The dependence of the apparent contact angle, θ_{a}, as a function of the material wettability, θ_{Y}, is depicted in Fig. B.3. We can observe that the solution space exhibits multiple S-shaped curves, similarly to the cylindrical droplet case wetting a stripe patterned solid surface (see Fig. 4.7. What is also important here is that the conventional Young-Laplace formulation cannot be applied in such a complex solid surface case, since air pockets are observed to be trapped between

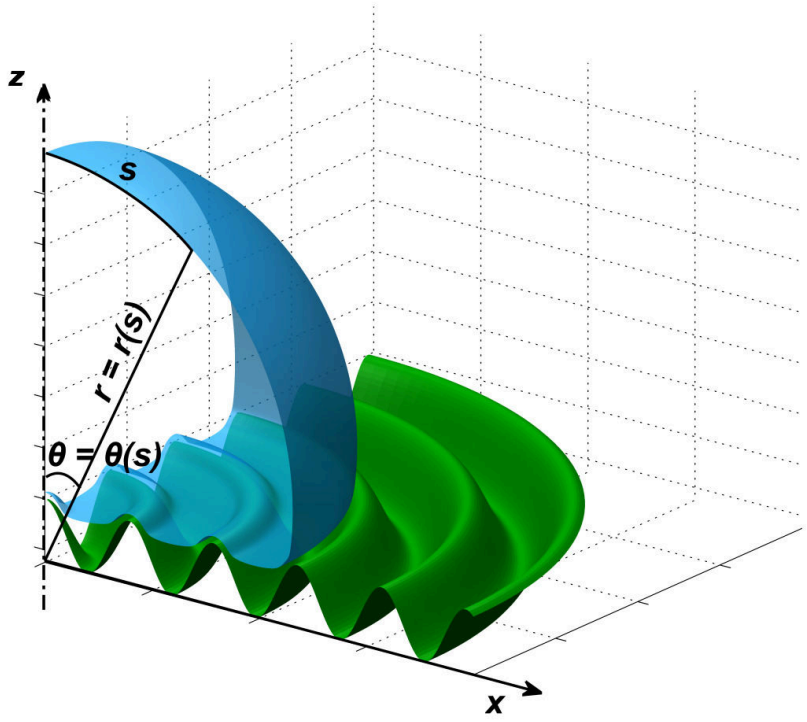

Figure B.2: Axisymmetric droplet (considering axial symmetry around the z-axis) on a ring-patterned solid surface ($p_4 = 8$, $p_5 = 2$ in Eq. 4.5).

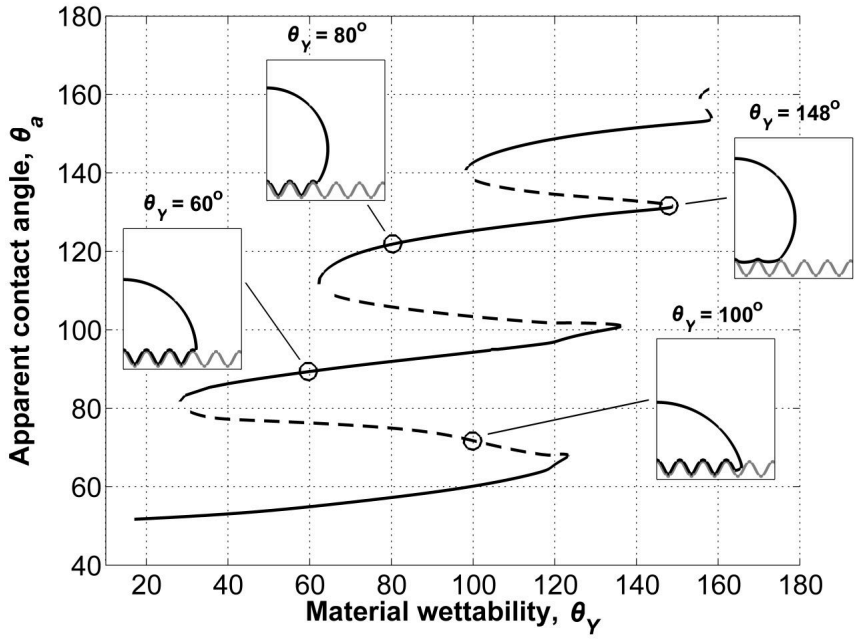

Figure B.3: Apparent wettability dependence of an axisymmetric droplet wetting a concentric rings-patterned solid surface (Eq. 4.5 with $p_4 = 8$, $p_5 = 2$), on the material wettability, θ_Y.

the liquid and the solid phases (see e.g. the droplet shape for $\theta_Y = 148^o$ in Fig. B.3).

B.4 Iterative solution of electrohydrostatics equations

The droplet profile, along with the electric potential distribution, is computed through an iterative process, which consists of the following steps:

1. Given an initial estimation for the droplet profile (provided by the polar coordinates r^{init} and θ^{init}), we compute the electric potential distribution $u(x, z)$ from Equation 5.3. In order to deal with the complex geometry of the droplet and the solid dielectric for the discretization of the electrostatics equation, we generate, using the Gmsh grid generator software [6], an unstructured two-dimensional mesh (due to the translational symmetry). In order to increase the accuracy of computations of the electric field, E, the mesh must be sufficiently dense in the vicinity of the droplet surface (see Fig. B.4). In particular, the produced mesh has a typical size of the order of 10^5 nodes.

2. We compute the magnitude of the electric field, $E = \| \nabla u \|$, and solve the system of non-linear Equations 5.2, 2.34, 2.28, 2.25, with the updated electric stress term, $\frac{N_e \widehat{E}^2}{2}$.

The updated droplet profile is then used in step (1) to compute the new electric field distribution and we repeat the iterative process until the droplet profile converges to an invariant shape. Steps (1) and (2) constitute a mapping:

$$[r\ \theta]^{\mathrm{T}} = \Phi([r^{\text{init}}\ \theta^{\text{init}}]^{\mathrm{T}}), \tag{B.8}$$

and the equilibrium droplet profile $[r^*\ \theta^*]$ satisfies:

$$\boldsymbol{R} \equiv [r^*\ \theta^*]^{\mathrm{T}} - \Phi([r^{\text{init}}\ \theta^{\text{init}}]^{\mathrm{T}} = \boldsymbol{0}. \tag{B.9}$$

The resulting set of non-linear equations, $\boldsymbol{R}$, is solved iteratively with an in-house code using matrix-free Newton-GMRES methods [10]. In particular, the solution of Eq. B.9 is obtained with an iterative Newton-Raphson method, which solves the linearized system:

$$\frac{\mathrm{d}\Phi(\boldsymbol{U})}{\mathrm{d}\boldsymbol{U}}\delta\boldsymbol{U} = -\boldsymbol{R}(\boldsymbol{U}), \tag{B.10}$$

where $\boldsymbol{U} = [r\ \theta]^{\mathrm{T}}$. At each iteration, the estimated steady state solution, $\boldsymbol{U}$, is iteratively updated through $\boldsymbol{U} \rightarrow \boldsymbol{U} + \delta\boldsymbol{U}$, until an adopted convergence criterion is satisfied (e.g., $\| \delta\boldsymbol{U} \| < 10^{-6}$). The computation of the Jacobian matrix, $\frac{\mathrm{d}\Phi(\boldsymbol{U})}{\mathrm{d}\boldsymbol{U}}$, as well as of the residual, $\boldsymbol{R}$, do not require knowledge of the explicit formulation of the equations to be solved. Their values can be estimated by computing the mapping, Φ, at appropriately perturbed values of the corresponding unknowns, $\boldsymbol{U}$. This approach is computationally

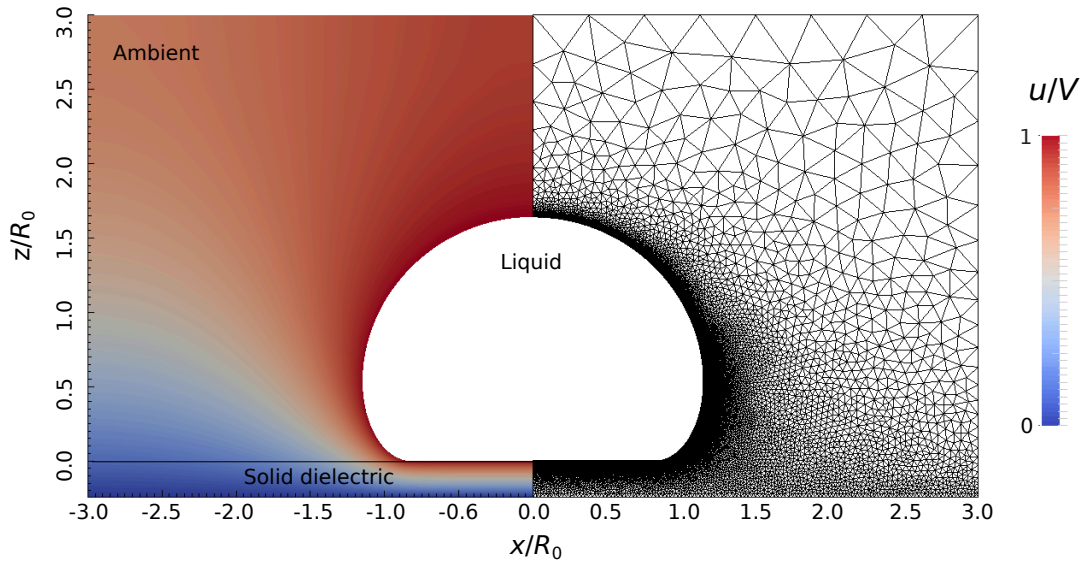

Figure B.4: Electric potential distribution (dimensionless) around a conductive water droplet in oil ambient for $\eta = 1.63$ and $d = 150$ μm PTFE (left side of the figure), along with the corresponding unstructured computational mesh, generated by the Gmsh software [6] (right side of the figure).

inefficient for large systems since the estimation of the Jacobian matrix involves the repeated computation of Φ for perturbations in each of the state space directions. Alternatively, one can use matrix-free iterative solvers for the B.10 system, e.g. the Generalized Minimal Residual Solver (GMRES) [11, 12], which overcomes this inefficiency given that its algorithmic implementation requires low-cost computation of matrix-vector product, $\frac{\mathrm{d}\Phi(\boldsymbol{U})}{\mathrm{d}\boldsymbol{U}}\boldsymbol{q}$. The set of vectors $\boldsymbol{q}$ ($\boldsymbol{q}$ is the orthonormal basis of the Krylov subspace, Kr=span$\{\boldsymbol{b}, \boldsymbol{A}\boldsymbol{b}, \boldsymbol{A}^2\boldsymbol{b}, \boldsymbol{A}^3\boldsymbol{b}, \ldots\}$, with $\boldsymbol{A} = \frac{\mathrm{d}\Phi(\boldsymbol{U})}{\mathrm{d}\boldsymbol{U}}$ and $\boldsymbol{b} = -\boldsymbol{R}$) is used to approximate the solution of the linearized system of equations. By computing Φ from perturbed values of $\boldsymbol{U}$ one estimates the action of the linearized map $\frac{\mathrm{d}\Phi(\boldsymbol{U})}{\mathrm{d}\boldsymbol{U}}$ on known vectors $\boldsymbol{q}$, since:

$$\frac{\mathrm{d}\Phi(\boldsymbol{U})}{\mathrm{d}\boldsymbol{U}}\boldsymbol{q} \approx \frac{\Phi(\boldsymbol{U} + \xi\boldsymbol{q}) - \Phi(\boldsymbol{U})}{\xi}, \tag{B.11}$$

where ξ is a small and appropriately chosen scalar (e.g. $\xi = 10^{-7}$) [11]. In addition, by applying a pseudo arc-length parametric continuation method [9] (see also B.2), we can compute the entire solution space including stable and unstable state solutions (see Section 5.2.4), where the stability is quantified by solving the eigenvalue problem of the Jacobian matrix, $\mathrm{d}\boldsymbol{R}/\mathrm{d}\boldsymbol{U}$.

B.5 Effect of the disjoining pressure parameters

In this Section we present the sensitivity of the augmented electrohydrostatics equations solution (see Chapter 5) by modifying the disjoining pressure profile (isotherm) (Eq. 2.42). In particular, we modify the values of exponents C_1 and C_2, which control

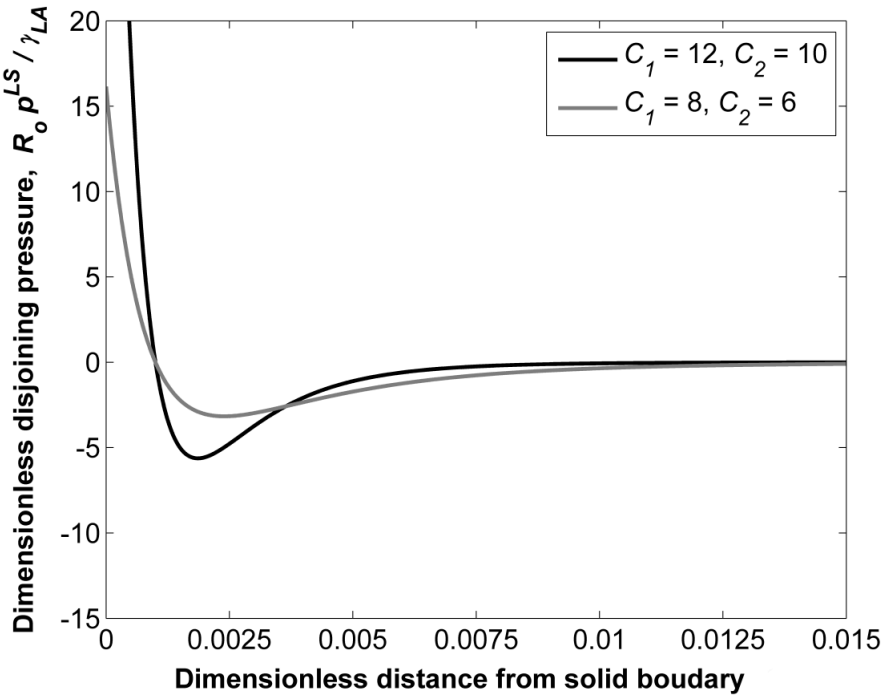

Figure B.5: Disjoining pressure profiles (isotherms), as a function of the dimensionless liquid-solid distance, δ/R_0, for different parameter values C_1 and C_2 (θ_Y=170°).

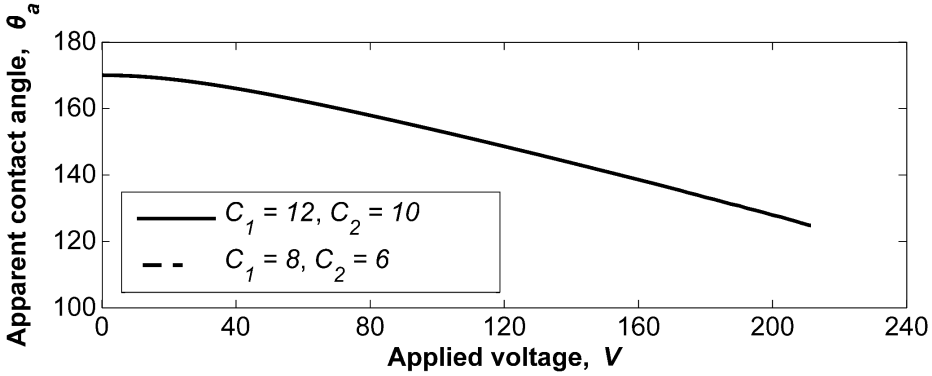

Figure B.6: Dependence of the apparent contact angle, θ_a, on the applied voltage for different parameter values (C_1, C_2) of the disjoining pressure (d = 10 μm).

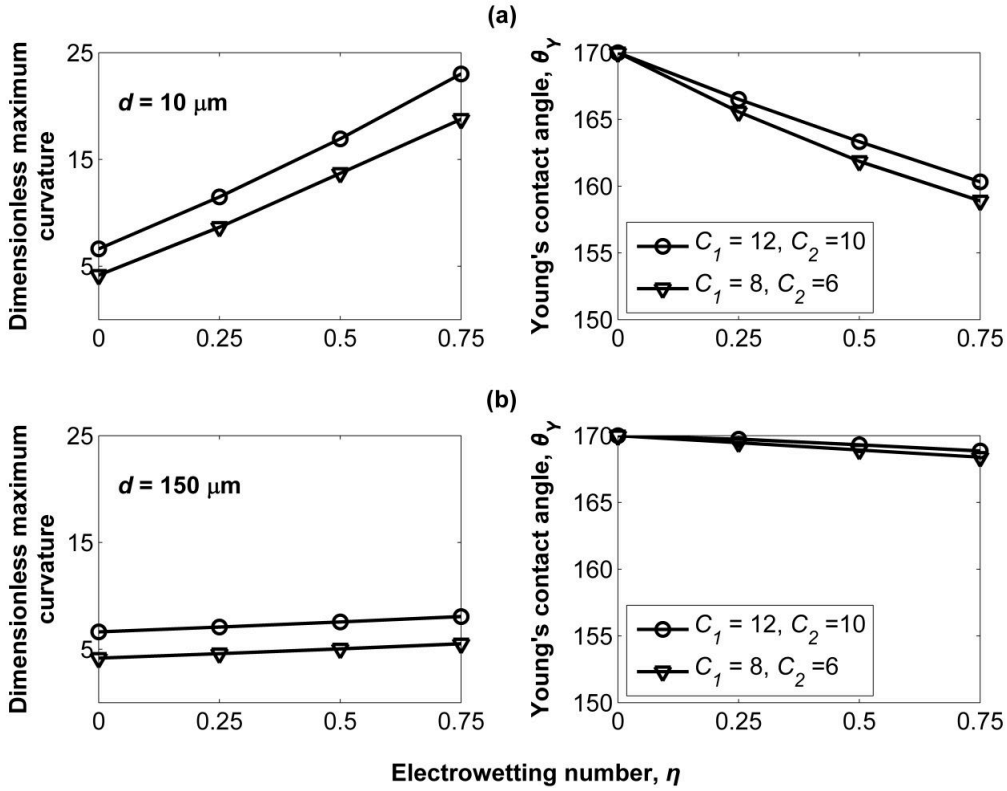

Figure B.7: Dependence of the dimensionless maximum curvature of the droplet surface (left panel) and of the Young's contact angle, θ_{Y}, (right panel) on the electrowetting number, η, for two sets of disjoining pressure exponents (C_1=8, C_2=6 and C_1 = 12, C_2 = 10) and dielectric thicknesses (a) d=10 μm and (b) d=150 μm.

the range within which the molecular forces are active . In particular, the pressure term, $\left[\frac{\gamma_{\mathrm{LA}}}{R_0}\left(\frac{\sigma}{\delta/R_0+\epsilon}\right)^{C_1}\right]$, dominating at short distance, models the repulsion between the solid and the liquid phases, whereas the pressure term, $\left[-\frac{\gamma_{\mathrm{LA}}}{R_0}\left(\frac{\sigma}{\delta/R_0+\epsilon}\right)^{C_2}\right]$, which is dominant at large distance, constitute the attractive part. In Fig. B.5, we illustrate the disjoining pressure isotherm for different C_1 and C_2 values. Essentially, we observe that by increasing C_1 and C_2, the range of molecular interactions decreases.

In Fig. B.6, we depict the effect of the applied voltage on the apparent contact angle, θ_{a}, of a cylindrical droplet on a PTFE substrate with thickness d = 10 μm for two different sets of C_1 and C_2 exponent values (C_1 = 12, C_2 = 10 and C_1 = 8, C_2 = 6). The results obtained for the different parameter set values are in excellent agreement (the lines are optically indistinguishable), which suggests that the macroscopic behavior of the droplet does not depend on the parameters C_1, C_2 values (of course when they vary in a specified range). The same applies for all dielectric thickness cases.

Computations of the curvature and field distribution in the vicinity of the TPL, (presented in Section 5.2.3), indicate that the magnitude of the developed electric stresses in the vicinity of the TPL is significantly large (compared to the disjoining pressure), when decreasing the thickness of the solid dialectic; this causes variations on the maximum

curvature, as well as the Young's contact angle values. Here, we examine whether a change of the disjoining pressure isotherm has an effect on this trend.

In Fig. B.7, we present computations of the dimensionless maximum local mean curvature of the droplet surface (left panel) and the Young's contact angle (right panel) as a function of the electrowetting number, η, for two different sets of parameter values C_1 and C_2 and dielectric thickness (a) d=10 μm and (b) d=150 μm. One can observe that the maximum curvature absolute values differ for different C_1 and C_2 values. However, changing the disjoining pressure isotherm type does not alter the general trend of the Young contact angle to remain practically insensitive to the applied voltage when the dielectric thickness is sufficiently large, as opposed to thinner dielectric thickness cases.

APPENDIX C

C.1 Viscous spreading: Validation with Tanner's law

In the case of wettability driven spreading, the radius of the wetted area can be described by the well-known Tanner's law [13]:

$$R_s \sim t^{1/10}, \tag{C.1}$$

where the only factor that limits spreading is the viscous dissipation near the contact line. Eq. C.1 has been experimentally verified [14] and is an excellent problem to benchmark our modeling approach for viscous-dominated dynamics. In Fig. C.1 we demonstrate the dynamic behavior of a glycerin/water mixture droplet spreading on a hydrophilic substrate ($\theta_{\mathrm{Y}} = 30^{\mathrm{o}}$), assuming an intrinsic surface roughness of $r_{\mathrm{f}} = 1.01$. Starting from an equilibrium solution of $\theta_{\mathrm{Y}} = 93.5^{\mathrm{o}}$, it is observed that our simulations can successfully capture Tanner's law at intermediate times ($t \in (1, 26)$ ms). For $t > 26$ ms the droplet reaches equilibrium and is finally immobilized. The dimensionless numbers in this case correspond to Re = 1.41 and Ca = 0.2, respectively. For both cases, we use $u_0 = \sqrt{gR_0} = 0.11$ m/s as a characteristic velocity (where g is the gravity constant), since the impact velocity is negligible.

Regarding the dynamic contact angle, our results follow roughly the Tanner's law predictions ($\theta_{\mathrm{d}} \approx t^{-3/10}$) for intermediate times ($5 < t < 26$ ms) (see Fig. C.2), however, smaller scale roughness is required in order to avoid the intense contact angle fluctuations (attributed to the contact line pinning-depinning on the substrate corrugations) and fully recover the Tanner's regime. For $t > 26$ ms the droplet reaches equilibrium and the dynamic contact angle is fixed at $\approx 35^{\mathrm{o}}$.

C.2 Spreading of a water droplet

Here we present computations for the case of a water droplet spreading on a flat surface with no initial velocity (see Fig C.3). It is observed that the simulation for a roughened

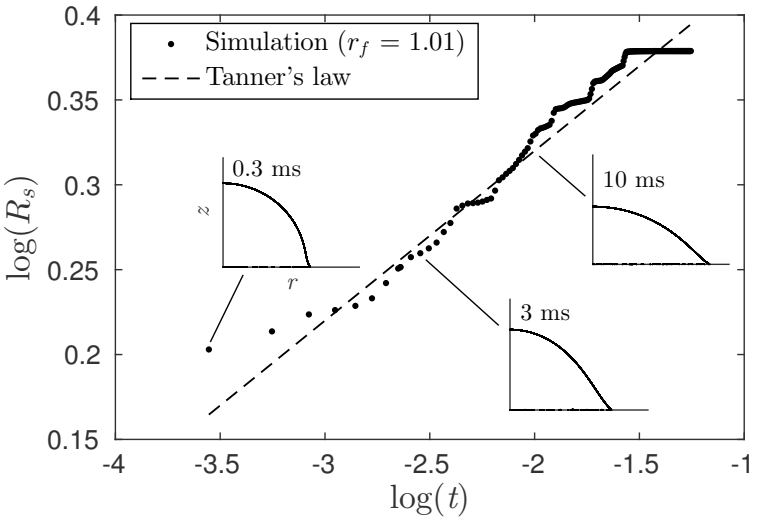

Figure C.1: Evolution of the contact radius as a function of time for a glycerin/water mixture droplet on a hydrophilic substrate (θ_Y = 30°).

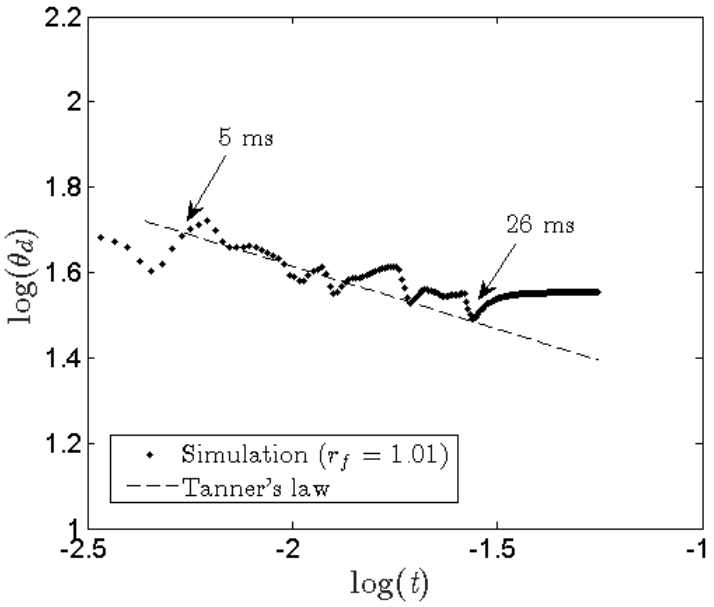

Figure C.2: Temporal evolution of the dynamic contact angle for a glycerin/water mixture droplet on a hydrophilic substrate (θ_Y = 30°).

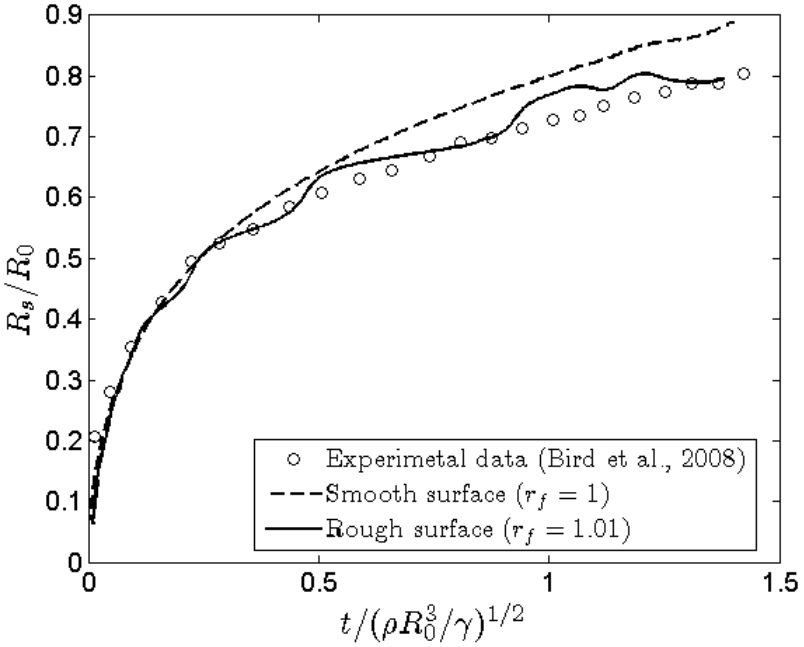

Figure C.3: Temporal evolution of the normalized contact radius of a water droplet spreading on a hydrophobic (θ_Y = 117°) surface: simulations against experimental data from Bird et al. [15] (R_0 = 1.225 mm, ρ = 1000 Kg/m^3, γ_{LA} = 0.072 N/m).

surface (assuming an intrinsic surface roughness of r_f = 1.01) adequately captures the droplet dynamic behavior (experimental data by Bird et al. [15]). On the contrary, the contact radius growth is overestimated when considering an ideally smooth solid surface. A similar droplet behavior is presented in Section 6.2.1 for the experiments of Sikalo et al. [16] (Fig. 6.3). The contact radius fluctuations, observed in the case of the rough surface, indicate that the roughness length scale is relatively large. A more fine-scale simulation (with smaller roughness micro-structures on the solid surface, still maintaining the same roughness factor) would be required in order to obtain a smoother curve, at the expense of considerably increased computational cost.

C.3 Effect of the disjoining pressure parameters

C.3.1 Spreading droplets

In this Section, we investigate whether a modification in the parameters C_1, C_2 and σ of the disjoining pressure (see Eq. 2.42) has an impact on the spreading behavior of a droplet on a solid substrate (see Chapter 6). In all cases we study a glycerin/water mixture droplet spreading on a wax solid surface with a roughness factor, r_f = 1.15. In particular, in Fig. C.4 by comparing the contact radius evolution for two different C_1, C_2 parameters sets ($C_1 = 12, C_2 = 10$ and $C_1 = 14, C_2 = 12$), we conclude that the results are in remarkable agreement despite the different disjoining pressure profiles (an increase

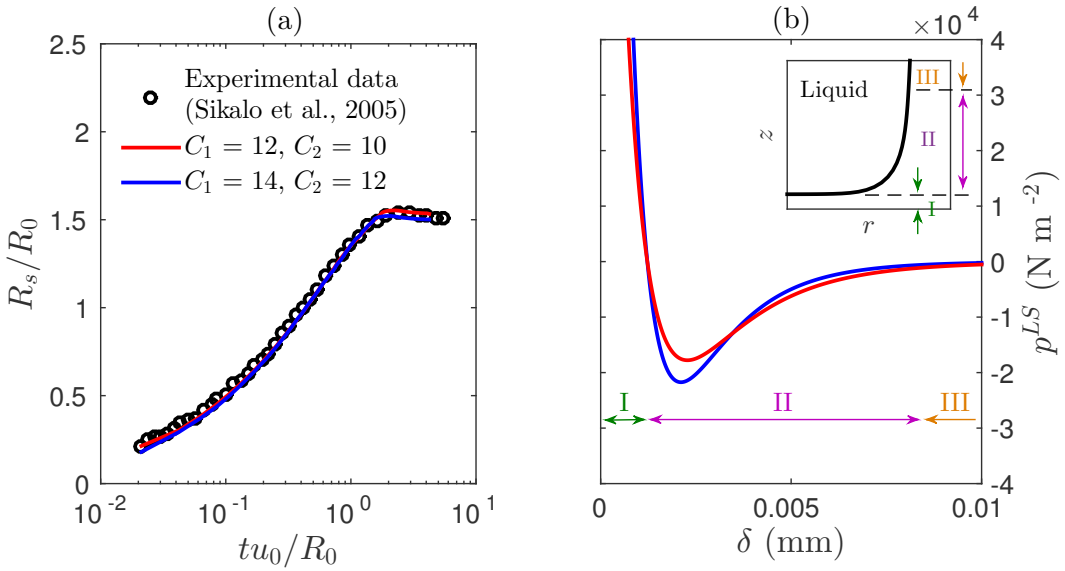

Figure C.4: (a) Normalized contact radius of a glycerin/water mixture droplet impacting on wax surface: simulations against experimental data from Sikalo et al. [16] for different C_1 and C_2 parameters of the disjoining pressure (see Eq. (2.42)). The arising disjoining pressure profiles are illustrated in (b) as a function of the distance from the solid boundary, δ. The inset in (b) shows the action range of the micro-scale forces in the vicinity of the contact line; attractive interactions are dominant in region (II), whereas repulsive forces are generated in region (I), keeping the liquid and solid phases separated. For $\delta \approx 0.01$ mm and beyond (region (III)), the micro-scale liquid-solid interactions are negligible.

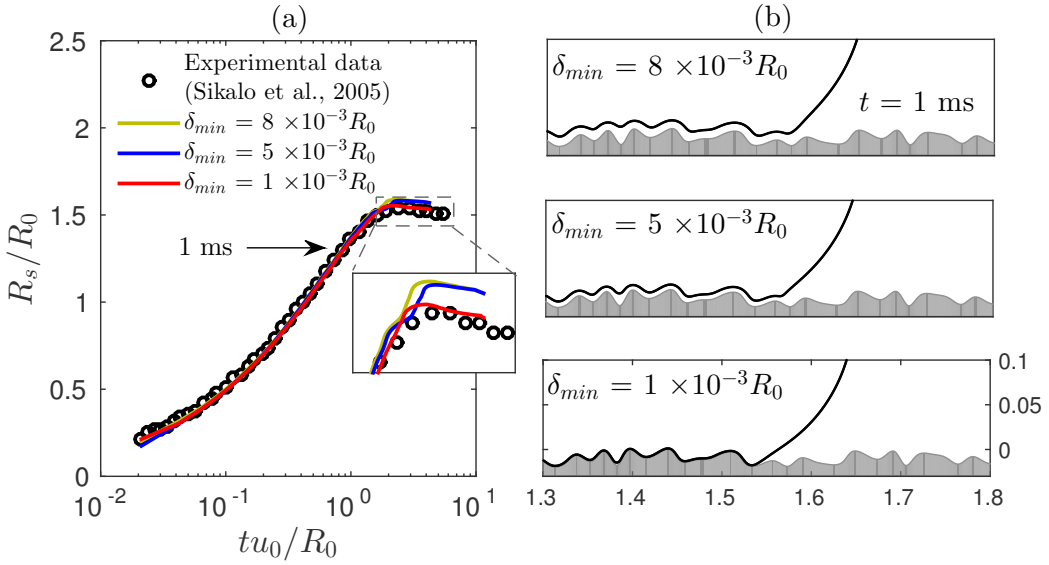

Figure C.5: (a) Normalized contact radius evolution of a glycerin/water mixture droplet impacting on wax surface: simulations against experimental data from Sikalo et al. [16] for different minimum distances ($\delta_{\min} \in [1 \times 10^{-3} R_0, 8 \times 10^{-3} R_0]$) between the solid and the liquid phase. The corresponding droplet profiles for the different values of $\delta_{\min}$ are demonstrated in (b) at t = 1 ms.

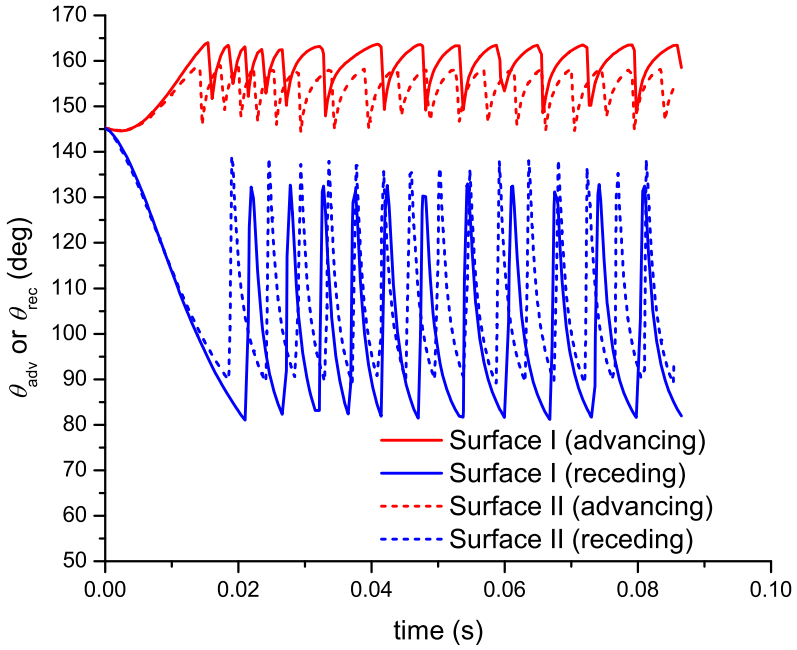

Figure C.6: Advancing and receding contact angles of a glycerin/water mixture droplet sliding on surfaces I and II (see Fig. 7.3 at Chapter 7), inclined at $\alpha = 60^{o}$. The average dynamic hysteresis is approximately equal to 53^{o} for the surface I (Wenzel state) and 44^{o} for the surface II (Cassie-Baxter state).

in the exponents C_1, C_2 leads to a narrower range of micro-scale interaction as shown in Fig. C.4b). Next, in Fig. C.5 we investigate the effect of the minimum distance, $\delta_{\min}$, between the liquid and solid phases, which encompasses the impact of σ and ϵ as follows: $\delta_{\min} = R_0(\sigma - \epsilon)$. Specifically, starting from a large initial value ($\delta_{\min} = 8 \times 10^{-3} R_0 = 9.8 \times 10^{-3}$ mm) we reduce the minimum distance by lowering the parameter σ ($\sigma \in [9{\times}10^{-3}, 16{\times}10^{-3}]$) keeping constant $\epsilon = 8{\times}10^{-3}$. Conclusively, as presented in Fig. C.5a, the computational results converge to the experimental data by reducing the minimum liquid-solid distance, $\delta_{\min}$; the lower $\delta_{\min}$ value is equal to $1 \times 10^{-3}\, R_0 = 1.225 \times 10^{-3}$ mm, which is obtained for $\sigma = 9 \times 10^{-3}$.

C.3.2 Sliding droplets

In this section we investigate the influence of the C_2 and σ parameters value on the dynamic hysteresis on the droplet. The C_2 parameter controls the range of attractive liquid-solid interactions and the σ parameter regulates the minimum distance of separation between the solid and the liquid phases. We initially present, in Fig. C.6, the temporal evolution of advancing and receding contact angles of a glycerin/water mixture droplet sliding on surfaces I and II (see also Fig. 7.3 at Chapter 7), inclined at $\alpha = 60^{o}$. The disjoining pressure parameters we use in this case are: $C_1 = 12$, $C_2 = 10$, $\sigma = 9{\times}10^{-3}$

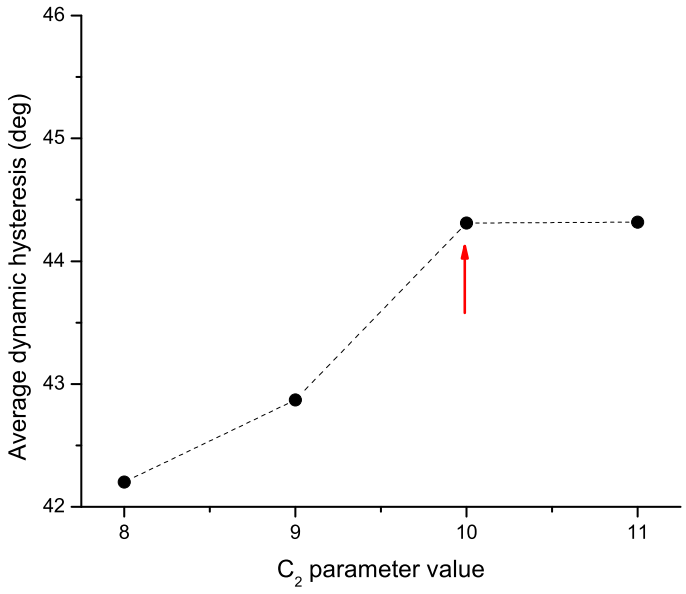

Figure C.7: Average dynamic hysteresis of a glycerin/water mixture droplet sliding on surface II for different C_2 parameter values. The C_2 value used in our simulations is marked with the red arrow.

and $\epsilon = 8 \times 10^{-3}$.

In Fig. C.7 we demonstrate the average dynamic hysteresis (the difference between the mean value of advancing and the receding contact angles) of a glycerin/water mixture droplet sliding on surface II (see Fig. 7.3 at Chapter 7), as a function of the C_2 parameter. We observe that our results converge to a constant value above a threshold C_2 value ($C_2 \geqslant 10$). Similarly, in Fig. C.8 we observe that the computational results are virtually the same below a threshold value of σ ($\sigma \leqslant 9 \times 10^{-3}$).

C.3.3 Oscillated droplets

Here we perform a sensitivity analysis regarding the impact of the C_2 and σ parameters value on the dynamic behavior of a droplet on an asymmetrically patterned surface (see Chapter 7). We have chosen to perform our analysis for vertical vibrations since the droplet deforms to a greater extend, resulting to an increased influence of the liquid-solid interactions. Moreover, in order to test the reliability of our formulation, we use the finest structure corrugations ($s = 0.75$).

In Fig. C.9 we present the droplet position, under the influence of vertical vibrations, at $t = 8T_f$, for different C_2 parameter values. We observe that the effect of this parameter is negligible above a threshold value ($C_2 \geqslant 9$). Note that in our simulations we use $C_2 = 10$ (red arrow in Fig. C.9). The above computations have been carried out for the same C_1 parameter value ($C_1 = 12$). Specifically, we have not performed the same analysis for

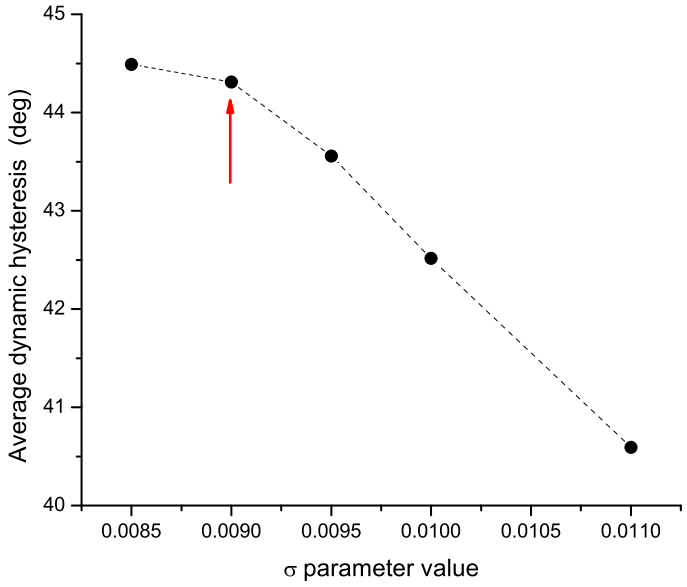

Figure C.8: Average dynamic hysteresis of a glycerin/water mixture droplet sliding on surface II for different σ parameter values. The σ value used in our simulations is marked with the red arrow.

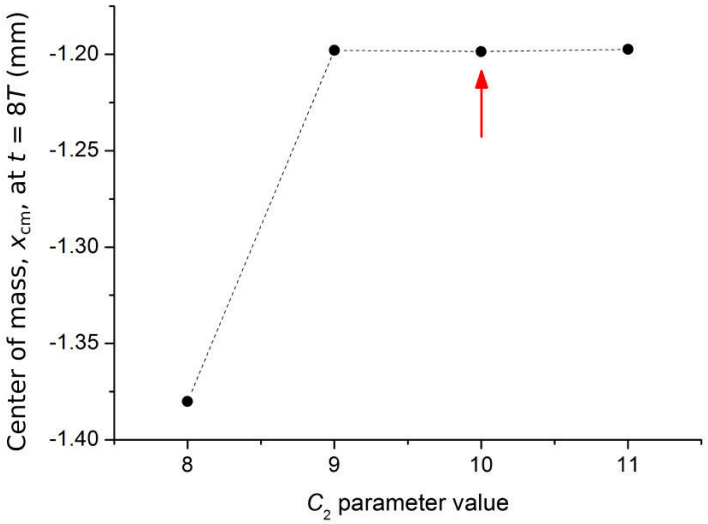

Figure C.9: Center of mass, x_{cm}, of a glycerin/water mixture droplet on a vertically vibrated asymmetrically patterned substrate (structure scaling, $s = 0.75$), at $t = 8T_{\mathrm{f}}$, for different C_2 parameter values. The oscillation frequency is set to the resonance ($f = 41.8$ Hz) and the amplitude is $A = 0.375$ mm. The C_2 value used in our simulations is marked with the red arrow.

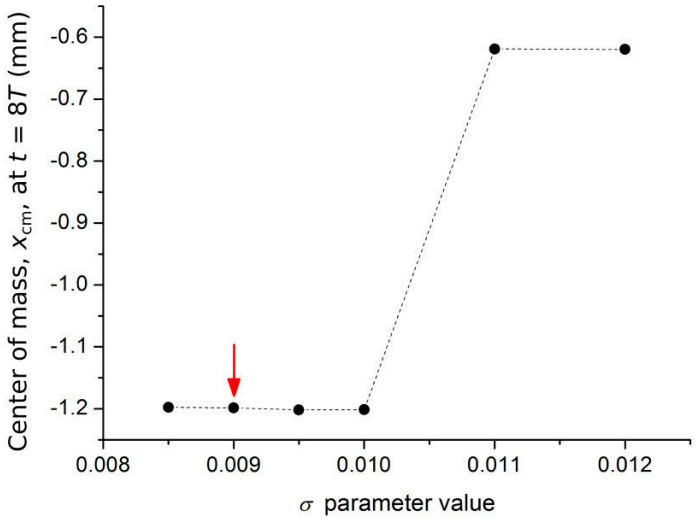

Figure C.10: Center of mass, x_{cm}, of a glycerin/water mixture droplet on a vertically vibrated asymmetrically patterned substrate (structure scaling, $s = 0.75$), at $t = 8T_f$, for different σ parameter values. The oscillation frequency is set to the resonance ($f = 41.8$ Hz) and the amplitude is $A = 0.375$ mm. The σ value used in our simulations is marked with the red arrow.

the latter parameter (C_1), which regulates the repulsive interactions magnitude as the droplet touches the solid surface, since it slightly affects the disjoining pressure isotherm at the contact line.

The effect of the liquid-solid minimum distance, δ_{min}, is also investigated in Fig. C.10. In particular, δ_{min} is defined as $R_0(\sigma - \epsilon)$. Thus by reducing the value of σ, keeping constant $\epsilon = 8 \times 10^{-3}$, we shrink this intermediate layer. By performing a sensitivity analysis we observe the computational results are identical below a threshold value of σ ($\sigma \leqslant 1 \times 10^{-2}$). Note that in our simulations we use $\sigma = 9 \times 10^{-3}$ (red arrow in Fig. C.10).

C.4 Effect of the computational mesh size

C.4.1 Spreading droplets

The position of the droplet interface is tracked by the deformed mesh and thus high mesh density is required along the boundary of the domain (see Fig. C.11). The accuracy of the results of an impacting droplets is tested against discretization refinement for the case of a glycerin/water mixture droplet impacting on the most roughened substrate ($r_f = 1.2$) (see Chapter 6). In particular in Fig. C.12 we depict the relative error of the droplet shape coordinates (r, z) for different meshes, compared with a reference solution. The reference solution has the denser mesh with 7×10^3 computational elements along the droplet surface (note that a typical size of the computational problem is of the order of

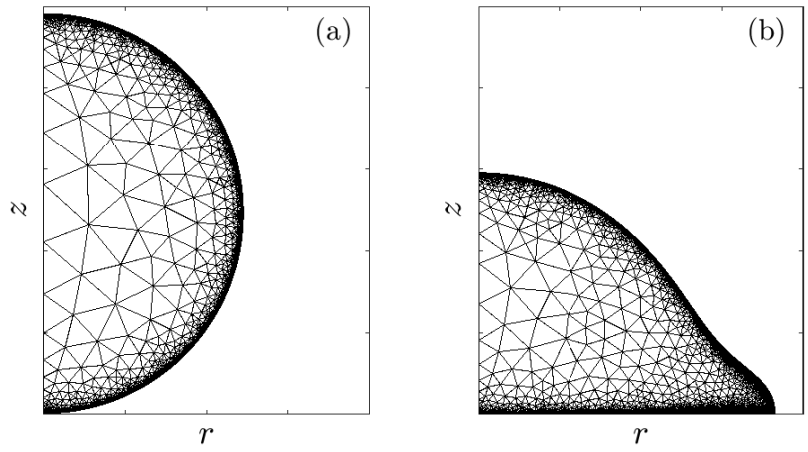

Figure C.11: (a) Initial and (b) deformed computational mesh of an axisymmetric droplet, impacting on a perfectly smooth solid surface, generated by the COMSOL Multiphysics® commercial software.

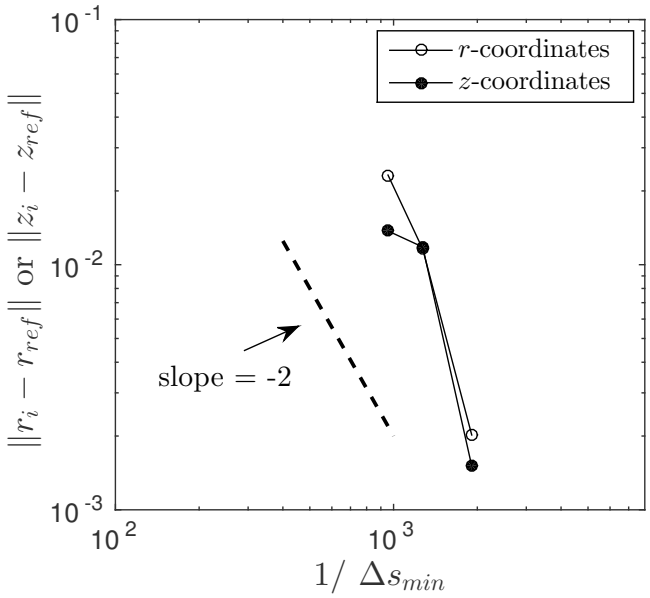

Figure C.12: The relative error of the droplet shape coordinates, when impacting on a rough wax surface (r_f = 1.2, t = 5 ms) for various meshes. A reference solution with 7×10^3 elements along the droplet surface is used (the length of the smallest computational element, Δs_{min} = 0.45×10^{-3} mm).

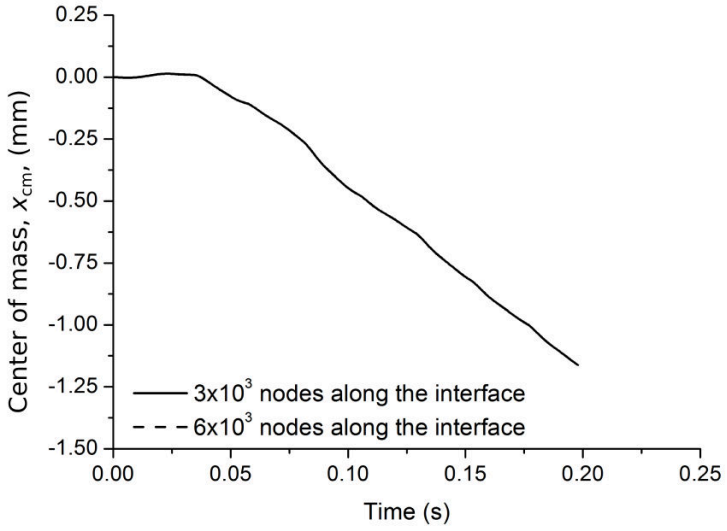

Figure C.13: Temporal evolution of the droplet's center of mass (the horizontal position), x_{cm}, of a glycerin/water mixture droplet on a vertically vibrated asymmetrically structured substrate (structure scaling, $s = 0.75$). Two cases, of different mesh size (with 3×10^3 and 6×10^3 nodes along the droplet surface), are examined. The oscillation frequency is set to the resonance ($f = 41.8$ Hz) and the amplitude equals to $A = 0.375$ mm, for both cases.

10^5 degrees of freedom, including the velocity field, pressure and mesh deformation). For the calculation of the norms, the values of the droplet shape coordinates (r, z) were interpolated at 250 points which are placed on equal distances throughout the droplet surface of the coarsest mesh. Next, the r, z coordinates were interpolated for the other meshes, at the positions corresponding to the 250 arc-length coordinates of the coarsest mesh. Finally, as presented in Fig. C.12 the convergence with mesh refinement is super-quadratic.

C.4.2 Oscillated droplets

In this section we test the accuracy of our results, of a droplet moving on an asymmetrically patterned surface (see Chapter 7), against mesh refinement. In particular, in Fig. C.13 we present the temporal evolution of the droplet's center of mass (the horizontal position), x_{cm}, under vertical forced vibrations, for different mesh sizes. We observe that both simulations are in remarkable agreement (the two lines are practicably indistinguishable) therefore we conclude that our results (featuring $\approx 6 \times 10^3$ nodes along the droplet surface) are insensitive with the discretization refinement. We have selected to perform the above analysis for vertical substrate vibrations due to the larger droplet deformation in this case.

APPENDIX D

D.1 Surface preparation for the electrowetting experiments

Two different stacks (one thin and one thick) were prepared to test the effect of dielectric thickness on the contact angle reversibility, in electrowetting experiments. First, one thin dielectric stack, consisting of a 400 nm TEOS and a 1 μm PMMA layer, was assembled on a silicon wafer. For the preparation of the thick dielectric layer, SU8 (Microchem, SU8 3050) was spun on a silicon wafer. The spinning speed was set to 1500 rpm to achieve a 75 μm thick SU8 film. After spinning the surface was exposed to UV light (wavelength 365 nm) for 3.5 min and hard baked at 150 °C for 30 min.

D.1.1 Submicron (quasi-)ordered pillar arrays

The pillar arrays were prepared using a combination of colloidal lithography and plasma etching. PS particles with initial diameter of 0.5 μm were self-assembled creating a monolayer using spin coating on top of the different dielectric layers following the same procedure described in the works [17, 18]. The etching conditions used to create the multiscale re-entrant pillar topography shown in Fig. 9.1a, were presented in a recent work about extremely robust superamphiphobic surfaces [19]. We note that the fabrication approach enables full control over the pillar diameter, profile, height and spacing, key factors in optimizing the surface wetting properties [18, 20]. The two step etching process followed to create the topography are:

1. 60 s anisotropic etching at 1900 W, 15 °C, 0.75 Pa, 100 sccm oxygen flow and 250 W bias power and
2. 15 s isotropic etching at 1900 W, 15 °C, 0.75 Pa, 100 sccm oxygen flow and 0 W bias power.

The plasma processes were done on the high-density plasma reactor (Helicon plasma reactor, Micromachining Etching Tool, MET, from Adixen-Alcatel) described elsewhere [21].

D.1.2 Random micro-nanotextured COP surfaces

188 μm thick COP film was micro-nanotextured for 4 min using conditions that create highly anisotropic etching (1900 W, 15 ^{o}C, 0.75 Pa, 100 sccm oxygen flow and 250 W bias power) in the same high-density plasma reactor. The resulting topography is shown in Fig. 9.1b.

D.1.3 Hydrophobization of the surface

All surfaces after the oxygen plasma etching became hydrophilic exhibiting contact angles below 10^{o}. To render them superhydrophobic a 1 wt% Teflon AF 1600 solution was spun at 7000 rpm on the top of the surfaces creating a conformal 30 nm thick coating. After the spinning process, the surfaces were baked in air, at 95 ^{o}C for 10 min. For the preparation of the 1 wt% Teflon AF 1600 solution Teflon® AF 1600 was diluted at Fluorinert® Fluid FC-77 solvent.

We report that the all surfaces described in this Appendix have been fabricated in the Institute of Nanoscience and Nanotechnology at NCSR "Demokritos" (Aghia Paraskevi, Attica, Greece).

References

[1] A. W. Adamson and A. P. Gast. *Physical Chemistry of Surfaces*. Wiley, 1997.

[2] P. Pujado, C. Huh, and L. Scriven. "On the attribution of an equation of capillarity to Young and Laplace". In: *Journal of Colloid and Interface Science* 38.3 (1972), pp. 662–663.

[3] C. Weatherburn. *Differential Geometry of Three Dimensions*. τ. 1. Cambridge University Press, 2016.

[4] B. Dacorogna and P. Marcellini. *Implicit partial differential equations, volume 37 of Progress in Nonlinear Differential Equations and their Applications*. 1999.

[5] E Fares and W Schröder. "A differential equation for approximate wall distance". In: *International Journal for Numerical Methods in Fluids* 39.8 (2002), pp. 743–762.

[6] C. Geuzaine and J.-F. Remacle. "Gmsh: A 3-D finite element mesh generator with built-in pre-and post-processing facilities". In: *International Journal for Numerical Methods in Engineering* 79.11 (2009), pp. 1309–1331.

[7] O. Zienkiewicz, R. Taylor, and J. Zhu. *The Finite Element Method: Its Basis and Fundamentals*. Elsevier Science, 2005.

[8] N. T. Chamakos. "Computational analysis of solid surfaces wetting by droplets". in Greek. Diploma Thesis. School of Chemical Engineering, National Technical University of Athens, Sept. 2011.

[9] H. Keller. "Lectures on numerical methods in bifurcation problems". In: *Applied Mathematics* 217 (1987), p. 50.

[10] M. E. Kavousanakis, C. E. Colosqui, I. G. Kevrekidis, and A. G. Papathanasiou. "Mechanisms of wetting transitions on patterned surfaces: continuum and mesoscopic analysis". In: *Soft Matter* 8.30 (2012), pp. 7928–7936.

[11] C. Kelley. *Iterative methods for linear and nonlinear equations*. Siam, 1995.

[12] Y. Saad. *Iterative methods for sparse linear systems*. Siam, 2003.

[13] L. Tanner. "The spreading of silicone oil drops on horizontal surfaces". In: *Journal of Physics D: Applied Physics* 12.9 (1979), p. 1473.

[14] A.-L. Biance, C. Clanet, and D. Quéré. "First steps in the spreading of a liquid droplet". In: *Physical Review E* 69.1 (2004), p. 016301.

[15] J. Bird, S. Mandre, and H. Stone. "Short-Time Dynamics of Partial Wetting". In: *Physical Review Letters* 100.23 (June 2008), p. 234501. ISSN: 0031-9007.

[16] Š Šikalo, C Tropea, and E. Ganić. "Dynamic wetting angle of a spreading droplet". In: *Experimental Thermal and Fluid Science* 29.7 (2005), pp. 795–802.

[17] K. Ellinas, A. Smyrnakis, A. Malainou, A. Tserepi, and E. Gogolides. ""Mesh-assisted" colloidal lithography and plasma etching: A route to large-area, uniform, ordered nano-pillar and nanopost fabrication on versatile substrates". In: *Microelectronic Engineering* 88.8 (2011), pp. 2547–2551.

[18] K Ellinas, A Tserepi, and E Gogolides. "From superamphiphobic to amphiphilic polymeric surfaces with ordered hierarchical roughness fabricated with colloidal lithography and plasma nanotexturing". In: *Langmuir* 27.7 (2011), pp. 3960–3969.

[19] K. Ellinas, M. Chatzipetrou, I. Zergioti, A. Tserepi, and E. Gogolides. "Superamphiphobic Polymeric Surfaces Sustaining Ultrahigh Impact Pressures of Aqueous High-and Low-Surface-Tension Mixtures, Tested with Laser-Induced Forward Transfer of Drops". In: *Advanced Materials* 27.13 (2015), pp. 2231–2235.

[20] K. Ellinas, S. P. Pujari, D. A. Dragatogiannis, C. A. Charitidis, A. Tserepi, H. Zuilhof, and E. Gogolides. "Plasma micro-nanotextured, scratch, water and hexadecane resistant, superhydrophobic, and superamphiphobic polymeric surfaces with perfluorinated monolayers". In: *ACS Applied Materials & Interfaces* 6.9 (2014), pp. 6510–6524.

[21] E Gogolides, M Vlachopoulou, K Tsougeni, N Vourdas, and A Tserepi. "Micro and nano structuring and texturing of polymers using plasma processes: potential manufacturing applications". In: *International Journal of Nanomanufacturing* 6.1-4 (2010), pp. 152–163.